Selda M. Sherifova, MSc.

Mechanical Testing and Modeling of Human Thoracic Aortic Tissues in Health and Disease

DOCTORAL THESIS

to achieve the university degree of

Doktorin der technischen Wissenschaften

submitted to

Graz University of Technology

Supervisor

Univ.-Prof. Dipl.-Ing. Dr.techn. Gerhard A. Holzapfel

Institute of Biomechanics

Graz, September 2019

AFFIDAVIT

I declare that I have authored this thesis independently, that I have not used other than the declared sources/resources, and that I have explicitly indicated all material which has been quoted either literally or by content from the sources used. The text document uploaded to TUGRAZonline is identical to the present doctoral thesis.

Date

Signature

Preface

Firstly, I would like to thank Prof. Gerhard A. Holzapfel for giving me the opportunity to move to a city with many sunny days to work on my PhD, and for supporting and guiding my career development. It was a pleasure to learn from him. I am thankful to Assoc. Prof. David Nordsletten for accepting to be the co-examiner of my thesis.

I would like to thank Gerhard Sommer for his guidance in the laboratory; and Peter Regitnig and Christian Viertler for their invaluable and delightful discussions. The work presented in this PhD thesis would not be possible without the valuable human tissue samples provided thanks to the donors, A. Donerer, T. Caranasos, A. DeAnda, O.E. Dapunt, P. Oberwalder, B.E Griffith, M.A. Smith, and T. Holt. Furthermore, I would like to thank Prof. Ray W. Ogden for his support.

Working with the past and the present members of the Institute of Biomechanics has been a unique experience and a great pleasure. In addition, I was lucky to have the opportunity to supervise students. This gave me the chance to see things both from student's and supervisor's perspective while trying to figure out the best ways to communicate. I would also like to thank my students I had the pleasure to supervise for their help in data collection.

It has been extremely challenging to find the right words to express my gratitude to my family. I am thankful for their support and guidance through life. I have always looked up to my mother for her incredible patience, to my father for his skills in mentorship, and to my brother for his ability and desire in taking the opposing position sometimes only to advance our perspectives.

Finally, I would like to thank all my friends for their support in good and bad days. In particular, I would like to thank Stefan and Dejan for their peculiar way of communication with each other but also for our great dinner sessions discussing about, in summary, physical and mental borders; Hanna for her companionship and for our little (!) trips; Feride for her joyful perspectives and for introducing me to opera; to Nadia for our balcony sessions; Justyna, Andreas, Markus, Manos, Bettina, Daniel and Jakob for our discussions; Thomas for telling me all those little historical stories and for the insider tips to Styria; Ece, Aysim, Elcin, Ozge, Kadircan, Aylin and Enes for being there at any step despite the physical distance. Much would be missing from my life without you.

Abstract

The aortic wall that consists of the collagen fibers embedded in an elastic matrix can be seen and modeled as a fiber-reinforced composite material. It is known that the microstructure, especially the mean orientation of collagen fibers and their dispersion around this orientation, determines the stress-strain response of the tissue. Thoracic aneurysms and dissections, the two pathologies that are the main subject herein, are fatal in case of rupture and they are characterized by changes to the wall microstructure. Hence, there is a pressing need to improve our understanding of the tissue failure.

To this aim, the first study presents the strength of the aneurysmatic and dissected human thoracic aortas under different loading modes focusing on failure properties under shear loading. The uniaxial tests revealed that the aortic media was the strongest in the circumferential direction, followed by the longitudinal and the radial directions. In addition, the failure stress was approximately 10-fold higher under out-of-plane shear loading compared with in-plane shear loading. These findings were explained by the collagen fiber architecture considering their fiber-reinforcing role in the aortic wall.

The subsequent study and the first review article of this PhD thesis stresses the crucial need to model the dispersed collagen fiber structure to accurately predict the deformation characteristics of soft biological tissues. It shows that the predictions from both the angular integration and the generalized structure tensor methods agree well with the experimental data. It also points to the need for additional mechanical and microstructural data to better inform the material modeling.

The second review article looks at aortic wall rupture and dissection from a material failure perspective. An extensive literature review on the mechanical tests that are used to quantify strength is provided. Based on the microstructural differences and the various mechanisms that can lead to rupture or dissection, it is suggested that an ideal failure model should reflect the influence of microstructure at different time and length scales on tissue strength under different loading modes.

The last study in this PhD thesis employed uniaxial extension tests, second-harmonic generation imaging and histological investigations to reveal the potential relations between the tissue strength and its microstructure. Mean collagen fiber angle from the loading direction and the in-plane dispersion of the collagen fibers were identified as the main contributors to strength. In addition, although the influence of content percentages was not obvious on the population basis, they should not be ignored especially in the extreme situations.

Zusammenfassung

Die Aortenwand, die aus in eine elastische Matrix eingebetteten Kollagenfasern besteht, kann als faserverstärktes Verbundmaterial gesehen und modelliert werden. Es ist bekannt, dass die Mikrostruktur, insbesondere die Hauptausrichtung der Kollagenfasern und ihre Verteilung um diese Ausrichtung, die Spannungs-Dehnungs-Reaktion des Gewebes bestimmt. Aneurysmen und Dissektionen der Thorakales Aorten, die beiden hier behandelten Pathologien, sind im Falle eines Risses tödlich und durch Veränderungen der Wandmikrostruktur gekennzeichnet. Daher besteht ein dringender Bedarf unser Verständnis der zu Grunde liegenden Gewebefehler zu verbessern.

Zu diesem Zweck wurde in der ersten Studie die Stärke der aneurysmatischen und präparierten menschlichen Brustaorta unter verschiedenen Belastungsmodi ermittelt, wobei die Versagensmerkmale unter Scherbelastung im Mittelpunkt stehen. Die einachsigen Tests ergaben, dass die Media der Aorta in Umfangsrichtung am stärksten war, gefolgt von der Längs- und der Radialrichtung. Zusätzlich war die Versagensspannung bei außer-Ebene-Scherbelastung ungefähr 10-fach höher als bei in-der-Ebene-Scherbelastung. Diese Ergebnisse wurden durch die Kollagenfaserarchitektur unter Berücksichtigung ihrer faserverstärkenden Rolle in der Aortenwand erklärt.

Die nachfolgende Studie und der erste Übersichtsartikel dieser Doktorarbeit unterstreichen die entscheidende Notwendigkeit, die dispergierte Kollagenfaserstruktur zu modellieren, um die Verformungseigenschaften von weichen biologischen Geweben genau vorherzusagen. Es zeigt sich, dass die Vorhersagen sowohl aus der Winkelintegration als auch aus den verallgemeinerten Strukturtensormethoden gut mit den experimentellen Daten übereinstimmen. Es wird auch auf die Notwendigkeit zusätzlicher mechanischer und mikrostruktureller Daten hingewiesen, um die Materialmodellierung zu verbessern.

Der zweite Übersichtsartikel befasst sich mit Aortenwandruptur und Dissektion aus der Perspektive des Materialversagens. Eine ausführliche Literaturübersicht zu den mechanischen Tests, mit denen die Festigkeit quantifiziert werden kann, wurde bereitgestellt. Basierend auf den Strukturunterschieden und den verschiedenen Mechanismen, die zum Riss oder zur Dissektion führen können, wurde vorgeschlagen, dass ein ideales Versagensmodell den Einfluss der Struktur auf die Gewebefestigkeitin verschiedenen Zeit- und Längenskalen unter verschiedenen Belastungsmodi widerspiegeln sollte.

Die letzte Studie in dieser Doktorarbeit verwendete uniaxiale Zugversuche, Struktur durch second-harmonic generation Mikroskopie und histologische Untersuchungen, um die möglichen Beziehungen zwischen der Gewebestärke und ihrer Mikrostruktur aufzudecken. Der mittlere Kollagenfaserwinkel aus der Belastungsrichtung und die Verteilung

der Kollagenfasern in der Ebene wurden als die Hauptfaktoren für die Festigkeit identifiziert. Zusätzlich sollte der prozentuale Anteil der jeweiligen Bestandteile der Aortenwand, besonders in extremen Fällen, berücksichtigt werden, obwohl sich der Einfluss in unseren Studien nicht als signifikant hervorgehoben hat.

CONTENTS

1 INTRODUCTION

Cardiovascular disease (CVD) is the leading cause of death worldwide and is expected to account for more than 23 million deaths by 2030, [13]. Two of these diseases that occur in the thoracic aorta – aneurysms (TAA) and dissections (TAD) – are rare but life threatening events with poorly understood pathophysiologies. Mortality rates approach 50% within the first 48 hours and 80% within 2 weeks for the dissections of the ascending aorta that are left untreated [48], and the periopeartive mortality rates for intact and ruptured TAA are 6.1% and 28%, respectively [13].

The aorta is the major artery originating from the heart's left ventricle and its main function is to deliver oxygenated blood to the rest of the body by the help of its branches. The part of the aorta originating from the heart is directed upwards (ascending thoracic aorta) until it deviates to the left by the aortic arch, which is then directed downwards. From the end of the aortic arch until the diaphragm it is called the descending thoracic aorta and below the diaphragm it is the abdominal aorta. At the arch, the aorta is connected to the pulmonary trunk via the ligamentum arteriosum, which is a blood vessel during fetal development that closes and becomes ligamentous after birth.

Aneurysms are defined as the dilations of the aorta when the diameter of the affected segment exceeds 1.5 times the normal diameter [68]. According to the morphology, aneurysms can be either saccular or fusiform, the latter being more common. They can also be classified according to the aortic segment involvement as thoracic, thoracoabdominal or abdominal. They are typically silent until they dissect or rupture. Acute aortic dissections, unlike aneurysms, are not silent (85%) and most patients report severe pain [68]. According to the Stanford classification, it can be either type A – involving the ascending aorta – or type B – affecting only the descending TA and below. Type B dissection is usually treated pharmacologically, whereas type A dissection is treated surgically. Dissections of the aorta typically involve a tear in the intima where blood can flow into and start creating an intimal flap. Separation of the wall proceeds helically, either antegrade or retrograde, within the media creating a false lumen. The false lumen can lead to dilation of the aorta, and in some cases block the true lumen impairing the blood flow significantly. Although it is typical, the aforementioned intimal flap is not always present. Dissections can be caused by intramural haematoma which is located around the circumference of the aorta or by penetrating aortic ulcers [68], as depicted in Fig. 1.1.

It is important to note here that although aneurysms can dissect, they are not a prerequisite for dissection to occur. In fact, more than 80% of dissections occur in the absence

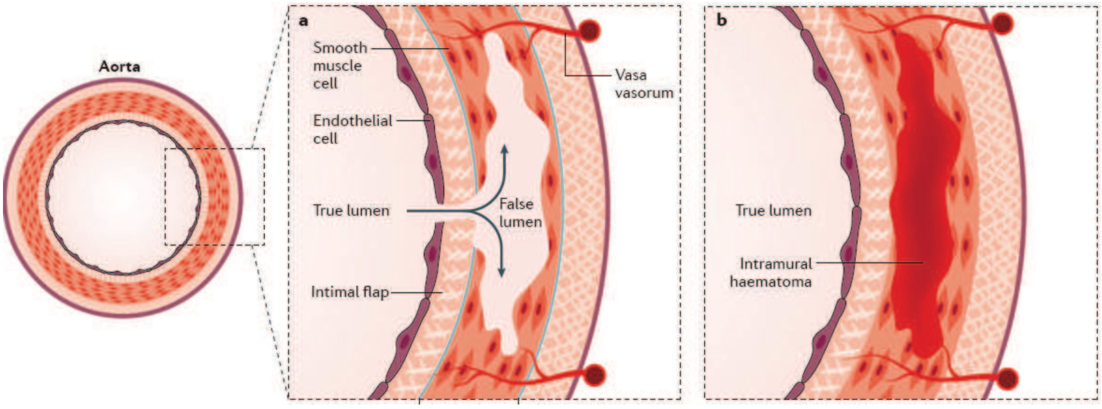

Figure 1.1 Dissection of the aorta: (a) involving an intimal tear and a flap; and (b) due to an intramural haematoma. Reproduced from Nienaber et al. [227], with permission from Springer Nature.

of a pre-existing aneurysm [93]. Except where a distinction is made, aneurysms and the dissections of the thoracic aorta are referred to as TAAD from hereon.

The major risk factor is hypertension for aneurysms and dissections of the ascending thoracic aorta similar to other CVDs, whereas the second major risk factor is inheritance [24, 68, 102]. Abdominal and descending thoracic aortic aneurysms, on the other hand, have more overlapping risk factors with CVDs and are commonly accompanied by atherosclerosis [68, 181]. The pathophysiology of aneurysms differ not only between the abdominal and the thoracic aorta [33, 275], but also between descending and ascending portions of the thoracic aorta (TA) [278]. Such differences are typically attributed to the embryonic origins of the cells involved in the process as there might be differences in how the signaling pathways function [275, 278]. This can provide an explanation for why aneurysms in the ascending aorta grow somehow slower than the aneurysms of the descending TA [68].

TAAD can be divided into syndromic and non-syndromic types, and the latter can be either familial or sporadic. Non-syndromic familial type is the one in which more than one family member is effected, whereas in the non-syndromic sporadic type no other family member is affected [253]. Genetic mutations are typically the cause of both syndromic and non-syndromic familial types [218], and mutations in 13 genes have been shown to predispose to thoracic aortic disease so far [219]. More specifically, syndromic TAADs are usually caused by mutations to the genes which are widely expressed in the body, whereas the non-syndromic familial ones result from mutations to the proteins with specific functions in the aorta, especially to the smooth muscle cell specific proteins [142].

Parts of the TA affected by aneurysms and/or dissections are typically treated surgically when certain criteria are met. The decision is mostly based on the critical diameter among others such as yearly growth rate. The patient suffering from an asymptomatic aneurysm is operated if the diameter is 5 – 5.5 cm for men and for women, respectively, to prevent it from rupturing or dissecting [135]. These diameter values are recommended since the statistical analyses show hinge points where dissection and rupture become common events rather than rarities, at a diameter of 6 cm for the ascending and 7 cm for the descending TA [42], see Fig. 1.2. If the patient suffers from a TAD or a symptomatic TAA the affected portion is suggested to be resected regardless of the size [69]. Adverse events such as rupture and dissection of the TAA can occur at any size [69, 242, 243, 278] and current guidelines are not able to prevent 60% of these adverse events [242].

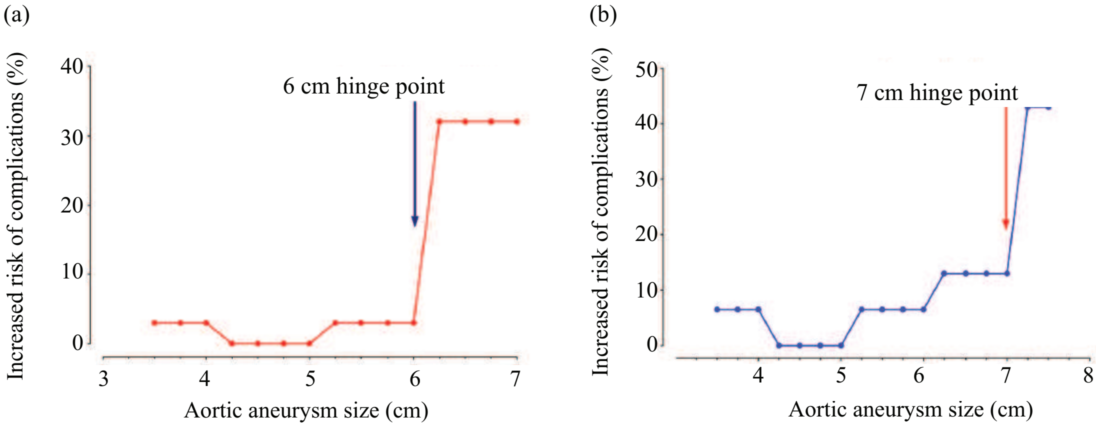

Figure 1.2 Increased risk of complications (%) in relation to aneurysm diameter in the (a) ascending and (b) descending thoracic aorta. Reproduced from Saeyeldin et al. [278], with permission from Springer Nature.

An increased aortic diameter is associated with decreased distensibility. More specifically, according to the observations in [165], the ascending aorta starts acting as a rigid tube at a diameter around 6 cm where it cannot stretch anymore to assist the systolic cardiac load. In other words, as the aorta grows its elastic energy storage capability becomes significantly impaired. Moreover, increased wall stiffness is associated with higher aortic root growth rates. Although treatments aiming to decrease stiffness may slow down the growth, they may also increase the risk of adverse events since fibrosis could be preventive against them [217].

In case the patient has a connective tissue disorder such as Marfan’s (MFS) or Ehler-Danlos (EDS) syndrome due to a mutation, the risk of suffering from aneurysms or dissections can increase substantially as well as the risk of adverse events. Hence, the recommendations for surgical intervention also reflect the observations from such mu-

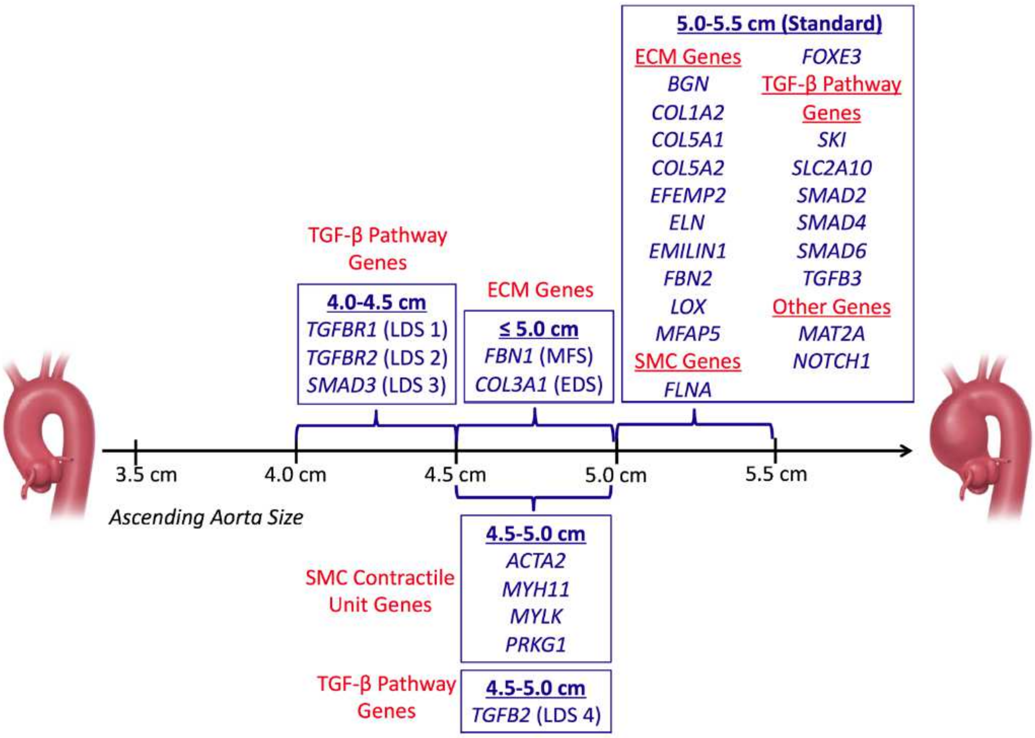

Figure 1.3 Size recommendations for surgical intervention on the ascending thoracic aorta depend on the mutations patient may suffer from, reproduced with permission from Brownstein et al. [23].

tations, see Fig. 1.3. Covering all genetic mutations related to TAADs would be out of the scope here, however, some of the selected mutations are briefly described in § 1.2.1. An extended list of mutations related to TAAD can be found in [23, 24, 142, 181].

To be able to reliably predict the adverse events, one needs to identify wall stresses and wall strength under different loading modes. This PhD Thesis deals with the latter; identification of wall strength under different loading modes and its structural determinants – especially collagen.

The following sections present the relevant background regarding the structure and the mechanical behavior of the thoracic aorta in health and disease. More specifically, § 1.1 provides an overview of healthy aortic wall microstructure and its mechanical behavior, presents detailed information on extracellular matrix components, how smooth muscle cells are involved in the aortic wall function, and how they take part in they are regulating the extracellular matrix. The following section, § 1.2 begins with n summary of selected non-genetic and genetic risk factors which have common structural manifestations. Subsequently, pathological structural changes in the TAADs are connected to the biomechanical characteristics of diseased thoracic aortic tissues. The final part, § 1.3 provides an overview of the organization of the remaining chapters.

1.1 Healthy Aortic Wall

Intramural cells – endothelial cells, smooth muscle cells, fibroblasts – and extracellular matrix (ECM) produced by these cells give rise to the aorta's layer-specific mechanical properties and functions. To keep a functional homeostasis, it is vital for the cells to sense their environment by interacting with each other and the ECM components to control the ECM organization: smooth muscle cells can contract or relax in response to changes in their biochemomechanical environment; and all intramural cells play a role in the synthesis and degradation of the ECM components. For example, an increase in the local forces applied by the ECM proteins at the cell junctions can activate signal transduction pathways, upon which a cascade of anabolic (matrix building) or catabolic (matrix degrading) reactions are triggered.

The focus in this section is the microstructure and the mechanical behavior of the aortic wall. This is further detailed by information on structural components of the wall and the role of smooth muscle cells in aortic wall function. Finally, since sustained disruptions to the preferred mechanical environment of cells may lead to pathological remodeling of the ECM and the components of the ECM has a key influence on the mechanical behavior of the tissue, regulation of the ECM through mechanostransduction is introduced.

1.1.1 Microstructure

The aortic wall constitutes of three layers: intima – the innermost layer, media, and adventitia – the outermost layer. The media is separated from the intima and adventitia via internal and external elastic lamina, respectively.

The *intima* of a young healthy adult reaches until the internal elastic lamina (IEL) and consists of a single layer of endothelial cells, a thin basal lamina and a subendothelial area. The subendothelium is supported by the IEL and contains elastic fibrils and collagen bundles [266]. Moreover, it may contain vascular smooth muscle cells in humans although it is acellular in small animals. Mechanical contribution of the intima as a load bearing element is negligible in a young healthy adult. However, this layer becomes mechanically significant with age due to intimal hyperplasia during which subendothelium thickens [127, 352].

The *media* is composed of 50-70 concentric lamellar units attached together. During the formation of the vessel wall, the number of these units in the aorta increases exponentially with increasing stroke volume [268] until a relatively constant tension per lamellar unit is reached [369]. A single lamellar unit consists of a fenestrated elastic sheet upon which smooth muscle cells are lying embedded in a network of collagen and elastin

[235]. Orientations of smooth muscle cell (SMC) nuclei and collagen fibers in a single unit correlate and are closer to the circumferential direction [132]. When the entire thickness of the medial layer is considered, collagen fibers exhibit helically arranged two symmetric families dispersed around a mean orientation closer to the circumferential direction [286]. Predominantly, type III (70%) and I (30%) fibrillar collagens are found in this layer, but fibril forming collagen type V and network forming collagen type IV are also present [56, 347].

The two symmetric collagen fiber families in the *adventitia* are dispersed around a mean fiber angle closer to the longitudinal direction in contrast to the media [286]. In addition to thick collagen fibers in bundles that are rich in type I collagen [347], fibroblasts are found in this layer.

1.1.2 Mechanical Behavior

The typical mechanical behavior of the aortic wall with respect to stretss-stretch is highly *nonlinear*. In other words, the tissue stiffens progressively with increasing applied load. The nearly linear stress-stretch behavior at low load levels is governed by the elastin, whereas collagen governs the nonlinear tissue behavior where the artery exhibits a typical J-shaped response curve at higher loads [269]. The blue curve in Fig. 1.4(a) depicts such a typical curve for an aortic tissue strip, and the black curve therein depicts the almost linear response of the tissue upon collagenase treatment [357]. Gradual employment – due to uncrimping and reorientation towards the loading direction – of collagen fibers embedded in the tissue with increasing load is responsible for the nonlinearity, whereas the preferred direction of the fibers results in *anisotropy*. More specifically, its behavior in circumferential and longitudinal directions are different [124].

Furthermore, due to its high water content hold by the proteoglycans, the aortic tissue can be assumed to undergo volume preserving deformation in response to mechanical load: it is *incompressible* [30, 57, 174]. However, incompressibility assumption may not be valid at the micromechanical level [230, 298].

The aortic wall is also *pseudoelastic* – it follows different paths when loaded and subsequently unloaded. The difference in loading-unloading paths is called hysteresis and it can be reduced by applying several loading-unloading cycles after which mechanical response becomes repetitive; upon which the tissue is said to be preconditioned [84]. Strips of human thoracic aortas with non-atherosclerotic intimal thickening treated with elastase to degrade elastin exhibit an increased softening with each additional load cycle [357], see Fig. 1.4(b). In other words, the behavior does not become repetitive after applying consecutive loading-unloading cycles, indicating that the integrity of the aortic wall is reduced upon elastase treatment. This observation is attributed to the collagen fiber network being inadequately connected to the non-collagenous matrix in the elastase treated tissue, therefore fibers being able to slide against each other [357].

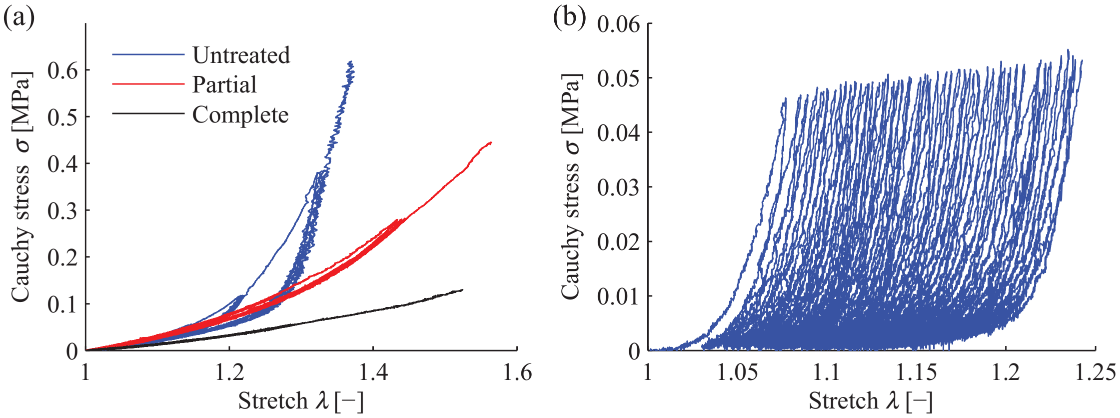

Figure 1.4 Stress-stretch behavior of aortic tissue strips: (a) the mechanical behavior gradually becomes linear and hystresis decreases upon treatment with collagenase; (b) the tissue keeps getting softer with each loading cycle upon elastase treatment during preconditioning, Reproduced from Weisbecker et al. [357], with permission from Elsevier.

In addition, when an unloaded arterial ring is cut radially it springs open and a longitudinal strip bends further away from the main vessel axis. This implies that the external part of the artery is under tension while the internal part is under compression [129]. In other words, arteries are *residually stressed* in both circumferential and longitudinal directions *in vivo*, for which elastin is mainly responsible [279]. It was suggested that these stresses are generated as a result of growth [299], they are necessary for a 'compatible growth' [300], and they homogenize the stress gradients across the wall [39]. In addition to their age-dependency [279], they are layer dependent [96] and more concentrated at the inner parts of the arteries where more elastin is found. In the outer layers, however, they contribute little to the stress state [96].

1.1.3 Extracellular Matrix Components

Components of the extracellular matrix that drew attention in relation to the pathological aortic wall – collagen, elastic fibers, proteoglycans and glycoproteins – are described in this section.

Collagen

Collagen, with 28 types identified in humans so far, is the most abundant protein in the body [81]. In addition to strengthening the tissue, collagen sequesters cytokines and mediate cellular activities by their connection to cell surface receptors [371]. Fibrillar collagens form highly hierarchical structures. Bundles of fibers can have diameters up to 500 μm, a single fiber can have a diameter in the range of $1-20\,\mu$m and it consists of several fibrils, a single fibril can have diameter in the range of $10-300$ nm [224].

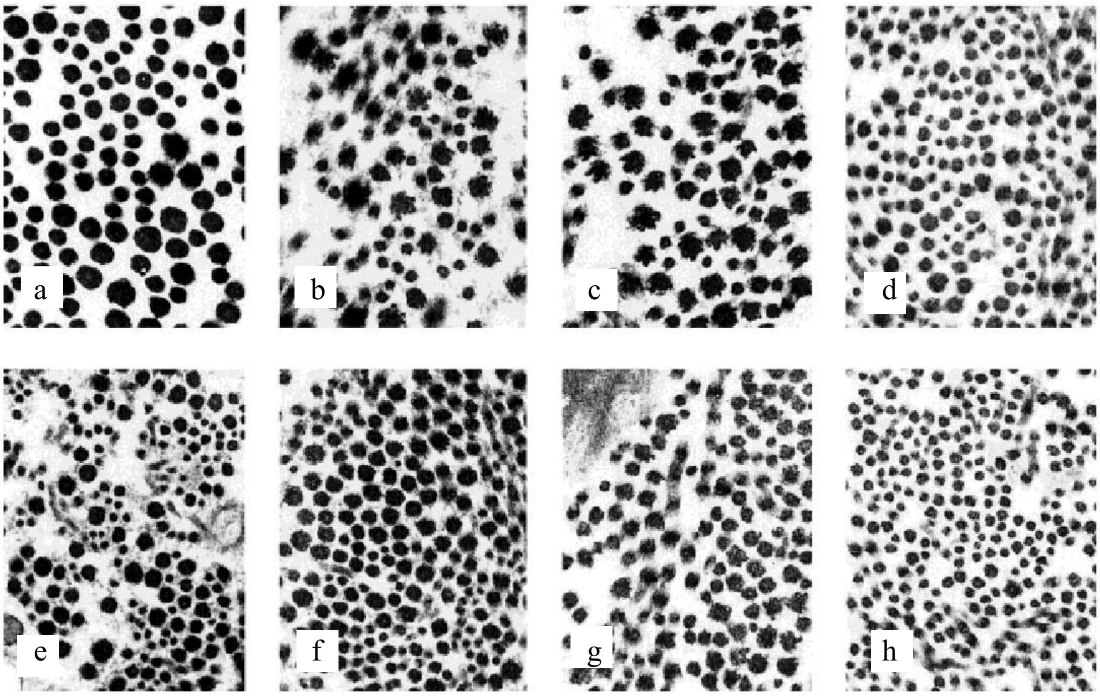

Figure 1.5 Fibril diameters in the aortic wall: (a) adventitia with thick fibrils; (b)-(g) media with variable fibril diameters, with the adventitial side containing fibrils with significantly larger diameter compared to the intimal side; (h) intima with thin fibrils, reproduced from Dingemans et al. [56], with permission from John Wiley & Sons.

Collagen fibril diameters are reported to be smallest in the intima and largest in the adventitia, whereas within the media they are heterogeneous even within a fiber [56], see Fig. 1.5. In addition to the preferred direction of fibers, which provide strength and resilience along the main direction of the *in vivo* load, fibrils with different diameters that constitute a fiber enable the fiber to exhibit high tensile strength and high creep resistance. Larger diameter fibrils in the tissue serve to increase the tensile strength of a fiber with their larger cross-sectional areas as in the case of the adventitia, whereas the smaller diameter fibrils ensure an increased inter-fibril binding thanks to their high surface to volume ratio [237].

Fibrils are formed via axially shifted lateral stacking of tropocollagen helices, as depicted in Fig. 1.6(a). Owing to the axial shift in the regular stacking, they exhibit a periodic structure with a d-period of approximately 67 nm [148, 149], see Fig. 1.6(a)-(b). The d-period consists of a gap and overlap zone of 35 and 32 nm, respectively [82], and its contribution to tissue level stretch is approximately one order of magnitude lower than the macroscopic stretch [284].

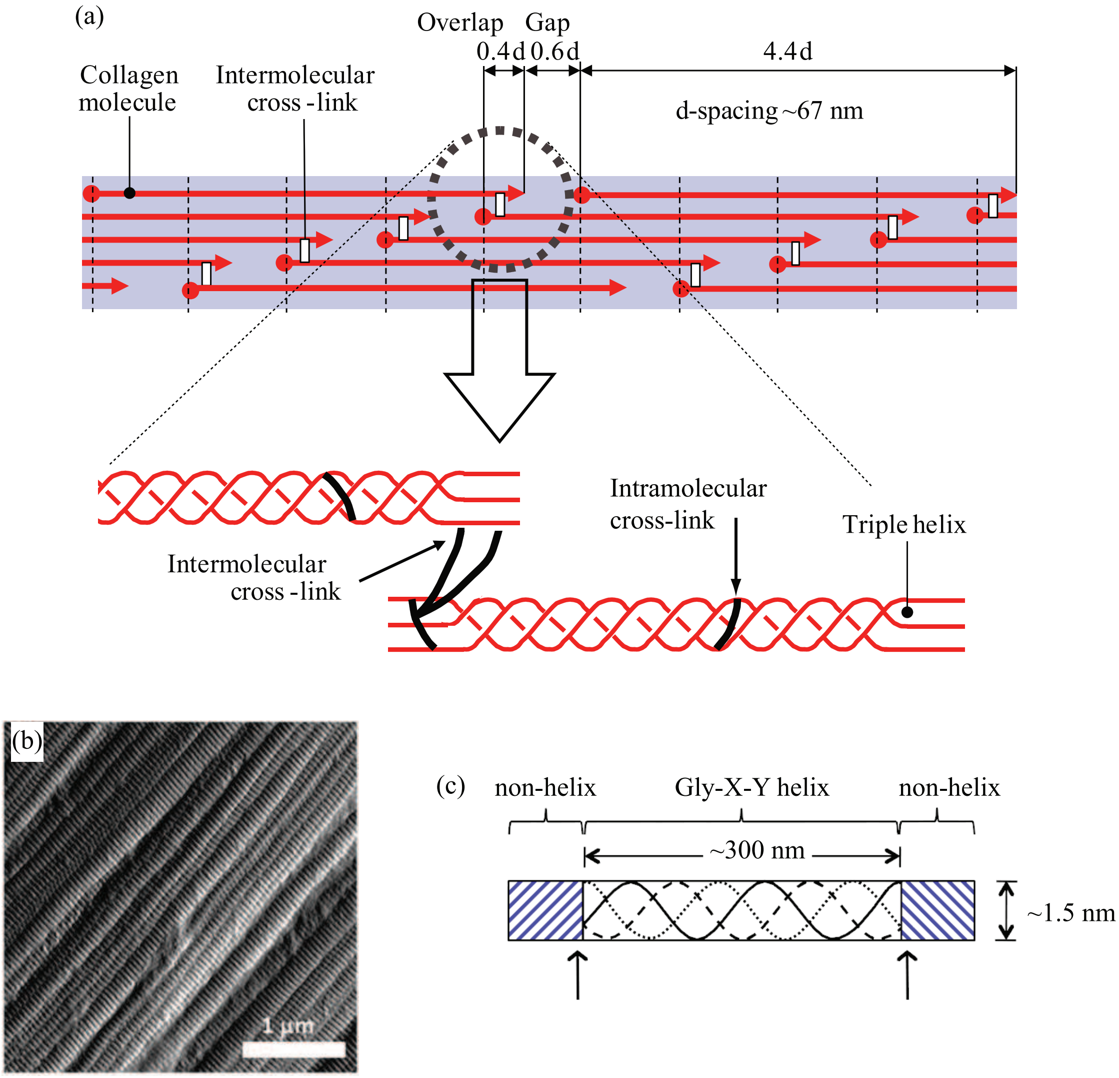

Figure 1.6 From procollagen to fibril: (a) schematic arrangement of collagen molecules linked to each other via covalent cross-links in a fibril unit cell exhibiting a d-period of 67 nm (modified from Holzapfel [115]); (b) electron micrograph of a tendon clearly showing the periodic structure of collagen fibrils (reproduced from Sawadkar et al. [282] with permission by Mary Ann Liebert, Inc., New Rochelle, NY); (c) schematic of a fibril forming procollagen molecule with shaded areas depicting non-helical N- and C- terminal ends, arrows indicate enzymatic cleavage sites (reproduced from Muiznieks and Keeley [224], with permission from Elsevier).

Each tropocollagen molecule is composed of three α chains each of which contain a distinct aminoacid triplet repeat, Gly-X-Y. Upon being synthesized, α chains are imported into rough endoplasmic reticulum (ER) [224], where they undergo hydroxylation that forms hydrogen bonds between the chains. The end-product is a triple helix called tropocollagen with N- and C- terminal domains [149], see Fig. 1.6(c).

Depending on the distinguishable chain types present in a collagen molecule, it can be classified as a homotrimer with three identical chains, or heterotrimer with two or three distinct chains [311]. While tropocollagen molecules are being transported from the ER by Golgi to plasma membrane carriers to the ECM, fibrils can already start forming following enzymatic removal of C-domains by procollagen C-proteinases exposing C-telopeptides [294]. Golgi to plasma membrane carrier pushes out the cell membrane creating a fibripositor (fibril depositor) which fuses into the membrane, creates an opening and subsequently deposits the fibril into the ECM [113, 294]. Stable assembly of fibrils require lysyl oxidase (LOX) to cross-link lysine and hydroxylysine residues at the N- and C-telopeptides covalently [224].

Type I collagen can form fibrils by self-assembly *in vitro*, however, proper *in vivo* assembly requires fibronectin, integrins that bind to fibronectin and collagen, as well as collagen types III and V [150]. In the absence of type III [184] and type V [288] collagen, type I rich fibrils have larger and inconsistent diameters. In the arteries, collagen types III and V are co-localized with collagen type I near the elastic lamina *in vivo* [56].

Fibrils are cross-linked to each other to form fibers on the fibril surface by small leucine rich proteoglycans (SLRPs) [359]. Different types of SLRPs are involved in different stages of fibril formation depending on the fibril requirements. Their binding to collagen molecules could (i) prevent uncontrolled fibril/fiber assembly by sterical hindrance, (ii) bridge different types of collagen, (iii) regulate cross-linking on each collagen monomer, or all [151]. Forming inter-fibril cross-links and cross-links with other matrix constituents contribute to a stable and functional matrix formation.

Elastic fibers

Functional elastic fibers contribute to the compliance and resilience of the aortic wall, and damage to them results in irreversible changes in function and wall structure [136]. They consist of cross-linked elastin (90%) covered by fibrillin microfibrils (10%). Figure 1.7(a) depicts the multiscale structure of elastic fibers together with elastic fiber-associated proteins such as microfibril-associated protein (MFAP), elastin-microfibril interface-located proteins (EMILIN) and microfibril-associated glycoprotein (MAGP).

Elastin is the main protein of elastic fibers, and it is secreted as tropoelastin by fibroblasts and SMCs upon the gene activation in response to stimulants such as insulin-like growth factor (ILGF) and nitric oxide (NO). Tropoelastin monomers bind to elastin-binding protein (EBP) prior to being secreted into the ECM, which protects tropoelastin

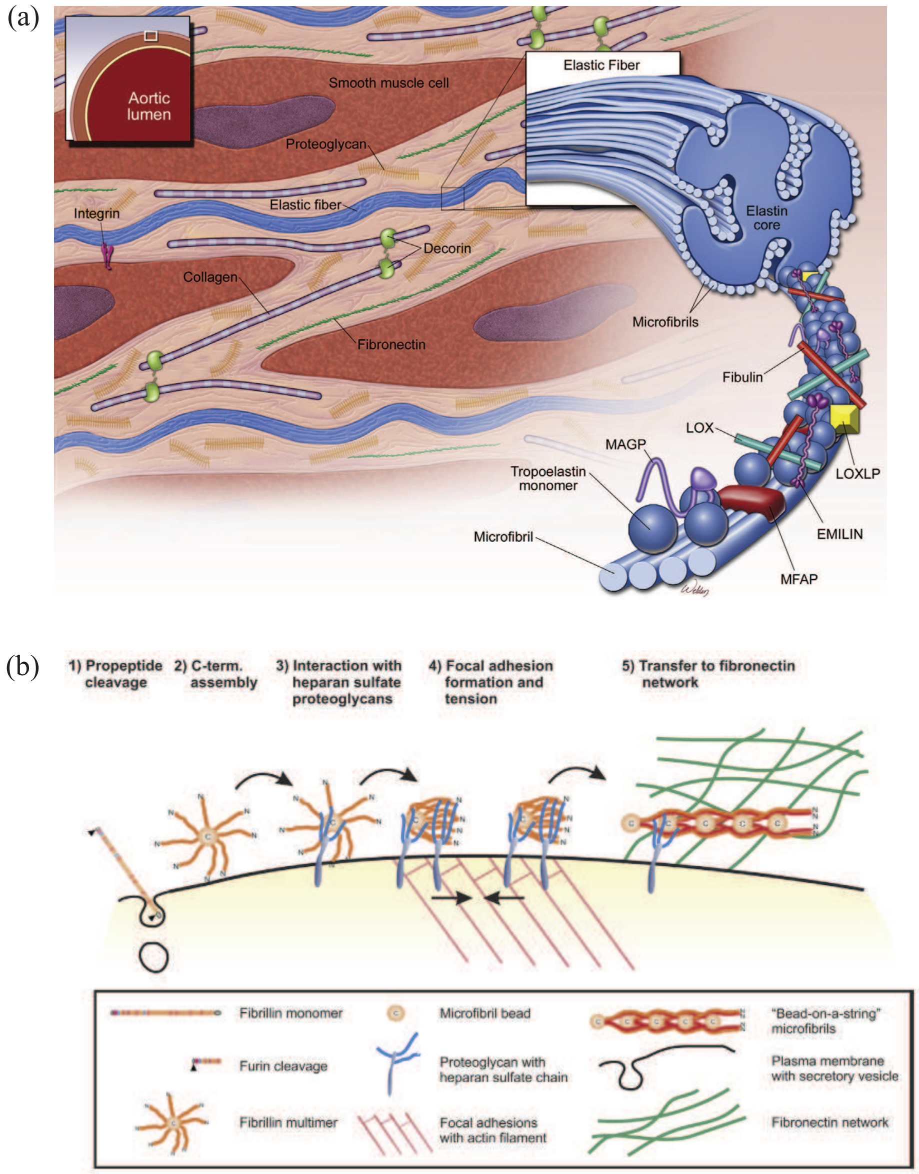

Figure 1.7 Elastic fiber structure in the medial layer of the aorta: (a) Elastin core consists of tropoelastin monomers connected by fibulins and cross-linked by lysyl oxidase (LOX) and lysyl oxidase-like protein (LOXLP). Microfibrils contain fibrillins, microfibril-associated glycoprotein (MAGP) and microfibril-associated protein (MFAP). The core is attached to microfibrils by elastin microfibril interface-located proteins (EMILINs) forming an elastic fiber, reproduced from Wu et al. [371] with permission from Elsevier; (b) model of a microfibril assembly: fibrillin monomers are secreted to the ECM where they first self assemble, and then assemble into bead on a string structure with the help of heparan sulfate proteoglycans and fibronectin, reproduced from Sabatier et al. [276], with permission from John Wiley & Sons.

from proteolysis. Furthermore, EBP aids the cross-linking by lysyl oxidase (LOX) and assembly of elastin onto the microfibrils. Upon the detachment of EBP from tropoelastin, a self-organized globular aggregate forms on the cell surface – a process called microassembly. Fibulins (fibulin-4 and fibulin-5) bind to this aggregate and mediate its deposition onto microfibrils. During the macroassembly, the mature insoluble elastic fiber is formed via enzymatic cross-linking of LOX and LOXLP [11, 224, 375].

Fibrillin rich microfibrils have a repeated beaded structure with a periodicity of 56 nm [159] and they consist of mainly fibrillins and MAGPs. Fibrillins (fibrillin-1, -2, -3) are large glycoproteins which become rod-like in the presence of Ca^{2+} [158]. Figure 1.7(b) depicts a model of microfibril formation. Upon the secretion from the cell, fibrillin monomers self-assemble into multimers. Following the interaction with heparan sulfate proteoglycans at focal adhesions, they can be formed into bead-like multimers. Connection with fibronectin fibers help microfibrils stabilize, elongate and interact with other ECM proteins [276].

Although microfibrils surround the elastin core and provide a scaffold for tropoelastin deposition and organization, their role is not limited to elastic fiber formation [375]. They can also form connections independent of elastic fibers, for example, as oxytalan fibers between smooth muscle cells and elastic lamellae and elastic struts between the lamellae [263]. In addition, microfibrils interact with other elastic fiber associated proteins and molecules such as latent transforming growth factor-β binding protein that play an important role in the organization of the ECM [371].

Proteoglycans

Proteoglycans (PGs) consist of glycosaminoglycans (GAGs) linked to a core protein, and are mainly found in the ECM although some PGs extend across the cell membrane or are directly attached to it by anchors [6, 140]. GAGs are negatively charged and hydrophilic unbranched polysaccharide chains composed of repeating dissacharide units. They can be divided into four groups by their sugars and links between the sugars: (i) chondroitin sulfate and dermatan sulfate, (ii) heparan sulfate, (iii) keratan sulfate and (iv) hyaluronan (also known as hyaluronic acid or hyaluronate). Hyaluronan typically presents as an extremely long chain as it is not linked to any core protein [6].

PGs take part in ECM remodeling and cell adhesion-migration-proliferation by interacting with or function as cell surface receptors to growth factors, matrix remodeling enzymes, and other ECM components [363]. PGs secreted by vascular endothelial cells can serve as structural organizers of the basal lamina by attaching to the other constituents, see Fig. 1.8, or contribute to the selective filtration of the basal lamina.

Smooth muscle cells synthesize primarily chondroitin sulfate (large and small), dermatan sulfate (small) based proteoglycans and small amounts of heparan sulfate pro-

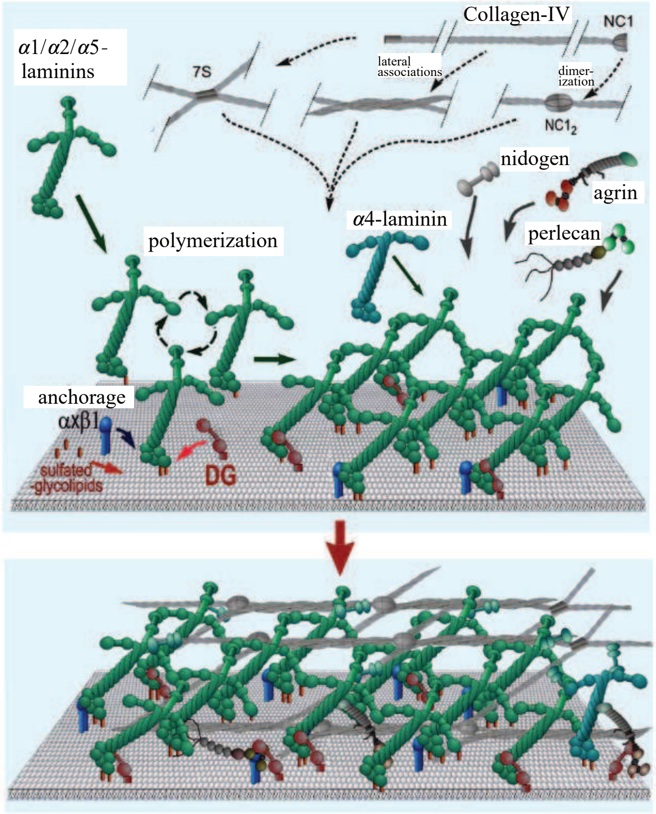

Figure 1.8 Model of the basement membrane assembly with laminin, perlecan (PG), type IV collagen and nidogen attached to each other to the cell surface, reproduced from Yurchenco and Patton [378] with permission by Bentham Science Publishers Ltd.

teoglycans, which are involved in stabilizing the ECM and regulating cell adhesion-migration-proliferation [361]. Proteoglycans can either promote or prevent these processes depending on which types of cells they are interacting with and in which environment [363]. For example, vascular endothelial cells switch to synthesizing chondroitin sulfate/dermatan sulfate based PG rich ECM from heparan sulfate based PG rich ECM when cell migration is induced [163], however, effect of heparan sulfate is inhibitory on the migration of smooth muscle cells [190].

PGs abundantly found in the ECM of the vessel wall can be divided to two main categories: (i) large PGs forming large aggregates by interacting with hyaluronan such as versican and aggrecan, see Fig. 1.9; and (ii) small leucine-rich proteoglycans (SLRP) such as decorin, biglycan, fibromodulin, osteoglycin and lumican [352]. Although not arterial wall specific, an extensive list of intracellular, cell-surface, pericellular and extracellular PGs can be found in [140].

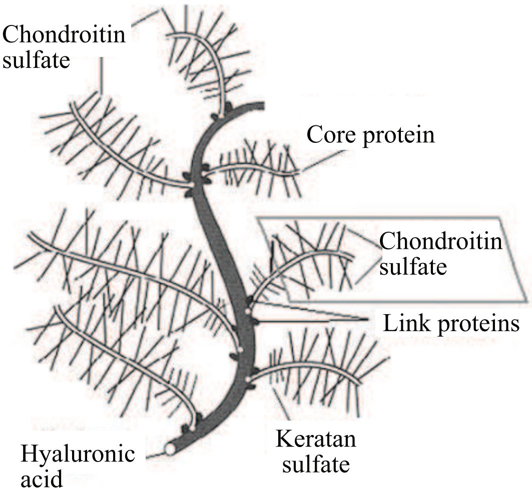

Figure 1.9 Sketch depicting the structure of a large proteoglycan aggregate consisting of keratan sulfate and chondroitin sulfate attached to the core protein, e.g., aggrecan or versican, that are attached to hylauronan molecule via linking proteins, reproduced from Gupta [101] with permission by Springer Nature.

Aggrecan consists of keratan sulfate and chondroitin sulfate GAGs attached to the core protein, as depicted in Fig. 1.9, and it is the primary load bearing PG of cartilage tissues [364]. Although its role in the aortic wall remains unclear, aggrecan is mainly found in the outer region of the developing wall [352]. Versican, a chondroitin sulfated PG prominent in the intima and adventitia, forms large aggregates on hylauronan molecule similar to aggrecan and it is mainly secreted by vascular smooth muscle cells. Versican aggregates surrounding SMCs create a viscoelastic coat in which cells can change shape to proliferate or migrate, and it is needed for the proliferative environment [362].

As mentioned before, decorin, biglycan and lumican in the SLRP family have been associated with collagen fibrillogenesis, specifically with fibril diameter and organization [352]. In contrast to decorin which is only found in the adventitia, biglycan has been found in all three layers, and lumican is found in the outer media and adventitia [352]. In addition to its role in collagen fibrillogenesis, lumican is reported to interact with integrins, matrix metalloproteinases (MMP9 and MMP14) in tumor genesis [152].

Glycoproteins

Glycoproteins are proteins with one or more saccharide or oligoscaccharide chains covalently bound to aminoacid side chains. They help enhance cell-cell and cell-ECM attachments. As glycoproteins such as fibrillins are already briefly explained previously, this section focuses on laminin and fibronectin.

Laminin takes part in cell differentiation, migration and adhesion. It is composed of a long arm which can bind to cells via integrins (or alternatively via dystroglycan), and three short arms that bind to other laminins, type IV collagen, perlecan and other gylcoproteins allowing the formation of a sheetlike structure called basal lamina connected to cell membrane [6], see Fig. 1.8.

Fibronectin plays an important role in cell adhesion, growth, migration during embryo development and differentiation. The soluble form can travel through the blood stream, whereas insoluble stable fibronectin fibrils bind, via their specific binding domains, to integrins on the cell membrane, collagen and heparin in the ECM. As the integrins are connected to intracellular actin, actin-myosin cytoskeleton can generate tension by pulling on the fibronectin matrix. This stretching exposes more binding sites on the fibronectin allowing for matrix assembly by promoting focal adhesion complexes [6].

1.1.4 Smooth Muscle Cells

Although the focus is on the passive mechanical behavior of the aortic wall in this PhD Thesis, smooth muscle cells play an important role on the mechanical state *in vivo*. With their mechanically active response, they control the lumen diameter regulating the circumferential and shear stresses acting on the wall. By maintaining a basal tone and thereby introducing residual strains, they can decrease the stress gradients further as well as the stress levels [204, 257]. For example, an increase in the basal tone causes an increase in the arterial pressure at which circumferential strain distribution throughout the wall thickness can be kept uniform under physiological conditions [109, 204, 257, 319]. Furthermore, they contribute to the passive mechanical behavior by regulating the ECM they are embedded in. Although there are several pathways which may be activated in this remodeling process, the roles of transforming growth factor β (TGF-β) and angiotensin-II (Ang-II) signaling are heavily investigated in relation to TAADs, hence, they are briefly described.

Active response

SMC contraction takes place mainly upon intracellular Ca^{2+} concentration increase due to neural, hormonal and local factors. Figure 1.10 depicts possible Ca^{2+} increase pathways, such as via the release from sarcoplastic reticulum upon activation of G-protein coupled receptor (GCPR) by vasoactive agents as well as influx through store-operated channels (SOC), second messenger operated channels (SMOC), receptor-operated channels (ROC), Na^{+}-Ca^{2+} exchanger (NCX), and voltage operated channels (VOC). Intracellular Ca^{2+} ions then bind to protein calmodulin forming a complex (CaM), which in turn binds to and activates myosin light chain kinase (MLCK). Active MLCK phosphorylates myosin light chain (MLC) via ATP hydrolization, exposing the actin binding sites on MLC to from cross-bridges [332].

In addition to intracellular Ca^{2+} concentration increase, SMC contraction can be modulated by calcium-independent mechanisms which influence the sensitivity of MLC to calcium. These mechanisms, such as DAG-PLC-PCK and RhoA-Rho kinase (ROCK) pathways regulate the phosphorylation state of MLC independent of CaM-MLCK signaling by inhibiting the MLCP activity [332].

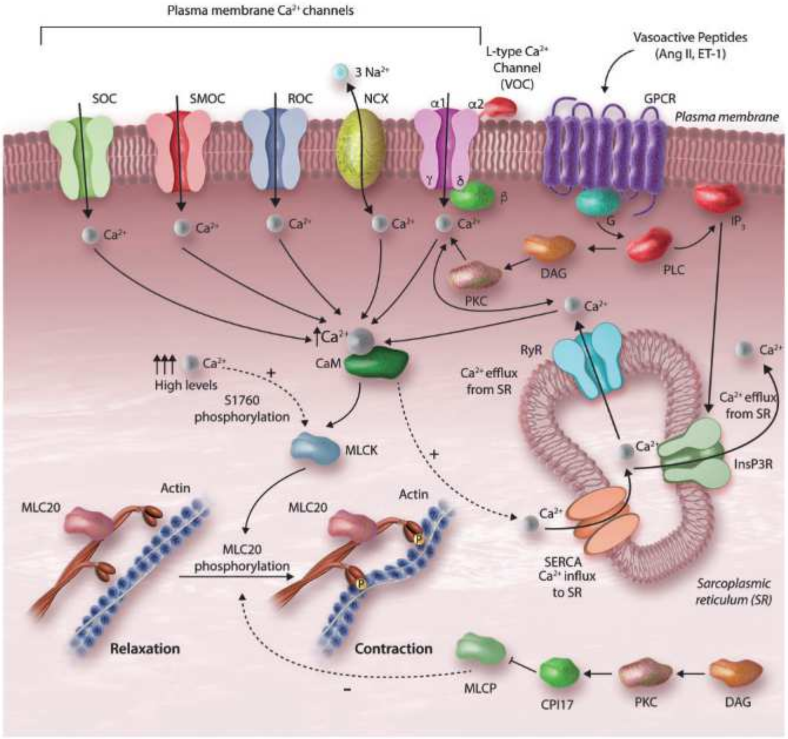

Figure 1.10 Ca^{2+} mediated smooth muscle cell contraction: intracellular Ca^{2+} concentration increases via (i) influx through store-operated channels (SOC), second messenger-operated channels (SMOC), receptor-operated channels (ROC), Na^+-Ca^{2+} exchanger (NCX), or voltage operated channels (VOC) on the cell membrane; or (ii) release from sarcoplasmic reticulum which can be triggered by IP_3 binding of vasoactive peptides to G protein-coupled receptors (GPCR). Activation of phospholipase C (PLC) through GPCR can either trigger production of IP_3 or formation of diacylglycerol (DAG). The latter results in activated protein kinase C (PKC) which can either influence the membrane channels to initiate contraction or prevent the activity of myosin light chain phosphatase (MLCP) to keep a contracted state. Reproduced from Touyz et al. [332].

Relaxation is initiated by a decrease in intracellular Ca^{2+} which results in dissociated calmodulin complex and dephosphorylated MLC by MLC phosphotase (MLCP) [185]. SMCs, however, do not completely relax but maintain a so-called basal tone. This energy efficient state has low ATP consumption since the cross-bridges are maintained without further MLC phosphorylation [41].

Vasoactive agents triggering SMC contraction such as Angiotension II (Ang II), Endothelin-1 (ET-1) and norepinephrine are known as vasoconstrictors and they decrease the lumen diameter, whereas agents inducing relaxation such as nitric oxide (NO), L-arginine and histamine are known as vasodilators and hence increase the lumen diameter. A local increase in the blood flow means a local increase in wall shear stress sensed by the endothelium, and the endothelial cell response is to increase the NO production and decrease the ET-1 production [133].

NO synthase (NOS) in the endothelial cells helps conversion of L-arginine and oxygen L-citruline and NO. NO then diffuses from the producer cell to the target cell, and binds to soluble guanyl cyclase (s-GC) on SMC membrane where it catalyzes intracellular guanosine triphosphate (GTP) conversion into cyclic guanosine monophosphate (cGMP). cGMP can induce SMC relaxation via various pathways resulting in two main actions: (i) decreasing the intracellular Ca^{2+} concentration, or by (ii) reducing the sensitivity of the contractile unit to Ca^{2+} [32]. SMC relaxation results in vasodilation, i.e. increased diameter and isochorically decreased thickness, decreased shear stress and blood pressure [133, 331].

A local increase in pressure, on the other hand, increases the lumen diameter and isochorically decreases the thickness – decreasing the shear stress and increasing the circumferential stress. Endothelial cells respond to the decreased shear stress with decreasing the NO production and increasing ET-1 production [133]. ET-1 is produced by converting enzyme (ECE) and it can bind to ET_A receptors on SMCs to act as a vasoconstrictor or they can bind to ET_B receptors on endothelial cells to act as a vasodilator [85]. Vasoconstriction function acts to increase intracellular Ca^{2+} release from the sarcoplasmic reticulum [340], and increased intracellular Ca^{2+} triggers SMC contraction reducing the lumen diameter.

Regulation of the ECM via mechanotransduction

Cell-to-cell and cell-to-ECM interactions are essential for the cells to communicate with their environment. These communications occur via occluding junctions such as tight junctions, communicating junctions such as chemical synapses and gap junctions. Moreover, anchoring junctions connect cells to cells or cells to the ECM. These junctions allow cells to sense their mechanical environment and activate different signaling pathways to modify it. This interaction called mechanotransduction occurs via force-induced conformational or organizational changes in molecules or structures such as ion channels activated with mechanical stimuli, cadherin complexes and integrins [63].

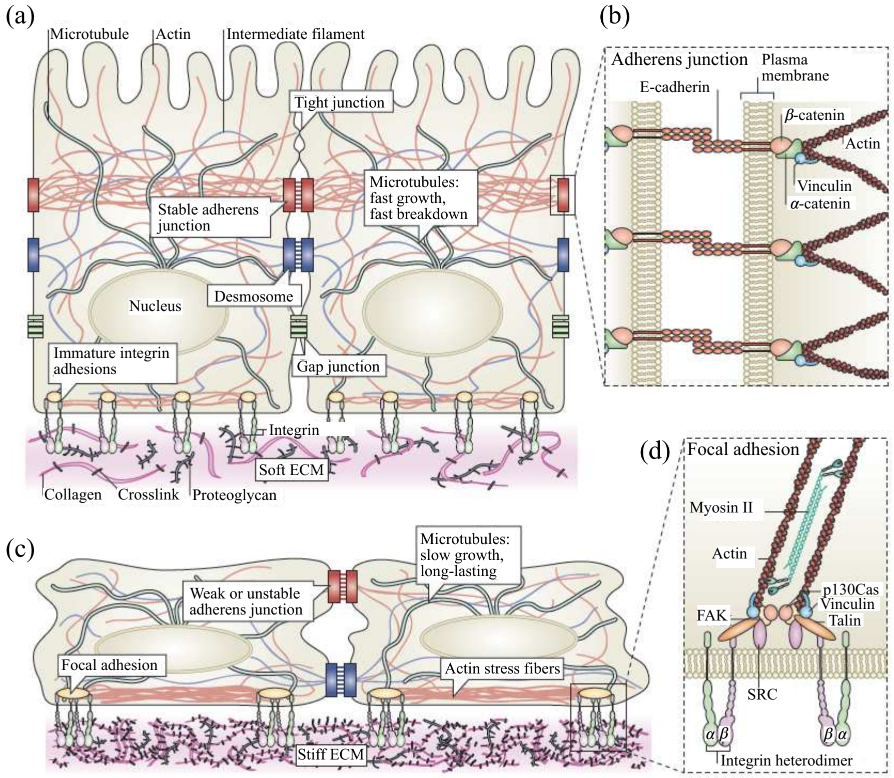

Figure 1.11 Mechanical network of cells: (a) cell-to-cell and cell-to-ECM interactions on soft ECM; (b) close-up of adherens junctions connecting actin networks of the two cells; (c) cell-to-cell and cell-to-ECM interactions on stiff ECM; (d) close-up of focal adhesions connecting microtubules and actin network of the cell to the ECM via integrins. Bundles of actin fibers are running parallel between adherens junctions and focal adhesions. Increased ECM stiffness due to remodeling can influence cell shape and intracellular actin distribution as well as organization of cell-to-cell and cell-to-ECM adhesions. Reproduced from DuFort et al. [63], with permission from Springer Nature.

Cell-to-cell anchoring junctions are (i) adherens junctions linking actin filaments and (ii) desmosomes linking intermediate filaments [6]. Figure 1.11 (a) depicts cell-to-cell and cell-to-ECM connections on soft ECM, with a focus on adherens junctions via cadherins in Fig. 1.11(b) [63]. Cell-to-ECM anchoring junctions are (i) focal adhesions and (ii) hemidesmosomes. Figure 1.11 (c) depicts cell-to-cell and cell-to-ECM connections on stiff ECM, with Fig. 1.11(d) focusing on the focal adhesions via transmembrane proteins called integrins connecting ECM proteins, i.e. fibronectin, with intracellular actin and microtubule. Hemidesmosome junctions, on the other hand, connect ECM proteins such as laminin with intracellular intermediate filaments [6].

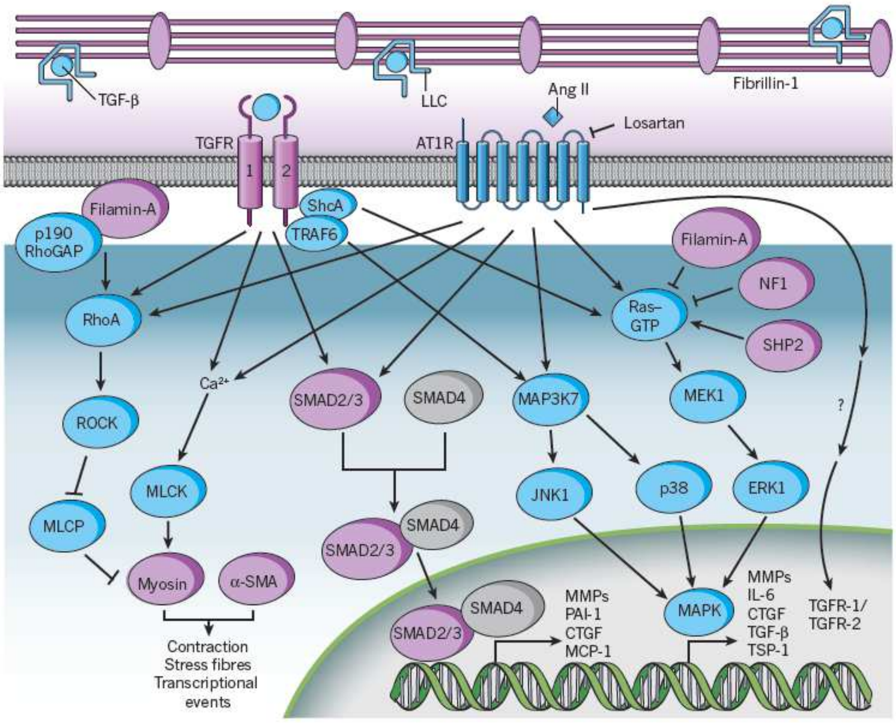

Figure 1.12 Signaling cascade upon activation of TGF-β R1/2 receptor complex by TGF-β, AT1 receptor by Ang-II, and possible interactions between them. LLC is bound to fibrillin-1 microfibrils and TGF-β is sequestered in the ECM. Upon release, it binds to the TGF-β R1/2 receptor complex and can initiate RhoA, MAPK, SMAD 2/3 cascades, similar to Ang-II upon binding to AT1 receptors. MMPs can be activated downstream to these cascades and promote ECM degradation. Reproduced from Lindsay and Dietz [182], by permission from Springer Nature.

TGF-β is a peptide that controls cell proliferation and differentiation [94]. It is well known for its role in ECM synthesis but it is also involved in ECM degradation by activating metalloproteinases (MMP2 and MMP9) [275, 371]. Latency associated proteins (LAPs) form a complex by binding to TGF-β intracellularly, which is then secreted and cross-linked to the ECM by latent TGF-β binding proteins (LTPBs). This TGF-β-LAP-LTPB complex is called large latent complex (LLC) and TGF-β is inactive in this cross-linked form. Activation takes place upon proteolytic release of this complex from the ECM [158], for example by fibrillin-1 fragmentation [371].

Subsequently, active TGF-β binds to the cell surface receptors – TGF-β receptor type I or II – activating canonical or non-canonical pathways. The canonical pathway through SMAD 2/3 cascade is associated with ECM synthesis and stabilization, whereas the non-canonical pathways such as mitogen-associated protein kinase (MAPK) and ERK1/2 cascades are associated with ECM degradation [275]. The end effect of TGF-β signaling highly depends on which receptors are activated, since any of the 7 type I and 5 type 2 receptors can be involved in the process introducing a high complexity [377]. In addition, the combined interactions between the two receptors types may determine the binding of the peptide and the resulting biological activity. Type I receptor plays role in the induction of genes involved in cell-matrix interactions, whereas type II receptor is involved in the anti-proliferation activity of TGF-β [66].

Angiotensin-II is a potent vasoconstrictor of the vascular system. Ang-II signaling in adults is mostly via the G-protein coupled pathway through Ang-II receptor 1 (AT1) which drives SMC contraction, whereas AT2 receptors are expressed during fetal development and pathophysiologies such as hypertension and atherosclerosis [377].

Multiple levels of interactions exist between TGF-β and Ang-II signaling, as depicted in Fig 1.12. For example, activation via AT1 receptors can enhance TGF-β signaling, or it can initiate MAPK (mitogen-activated protein kinase) cascade leading to ECM degradation independent of TGF-β [275, 371]. AT2 receptor, on the other hand, attenuates both canonical and non-canonical pathways of AT1 induced TGF-β signaling in addition to promoting SMC apoptosis [371].

1.2 Aortic Wall in Thoracic Aortic Aneurysms and Dissections

"*Homeostasis requires that intramural cells can sense their chemo-mechanical environment to keep the homeostasis and establish, maintain, repair or remodel the ECM to provide suitable compliance and yet sufficient strength [136].*"

Sustained imbalances in the chemical and mechanical signals as well as disturbances to these chain of events starting with sensation via genetic mutations can disrupt the ECM leading to pathological formations. For example, as mentioned before, endothelial cells respond to locally increased blood flow by inducing dilation of the vessel which decreases the wall shear stress, while increasing the circumferential stress temporarily, both of which goes back to normal values under normal circumstances. If, however, the increased flow is sustained, so are the increased diameter and isochorically decreased thickness, resulting in a sustained increase in circumferential stress. This leads to cell-matrix reorganization or ECM turnover to increase the thickness in the dilated state to restore the shear and circumferential stresses back to normal where smooth muscle cells proliferate initially, and endothelial cells and fibroblasts initiate growth and remodeling [133]. Since the microstructure of the aorta – especially the collagen architecture at high loads – governs mechanical behavior, certain risk factors influencing the microstructure and the structural changes in the TAADs are summarized before introducing the findings on the mechanical behavior of the diseased thoracic aortic wall.

1.2.1 Risk Factors

Hypertension: An experimental acute hypertension model on rats [374], where the authors created hypertensive environment by inducing co-arctation to the mid thoracic aorta, detected an immediate increase in TGF-β1 and TGF-β3 levels as well as increased cell proliferation for smooth muscle and endothelial cells. TGF-β levels returned back to normal levels after 2 weeks, however, cell proliferation was followed by cell apoptosis in 4 weeks. The wall thickness was increased in week 1, and this increase was preserved at weeks 2 and 4, without significant changes in the lumen diameter [374]. These changes in the wall serve to restore the homeostatic stress levels and to preserve them [133]. Sustained increase in circumferential stress due to a sustained increase in blood pressure can trigger SMCs, endothelial cells, and fibroblasts to remodel the ECM. These actions result in a thickness increase at the constricted state until the stresses are restored to their preferred levels at a preserved lumen diameter. A return to these stress levels would ideally restore NO production levels, however, this may not happen in hypertension (endothelial dysfunction) [133].

Bicuspid aortic valve (BAV) is a congenital disorder where the aortic valve has two leaflets instead of three. Although BAV has been associated with mutations in FBN1 [72] and NOTCH1 [87] genes, the mechanisms are not yet fully understood. Cystic medial necrosis, a common finding in the aortas affected by TAAD, in the ascending aorta of BAV patients has been reported [52]. Even in the absence of genetic mutations, which can also directly influence the structural arrangements in the aorta, altered haemodynamics due to BAV may influence the microstructure of the wall through mechanosensing [43, 250].

Diabetes mellitus (DM): Interestingly, the aneurysmatic aortas of DM patients grow at a slower rate [372]; and they appear to be thickened, denser and fibrous [245]. These observations led to DM being regarded as protective against aneurysm formation and rupture in all sections of the aorta. Advanced glycation end products (AGEs) may be responsible for this observation as they are increased in diabetic patients, resulting in proteolysis resistant and stiffer aortic wall. Moreover, the diabetic medications might also contribute to this stability by blocking the production of ECM degrading enzymes and/or their pathways [245].

Extracellular matrix related mutations

FBN1: MFS is a heritable fibrous connective tissue disorder effecting the microfibril assembly and it is caused by mutations in the fibrillin-1 (FBN1) gene [55]. Histopathology of patients with manifestations of the cardiovascular system include disruptions to the elastic lamellae, excessive amounts of collagen, proteoglycan accumulation, and SMC loss [264]. Mutations can either disrupt the deposition of fibrillin-1 microfibrils or decrease the amount of available fibrillin to from microfibrils [153]. These changes are primarily thought to disrupt TGF-β signaling pathways [264], although other signaling pathways such as epidermal growth factor (EGF) may also be affected [51]. Aneurysm development can easily be triggered when such disruptions are combined with the hemodynamic loading conditions on the thoracic aorta [136]. For example, the study [247] on mice suggested that aortic dilation in patients with Marfan's syndrome is primarily due to the failure of microfibrillar array of the adventitia to sustain physiological hemodynamic stress, and the disruptions to the elastic network assembly in the media is secondary. MASS syndrome, also caused by mutations to the FBN1 gene, has similar characteristics to MFS, except that the thoracic aorta is not prone to progressive dilation although patients manifest with mildly enlarged aortic root [80, 236] (MIM no. 604308, updated on 08/06/2010).

COL3A1: Vascular type (type IV) of EDS is caused by mutations in COL3A1 gene which encodes the $\alpha 1$ chain of type III collagen [236] (MIM no. 120180, updated on 21/12/2017). Patients suffering from this mutation are prone to spontaneous rupture of large arteries [236] (MIM no. 130050, updated on 22/12/2017) and are known to have fragile arteries [253]. Abnormally low intima-media thickness in elastic arteries of these patients may result in higher wall stresses, which can increase the risk of dissection and rupture [22]. The mutations in this gene result in the production of mutant type III procollagen, which was reported to have decreased thermal stability [212]. The structural defects in the procollagens can cause delayed formation as well as destabilization of the triple helix resulting in reduced secretion [213]. Type III rich fibrils with smaller diameter as a result of the mutations were also reported [27]. As opposed to creating structurally altered type III fibrils, the study [289] suggested that the mutations may rather result in the deficiency of the protein. Normal formation of type III collagen was suggested to be essential for type I collagen fibrils to form also normally [184].

Smooth muscle cell related mutations

ACTA2: Mutations to the gene encoding smooth muscle aortic α_2 actin creates disruptions to the cyclic interactions between α-actin and β-myosin heavy chain [236] (MIM no. 102620, updated on 26/10/2017). These mutations was found responsible for 14% of inherited TAAD [100] and they interfere with actin filament assembly causing decreased SMC contractility [181].

MYH11: Mutations to this smooth muscle β-myosin heavy chain coding gene [236] (MIM no. 160745, updated on 02/10/2017) are thought to affect the structure of smooth muscle myosin heavy chain and the assembly of myosin filament [380]. Angiotensin II and insulin growth factor I were observed to increase in patients with this mutation, however, it remains unclear how [241]. The patients present with reduced compliance and severe decrease in the elasticity of the aorta, and the histological investigations of the affected aortas show SMC, elastic fiber and collagen loss [380]. Increase of vasa vasorum in cases of mutations in ACTA2 and MYH11 genes suggests active inflammation processes [67].

MYLK: This gene encodes the myosin light chain kinase enzyme, which positively regulates muscle contraction [236] (MIM no. 600922, updated on 19/12/2013). The mutations causes loss of enzyme function by altered calmodulin binding [353]. Mice with knockdown MYLK gene showed proteoglycan pooling in the media consistent with increased expressions of lumican and decorin, however, there was no elastic fiber degradation [353]. The authors also reported an increase in type III collagen in the adventitia.

TGF-β related mutations

Direct mutations of the TGF-β signaling pathways are associated with different phenotypes of Loeys-Dietz syndrome (LDS). Three of these phenotypes (LDS1, LDS2, LDS4) are related to the ones explained below, whereas LDS3 and LDS5 are related to the mutations in SMAD3 [236] (MIM no. 613795, updated on 21/10/2016) and TGFB3 [236] (MIM no. 190230, updated on 14/04/2017) genes, respectively.

Loss-of-function mutations affecting a certain isoform may result in seemingly contradictory increases in the related TGF-β activity detected by an increase downstream signaling [4]. Different isoforms of TGF-β can substitute for each other or they can activate a different signaling pathway which in turn manifests as increased TGF-β activity [4, 14, 183].

TGFB2 (LDS4): Mice with this mutation presented with small and thin walled ascending aortas [280] as well as increased canonical and non-canonical TFG-β signaling [183]. Histological sections of the aortas from mice with heterozygous mutations showed elastic fiber fragmentation and collagen deposition [183].

TGFBR1 (LDS1): This gene encodes the serine/threonine kinase receptor type I for TGF-β [236] (MIM no. 190181, updated on 28/09/2018). The mutations are reported to result in LDS1 and to cause activation of the TGF-β signaling pathway [94]. In the study [172] mice embryos died prematurely. The authors also reported severe defects in vascular development and absence of circulating red blood cells.

TGFBR2 (LDS2): This gene encodes the serine/threonine kinase receptor type II for TGF-β [236] (MIM no. 190182, updated on 11/07/2017). The study [186] reported loss of elastin content as well as disrupted organization of elastic fibers in the aortic media. The authors suggested that these characteristics were due to the disruptions in elastogenesis rather than secondary destruction of the elastic fibers. In addition, the aortas from patients with MFS presented even higher collagen content when TGFBR2 mutation was accompanied by MFS.

1.2.2 Microstructure

Elastic fiber fragmentation accompanied by proteoglycan pooling and SMC loss has been reported by several studies for aortic dissections and dissecting aneurysms of the thoracic aorta [18, 21, 70, 225, 371]. These pools were observed to span over 3-4 lamellar units and corresponded to the areas with SMC loss [20]. Accumulation of GAGs can result in significant stress concentrations as well as contributing to intra-lamellar Donan swelling pressures leading to disruptions to the SMC signaling and delamination of the wall [134, 271]. Recently, versican and aggreacan were identified as the major components of such accumulations in TAAD patients [40]. Versican accumulation has been related to atherosclerosis, restenosis and inflammatory processes although exact mechanisms remain unclear [362]. In addition to the three main cell types in the aortic wall, inflammatory cells such as neutrophils, monocytes/macrophages, lymphocytes, adipocytes, mast cells and platelets are also active in the remodeling of the pathological aortic wall [256].

Smooth muscle cells isolated from the media of aortic dissection and aneurysm patients exhibit reduced expression of contractile proteins [21, 191, 219, 354]. SMCs isolated from dissection patients and cultured *ex vivo* have been reported to show increased proliferation rates [354], whereas SMCs isolated from aneurysm patients were less proliferative [191] compared to controls. Reduced expression of contractile proteins of the SMCs indicate a phenotype switch from contractile to the synthetic type; and such a phenotype switch is typically accompanied by collagen deposition and elastic fiber degradation, as observed for dissection [34, 354, 355] and aneurysm patients [191]. Although the study [21] also found reduced contractile properties for the aneuryms and dissections of the ascending aorta, the authors reported disorganized and decreased collagen content instead of increase in collagen [19, 21].

1.2.3 Mechanical Behavior

Significantly stiffer aneurysmatic tissue behavior in circumferential direction by [138] and on the contrary in longitudinal direction by [351] compared with control tissue was reported by comparing peak elastic modulus from uniaxial tensile test data. On the other hand, biaxial tensile test data at physiological load levels [9] showed aneurysmatic tissue to be stiffer than control tissues in both directions. The study in [302] found strips from ascending aneurysm and control tissue to be significantly stiffer and stronger in circumferential direction compared with the longitudinal direction. The authors also observed that aneurysms did not cause wall weakening, but the strips from aneurysmatic tissues were stiffer and less extensible than the strips from the control tissue. Furthermore, the study [10] reported that the dissected tissues were significantly stiffer in their collagen dominated response in circumferential direction compared with control tissues in [35].

Unfortunately, none of the above mentioned biomechanical studies quantified the collagen architecture in terms of fiber orientation which could shed light on the findings regarding anisotropy and heterogeneity of the pathological and control aortic tissues. Regardless, [35, 138, 302] reported reduced elastin accompanied with unchanged collagen content.

The aneurysmatic aortic wall from older patients were stiffer compared with younger patients [233], similar to the healthy aortic wall. The degree of collagen fiber alignment increases with age and it causes a stiffening that is primarily seen in the abdominal aorta, although collagen fibers in the intact wall are predominantly aligned circumferentially in all aortic locations for all age groups [107]. In contrast, the study [10] found no influence of age on the mechanical behavior of dissected tissues.

Uniaxial tensile tests were used to characterize the regional and directional differences by comparing the low and high elastic moduli (related to initial compliant region and stiff region of the tensile curve, respectively) of ascending aortic aneurysms [76]. The authors reported a significantly higher maximum elastic modulus for specimens from both posterior and anterior regions in the circumferential than in the longitudinal direction, whereas there was no significant differences in the low elastic modulus. Transition stretch was significantly higher in the circumferential compared with the longitudinal specimens from both anterior and posterior regions. Anisotropy of aortic tissues from ascending aneurysms has been confirmed by other studies using uniaxial tests [64, 75, 137, 157]. In contrast, other studies did not find an evidence for anisotropy of aneurysmatic tissues under uniaxial [351] and biaxial loading [35], and of dissected tissue under biaxial loading [10].

Layer-specific uniaxial tensile tests on human ascending aortic aneurysms in [303] demonstrated regional heterogeneities in tissue stiffness for all layers. Highest and lowest values for the media and the adventitia observed for the right and left lateral regions, respectively, similar to the observations for the intact wall [137]. The authors reported significantly higher stiffness in circumferential strips compared with the longitudinal ones for both medial and adventitial layers [303].

The study [37] found significantly higher energy loss in the longitudinal direction, defined as the hysteresis divided by the total strain energy, under biaxial testing in samples from aneurysmatic walls compared with the control tissue. The authors reported that this energy loss was correlated with aortic size and associated with medial degeneration and increased collagen to elastin ratio. In a follow-up study [38], they reported higher energy loss in the circumferential than in the longitudinal direction for both control and aneurysmatic aortas pointing to anisotropy. However, the degree of anisotropy was different for the individual samples. A tendency towards energy loss isotropy was observed for the aortas with high collagen to elastin ratios. This loss of anisotropy was the mechanical demonstration of severe medial degeneration, which is characterized by elastic fiber fragmentation. Moreover, it has been shown recently that not only elastin, but properly assembled and cross-linked elastic fibers are responsible for low energy loss in the aorta [160].

1.3 Organization of the PhD Thesis

Based on the information presented hitherto, it is clear that quantifying the changes in the collagen fiber distribution as well as the ground matrix in healthy and diseased thoracic aortas are necessary to reliably estimate their effect on the mechanical response. The following chapters indicate that this is also the case for modeling tissue failure. Chapter 2 presents the primary findings on how collagen structure influences failure properties under different shear loading modes. Chapters 3 and 4 review the continuum modeling of collagen fiber dispersion and failure properties of aortic tissues, respectively. Last but not least, the final chapter presents how collagen fiber distribution governs the failure properties under uniaxial loading.

1. *Mechanical strength of aneurysmatic and dissected human thoracic aortas at different shear loading modes*
   G. Sommer, S. Sherifova, P.J. Oberwalder, O.E. Dapunt, P.A. Ursomanno, A. DeAnda, B.E. Griffith and G.A. Holzapfel, Journal of Biomechanics, 49:7–13, 2016.

   The paper reports on the mechanical strength of healthy and diseased human thoracic aortic medias under different loading modes. In particular, in-plane and out-of-plane shear tests in addition to uniaxial tensile and direct tension tests were performed. Under different loadings the aortic tissues revealed anisotropic failure properties. In addition, it is evident that the aortic media is significantly resistant to rupture under 'out-of-plane' than under 'in-plane' shear loading, which can be explained by the collagen architecture of the tissue. Under tensile loading the tissue strength decreased as follows: circumferential > longitudinal > radial. The results clearly showed inter-specimen differences influenced by the anamnesis of the donors such as aortic diseases or connective tissue disorders, e.g., dissected specimens exhibited on average a markedly lower mechanical strength than aneurysmatic specimens. The rupture data based on the combination of tests are unique and provide a good basis for developing a 3D failure criterion of diseased human thoracic aortic media. This is a step forward to more realistic modeling of mechanically induced tissue failure i.e. rupture of aneurysms or progression of aortic dissections.

2. *On fibre dispersion modelling of soft biological tissues: a review*
   G.A. Holzapfel, R.W. Ogden and S. Sherifova, Proceedings of the Royal Society A, 475:20180736, 2019.

This study provides a review of the continuum modeling of fiber dispersion, in particular the angular integration (AI) approach and generalized structure tensor (GST) models. Collagen fibers in soft biological tissues such as artery, cartilage, myocardium and heart valves are responsible for their anisotropic mechanical behavior and the dispersed orientation of these fibers has a significant effect on the mechanical response of these tissues. Hence, the modeling of the dispersed structure is indispensable for the accurate prediction of stress and deformation characteristics of (patho)physiological tissues under various loading conditions. AI approach and GST models were used in representative numerical examples to fit sets of experimental data from mechanical tests and the fiber architecture from second-harmonic generation imaging. Predictions from both methods agree very well with the experimental data and these methods can enable more realistic boundary value problems to be solved. The study also provides a basis for improvement of material models and points to the need for additional mechanical and microstructural data to inform material modeling.

3. *Biomechanics of aortic wall failure with a focus on dissection and aneurysm: A review*
   S. Sherifova and G.A. Holzapfel, Acta Biomaterialia, in press.

   In clinical practice, dilated aortas are typically operated on if the diameter of the organ is approximately 5.5 cm. This approach is unable to predict the rupture at smaller diameters while it can overestimate the risk of rupture at larger diameters. Rupture risk prediction models developed with the aid of biomechanics community are a great improvement of the diameter criterion, however, these models do not attempt to model material failure. This article puts the rupture and dissection of the aorta into a material failure perspective. It begins with a summary of the microstructure of the aorta in health and disease, followed by loads and mechanisms which can lead to dissection and/or rupture. The focus of the study is an extensive literature review of the mechanical tests used to quantify the strength of the organ, such as uniaxial, bulge inflation and peeling tests as well as their findings. Based on the observations from these studies and large variations in strength, it is suggested that an effective material failure criterion for the aortic tissue must reflect the influence of microstructure on the failure properties.

4. *Failure properties and microstructure of healthy and aneurysmatic human thoracic aortas subjected to uniaxial extension with a focus on the media*
   S. Sherifova, G. Sommer, C. Viertler, P. Regitnig, T. Caranasos, M.A. Smith, B.E. Griffith, R.W. Ogden and G.A. Holzapfel, Acta Biomaterialia, in press.

   In this study, a unique set of data relating failure properties under uniaxial tensile loading and the microstructure of human thoracic aortic medias of control

> and disease groups is presented. The failure stresses of the control samples were significantly higher in the circumferential than in the longitudinal direction. The average failure stresses were the highest in the circumferential direction of the control, followed by the circumferential and longitudinal directions of the disease and the longitudinal direction of the control. Opposite trends were observed for the mean fiber direction from the loading axis suggesting that the observations in failure stresses can be attributed to the collagen architecture. Although other structural parameters investigated herein did not show a pronounced effect on the failure properties of the groups, the amount of dispersion around the mean fiber angle as well as content percentages seem to have a substantial effect on the failure properties when comparing specimens separately.

In addition, the following abstracts were accepted for the dissemination of the findings of this PhD Thesis:

- S. Sherifova, G. Sommer, B.E. Griffith and G.A. Holzapfel: *Influence of the microstructure on failure properties of soft fibrous tissues.* 25th Congress of the European Society of Biomechanics (ESB), Vienna, Austria, July 7–10, 2019.
- G.A. Holzapfel, K. Li, R.W. Ogden, S. Sherifova and G. Sommer: *Continuous versus discrete fiber dispersion in fibrous soft tissues.* 90th Annual Meeting of the International Association of Applied Mathematics and Mechanics (GAMM), Vienna, Austria, February 18–22, 2019.
- S. Sherifova, G. Sommer, B.E. Griffith and G.A. Holzapfel: *Failure properties of thoracic aortic media and its microstructure.* 42. Jahrestagung der Österreichischen Gesellschaft für Chirurgische Forschung, Schladming, Austria, November 15–17, 2018.
- S. Sherifova, G. Sommer, B.E. Griffith and G.A. Holzapfel: *Failure properties of human thoracic aortas in relation to their microstructure.* 8th World Congress of Biomechanics (WCB), Dublin, Ireland, July 8–12, 2018.
- S. Sherifova, G. Sommer and G.A. Holzapfel: *Mechanical strength of human thoracic aortas in health and disease.* 23rd Congress of the European Society of Biomechanics (ESB), Seville, Spain, July 2–5, 2017.

2 MECHANICAL STRENGTH OF ANEURYSMATIC AND DISSECTED HUMAN THORACIC AORTAS AT DIFFERENT SHEAR LOADING MODES

Abstract Rupture of aneurysms and acute dissection of the thoracic aorta are life-threatening events which affect tens of thousands of people per year. The underlying mechanisms remain unclear and the aortic wall is known to lose its structural integrity, which in turn effects its mechanical response to the loading conditions. Hence, research on such aortic diseases is an important area in biomechanics. The present study investigates the mechanical properties of aneurysmatic and dissected human thoracic aortas via triaxial shear and uniaxial tensile testing with a focus on the former. In particular, ultimate stress values from triaxial shear tests in different orientations regarding the aorta's orthotropic microstructure, and from uniaxial tensile tests in radial, circumferential and longitudinal directions were determined. In total, 16 human thoracic aortas were investigated from which it is evident that the aortic media has much stronger resistance to rupture under 'out-of-plane' than under 'in-plane' shear loadings. Under different shear loadings the aortic tissues revealed anisotropic failure properties with higher ultimate shear stresses and amounts of shear in the longitudinal than in the circumferential direction. Furthermore, the aortic media decreased its tensile strength as follows: circumferential direction > longitudinal direction > radial direction. Anisotropic and nonlinear tissue properties are apparent from the experimental data. The results clearly showed interspecimen differences influenced by the anamnesis of the donors such as aortic diseases or connective tissue disorders, e.g., dissected specimens exhibited on average a markedly lower mechanical strength than aneurysmatic specimens. The rupture data based on the combination of triaxial shear and uniaxial extension testing are unique and build a good basis for developing a 3D failure criterion of diseased human thoracic aortic media. This is a step forward to more realistic modeling of mechanically induced tissue failure i.e. rupture of aneurysms or progression of aortic dissections.

2.1 Introduction

Thoracic aortic aneurysms (TAAs) are localized dilatations of the ascending or descending thoracic aorta which develop over a span of years and may dissect (dissecting aneurysm) or rupture which is the most fatal condition. The mortality of thoracic aneurysms is estimated to be 50% over 5 years [68], whereas the mortality of an untreated Type A dissection approaches 50% in the first 48 hours. The pathogenesis of thoracic aneurysmal disease involves extracellular matrix degradation and loss of smooth muscle cells, causing a decrease in aortic wall integrity. The etiologies for these processes include atherosclerosis and genetic conditions such as Marfan's syndrome and Loey-Dietz syndrome [9, 68]. Hypertension has also been implicated as a cause.

Aortic dissection (AD) is an acute condition of the aorta which typically begins with a primary intimal tear on the right lateral wall of the ascending thoracic aorta (ATA), where the hydraulic shear force is at its peak, or at the descending thoracic aorta (DTA) directly after the ligamentum arteriosum [154]. The dissection first propagates in the radial direction towards the medial layer. Then, it proceeds within the media, or between the media and the adventitia, causing the layers of the aortic wall to separate [216]. The separation allows the blood flow to enter the aortic wall, whereby a secondary channel, a so called false lumen, is created. This leads to dilatation and weakening of the remaining outer wall of the false lumen which in turn increases the probability of the rupture and causes the patient to bleed to death within minutes [48, 231].

Interestingly, TAAs and ADs occur at similar locations in the thoracic aorta, presumably triggered by large hemodynamic forces and tissue stresses created in the left ventricular outflow tract when the heart contracts. Furthermore, the biomechanically important constituents of the elastic arterial wall are degraded during the process of the formation of TAA and AD. The main cause of TAA or AD is assumed to be hypertension, with an occurrence of 70%, and medial degeneration of the aorta [141, 154]. Rupture of the thoracic aorta is the main reason for morbidity and mortality of patients with Marfan's or Ehlers–Danlos syndromes [154]. Due to elevated cardiovascular stress, the appearance of a dissection or aneurysm increases with gestational age, i.e. it mostly occurs in older persons (>50 years) [139, 231].

Considering the variety of reasons for developing thoracic aortic diseases, a better understanding of patient-specific biomechanical properties is essential for developing biomechanical markers to predict adverse events. Moreover, patient-specific biomechanics-based computational approaches which use wall stress and strength distributions will provide more reliable estimates of aneurysm rupture or aortic dissection initiation/ progression [9, 343]. However, validation of biomechanics-based rupture indicators is needed before adaptation into the clinical paradigm.

A detailed analysis of the mechanical failure properties of aneurysmatic and dissected human thoracic aortas with a particular focus on four different shear tests is presented in this study. In particular, ultimate shear stresses and corresponding amount of shear values from mode II tests in four orientations, in addition to ultimate tensile stresses and corresponding stretch values from uniaxial tensile tests (in circumferential and longitudinal directions) and direct tension tests (in radial direction) of the aortic media were determined.

2.2 Materials and Methods

In the present study the media of diseased aortas ($n = 16$; age: 58 ± 12 years) was investigated. The aortas were subdivided into three categories: 'aneurysmatic', 'aneurysmatic with connective tissue disorder (CTD)', and 'dissected'. In Table 2.1, the anamnesis of

Table 2.1 Donor information such as age, gender, connective tissue disorder (CTD), and risk factor are stated. Moreover, the condition of the aorta and the harvesting position are provided.

	Specimen denotation															
	AI	*AII*	*AIII*	*AIV*	*AV*	*AVI*	*AVII*	*AVIII*	*AIX*	*CI*	*CII*	*CIII*	*DI*	*DII*	*DIII*	*DIV*
Institute	MUG	MUG	NYU	MUG	NYU	NYU	NYU	NYU	MUG	MUG	NYU	NYU	NYU	MUG	MUG	MUG
Age, yr	71	71	64	50	72	62	43	50	66	56	52	28	43	65	58	73
Gender	M	M	M	M	F	M	M	M	M	F	M	F	M	M	M	M
Condition	AN	AN	AN	AN	AN	AN	AN	AN	AN	AN	AN	AN	DI	DI	DI	DI
Position	ATA	ATA	ATA	ATA	ATA	ATA	ATA	ATA	ATA	ATA	ATA	DTA	DTA	ATA	ATA	ATA
CTD	-	-	-	-	-	-	-	-	-	FD	MA	MF	-	-	-	-
Risk factors	HT	HT HL	HT HL	HT HL OB	HT HM	AS	AR	AS	HT HL SM	HT SM	HT HL OB	HT	HT SM	HT	HT	HT DM

AN, aneurysmatic; AR, aortic regurgitation; AS, atherosclerosis; ATA, ascending thoracic aorta; DI, dissected; DM, diabetes mellitus; DTA, descending thoracic aorta; F, female; FD, fibromyxoid degeneration; HM, heart murmur; HL, hyperlipidemia; HT, hypertension; M, male; MA, MASS syndrome; MF, Marfan's syndrome; MUG, Medical University Graz; NYU, New York University; OB, obesity; SM, smoker

all donors from which the specimens were obtained are listed. Aneurysmatic specimens ($n = 9$) are denoted as *AI*−*AIX*, aneurysmatic specimens with CTD ($n = 3$) are denoted as *CI*−*CIII*, and dissected specimens ($n = 4$) are denoted as *DI*−*DIV*. More specifically, the donors of the CTD specimens had fibromyxoid degeneration (*CI*), MASS syndrome (*CII*), and Marfan's syndrome (*CIII*). Fibromyxoid degeneration is the transformation of fibrous tissue into a mucous-like 'connective' tissue characterized by the accumulation of glycosaminoglycans [232]. Marfan's syndrome is the result of a mutation in the FBN1 gene (gene for fibrillin-1) disrupting the elastic fiber assembly in the connective tissue by altering the regulation of TGF-β production [55, 147], while MASS (mitral, aortic, skin, skeletal) syndrome, also the result of a mutation in the FBN1 gene, is very similar to Marfan's syndrome but with some differences in clinical manifestations [147]. In addition to the anamnesis, the aortic disease and the position where the specimens were harvested are provided.

Both dissected thoracic sections and unruptured TAA sections were obtained from consented patients undergoing surgical repair at the Department of Cardiothoracic Surgery, NYU Langone Medical Center, and the Department of Cardiac Surgery, Medical University of Graz, Austria. The study protocol and the use of material from human subjects were approved by the local Ethics Committee, Medical University of Graz, Austria. In Fig. 2.1(a) a typically obtained aneurysmatic tissue sample (*CI*) with a severely dilated diameter is presented.

2.2.1 Shear Testing

Tubular aortic samples were cut along the longitudinal direction to obtain flat and rectangular sheets, and the media was separated with surgical tools. With the assumption of

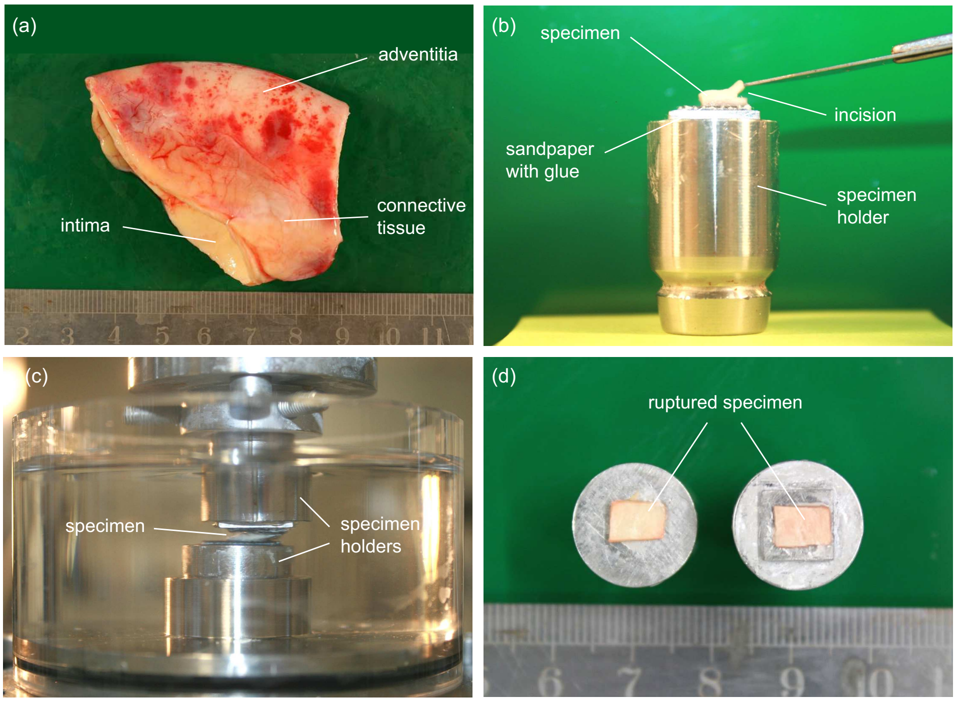

Figure 2.1 (a) representative photograph of a human ascending aortic aneurysm sample (*CI*) with a severely dilated diameter; (b) typical specimen with an incision of $\sim 1\,\mathrm{mm}$ for in-plane shear testing, which is glued to the upper specimen holder before insertion in the testing apparatus; (c) photograph of an 'in-plane' specimen subjected to simple shear loading; (d) ruptured into two parts and successfully tested 'in-plane' specimen.

an orthotropic structure of the aortic tissue, the behavior under six possible shear modes are identified, i.e. two different shear properties in each of the three planes [58, 307]. Using cylindrical coordinates, these planes are referred to as the $z\theta$-, rz- and $r\theta$-planes (Fig. 2.2). We refer to the shear modes in the $z\theta$-plane as 'in-plane' shear modes, and the shear modes regarding the rz- and $r\theta$-planes as 'out-of-plane' shear modes, and emphasize that the 'out-of-plane' shear mode should not be confused with *mode III* fracture testing. In particular, 'in-plane' shear tests in the circumferential and longitudinal directions of the $z\theta$-plane determine the ultimate shear stresses $\tau^{\mathrm{u}}_{r\theta}$ and τ^{u}_{rz}, respectively (Fig. 2.2(a)), whereas shearing in the radial and longitudinal directions of the rz-plane results in the 'out-of-plane' shear stress values $\tau^{\mathrm{u}}_{\theta r}$ and $\tau^{\mathrm{u}}_{\theta z}$, respectively (Fig. 2.2(b)). In an analogous manner, 'out-of-plane' shear tests in the radial and circumferential directions of the $r\theta$-plane results in the ultimate shear stresses τ^{u}_{zr} and $\tau^{\mathrm{u}}_{z\theta}$, respectively (Fig. 2.2(c)). Unfortunately, due to the restrictions arising from the specimen dimensions, we were only able to experimentally determine two out of four 'out-of-plane' shear stress values, $\tau^{\mathrm{u}}_{\theta z}$ and $\tau^{\mathrm{u}}_{z\theta}$.

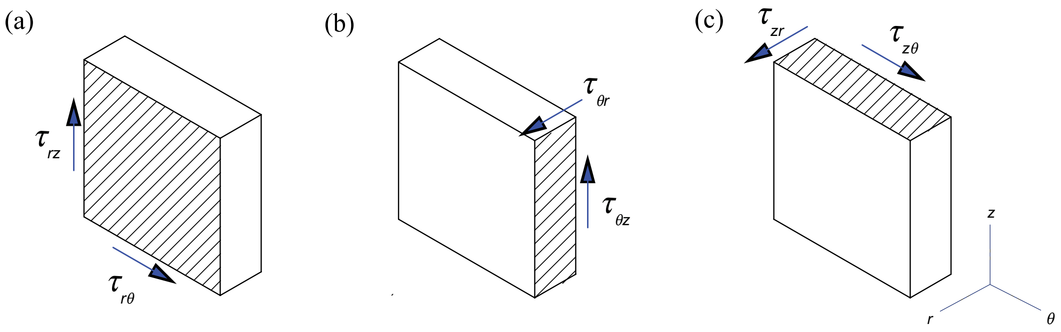

Figure 2.2 Sketches of six shear modes defined with respect to the radial (r-axis), circumferential (θ-axis), and longitudinal (z-axis) direction on an orthotropic tissue piece. Arrows indicate shear directions with corresponding shear stresses τ_{ij} and $i,j \in \{r,\theta,z\}$, where i denotes the normal vector of the plane that is being sheared, and j denotes the direction in which the face is shifted. For example, (a) shows 'in-plane'-shear modes in the $z\theta$-plane with shear in z- and θ-directions, respectively, while (b) and (c) show 'out-of-plane'-shear modes in the rz- and $r\theta$-plane, respectively.

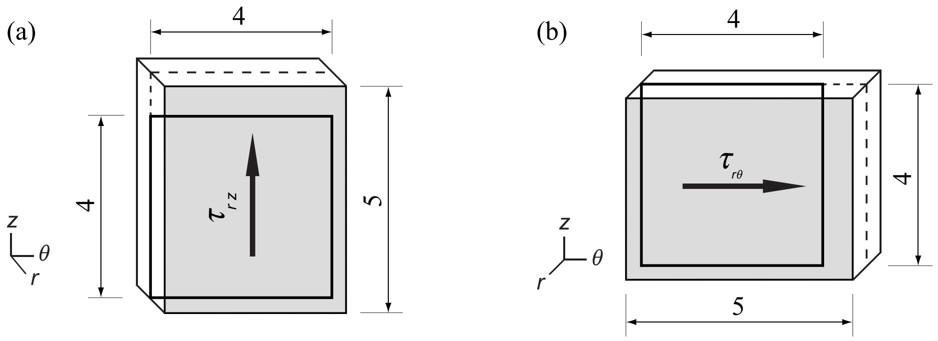

Figure 2.3 Sketches of 'in-plane' shear test specimens in the longitudinal direction (rz-mode), (a), and in the circumferential direction ($r\theta$-mode), (b), to obtain shear properties of the $z\theta$-plane. The shaded surfaces are glued to the specimen holders of the apparatus and sheared. The specimen is longer in the direction in which it is being sheared (~ 5 mm). On the shorter edge an incision of 1 mm parallel to the shearing direction is introduced (dashed lines). The remaining area (thick-lined black rectangular) is sheared until rupture occurs. Arrows indicate the shear directions.

For 'in-plane' shear tests, small rectangular tissue samples with the dimensions of 5 mm in length and 4 mm in width were prepared. An incision of 1 mm in depth along the width of the specimen was introduced to induce a predetermined breaking point, leaving the area on which the load was applied 4 × 4 mm (Figs. 2.1(b) and 2.3). Representative photographs during and after a successful ‘in-plane’ shear test are shown in Figs. 2.1(c) and 2.1(d), respectively.

A special specimen geometry and preparation had to be developed to ensure failure of the tissue in the correct plane during ‘out-of-plane’ shear tests. A variety of specimen geometries were tested to obtain the ‘out-of-plane’ shear stress. The final working geometry of the specimen had the dimensions 8×3 mm (length × width) with non-symmetric incisions (dashed lines) from both sides on the long edge (Fig. 2.4). Sandpaper and a thin consistent layer of cyanoacrylate adhesive were used to fix the specimen between two cylindrical specimen holders [305, 307]. Additionally, a compressive force of 0.5 N was applied to the specimens for 5 mins to ensure hardening of the adhesive and proper fixation of the specimen to the specimen holders. After 5 mins of adhesive hardening, the compressive force was reduced to 0 N, and the actual shear test was started.

During testing, the lower platform moved relative to the fixed upper platform with a constant speed of 1 mm/min. The applied force that led to failure was defined as the shear failure force. The ‘amount of shear’ was calculated as the ratio of the relative in-plane displacement of two parallel plates to their separation distance. The shear stress τ was calculated as the shear force f divided by the sheared area a.

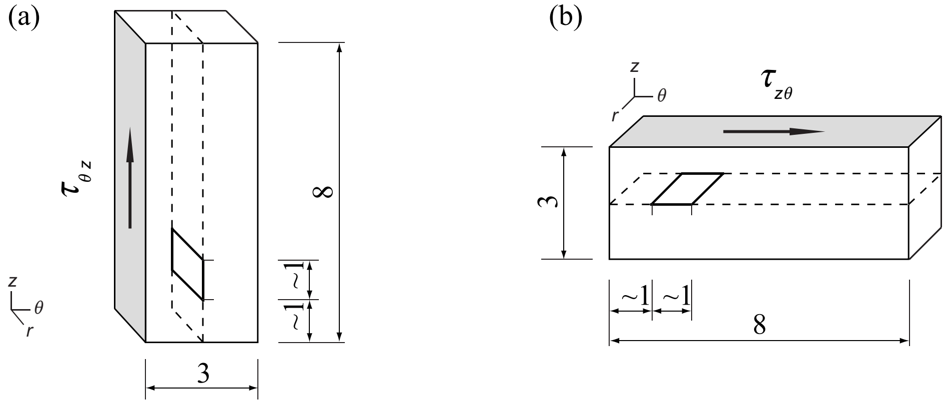

Figure 2.4 Sketches of ‘out-of-plane’ shear test specimens: (a) shear properties in the rz-plane; (b) shear properties in the $r\theta$-plane obtained from these tests. The shaded surfaces are glued to the specimen holders of the apparatus and sheared. The specimen is longer in the direction in which it is being sheared (8 mm). On the shorter edge (3 mm), incisions parallel to the shearing direction are introduced from both sides (dashed lines). The thick-lined black parallelogram between the incised surfaces is the sheared surface, with the dimension of ∼ 1 mm, parallel to the longer edge. Arrows indicate the shear directions.

2.2.2 Uniaxial Tensile Testing

In addition to shear tests, uniaxial tensile rupture tests in the radial, circumferential and longitudinal directions were conducted. For the determination of the radial failure stress, direct tension tests were performed with cylindrical specimens (d = 6.0 mm) with an incision of ~ 1.0 mm around the circumference until failure. For more details the reader is referred to [304]. For uniaxial tensile tests until rupture in the circumferential and longitudinal directions, dog-bone-shaped specimens were elongated until failure. For more details about specimen geometry, testing protocol and setup see [306].

All tests, except direct tension tests, were performed with the specimens inside a perspex container filled with PBS solution, which was maintained at a constant temperature of 37 °C [305–307]. Upon completion of the individual tests, each sample was inspected regarding the penetration of glue along its unattached sides.

2.2.3 Microstructural Investigation

Second-harmonic generation (SHG) imaging of ‘in-plane’ and ‘out-of-plane’ tests in the circumferential direction of specimen *AIX* was performed after mechanical testing, and after optical clearing following the procedure in [287].

2.2.4 Statistical Analyses

Statistical analyses were performed to test for significant differences of the mechanical stress values between different orientations and shear testing modes, i.e. between ultimate shear stresses and stretches in the circumferential and longitudinal directions, and between ‘in-plane’ and ‘out-of-plane’ shearing using paired two-sample t-test. p-values were determined based on Student’s t-distribution, where $p < 0.05$ was considered to be significant. Statistical analyses were performed using the OriginLab ORIGIN 7.5 program package. All data values are presented as mean values (mean) ± standard deviation (SD).

2.3 Results

In total, 16 diseased human thoracic aortas – 9 aneurysmatic, 3 aneurysmatic with CTD and 4 dissected– were investigated in this study.

2.3.1 Ultimate Shear Stress from ‘In-plane’ and ‘Out-of-plane’ Testing

‘In-plane’ shear stress vs. amount of shear behavior of successfully tested specimens in the circumferential ($r\theta$-mode) and longitudinal directions (rz-mode) of aneurysmatic and aneurysmatic with CTD are shown in Fig. 2.5. Corresponding results of the ‘out-of-plane’ shear tests in the circumferential ($z\theta$-mode) and longitudinal (θz-mode) directions of all aneurysmatic and aneurysmatic with CTD specimens are given in Fig. 2.6.

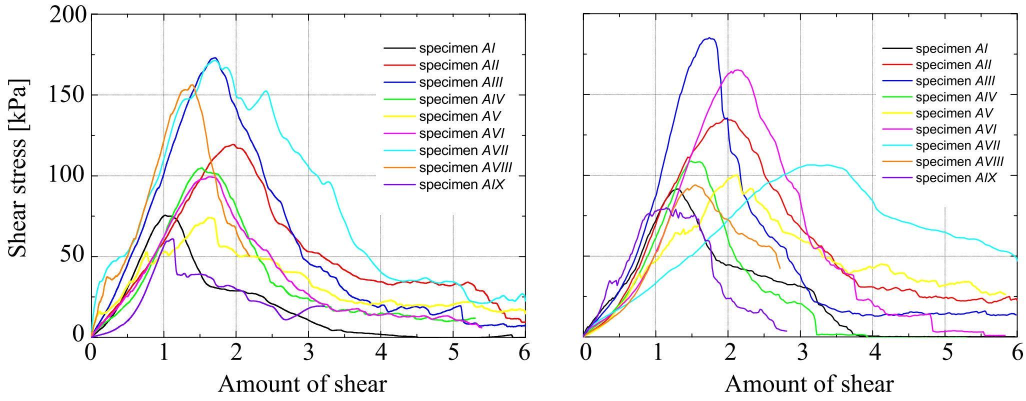
(a) Aneurysmatic tissue ($r\theta$-mode) (b) Aneurysmatic tissue (rz-mode)

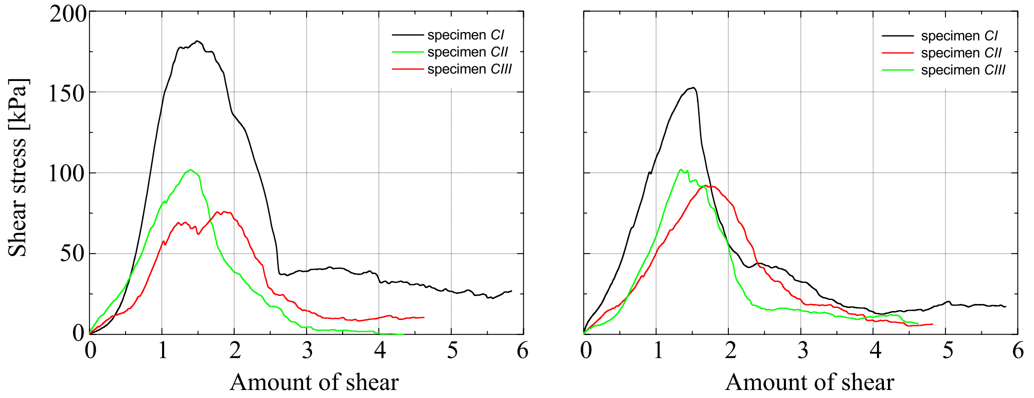
(c) Aneurysmatic tissue with CTD ($r\theta$-mode) (d) Aneurysmatic tissue with CTD (rz-mode)

Figure 2.5 Cauchy shear stress vs. amount of shear relationship during ‘in-plane’ shear tests of aneurysmatic human thoracic aortic tissues: (a),(b) ‘in-plane’ shear behavior within the $r\theta$- and rz-modes of aneurysmatic tissues, respectively; (c),(d) ‘in-plane’ shear behavior within the $r\theta$- and rz-modes of aneurysmatic tissues with connective tissue disorders (CTD).

In Tables 2.2 and 2.3, ultimate shear stresses and corresponding amount of shear values obtained from ‘in-plane’ and ‘out-of-plane’ shear tests of aneurysmatic and aneurysmatic with CTD are listed. Moreover, ‘in-plane’ shear responses in the circumferential ($r\theta$-mode) and longitudinal (rz-mode) directions of dissected specimens are given in Fig. 2.7. Unfortunately, due to the small specimen size ‘out-of-plane’ shear tests for dissected specimens could not be performed.

Table 2.4 states the ultimate shear stresses and corresponding amount of shear values from ‘in-plane’ tests of the dissected thoracic aortas. Interestingly, most tissue specimens from the *AI–AIX* and *DI–DIV* groups (except *AVII* and *AVIII*) revealed higher

(a) Aneurysmatic tissue ($z\theta$-mode) (b) Aneurysmatic tissue (θz-mode)

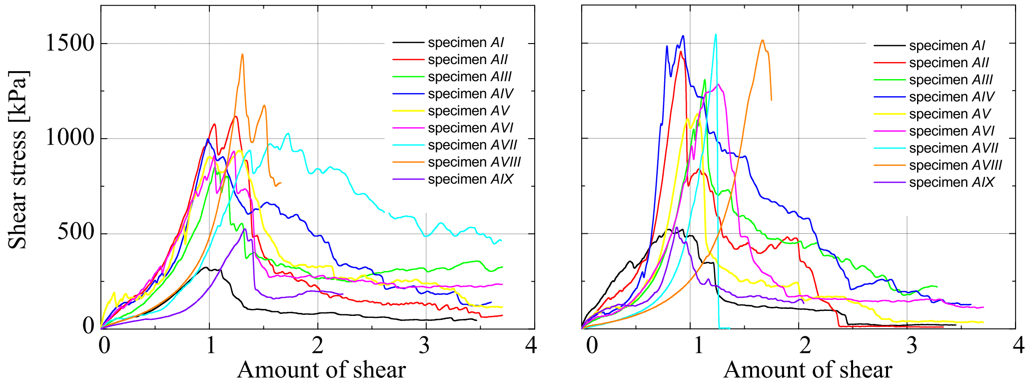

(c) Aneurysmatic tissue with CTD ($z\theta$-mode) (d) Aneurysmatic tissue with CTD (θz-mode)

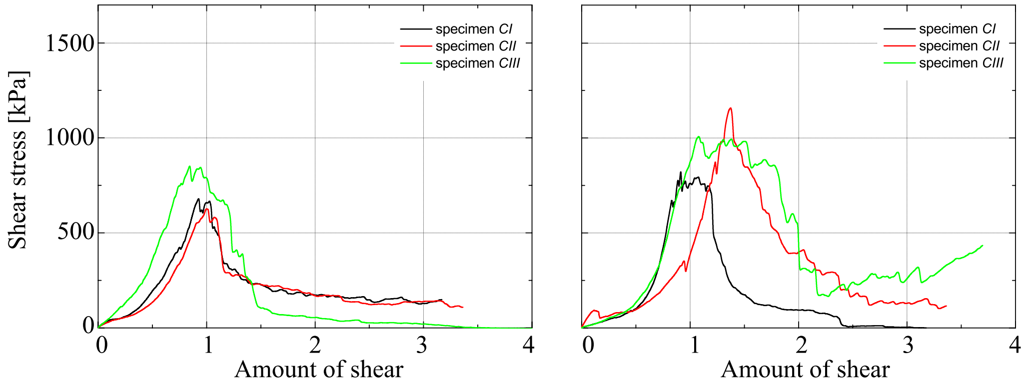

Figure 2.6 Cauchy shear stress vs. amount of shear relationship during ‘out-of-plane’ shear tests of aneurysmatic human thoracic aortic tissues: (a),(b) ‘out-of-plane’ shear behavior of aneurysmatic tissues within the $z\theta$- and θz-modes, respectively; (c),(d) ‘out-of-plane’ shear behavior of aneurysmatic tissues with connective tissue disorders (CTD).

ultimate shear stresses in the longitudinal direction when compared with the circumferential direction under ‘in-plane’ shear loading (Tables 2.2-2.4). Similarly, all specimens showed higher ultimate stresses in the longitudinal than in the circumferential direction under ‘out-of-plane’ shear loading (Tables 2.2 and 2.3).

In comparison with ‘in-plane’ shear tests, ‘out-of-plane’ shear tests exhibited much higher ultimate shear stress values. Consequently, aortic tissues indicate a much higher resistance to rupture subjected to ‘out-of-plane’ shear loading than ‘in-plane’ shear loading.

Table 2.2 Ultimate failure shear stress τ^{u} and corresponding amount of shear γ^{u} for aneurysmatic specimens subjected to ‘in-plane’ shear testing within the $r\theta$- and rz-modes, and ‘out-of-plane’ shear testing within the $z\theta$- and θz-modes.

	‘in-plane’ shear				‘out-of-plane’ shear			
Specimen	$\tau^{\mathrm{u}}_{r\theta}$ [kPa]	$\gamma^{\mathrm{u}}_{r\theta}$ [-]	τ^{u}_{rz} [kPa]	γ^{u}_{rz} [-]	$\tau^{\mathrm{u}}_{z\theta}$ [kPa]	$\gamma^{\mathrm{u}}_{z\theta}$ [-]	$\tau^{\mathrm{u}}_{\theta z}$ [kPa]	$\gamma^{\mathrm{u}}_{\theta z}$ [-]
AI	76	1.02	92	1.30	325	0.97	528	0.94
AII	120	1.97	135	1.98	1122	1.24	1467	0.92
AIII	105	1.53	109	1.49	860	1.05	1349	1.14
AIV	173	1.71	185	1.74	1011	0.99	1563	0.79
AV	74	1.63	100	2.12	946	1.27	1138	1.08
AVI	100	1.63	165	2.13	947	1.23	1292	1.26
AVII	173	1.73	106	3.14	1035	1.74	1565	1.24
AVIII	157	1.40	94	1.55	1479	1.31	1529	1.67
AVIX	61	1.12	80	1.15	533	1.33	548	0.88
Mean	115	1.53	118	1.84	918	1.24	1221	1.10
SD	41	0.28	34	0.56	313	0.22	388	0.25
n	9		9		9		9	

Table 2.3 Ultimate failure shear stress τ^{u} and corresponding amount of shear γ^{u} for aneurysmatic with CTD specimens subjected to ‘in-plane’ shear testing within the $r\theta$- and rz-modes, and ‘out-of-plane’ shear testing within the $z\theta$- and θz-modes.

	‘in-plane’ shear				‘out-of-plane’ shear			
Specimen	$\tau^{\mathrm{u}}_{r\theta}$ [kPa]	$\gamma^{\mathrm{u}}_{r\theta}$ [-]	τ^{u}_{rz} [kPa]	γ^{u}_{rz} [-]	$\tau^{\mathrm{u}}_{z\theta}$ [kPa]	$\gamma^{\mathrm{u}}_{z\theta}$ [-]	$\tau^{\mathrm{u}}_{\theta z}$ [kPa]	$\gamma^{\mathrm{u}}_{\theta z}$ [-]
CI	182	1.48	153	1.52	688	0.93	836	0.92
CII	102	1.40	92	1.69	629	1.00	1163	1.38
CIII	76	1.85	103	1.35	859	0.84	1011	1.08
Mean	120	1.58	116	1.52	725	0.92	1003	1.13
SD	45	0.20	27	0.14	98	0.07	134	0.19
n	3		3		3		3	

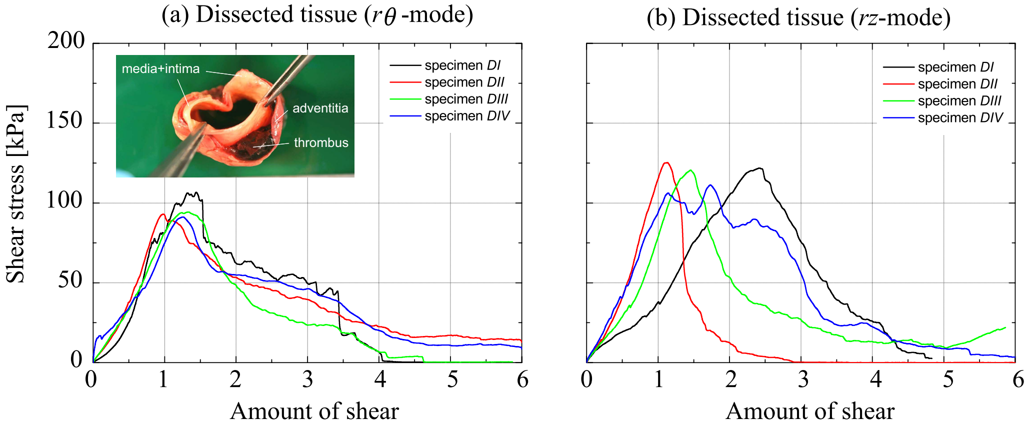

Figure 2.7 Cauchy shear stress vs. amount of shear relationship during ‘in-plane’ shear tests of dissected human thoracic aortic tissues: (a),(b) in the $r\theta$- and rz-modes, respectively.

Table 2.4 Ultimate failure shear stress τ^{u} and corresponding amount of shear γ^{u} for dissected specimens subjected to ‘in-plane’ shear testing within the $r\theta$- and rz-modes.

Specimen	$\tau^{\mathrm{u}}_{r\theta}$ [kPa]	$\gamma^{\mathrm{u}}_{r\theta}$ [-]	τ^{u}_{rz} [kPa]	γ^{u}_{rz} [-]
DI	107	1.45	122	2.42
DII	93	0.98	126	1.13
DIII	95	1.33	121	1.46
DIV	91	1.27	111	1.74
Mean	97	1.26	120	1.69
SD	6	0.17	6	0.47
n	4		4	

2.3.2 Ultimate Tensile Stress in Radial, Circumferential, and Longitudinal Directions

A characteristic behavior in all radial tests could be observed (not shown herein). During direct tension tests in the radial direction, the tissue showed an elastic behavior at small displacements represented by an ascending steep slope (nonlinear stiffening). After an ‘elastic limit’ was reached, a second phase, a strongly nonlinear softening behavior, started where damage and micro-defects gradually occurred. After reaching the maximal force (radial failure force) a third phase started, where the tissue dissected until complete tissue failure, which was very similar to the behavior observed in [304]. The average ultimate tensile stress and stretch of the samples ($n = 13$) were determined to be $\overline{\sigma}^{\mathrm{u}}_{rr} = 131 \pm 56\,\mathrm{kPa}$ and $\overline{\lambda}^{\mathrm{u}}_{r} = 2.66 \pm 0.68$, respectively.

Average ultimate tensile stresses and corresponding stretches in the circumferential and longitudinal directions were determined to be $\overline{\sigma}^{\mathrm{u}}_{\theta\theta} = 1282 \pm 822\,\mathrm{kPa}$, $\overline{\lambda}^{\mathrm{u}}_{\theta} = 1.52 \pm 0.20$ ($n = 7$) and $\overline{\sigma}^{\mathrm{u}}_{zz} = 565 \pm 198\,\mathrm{kPa}$, $\overline{\lambda}^{\mathrm{u}}_{z} = 1.50 \pm 0.18$ ($n = 10$), respectively. These values indicate anisotropic mechanical failure properties, with preferably higher mechanical strength in the circumferential than in the longitudinal direction. This anisotropic behavior may be explained by the preferred collagen fiber alignment in the circumferential direction of the thoracic aortic media [286].

2.3.3 Microstructural Investigation

Representative SHG images of sample *AIX* are shown in Fig. 2.8. Panels (a) and (b) show the collagen architecture in the $r\theta$- and $z\theta$-planes of the ‘in-plane’ shear test in the circumferential direction, respectively, while panels (c) and (d) show the collagen architecture in $r\theta$- and $z\theta$-planes of the ‘out-of-plane’ shear test in the circumferential direction, respectively. Images in panels (b) and (c) are parallel, whereas panels (a) and (d) are normal to the planes being sheared in ‘in-plane’ and ‘out-of-plane’ shear tests.

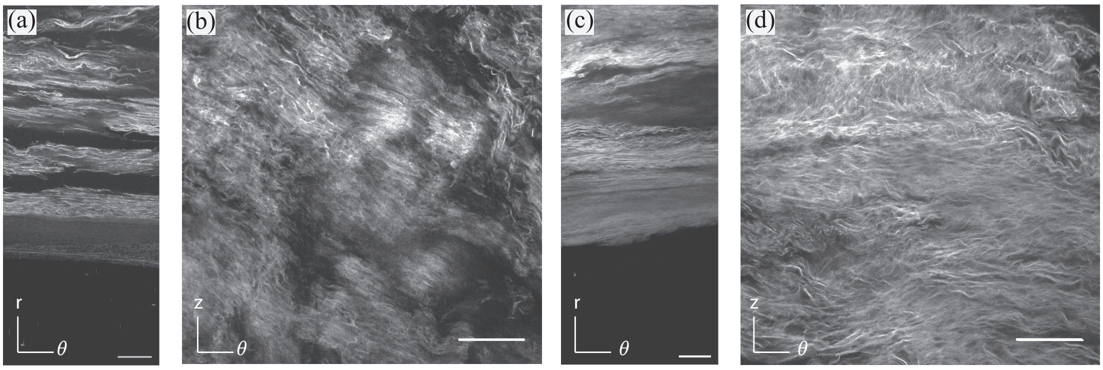

Figure 2.8 Representative SHG images of specimen *A*IX showing the collagen architecture: (a), (c) images taken from the $r\theta$-plane and (b), (d) images from the $z\theta$-plane of shear test samples in circumferential direction. Panels (a), (b) represent the planes normal and parallel to the plane of shearing of an ‘in-plane’ test sample, respectively; panels (c), (d) represent the planes parallel and normal to the shearing plane of an ‘out-of-plane’ test sample, respectively. White bars indicate $100\,\mu$m.

2.4 Discussion

The present study investigates the mechanical strength of diseased human thoracic aortas with respect to its anisotropic structure, with a particular emphasis on the shear properties. It is required to obtain relevant mechanical data of human thoracic aortas to better understand which type of stresses are responsible for inducing a crack and how this crack is propagating in the arterial wall to study rupture of diseased walls and propagation of aortic dissections more deeply. Furthermore, such data are prerequisites for the development of a failure criterion in thoracic aortic tissues, or for the design of better aortic grafts. To the authors' knowledge, this is the first investigation of the failure properties of diseased human thoracic aortic tissues under combined simple shear and uniaxial extension loadings.

2.4.1 Shear Testing

'In-plane' shear tests revealed anisotropic failure properties of thoracic aortic tissue with slightly higher ultimate shear stresses ($p = 0.44$) and significantly higher amounts of shear ($p = 0.02$) in the longitudinal than in the circumferential direction. Interestingly, ultimate 'in-plane' shear stresses in the circumferential and longitudinal directions were not significantly different for aneurysmatic tissues ($p = 0.84$), but significantly different for dissected tissues ($p = 0.009$). However, this trend was not observed for the corresponding amount of shear values ($p > 0.07$). Similar to 'in-plane' shearing, 'out-of-plane' shear tests showed significant anisotropic failure properties with higher ultimate shear stresses in the longitudinal than in the circumferential direction ($p = 0.0003$), but with not significantly different amounts of shear ($p = 0.57$) (see also Tables 2.2, 2.3, and 2.4). Remarkably, the aortic media revealed approximately one order of magnitude higher ultimate shear stress values for 'out-of-plane' loading than for 'in-plane' loading ($p < 0.0001$) with significantly smaller amounts of shear for 'out-of-plane' loading than 'in-plane' loading ($p < 0.006$). Consequently, under mixed shear loading state, the tissue will most likely fail due to 'in-plane' shearing and not due to 'out-of-plane' shearing. Furthermore, we observed several 'peaks' in the shear stress vs. amount of shear plots obtained from 'out-of-plane' tests, as can be seen in Fig. 2.6, which did not occur during 'in-plane' shear tests (see Fig. 2.5). This behavior may be attributed to the irregular rupture of collagen fibers and their interconnections.

Collagen fibers are the main load bearing structures in the arterial wall at large deformation and are known to be responsible for the high strength of arterial tissues subjected to tensile and shear loading. The elastin network in the media, including elastic lamellae, interlamellar elastin fibers, and radial elastin struts, certainly contribute to the shear properties at small deformation. However, the contribution of the elastin network to the shear strength behavior is small since failure occurs at large deformation. Moreover, for aneurysmatic and dissected tissues the contribution of the elastin network is very small, because elastin is usually disintegrated in such diseased tissues. Studies on aortic aneurysmatic tissues by, e.g., Tong et al. [327], revealed a very low elastin contents in the abdominal aortic aneurysms due to pathological changes and remodeling. The collagen architecture, visualized by second-harmonic generation (SHG) imaging (Fig. 2.8), suggests that the large difference in the ultimate shear stresses may be related to the collagen fiber orientation and dispersion. From Fig. 2.8 one can appreciate that the collagen fibers embedded within the parallel planes to the plane of shearing have only little resistance to shear displacements. In other words, fibers embedded in the $z\theta$-plane hardly contribute to the resistance of the specimen which is being sheared in the $z\theta$-plane (‘in-plane’ testing modes). However, this is an idealization of the real structure. One should consider that the collagen fibers embedded in these parallel planes are interconnected by, e.g., proteoglycans, smooth muscle cells, remaining elastin network etc., which might also contribute to the shear strength. Furthermore, the dispersed fibers connecting these parallel planes create a resistance in the planes normal to the plane of shearing. For example, out-of-plane fiber dispersion will resist shear displacement under ‘in-plane’ testing. We expect that the resistance to shearing, hence the shear strength, to be correlated with the mean fiber direction and the in plane dispersion of the fibers in the case of ‘out-of-plane’ testing, and with the out of plane fiber dispersion in the case of ‘in-plane’ testing (for the definitions of mean fiber direction and fiber dispersion see [130]).

Recently Haslach et al. [207] also performed shear tests on rectangular blocks, but on bovine aortas, which correspond to ‘in-plane’ shear in the present paper. In line with our findings, they reported no significant differences in stresses between the longitudinal and circumferential directions. Furthermore, they observed voids in the histology of test samples in the plane normal to the applied shear which is also evident in Fig. 2.8(a). Since their testing protocol and reporting method are different, we are not able to make a direct comparison with shear stress and amount of shear values that we have obtained. To identify the shear modulus (ratio between shear stress and amount of shear) inflation-extension-torsion tests were performed on human common carotid arteries [155], on rat thoracic aortas [53], and on porcine coronary arteries [187]. All these studies showed that the shear modulus was constant with changing twist angle while the longitudinal stretch and the inner pressure were kept constant at chosen physiological levels. Furthermore, the shear modulus was different for different values of longitudinal stretch and applied internal pressure [155, 187], and the relation became nonlinear at pressure levels higher than 120 mmHg [155]. The maximum twist angles applied in these studies was 25° under a mixed loading state. The experimental curves presented in the present study, both ‘in-plane’ and ‘out-of-plane’, also showed linearity at low amount of shear, but with a larger variability, as evident from Fig. 2.5. Interestingly, the study [155] stated that at twist angles of 70°–80° the tubular specimens lost their resistance. The maximum amount of shear ($\gamma_{rz} = 3.14$, sample AVII) in our study corresponds approximately to 72° shearing of a rectangular sample. However, we cannot make direct comparisons since the authors did not report any failure values. To the authors’ knowledge, comparable data in which shear loadings lead to failure of arterial tissues are not available in the literature.

2.4.2 Uniaxial Tensile Testing

In comparison with existing data, the average radial failure stress of the diseased human thoracic aortic media ($\overline{\sigma}^{\mathrm{u}}_{rr} = 131 \pm 56\,\mathrm{kPa}$ ($n = 13$)) was slightly higher than that of the human carotid bifurcations ($124 \pm 25\,\mathrm{kPa}$ ($n = 25$)) [326], and it was very similar to the average radial failure stress of aged healthy human abdominal aortic medias ($140.1 \pm 15.9\,\mathrm{kPa}$ ($n = 8$)) [304].

The average radial failure stresses of the diseased thoracic aorta were significantly lower than corresponding stresses in the circumferential ($\overline{\sigma}^{\mathrm{u}}_{\theta\theta} = 1282 \pm 822\,\mathrm{kPa}$ ($n = 7$)) ($p < 0.001$) and longitudinal directions ($\overline{\sigma}^{\mathrm{u}}_{zz} = 565 \pm 198\,\mathrm{kPa}$ ($n = 10$)) ($p < 0.001$), which may be explained by the laminar organization of the media with collagen fibers preferably found in the circumferential-longitudinal plane. Ultimate tensile stresses in the circumferential direction were on average significantly higher (about twice as high) than the ultimate stresses in the longitudinal direction ($p = 0.03$), which reflects pronounced anisotropic behavior. This anisotropy may be explained by the orientation of embedded collagen fibers, which are preferably orientated in the circumferential direction [286]. In contrast, the study [351] found similar ultimate tensile stresses in the circumferential ($1180 \pm 120\,\mathrm{kPa}$ ($n = 23$)) and longitudinal directions ($1210 \pm 90\,\mathrm{kPa}$ ($n = 17$)) of thoracic aortic aneurysms. However, a more recent study [251] revealed, in average, very similar ultimate tensile stresses in thoracic aortic aneurysms to our study ($1309 \pm 80\,\mathrm{kPa}$ ($n = 38$) in the circumferential direction and $619 \pm 34\,\mathrm{kPa}$ ($n = 38$) in the longitudinal direction).

Interestingly, ultimate stretches in the radial direction ($\overline{\lambda}^{\mathrm{u}}_{r} = 2.66 \pm 0.68$ ($n = 13$)) were significantly higher than ultimate stretches in the circumferential ($\overline{\lambda}^{\mathrm{u}}_{\theta} = 1.52 \pm 0.20$ ($n = 7$)) ($p < 0.001$) and longitudinal directions ($\overline{\lambda}^{\mathrm{u}}_{z} = 1.50 \pm 0.18$ ($n = 10$)) ($p < 0.001$). Average ultimate stretches in the circumferential and longitudinal directions were not significantly different ($p = 0.85$). However in the literature, failure stretches in the circumferential and longitudinal directions of thoracic aortic aneurysms were determined to be different (1.95 ± 0.05 vs. 1.55 ± 0.03) [251].

Moreover, we found correlations between the mechanical properties of the tested aortic tissues and the anamnesis of the patients. For example, it is interesting how ultimate stresses differ with respect to the underlying disease (aneurysm, tissue disorder, or dissection). Dissected specimens exhibited on average a markedly lower mechanical strength, than aneurysmatic specimens. Similarly, aneurysmatic specimens from donors suffering from connective tissue disorders showed distinctly lower ultimate stress values than other aneurysmatic specimens. This may reflect the risk of patients with connective tissues disorders developing or suffering from aneurysms. The variability in the mechanical strength of the aneurysmatic samples may be attributed to different stages of aneurysms.

2.4.3 Limitations

Due to the small specimen size it was not always possible to conduct all tests on every specimen. This is the reason for not representing ‘out-of-plane’ shear data for dissected specimens. Tissues with pronounced inhomogeneities such as atherosclerotic plaques were unsuitable for this investigation, resulting in the reduction of the amount of tissue available for testing, and hence in a reduced specimen number. Furthermore, a large number of uniaxial tension tests (in circumferential or longitudinal directions) failed because the rupture occurred near one of the clamps instead of the gage region. When there was adequate tissue material available, however, a second specimen was prepared and tested. SHG through the thickness of sample *AIX* revealed that there were thin intimal-like collagen fibers on one end, and thick adventitial-like collagen fibers at the other end of the image stack. Even though the layers could be easily peeled off in several cases, the borderlines between the intima/media and media/adventitia, especially for aneurysmatic samples, were not always clearly visible due to the process of aneurysm formation. For more discussion on that issue see [228]. All tests were conducted with an extension rate of 1.0 mm/min, although it is not established that this rate corresponds to a physiological value. However, there are no data available at which speed a dissection or rupture propagates in the case of an *in vivo* situation. The small amount of dissected and connective tissue disorder samples may lead to inadequate statistically relevant results. This also presents an obstacle to draw further meaningful conclusions.

Nevertheless, for the first time, this study presents methodologies for investigating biomechanical rupture properties of soft biological tissues in the context of different failure modes. Furthermore, the rupture data based on the combination of triaxial shear and uniaxial extension testing data are unique and build a good information basis for developing a 3D failure criterion of the diseased human thoracic aortic media; taking us a step closer to a realistic modeling of mechanically induced tissue failure.

Acknowledgement The authors are indebted to Anju R. Babu, Florian Hartmann, Gabrijela Korica, Franz Seiringer, and David Walk for their valuable contributions to the experimental tests and structural investigations. We would like to thank Annette E. Rabinovich for her valuable support during tissue transportation. Furthermore, we gratefully acknowledge the financial support of the National Institutes of Health (NIH), research grant no. NIH R01HL117063.

3 ON FIBRE DISPERSION MODELLING OF SOFT BIOLOGICAL TISSUES: A REVIEW

Abstract Collagen fibres within fibrous soft biological tissues such as artery walls, cartilage, myocardiums, corneas and heart valves are responsible for their anisotropic mechanical behaviour. It has recently been recognized that the dispersed orientation of these fibres has a significant effect on the mechanical response of the tissues. Modelling of the dispersed structure is important for the prediction of the stress and deformation characteristics in (patho)physiological tissues under various loading conditions. This paper provides a timely and critical review of the continuum modelling of fibre dispersion, specifically the angular integration and the generalized structure tensor models. The models are used in representative numerical examples to fit sets of experimental data that have been obtained from mechanical tests and fibre structural information from second-harmonic imaging. In particular, patches of healthy and diseased aortic tissues are investigated, and it is shown that the predictions of the models fit very well with the data. It is straightforward to use the models described herein within a finite element framework, which will enable more realistic (and clinically relevant) boundary-value problems to be solved. This also provides a basis for further developments of material models and points to the need for additional mechanical and microstructural data that can inform further advances in the material modelling.

3.1 Introduction

In recent years it has become apparent that in the modelling of fibrous soft biological tissues the dispersion of the collagen fibres has a significant effect on the mechanical response compared with the case when no dispersion is assumed (Gasser *et al.* [88]). Various models have been proposed to take account of different dispersion arrangements on the basis of continuum theory (Lanir [170], Driessen *et al.* [62], Freed *et al.* [83], Federico & Gasser [73], Holzapfel and Ogden [118], Agianniotis *et al.* [3], Pandolfi & Vasta [240], Melnik *et al.* [214], Holzapfel *et al.* [130], Holzapfel & Ogden [122], Melnik *et al.* [215]). The continuum approach has been shown to be very successful in modelling the elastic behaviour of many types of fibrous tissues, including artery walls (Holzapfel & Ogden [118]), cartilage (Ateshian *et al.* [8]), myocardiums (Eriksson *et al.* [71]), corneas (Pandolfi & Holzapfel [239]) and heart valves (Freed *et al.* [83]). In this approach the material is considered to be a fibre-reinforced composite with the fibres distributed within an isotropic matrix; the models developed within this framework describe the effect of the structural arrangement of the fibres on the mechanical response very well.

To inform the modelling it is important to have structural data from various imaging techniques in addition to data from mechanical tests. In recent years advances have been made that improve understanding of the microstructure of fibrous tissues; however, more information, such as the structure of the cross-linking of the collagen fibres and the effect this has on the mechanical response, is still needed to capture more details of the microstructure. Currently, available mechanical tests are insufficiently general to fully characterize the 3D mechanical response (Holzapfel & Ogden [117]). There is therefore a need for more general test protocols such as planar biaxial tests combined with in-plane shear, and/or through-thickness shear, or, as an alternative, extension/inflation tests combined with torsion and azimuthal or axial shear.

One consideration in modelling the collagen fibre structure is whether or not collagen fibres, in view of their very slender nature, can support compression. This is particularly important where the volume fraction of fibres is relatively small and the fibres under compression do not contribute to the mechanical response. In recent years several models have been proposed for excluding compressed collagen fibres from the mechanical response. To the authors' knowledge the study of Holzapfel & Ogden [119] was the first to analyse the set of orientations for which fibres are compressed and should therefore be excluded, while the study of Li *et al.* [176] used this theory as a basis for a finite element realization. Another approach for excluding compressed fibres is based on the use of a Heaviside function, as suggested by Federico and Herzog [74]. An efficient computational scheme for excluding fibres under compression has been developed more recently by Li *et al.* [179]. This involves discretizing a unit hemisphere with a finite number of spherical triangles and averaging the fibre density over each triangle.

In view of these recent developments and as a basis for further advances it is an appropriate time to provide a review of fibre dispersion modelling . This is the purpose of the first part of the present paper, while in the second part the theory is applied to some representative examples. In particular, §2 provides the equations for transversely isotropic elastic materials and extensions of these to account for fibre dispersion, including the angular integration (Lanir [170]) and the generalized structure tensor (Gasser *et al.* [88]) approaches, and a further extension to allow for excluding compressed fibres. In §3 the theory is applied to the special deformations of biaxial extension, equibiaxial extension and uniaxial extension, and provides explicit stress–deformation relations for these cases for both the angular integration and generalized structure tensor models. In §4 the first numerical example relates to the equibiaxial deformation of a tissue taken from an abdominal aortic aneurysm for which the published structural and mechanical test data of the tissue were used as a basis for fitting each model. The second numerical example relates to the uniaxial extension of two strips taken from the circumferential and longitudinal (axial) directions of a healthy human thoracic aorta. The novel structural and mechanical test data for the elastic domain (as yet unpublished) were used to identify an optimal set of the material parameters for each model. The overall agreement between the model predictions and the data is very good. The final section, §5, concludes this present study and points to the need for further developments.

3.2 Modelling Anisotropy for Fibrous Materials

In this section we introduce transverse isotropy and the fibre dispersion for which we critically analyse the AI and GST approaches and model approaches that exclude compressed fibres. For an overview of the main existing continuum mechanical models which take fibre dispersion into account the reader is referred to Table 1 of Holzapfel *et al.* [130]. In particular, different approaches, probability density functions, parameters describing the fibre dispersion and the type of dispersion are compared.

3.2.1 Transverse Isotropy

We introduce the deformation gradient **F** relative to an undeformed reference configuration, the right Cauchy–Green tensor $\mathbf{C} = \mathbf{F}^{\mathrm{T}}\mathbf{F}$ and the left Cauchy–Green tensor $\mathbf{b} = \mathbf{F}\mathbf{F}^{\mathrm{T}}$ as the basic kinematic variables. For an incompressible transversely isotropic elastic material, for which $\det \mathbf{F} \equiv 1$, with preferred direction **M** in the reference configuration, which is associated with the direction of a collagen fibre, the strain-energy function Ψ can be expressed in terms of four invariants, typically taken to be

$$I_1 = \mathrm{tr}\mathbf{C}, \quad I_2 = \frac{1}{2}[I_1^2 - \mathrm{tr}(\mathbf{C}^2)], \quad I_4 = \mathrm{tr}(\mathbf{C}\mathbf{M}\otimes\mathbf{M}), \quad I_5 = \mathrm{tr}(\mathbf{C}^2\mathbf{M}\otimes\mathbf{M}) \tag{3.1}$$

where $\mathbf{M}\otimes\mathbf{M}$ is referred to as a structure tensor. The Cauchy stress tensor $\boldsymbol{\sigma}$ is given by (see, for example, Holzapfel [114])

$$\boldsymbol{\sigma} = -p\mathbf{I} + 2\psi_1\mathbf{b} + 2\psi_2(I_1\mathbf{b} - \mathbf{b}^2) + 2\psi_4\mathbf{m}\otimes\mathbf{m} + 2\psi_5(\mathbf{m}\otimes\mathbf{bm} + \mathbf{bm}\otimes\mathbf{m}), \tag{3.2}$$

where $\mathbf{m} = \mathbf{FM}$ is the preferred direction mapped to the deformed configuration, and $\psi_i = \partial\Psi/\partial I_i$, $i = 1,2,4,5$. For the reference configuration to be stress free we require

$$2\psi_1 + 4\psi_2 - p = 0 \quad \text{and} \quad \psi_4 + 2\psi_5 = 0, \tag{3.3}$$

although, in general, the reference configuration may be residually stressed, but residual stresses are not considered here. For reasons discussed by Holzapfel *et al.* [124] we consider an energy function Ψ that reflects the isotropy through I_1 and the fibre content through I_4 so that (3.2) reduces to

$$\boldsymbol{\sigma} = -p\mathbf{I} + 2\psi_1\mathbf{b} + 2\psi_4\mathbf{m}\otimes\mathbf{m}, \tag{3.4}$$

where now Ψ is a function of I_1 and I_4 only, and the conditions (3.3) specialize accordingly. For many applications the strain-energy function Ψ is decoupled in the form

$$\Psi = \Psi_{\mathrm{iso}} + \Psi_{\mathrm{fib}}, \tag{3.5}$$

where Ψ_{iso} is the combined isotropic contribution of the extrafibrillar matrix and the elastic fibres, generally considered to be a function of I_1 alone and frequently characterized by the neo-Hookean model according to

$$\Psi_{\text{iso}} = \frac{1}{2}\mu(I_1 - 3), \tag{3.6}$$

where $\mu > 0$ is the reference state shear modulus of the isotropic material. The function Ψ_{fib} is connected with the energy stored in the collagen fabric and is often given by Holzapfel *et al.* [124]

$$\Psi_{\text{fib}} = \frac{c_1}{2c_2}\{\exp[c_2(I_4 - 1)^2] - 1\}, \tag{3.7}$$

where $c_1 > 0$ is a parameter with the dimension of stress and $c_2 > 0$ is dimensionless.

3.2.2 Fibre Dispersion

The AI Approach

Instead of considering fibres to be locally aligned we consider now a more realistic situation where there is a distribution of orientations. If a typical fibre has an orientation **N** in the reference configuration then a strain-energy function per unit volume associated with the stretching of all the fibres in that direction is given by $W(I_4)$, where $I_4 = \mathbf{N} \cdot \mathbf{CN} \equiv \text{tr}(\mathbf{CN} \otimes \mathbf{N})$, with $W(I_4) = W'(I_4) = 0$ for $I_4 \leq 1$ and $W'(I_4) > 0$ for $I_4 > 1$. Suppose that the fibre orientations are distributed according to a probability density $\rho(\mathbf{N})$ so that the total energy associated with the fibres is

$$\Psi_{\text{fib}} = \Psi_{\text{AI}} = \frac{1}{4\pi}\int_{\Omega} \rho(\mathbf{N})W(I_4)\text{d}\Omega, \tag{3.8}$$

where Ω is a unit sphere. Note that the total strain energy Ψ also includes an isotropic part as in (3.5), where Ψ_{iso} depends only on I_1. Several other formulations consider a multiplier n to describe the number of fibres per unit reference volume, but this is now absorbed into W. The factor $1/4\pi$ is not always used but is included here so that (3.8) reduces to $W(I_4)$ when there is no dispersion about some fixed direction **M** with $I_4 = \text{tr}(\mathbf{CM} \otimes \mathbf{M})$. Note that the orientation density function is normalized according to

$$\frac{1}{4\pi}\int_{\Omega} \rho(\mathbf{N})\text{d}\Omega = 1. \tag{3.9}$$

This integral formulation is called the *angular integration* (AI) approach, which was introduced by Lanir [170]. It is worth noting that in the original Lanir AI approach no isotropic part was included in the energy function and the possibility of different properties for different fibres within the dispersion was allowed for. The Cauchy stress tensor $\boldsymbol{\sigma}$ has the form

$$\boldsymbol{\sigma} = \boldsymbol{\sigma}_{\text{iso}} + \boldsymbol{\sigma}_{\text{AI}} - p\mathbf{I}, \qquad \boldsymbol{\sigma}_{\text{AI}} = \frac{1}{2\pi}\int_{\Omega} \rho(\mathbf{N}) W'(I_4)\mathbf{n}\otimes\mathbf{n}\,\mathrm{d}\Omega, \tag{3.10}$$

where $\mathbf{n} = \mathbf{FN}$ and $\boldsymbol{\sigma}_{\text{iso}}$ is the isotropic stress contribution from the non-collagenous material.

Some modifications of the AI approach adopted in the literature are as follows: the model of Sacks [277] incorporates a 2D AI distribution in a strain-energy function based on the Beta distribution, while the theory was applied to bovine pericardium. Also using the AI approach the model of Driessen *et al.* [62], which is based on Billar & Sacks [17] following Lanir [170], studied the biaxial behaviour of arterial walls and aortic valves with a planar fibre dispersion and a Gaussian probability density function. The model documented by Alastrué *et al.* [5] used an eight-chain model, where the chains are described as worm-like chains together with a repulsive energy function. This is based on the von Mises distribution with a non-symmetric dispersion and a microsphere model, and it was applied to artery walls with two fibre families. The study of Ateshian *et al.* [8] used an ellipsoidal distribution with a power-law strain-energy function to analyse the solid matrix of the cartilage fibres with fibres under compression excluded by use of the Heaviside function. Using the von Mises distribution the study of Raghupathy & Barocas [261] derived a closed-form solution in terms of modified Bessel functions of the first kind for an exponential fibre stress–strain law. The model was fitted to experimental data and applied to planar biaxial extension of a bioartificial tissue.

The paper of Federico & Gasser [73] documents a computational method for treating AI models using a Heaviside function to exclude compressed fibres and a planar von Mises distribution to examine the in-plane dispersion of collagen fibres. The model and a numerical integration method were implemented into FEAP (Taylor [321]) and applied to simulate the response of articular cartilage. The study of Agianniotis *et al.* [3] examined in-plane dispersion of collagen fibres and was fitted to experimental data on rabbit facial veins obtained from inflation/extension tests. Wavy collagen fibres were modelled so that they engage and bear stress at a critical value of the extension. Elastin was captured by a neo-Hookean term and a term which depends on I_4, while individual collagen fibres were modelled by using quadratic functions of the strain. On the basis of a Bingham distribution the study of Gasser *et al.* [89] proposed a constitutive law depending on the collagen fibre orientation and the authors applied the model to predict the biaxial response of abdominal aortic aneurysms and compared with synthetic data. A method for excluding compressed fibres within the AI framework was proposed by Holzapfel & Ogden [119] and a general formulation for the Cauchy stress and the critical angles at the boundary of the region where the fibres are stretched were provided. The review article of Limbert [180] on aspects of the mathematical and computational modelling of skin biophysics refers to several models including the AI model.

The GST Approach

An alternative approach for describing fibre dispersion, referred to as the *generalized structure tensor* (GST) approach, was developed by Gasser *et al.* [88] on the basis of a generalized structure tensor **H** defined by

$$\mathbf{H} = \frac{1}{4\pi}\int_{\Omega} \rho(\mathbf{N})\mathbf{N}\otimes\mathbf{N}\mathrm{d}\Omega, \tag{3.11}$$

with $\mathrm{tr}\mathbf{H} = 1$, which results from the normalization (3.9). A similar tensor was introduced in the context of the rheology of short fibre composites by Advani and Tucker [2], and referred to as an orientation tensor. Therein planar orientation states were discussed with applications to linear elasticity. The Advani and Tucker orientation tensors were also considered within the more recent paper of Lanir [171], which concluded that higher-order tensors are needed to better represent the geometrical fibre structure of the material. However, this is a purely geometrical consideration and does not take account of the actual material response, which can be well represented in terms of a second-order orientation tensor.

The tensor **H** is an averaged version of the individual structure tensors $\mathbf{N}\otimes\mathbf{N}$ of the fibres within the dispersion. A general strain-energy function involving the structure tensor **H** has the form $\Psi_{\mathrm{fib}} = \Psi_{\mathrm{GST}}(\mathbf{C},\mathbf{H})$ and can be represented in terms of the invariants of **C** and **H**. For example, the generalized invariant $I_4^\star = \mathrm{tr}(\mathbf{CH})$ is analogous to $\mathrm{tr}(\mathbf{CN}\otimes\mathbf{N})$ with $\mathbf{N}\otimes\mathbf{N}$ replaced by its generalized counterpart **H**, and the generalized invariant $I_5^\star = \mathrm{tr}(\mathbf{C}^2\mathbf{H})$ is similarly analogous to I_5. If we suppose that Ψ_{GST} depends only on $I_4^\star$ and $I_5^\star$, then the Cauchy stress tensor $\boldsymbol{\sigma}$ takes on the form

$$\boldsymbol{\sigma} = \boldsymbol{\sigma}_{\mathrm{iso}} + \boldsymbol{\sigma}_{\mathrm{GST}} - p\mathbf{I}, \qquad \boldsymbol{\sigma}_{\mathrm{GST}} = 2\psi_4^\star\mathbf{h} + 2\psi_5^\star(\mathbf{bh}+\mathbf{hb}), \tag{3.12}$$

where $\psi_i^\star = \partial\Psi_{\mathrm{GST}}/\partial I_i^\star$, $i = 4,5$, $\mathbf{h} = \mathbf{FHF}^{\mathrm{T}}$, and $\boldsymbol{\sigma}_{\mathrm{iso}}$ is the isotropic contribution of the non-collagenous material, as in (3.10).

When specialized to a transversely isotropic distribution where the fibres are distributed symmetrically around a mean direction **M**, **H** and **h** are given by

$$\mathbf{H} = \kappa\mathbf{I} + (1-3\kappa)\mathbf{M}\otimes\mathbf{M}, \quad \mathbf{h} = \kappa\mathbf{b} + (1-3\kappa)\mathbf{m}\otimes\mathbf{m}, \tag{3.13}$$

where **I** is the identity tensor and κ is the dispersion parameter defined by

$$\kappa = \frac{1}{4}\int_0^{\pi} \rho(\Theta)\sin^3\Theta\mathrm{d}\Theta, \tag{3.14}$$

where $\rho(\mathbf{N})$ is replaced by $\rho(\Theta)$. In general, κ is contained in $[0,1/2]$ but for reasons discussed by Holzapfel & Ogden [118] it is usually restricted to $[0,1/3]$.

We now represent a general fibre direction $\mathbf{N}$ within a dispersion in terms of spherical polar angles Θ and Φ as

$$\mathbf{N}(\Theta,\Phi) = \sin\Theta\cos\Phi\mathbf{e}_1 + \sin\Theta\sin\Phi\mathbf{e}_2 + \cos\Theta\mathbf{e}_3, \tag{3.15}$$

with $\Theta \in [0,\pi]$, $\Phi \in [0,2\pi]$, and where $\mathbf{e}_1$, $\mathbf{e}_2$, $\mathbf{e}_3$ are fixed rectangular Cartesian unit vectors. We then multiplicatively decompose the density function ρ according to

$$\rho(\mathbf{N}) = \rho_{\mathrm{op}}(\Theta)\rho_{\mathrm{ip}}(\Phi), \tag{3.16}$$

where ρ_{op} and ρ_{ip} denote the orientation densities in the $\mathbf{e}_3$ (out-of-plane) direction and the $(\mathbf{e}_1,\mathbf{e}_2)$ plane (in-plane), respectively. We impose symmetry conditions, which are based on experiments (Schriefl *et al.* [286]) and have also been used by Holzapfel *et al.* [130], according to

$$\rho_{\mathrm{op}}(\pi-\Theta) = \rho_{\mathrm{op}}(\Theta) \quad \text{and} \quad \rho_{\mathrm{ip}}(\pi+\Phi) = \rho_{\mathrm{ip}}(\Phi). \tag{3.17}$$

Now, in the case when the fibre dispersion is non-symmetric the structure tensors $\mathbf{H}$ and $\mathbf{h}$ take on the particular forms (Holzapfel *et al.* [130])

$$\mathbf{H} = 2\kappa_{\mathrm{op}}\kappa_{\mathrm{ip}}\mathbf{I} + 2\kappa_{\mathrm{op}}(1-2\kappa_{\mathrm{ip}})\mathbf{M}\otimes\mathbf{M} + (1-2\kappa_{\mathrm{op}}-2\kappa_{\mathrm{op}}\kappa_{\mathrm{ip}})\mathbf{M}_{\mathrm{n}}\otimes\mathbf{M}_{\mathrm{n}}, \tag{3.18}$$

and

$$\mathbf{h} = 2\kappa_{\mathrm{op}}\kappa_{\mathrm{ip}}\mathbf{b} + 2\kappa_{\mathrm{op}}(1-2\kappa_{\mathrm{ip}})\mathbf{m}\otimes\mathbf{m} + (1-2\kappa_{\mathrm{op}}-2\kappa_{\mathrm{op}}\kappa_{\mathrm{ip}})\mathbf{m}_{\mathrm{n}}\otimes\mathbf{m}_{\mathrm{n}}, \tag{3.19}$$

where $\mathbf{M}$ here denotes the mean fibre direction lying in the $(\mathbf{e}_1, \mathbf{e}_2)$-plane, $\mathbf{M}_{\mathrm{n}}$ is the out-of-plane unit vector $\mathbf{e}_3$, and $\mathbf{m}_{\mathrm{n}} = \mathbf{F}\mathbf{M}_{\mathrm{n}}$ is the push forward of $\mathbf{M}_{\mathrm{n}}$. The parameters κ_{op} and κ_{ip} quantify the out-of-plane and in-plane dispersions and are defined by

$$\kappa_{\mathrm{op}} = \int_0^{\pi/2} \rho_{\mathrm{op}}(\Theta)\sin^3\Theta\mathrm{d}\Theta \quad \text{and} \quad \kappa_{\mathrm{ip}} = \frac{1}{\pi}\int_0^{\pi} \rho_{\mathrm{ip}}(\Phi)\sin^2\Phi\mathrm{d}\Phi, \tag{3.20}$$

with the normalization conditions

$$\frac{1}{2}\int_0^{\pi/2} \rho_{\mathrm{op}}(\Theta)\sin\Theta\mathrm{d}\Theta = 1 \qquad \text{and} \qquad \frac{1}{\pi}\int_0^{\pi} \rho_{\mathrm{ip}}(\Phi)\mathrm{d}\Phi = 1, \tag{3.21}$$

and the ranges of values

$$0 \le \kappa_{\mathrm{op}} \le 1/2 \quad \text{and} \quad 0 \le \kappa_{\mathrm{ip}} \le 1. \tag{3.22}$$

The dispersion parameter κ_{op} corresponds to a rotationally symmetric dispersion about the direction $\Theta = 0$, while κ_{ip} represents a planar dispersion in the plane $\Theta = \pi/2$. In the case of a non-symmetric fibre dispersion the contribution $\boldsymbol{\sigma}_{\mathrm{GST}}$ to the Cauchy stress tensor is again given by (3.12), but with $\mathbf{h}$ now coming from (3.19).

It has been found convenient to use von Mises distributions to represent the probability density functions according to

$$\rho_{\mathrm{ip}}(\Phi) = \frac{\exp(-a\cos 2\Phi)}{I_0(a)} \quad \text{and} \quad \rho_{\mathrm{op}}(\Theta) = 4\sqrt{\frac{b}{2\pi}}\frac{\exp(-2b\cos^2\Theta)}{\operatorname{erf}(\sqrt{2b})}, \tag{3.23}$$

where the constants a and b are concentration parameters, $I_0(a)$ is the Bessel function of the first kind of order 0, and erf denotes the error function. The dispersion parameters κ_{ip} and κ_{op} then have the explicit forms

$$\kappa_{\mathrm{ip}} = \frac{1}{2} - \frac{I_1(a)}{2I_0(a)} \quad \text{and} \quad \kappa_{\mathrm{op}} = \frac{1}{2} - \frac{1}{8b} + \frac{1}{4}\sqrt{\frac{2}{\pi b}}\frac{\exp(-2b)}{\operatorname{erf}(\sqrt{2b})}, \tag{3.24}$$

where $I_1(a)$ is the modified Bessel function of the first kind of order 1. An alternative to the von Mises distribution is the Bingham model used by Gasser *et al.* [89] although it has not been adopted subsequently to any great extent.

A specific form of Ψ_{GST} which depends only on $I_4^\star$ is commonly used in the form (Gasser *et al.* [88])

$$\Psi_{\mathrm{GST}} = \frac{k_1}{2k_2}\{\exp[k_2(I_4^\star - 1)^2] - 1\}, \tag{3.25}$$

which, with (3.6), is frequently referred to as the GOH model. Here it is important to note that the parameters k_1 and k_2 are in general not the same as those involved in (3.7). Note that $I_4^\star = \mathrm{tr}(\mathbf{CH}) = \mathrm{tr}\mathbf{h}$, and hence, with $(3.13)_2$ and (3.19), the specifications

$$\begin{aligned} I_4^\star &= \kappa I_1 + (1-3\kappa)I_4 \quad \text{and} \\ I_4^\star &= 2\kappa_{\mathrm{op}}\kappa_{\mathrm{ip}}I_1 + 2\kappa_{\mathrm{op}}(1-2\kappa_{\mathrm{ip}})I_4 + (1-2\kappa_{\mathrm{op}}-2\kappa_{\mathrm{op}}\kappa_{\mathrm{ip}})I_{\mathrm{n}} \end{aligned} \tag{3.26}$$

follow, respectively, where $I_{\mathrm{n}} = \mathbf{m}_{\mathrm{n}} \cdot \mathbf{m}_{\mathrm{n}}$. The specific expression for $\boldsymbol{\sigma}_{\mathrm{GST}}$ in this case is

$$\boldsymbol{\sigma}_{\mathrm{GST}} = 2k_1(I_4^\star - 1)\exp[k_2(I_4^\star - 1)^2]\mathbf{h}, \tag{3.27}$$

with $\mathbf{h}$ given by $(3.13)_2$ or (3.19) as appropriate.

We remark in passing that the general structure-like approach provided by Freed *et al.* [83] has some similarities with that developed here in terms of invariants, and it was applied to aortic heart valves. The paper of Melnik *et al.* [214] on the modelling of fibre dispersion in fibre-reinforced elastic materials introduced a modified structure tensor **H** in which compressed fibres are removed from the integral by use of a Heaviside function, as previously suggested by Federico & Herzog [74] with respect to the AI approach, and used by Federico & Gasser [73]. In considering the original GST model the authors of [214] unfortunately included the isotropic part of the structure tensor when the mean fibre direction was compressed instead of completely omitting the anisotropic contribution to the strain-energy function in this case; see eqn (26) therein. This is a misinterpretation of a statement on p. 26 by Gasser *et al.* [88], and leads to unphysical predictions of the uniaxial tension-stretch behaviour in section 2 of their paper. A similar misinterpretation is contained in Latorre & Montáns [173] (see eqn (17) therein), and the results obtained on that basis are not clear. This misinterpretation motivated the development of a model for excluding fibres in compression. Unfortunately, this model does not achieve this aim because it uses the mean squared stretch of the fibres in the plane transverse to the mean fibre direction, and this does not guarantee the exclusion of all compressed fibres.

On the basis of a GST model, in Roohbakhshan *et al.* [274] a projection method was presented to reduce 3D constitutive models to membrane formulations, which considerably reduces the number of degrees of freedom compared with the 3D solid finite element discretization. The follow-up study of Roohbakhshan & Sauer [273] developed rotation-free shell models by using the GST approach; NURBS-based FEs were used for the FE discretization and pure membrane, pure bending and mixed modes of the shell deformation were examined.

By using the GST model of Gasser *et al.* [88], the authors Ferreira *et al.* of the recent study [77] also incorporated a damage formulation and its non-local averaging of integral type, which seeks to include the effects of the microstructure in order to limit the localization induced by the damage variables. The study of Volokh [346] presents AI-based models using multiple (16 and 8) structure tensors and the author applied the models to analyse uniaxial extension in the circumferential and axial directions of arterial walls.

The motivation of an alternative approach documented by Pandolfi & Vasta [240], and subsequent papers, e.g., by Vasta *et al.* [344] and Gizzi *et al.* [90, 91], was based on errors in Federico & Herzog [74] and Cortes *et al.* [45], which have been followed by Pandolfi & Vasta [240] with the conclusion *'that for all the loading cases for which GST models introduce large errors, such as uniaxial loading, shear and biaxial loading, the proposed model has a better performance, in the sense that it provides results closer to the ones furnished by an exact angular integration of the fibre orientation distribution'*. Holzapfel & Ogden [120, 121] have pointed out that the errors of the papers by Federico & Herzog [74] and Cortes *et al.* [45] are based on incorrect analysis. Part of the motivation of the approach by Pandolfi & Vasta [240] was to incorporate higher order statistics to try and correct the supposed (but non-existent) errors. We now outline their formulation, which was designed to modify the GST model $\Psi_{\mathrm{fib}} = \Psi_{\mathrm{GST}}(I_4^\star)$ by including second-order statistics. Consider the AI model (3.8) and expand $W(I_4)$ as a Taylor series around $I_4^\star$ as

$$W(I_4) = W(I_4^\star) + (I_4 - I_4^\star)W'(I_4^\star) + \frac{1}{2}(I_4 - I_4^\star)^2 W''(I_4^\star) + \dots \tag{3.28}$$

Since, by (3.11) and the definition of $I_4^\star$, $(1/4\pi)\int_\Omega \rho(\mathbf{N}) I_4 \mathrm{d}\Omega = I_4^\star$, after substitution into (3.8) the approximation reads

$$\begin{aligned} \Psi_{\mathrm{fib}} &\simeq W(I_4^\star) + \frac{1}{2}W''(I_4^\star)\frac{1}{4\pi}\int_\Omega \rho(\mathbf{N})(I_4 - I_4^\star)^2 \mathrm{d}\Omega \\ &= \Psi_{\mathrm{GST}}(I_4^\star) + \frac{1}{2}W''(I_4^\star)[(\mathbb{H}\mathbf{C}) : \mathbf{C} - I_4^{\star 2}], \end{aligned} \tag{3.29}$$

where : denotes the double contraction. The latter term follows since, from (3.11) and the definition

$$\mathbb{H} = \frac{1}{4\pi}\int_\Omega \rho(\mathbf{N})\mathbf{N}\otimes\mathbf{N}\otimes\mathbf{N}\otimes\mathbf{N}\mathrm{d}\Omega, \tag{3.30}$$

we obtain

$$\frac{1}{4\pi}\int_\Omega \rho(\mathbf{N})(I_4^2 - 2I_4 I_4^\star + I_4^{\star 2})\mathrm{d}\Omega = (\mathbb{H}\mathbf{C}) : \mathbf{C} - (\mathbf{H} : \mathbf{C})^2. \tag{3.31}$$

Herein $\mathbb{H}$ is a fourth-order structure tensor which, without the factor $1/4\pi$, was introduced by Advani & Tucker [2] and referred to as an orientation tensor. It should be emphasized that this approximation is only valid for dispersions for which $I_4^\star$ is close to I_4, i.e. for narrow dispersions.

Given the energy function $(3.29)_2$ we can derive the rather complex Cauchy stress tensor $\boldsymbol{\sigma}_{\mathrm{fib}}$, i.e.

$$\begin{aligned} \boldsymbol{\sigma}_{\mathrm{fib}} = &\{2W'(I_4^\star) - 2I_4^\star W''(I_4^\star) + W'''(I_4^\star)[(\mathbb{H}\mathbf{C}) : \mathbf{C} - I_4^{\star 2}]\}\mathbf{h} \\ &+ 2W''(I_4^\star)\mathbf{F}(\mathbb{H}\mathbf{C})\mathbf{F}^{\mathrm{T}}. \end{aligned} \tag{3.32}$$

As Holzapfel & Ogden have shown in, e.g., [120] the GST and AI models have very similar predictive powers. It is inappropriate to argue that an additional term of the type considered here is needed to improve accuracy. In addition, the resulting stress tensor and elasticity tensor (not shown here) are relatively complicated to handle and to implement.

Model Approaches Excluding Compressed Fibres

Collagen fibres are embedded in a matrix material in a wavy form, as can be seen in particular in healthy artery tissues in the unloaded state. During loading the collagen fibres are straightened and then bear tension, leading to a stiffening response which is typically described by an exponential function. Under compression, however, the collagen fibres store very little or no energy because they are very slender, and the matrix material bears the compressive load. Moreover, for a mathematical model to be well behaved it should satisfy certain convexity conditions, which cannot be guaranteed when compressed fibres store energy (Holzapfel *et al.* [124, 125]). For this reason exclusion of compressed fibres is also important from the mathematical point of view in order to properly reflect the overall behaviour of the tissue.

It appears that the study of Weiss *et al.* [358] was the first to describe this switch between tension and compression in modelling the human medial collateral ligament. This was followed by Holzapfel *et al.*[124] who used this switch in a constitutive framework for arterial walls although the model therein does not consider dispersion. The key point is that the anisotropic part of the strain-energy function only contributes when either one or both of the fibre families is/are extended ($I_4 > 1$ or $I_6 > 1$ or both). This model was then extended by Gasser *et al.* [88] to accommodate dispersion based on the stretch in the mean fibre direction. However, using a criterion for which the mean fibre direction is extended does not, in general, allow exclusion of all compressed fibres within a dispersion. In fact, it has been claimed in the literature that it is not possible to exclude compressed fibres in the GST model of Cortes *et al.* [45], although Holzapfel & Ogden [120] have shown that this is not the case.

The following simple example of homogeneous uniaxial deformation illustrates how some fibres are compressed when the mean fibre direction is extended. Suppose a stretch $\lambda_3 = \lambda$ is applied in the mean fibre direction $\mathbf{M}$, which is taken to be the $\mathbf{e}_3$ direction so that by symmetry and incompressibility $\lambda_1 = \lambda_2 = \lambda^{-1/2}$. According to $(3.1)_1$ and $(3.1)_3$ we have

$$I_1 = \lambda^2 + 2\lambda^{-1} \quad \text{and} \quad I_4 = \lambda^2, \tag{3.33}$$

and from (3.25) and $(3.26)_1$ we then obtain

$$I_4^\star = \lambda^2(1-2\kappa) + 2\kappa\lambda^{-1}. \tag{3.34}$$

A plot of this relationship is shown in Fig. 3.1 for five different values of κ. As the plot indicates, $I_4^\star > 1$ for $\lambda > 1$, but, for some κ, $I_4^\star$ can also be greater than 1 when λ is less than 1, which means that the mean fibre direction can also be under compression.

Another point is that there exists a range of the angles of individual fibres for which the

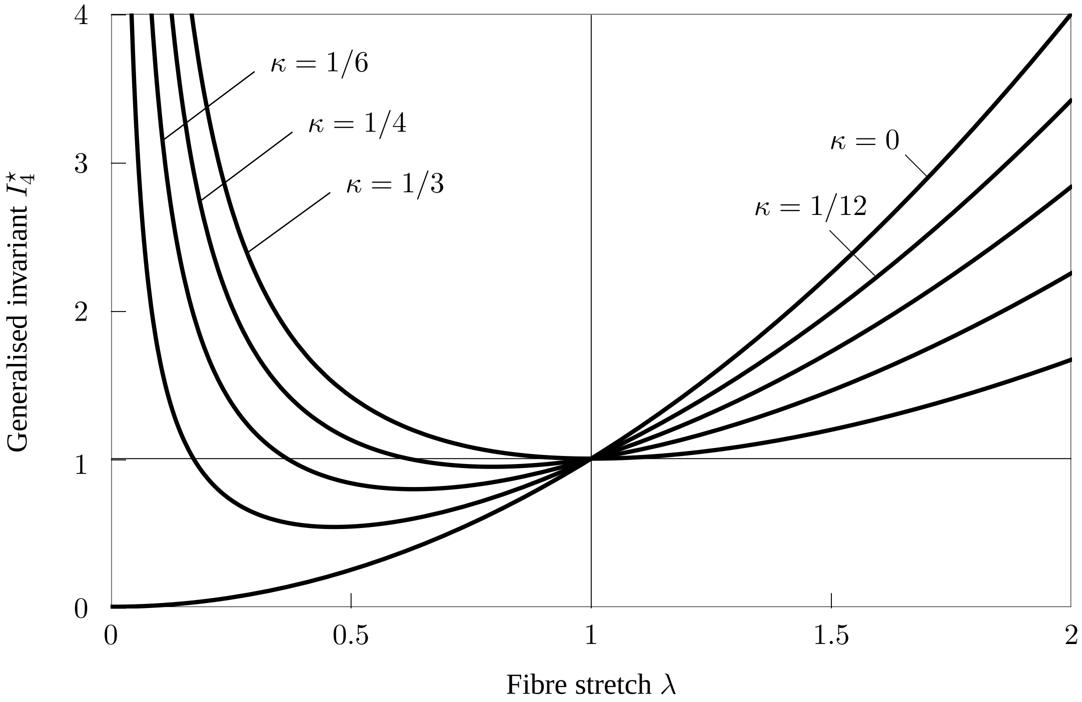

Figure 3.1 Plots of the generalized invariant $I_4^\star$ as a function of the fibre stretch λ for five different values of the dispersion parameter κ in the range $[0, 1/3]$.

fibres are *shortened* when $\lambda > 1$ in the mean fibre direction. Hence such fibres should be excluded from the energy function. We now consider $\mathbf{N}$, as given by (3.15), which makes an angle Θ with the mean fibre direction $\mathbf{M} = \mathbf{e}_3$. Because of symmetry, the square of the stretch in the direction $\mathbf{N}$ (i.e. $\mathbf{N}\cdot(\mathbf{CN})$) is independent of Φ, and hence

$$\mathbf{N}\cdot(\mathbf{CN}) = \lambda^2\cos^2\Theta + \lambda^{-1}\sin^2\Theta \equiv \lambda^{-1} + \lambda^{-1}(\lambda^3 - 1)\cos^2\Theta = I_4(\Theta), \qquad (3.35)$$

which defines the notation $I_4(\Theta)$. Thus, for $\mathbf{N}\cdot(\mathbf{CN}) > 1$ with $\lambda > 1$, we require

$$\cos^2\Theta > \frac{1}{\lambda^2 + \lambda + 1} = \cos^2\Theta_c, \qquad (3.36)$$

which identifies the range of values of Θ for which the fibres are extended, i.e. $-\Theta_c < \Theta < \Theta_c$ or $\pi - \Theta_c < \Theta < \pi + \Theta_c$. This means that the fibres should only contribute to the strain-energy function if $\cos^2\Theta$ is larger than $\cos^2\Theta_c$. Thus, if extension of the mean fibre direction of the dispersion is used as a criterion for including the anisotropic term in the strain-energy function then some compressed fibres will also be included, i.e. those outside these two ranges.

To our knowledge it was the study of Federico & Herzog [74] which first suggested the possibility, following a comment by Gasser *et al.* [88] in relation to the GST model, of using a Heaviside function $\mathcal{H}$ in the AI model for excluding compressed fibres, which in our notation reads

$$\Psi_{\text{fib}} = \Psi_{\text{AI}} = \frac{1}{4\pi} \int_{\Omega} \rho(\mathbf{N}) \mathcal{H}(I_4 - 1) W(I_4) \mathrm{d}\Omega. \tag{3.37}$$

Subsequently, that approach was pursued by Federico & Gasser [73] and applied to analyse articular cartilage numerically. The idea of considering a Heaviside function in the energy for the collagen fibres was also used in the study of Ateshian *et al.* [8] and applied to articular cartilage. The more recent paper of Melnik *et al.* [214] employed a deformation-dependent structure tensor in order to exclude compressed fibres, which the authors applied to uniaxial extension with two families of fibres. The study of Hashlamoun *et al.* [106] also used a Heaviside function to exclude compressed fibres, and the authors compared the results for three different polynomial expansions of the energy function about $I_4 = 1$, and they also performed comparisons of the Cauchy stresses σ_{11} and σ_{22} as functions of stretch for equibiaxial and biaxial deformations. Note that the comparison in the exponential case was performed with the same parameters $c_1 = k_1$ and for $c_2 = k_2 = 1$ for each case. The comparison of the GOH model and the AI-based model is therefore erroneous and misleading, as pointed out by Holzapfel & Ogden [120, 121].

In the study of Holzapfel & Ogden [119] the effect of using an inappropriate tension–compression switch for excluding the contribution of fibres under compression was analysed. A simple tension illustration indicates that the stiffness of the composite is in general significantly overestimated by not excluding fibres under compression. We have also computed the critical angle of the individual fibres relative to the fibre direction that corresponds to the switch. The subsequent paper of Li *et al.* [176] documents computational aspects of the model, and in particular expressions for the elasticity tensor and the integration boundary that admits only fibres which are extended were provided. The work of Gizzi *et al.* [90] introduced a probability density of I_4 to average I_4 itself over the range of values for $I_4 > 1$ as a means to exclude compressed fibres in the energy function. They also introduced two dispersion parameters, one as for the standard GST model and another one which is related to the second-order approximation. This approach was applied to uniaxial loading in the mean fibre direction in 3D, and to a planar dispersion for uniaxial loading in the mean fibre direction.

Alternative schemes for omitting compressed fibres in the calculations based on a particular constitutive law have been detailed by Li *et al.* [177–179]. In [177] the exclusion was effected by a restriction of the domain of integration in the AI energy function so that this domain becomes deformation dependent. The method was applied to some representative numerical examples including uniaxial extension, simple shear and extension–inflation of a residually-stressed carotid artery. In [178] a new general invariant which depends on only the fibres under tension was introduced, and then used to form the exponential energy function in place of I_4. This approach was applied to simple tension/compression, simple shear and unconfined compression of articular cartilage. A very efficient computational scheme based on discretizing a unit hemisphere with a finite number of spherical triangles and averaging the fibre density over each triangle was recently presented in [179]. The method was again applied to uniaxial extension, simple shear and also to the non-homogeneous extension of a rectangular strip.

3.3 Applications to Specific Deformations

3.3.1 Biaxial Extension

Here we consider a sheet of arterial tissue in the $\mathbf{e}_1$, $\mathbf{e}_2$ plane which is biaxially stretched so as to minimize the amount of shearing. For arterial tissue two families of fibres are present and we now introduce the necessary equations to describe this.

While the mean fibre direction of the first family of fibres in the reference configuration is denoted by $\mathbf{M}$, that of the second family of fibres is denoted by $\mathbf{M}'$, and the associated squares of the stretches in these two directions are denoted I_4 and I_6. The corresponding generalized invariants analogous to (3.26) are the same except that I_4 is changed to I_6, and $I_4^\star$ to $I_6^\star$, while Ψ_{GST} depends now only on $I_4^\star$ to $I_6^\star$. The corresponding contribution $\boldsymbol{\sigma}_{\mathrm{GST}}$ to the Cauchy stress tensor is

$$\boldsymbol{\sigma}_{\mathrm{GST}} = 2\psi_4^\star \mathbf{h} + 2\psi_6^\star \mathbf{h}', \tag{3.38}$$

where $\psi_i^\star = \partial\Psi_{\mathrm{GST}}/\partial I_i^\star$, $i = 4, 6$, and $\mathbf{h}'$ is given by (3.19), with $\mathbf{m}$ is replaced by $\mathbf{m}' = \mathbf{FM}'$. By incompressibility the stretch in the thickness direction is $\lambda_3 = (\lambda_1\lambda_2)^{-1}$. We assume that each mean fibre direction makes an angle α with the direction 1 so that $\mathbf{M} = \cos\alpha\mathbf{e}_1 + \sin\alpha\mathbf{e}_2$ and $\mathbf{M}' = \cos\alpha\mathbf{e}_1 - \sin\alpha\mathbf{e}_2$; for the arrangement in an arterial sheet see Fig. 3.2. The right Cauchy–Green tensor $\mathbf{C}$ has diagonal components λ_1^2, λ_2^2, λ_3^2 with respect to Cartesian axes $\mathbf{e}_1$, $\mathbf{e}_2$, $\mathbf{e}_3$. From (3.1), $I_1 = \lambda_1^2 + \lambda_2^2 + \lambda_3^2$, and from the symmetry, $I_4 = I_6 = \lambda_1^2\cos^2\alpha + \lambda_2^2\sin^2\alpha$, while $I_{\mathrm{n}} = \lambda_3^2$. By using (3.19) the nonzero components of $\mathbf{h}$ and $\mathbf{h}'$ are given as

$$h_{11} = h'_{11} = \bar{a}\lambda_1^2, \qquad \bar{a} = 2\kappa_{\mathrm{op}}[\kappa_{\mathrm{ip}} + (1-2\kappa_{\mathrm{ip}})\cos^2\alpha], \tag{3.39}$$

$$h_{22} = h'_{22} = \bar{b}\lambda_2^2, \qquad \bar{b} = 2\kappa_{\mathrm{op}}[\kappa_{\mathrm{ip}} + (1-2\kappa_{\mathrm{ip}})\sin^2\alpha], \tag{3.40}$$

$$h_{33} = h'_{33} = \bar{c}\lambda_3^2, \qquad \bar{c} = (1-2\kappa_{\mathrm{op}}), \tag{3.41}$$

and

$$h_{12} = -h'_{12} = 2\kappa_{\mathrm{op}}(1-2\kappa_{\mathrm{ip}})\lambda_1\lambda_2\sin\alpha\cos\alpha, \tag{3.42}$$

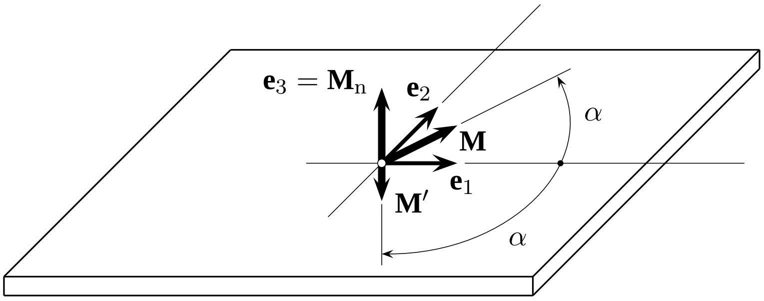

Figure 3.2 Sheet of arterial tissue in the $\mathbf{e}_1$, $\mathbf{e}_2$ plane which is biaxially stretched (λ_1 in $\mathbf{e}_1$ and λ_2 in $\mathbf{e}_2$ direction). Two families of fibres are present with mean fibre directions $\mathbf{M}$ and $\mathbf{M}'$, each making an angle α with the $\mathbf{e}_1$ direction. The normal direction to the plane is $\mathbf{e}_3 = \mathbf{M}_\mathrm{n}$.

where $\bar{a} + \bar{b} = 2\kappa_\mathrm{op}$ and $\bar{a} + \bar{b} + \bar{c} = 1$. Consequently, for $I_4^\star$ and $I_6^\star$ we can write

$$I_4^\star = I_6^\star = \mathrm{tr}\mathbf{h} = h_{11} + h_{22} + h_{33}. \tag{3.43}$$

The nonzero components of the Cauchy stress tensor $\boldsymbol{\sigma} = \boldsymbol{\sigma}_\mathrm{iso} + \boldsymbol{\sigma}_\mathrm{GST} - p\mathbf{I}$ are obtained as

$$\begin{aligned} \sigma_{11} &= 2\psi_1\lambda_1^2 + 4\psi_4^\star h_{11} - p, \quad \sigma_{22} = 2\psi_1\lambda_2^2 + 4\psi_4^\star h_{22} - p \quad \text{and} \\ \sigma_{33} &= 2\psi_1\lambda_3^2 + 4\psi_4^\star h_{33} - p, \end{aligned} \tag{3.44}$$

where $\psi_1 = \partial\Psi_\mathrm{iso}/\partial I_1$, with Ψ_iso now just a function of I_1. Since we are considering a thin sheet under plane stress conditions we have $\sigma_{33} = 0$ and on elimination of p the equations $(3.44)_1$ and $(3.44)_2$ can be written as

$$\begin{aligned} \sigma_{11} &= 2\psi_1(\lambda_1^2 - \lambda_3^2) + 4\psi_4^\star(h_{11} - h_{33}) \quad \text{and} \\ \sigma_{22} &= 2\psi_1(\lambda_2^2 - \lambda_3^2) + 4\psi_4^\star(h_{22} - h_{33}). \end{aligned} \tag{3.45}$$

Now by using the neo-Hookean model (3.6) and the exponential (3.25) in (3.45) we obtain

$$\sigma_{11} = \mu(\lambda_1^2 - \lambda_3^2) + 4k_1(I_4^\star - 1)\exp[k_2(I_4^\star - 1)^2](h_{11} - h_{33}), \tag{3.46}$$

and

$$\sigma_{22} = \mu(\lambda_2^2 - \lambda_3^2) + 4k_1(I_4^\star - 1)\exp[k_2(I_4^\star - 1)^2](h_{22} - h_{33}), \tag{3.47}$$

where h_{11}, h_{22}, h_{33} are given by (3.39)–(3.41) and $I_4^\star$ by (3.43). For the special case of equibiaxial extension $\lambda_1 = \lambda_2 = \lambda$, $\lambda_3 = \lambda^{-2}$, $I_4^\star = (\bar{a} + \bar{b})\lambda^2 + \bar{c}\lambda^{-4}$, and $h_{11} = \bar{a}\lambda^2$, $h_{22} = \bar{b}\lambda^2$, $h_{33} = \bar{c}\lambda^{-4}$.

We now provide the corresponding stress expressions for the AI model. By using the expression (3.15) for **N**, the related vector $\mathbf{n} = \mathbf{FN}$ in the deformed configuration has the form

$$\mathbf{n} = \lambda_1 \sin\Theta\cos\Phi\mathbf{e}_1 + \lambda_2 \sin\Theta\sin\Phi\mathbf{e}_2 + \lambda_3 \cos\Theta\mathbf{e}_3. \tag{3.48}$$

Then, from (3.10) we obtain

$$\sigma_{11} = \frac{\lambda_1^2}{2\pi}\int_\Omega \rho(\mathbf{N})W'(I_4)\sin^2\Theta\cos^2\Phi\mathrm{d}\Omega + 2\psi_1\lambda_1^2 - p, \tag{3.49}$$

$$\sigma_{22} = \frac{\lambda_2^2}{2\pi}\int_\Omega \rho(\mathbf{N})W'(I_4)\sin^2\Theta\sin^2\Phi\mathrm{d}\Omega + 2\psi_1\lambda_2^2 - p, \tag{3.50}$$

and

$$\sigma_{33} = \frac{\lambda_3^2}{2\pi}\int_\Omega \rho(\mathbf{N})W'(I_4)\cos^2\Theta\mathrm{d}\Omega + 2\psi_1\lambda_3^2 - p, \tag{3.51}$$

where the density function $\rho(\mathbf{N})$ is decoupled according to (3.16), with the von Mises distributions (3.23). By symmetry we have $\sigma_{12} = \sigma_{13} = \sigma_{23} = 0$. From (3.48) we can now derive an explicit expression for the invariant I_4, i.e.

$$I_4 = \lambda_1^2\sin^2\Theta\cos^2\Phi + \lambda_2^2\sin^2\Theta\sin^2\Phi + \lambda_3^2\cos^2\Theta. \tag{3.52}$$

By writing Ψ_{fib} as $W(I_4)$ from (3.7), we calculate $W'(I_4)$, which is required in (3.49)–(3.51), as

$$W'(I_4) = c_1(I_4 - 1)\exp[c_2(I_4 - 1)^2]. \tag{3.53}$$

Finally, with the plane stress condition $\sigma_{33} = 0$, the use of the neo-Hookean model (3.6), and on elimination of p equations (3.49) and (3.50) read

$$\sigma_{11} = \frac{1}{2\pi}\int_\Omega \rho(\mathbf{N})W'(I_4)(\lambda_1^2\sin^2\Theta\cos^2\Phi - \lambda_3^2\cos^2\Theta)\mathrm{d}\Omega + \mu(\lambda_1^2 - \lambda_3^2), \tag{3.54}$$

$$\sigma_{22} = \frac{1}{2\pi}\int_\Omega \rho(\mathbf{N})W'(I_4)(\lambda_2^2\sin^2\Theta\sin^2\Phi - \lambda_3^2\cos^2\Theta)\mathrm{d}\Omega + \mu(\lambda_2^2 - \lambda_3^2). \tag{3.55}$$

A similar derivation for uniaxial extension and simple shear was documented by Holzapfel & Ogden [121]. For the special case of equibiaxial extension with $\lambda_1 = \lambda_2 = \lambda$ the above equations apply with $I_4 = \lambda^2\sin^2\Theta + \lambda^{-4}\cos^2\Theta$.

3.3.2 Homogeneous Uniaxial Extension

We now consider a strip of an incompressible arterial tissue which is loaded by a stretch $\lambda_1 = \lambda$ in the $\mathbf{e}_1$ direction. There are two families of fibres symmetrically disposed with respect to the $\mathbf{e}_1$ direction but with non-symmetric dispersion, and mean fibre directions **M** and **M′**, as indicated in Fig. 3.3.

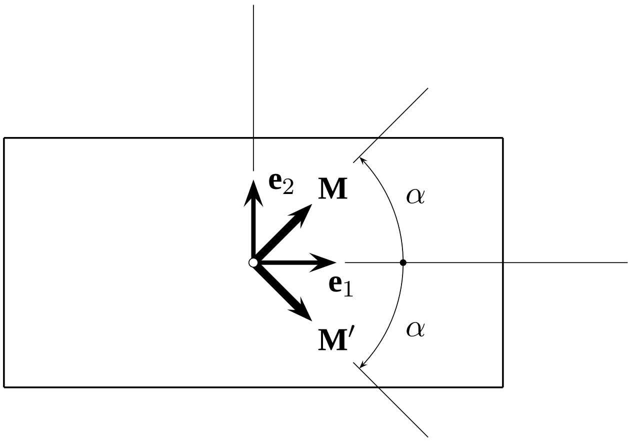

Figure 3.3 Sheet of arterial tissue in the $\mathbf{e}_1$, $\mathbf{e}_2$ plane which is uniaxially stretched ($\lambda_1 = \lambda$ in $\mathbf{e}_1$ direction). Two fibre families are symmetrically disposed with mean fibre directions $\mathbf{M}$ and $\mathbf{M}'$, each making an angle α with the $\mathbf{e}_1$ direction.

We introduce the notation

$$f(I_4^\star) = 4\bar{k}_1(I_4^\star - 1)\exp[k_2(I_4^\star - 1)^2] \quad \text{and} \quad \bar{k}_1 = \frac{k_1}{\mu}. \tag{3.56}$$

Then, with the condition $\sigma_{22} = 0$ we obtain from (3.47) that

$$\frac{\sigma_{22}}{\mu} = \lambda_2^2 - \lambda_3^2 + f(I_4^\star)(h_{22} - h_{33}) = 0. \tag{3.57}$$

With the expressions for h_{22} and h_{33} from $(3.40)_1$ and $(3.41)_1$ we then obtain, on suppressing the argument $I_4^\star$ in $f(I_4^\star)$,

$$(1 + \bar{b}f)\lambda_2^2 = (1 + \bar{c}f)\lambda_3^2. \tag{3.58}$$

We also have the incompressibility condition $\lambda_2\lambda_3 = \lambda_1^{-1}$ so that from (3.58) and (3.43) we obtain

$$\lambda_2^2 = \left(\frac{1 + \bar{c}f}{1 + \bar{b}f}\right)^{1/2} \lambda_1^{-1} \quad \text{and} \quad \lambda_3^2 = \left(\frac{1 + \bar{b}f}{1 + \bar{c}f}\right)^{1/2} \lambda_1^{-1}, \tag{3.59}$$

and the following cubic for λ_1

$$\bar{a}\lambda_1^3 - I_4^\star\lambda_1 + \frac{\bar{b} + \bar{c} + 2\bar{b}\bar{c}f}{(1 + \bar{b}f)^{1/2}(1 + \bar{c}f)^{1/2}} = 0. \tag{3.60}$$

By recalling (3.46), (3.56), $(3.39)_1$, $(3.41)_1$ and $(3.59)_2$ we find the Cauchy stress σ_{11}

in the $\mathbf{e}_1$ direction is given by

$$\frac{\sigma_{11}}{\mu} = \lambda_1^2 - \lambda_3^2 + f(h_{11} - h_{33}) = (1 + \overline{a}f)\lambda_1^2 - (1 + \overline{b}f)^{1/2}(1 + \overline{c}f)^{1/2}\lambda_1^{-1}, \tag{3.61}$$

where λ_1 is provided in (3.60).

Note that if $\lambda_2 = \lambda_3$ then we obtain from (3.58) that $1 + \overline{c}f = 1 + \overline{b}f$. So, either $I_4^\star = 1$, which is a trivial case, or $\overline{b} = \overline{c}$, which, using $(3.40)_2$ and $(3.41)_2$ (for $\overline{b}$ and $\overline{c}$), leads to the condition

$$2\kappa_{\mathrm{op}}[1 + \kappa_{\mathrm{ip}} + (1 - 2\kappa_{\mathrm{ip}})\sin^2\alpha] = 1. \tag{3.62}$$

This condition can be satisfied for quite a wide range of connections between α, κ_{ip} and κ_{op}. For example, if $\kappa_{\mathrm{op}} = 1/3$ then $\sin^2\alpha = 1/2$ independently of κ_{ip}. On the other hand if $\kappa_{\mathrm{ip}} = 1/2$ then $\kappa_{\mathrm{op}} = 1/3$ independently of α (the isotropic case). If $\kappa_{\mathrm{ip}} = 0$ then $\sin^2\alpha = (1 - 2\kappa_{\mathrm{op}})/\kappa_{\mathrm{op}}$, which requires $1/4 \le \kappa_{\mathrm{op}} \le 1/2$. Similarly, $\kappa_{\mathrm{ip}} = 1$ requires $\sin^2\alpha = (4\kappa_{\mathrm{op}} - 1)/2\kappa_{\mathrm{op}}$, which again requires $1/4 \le \kappa_{\mathrm{op}} \le 1/2$. If $\kappa_{\mathrm{ip}} = 1/4$ then $\sin^2\alpha = (2 - 5\kappa_{\mathrm{op}})/\kappa_{\mathrm{op}}$, which requires $2/7 \le \kappa_{\mathrm{op}} \le 2/5$. There is no solution for either $\kappa_{\mathrm{op}} = 0$ or $\kappa_{\mathrm{op}} = 1/2$, which are limiting cases that are not physiologically relevant.

With (3.62), the cubic equation (3.60) reduces to

$$\overline{a}\lambda_1^3 - I_4^\star\lambda_1 + 2\overline{b} = 0. \tag{3.63}$$

Since $\overline{a} + \overline{b} = 2\kappa_{\mathrm{op}}$ and $\overline{b} = \overline{c}$ we deduce that $\overline{b} = 1 - 2\kappa_{\mathrm{op}}$ and $\overline{a} + 2\overline{b} = 1$ so that (3.63) can be written as

$$I_4^\star = \frac{\overline{a}\lambda_1^3 + 2\overline{b}}{\lambda_1} \tag{3.64}$$

and hence $(3.61)_3$ gives

$$\frac{\sigma_{11}}{\mu} = \lambda_1^2 - \lambda_1^{-1} + (\overline{a}\lambda_1^2 - \overline{b}\lambda_1^{-1})f(I_4^\star), \tag{3.65}$$

which becomes an explicit expression in terms of λ_1 when (3.64) is substituted in (3.56).

We now provide the corresponding equations for the AI approach. For uniaxial extension we require that $\sigma_{22} = 0$ so that with $\lambda_3 = \lambda_1^{-1}\lambda_2^{-1}$ we have from (3.55)

$$\frac{1}{2\pi}\int_\Omega \rho W'(I_4)(\lambda_2^2\sin^2\Theta\sin^2\Phi - \lambda_1^{-2}\lambda_2^{-2}\cos^2\Theta)\mathrm{d}\Omega + \mu(\lambda_2^2 - \lambda_1^{-2}\lambda_2^{-2}) = 0, \tag{3.66}$$

which gives λ_2 in terms of λ_1 on noting that I_4 is given by (3.52) with $\lambda_3^2 = \lambda_1^{-2}\lambda_2^{-2}$.

Now, by subtracting (3.55) from (3.54) with $\sigma_{22} = 0$, we obtain

$$\sigma_{11} = \frac{1}{2\pi} \int_\Omega \rho W'(I_4)(\lambda_1^2 \cos^2\Phi - \lambda_2^2 \sin^2\Phi)\sin^2\Theta \mathrm{d}\Omega + \mu(\lambda_1^2 - \lambda_2^2), \tag{3.67}$$

with λ_2 in terms of λ_1 from (3.66), which gives σ_{11} as a function of λ_1.

Finally, let us discuss the special case $\lambda_2 = \lambda_3 = \lambda_1^{-1/2}$. Then, by using $\sin^2\Phi = 1 - \cos^2\Phi$ and $\cos^2\Theta = 1 - \sin^2\Theta$, (3.66) gives

$$\int_\Omega \rho W'(I_4) \sin^2\Theta \cos^2\Phi \mathrm{d}\Omega = \int_\Omega \rho W'(I_4) \cos^2\Theta \mathrm{d}\Omega, \tag{3.68}$$

so that (3.67) reduces to

$$\sigma_{11} = \frac{1}{2\pi}(\lambda_1^2 + 2\lambda_1^{-1}) \int_\Omega \rho W'(I_4)\cos^2\Theta \mathrm{d}\Omega - \frac{\lambda_1^{-1}}{2\pi} \int_\Omega \rho W'(I_4)\mathrm{d}\Omega + \mu(\lambda_1^2 - \lambda_1^{-1}), \tag{3.69}$$

where ρ is given by (3.16) and (3.23), and I_4 is given by

$$\begin{aligned} I_4 &= \lambda_1^2 \sin^2\Theta \cos^2\Phi + \lambda_1^{-1}(\sin^2\Theta \sin^2\Phi + \cos^2\Theta) \\ &= (\lambda_1^2 - \lambda_1^{-1})\sin^2\Theta\cos^2\Phi + \lambda_1^{-1}, \end{aligned} \tag{3.70}$$

which results from (3.52).

3.4 Numerical Examples

In this section we illustrate the theory in Section 3.3 by relating it to sets of data for (a) equibiaxial extension of a tissue sample obtained from an abdominal aortic aneurysm and (b) uniaxial extension of strips from the circumferential and axial directions of a media from a healthy thoracic aorta.

3.4.1 Equibiaxial Extension

Here we use experimental data which were obtained from an equibiaxial test of a tissue taken from a human abdominal aortic aneurysm, as documented in fig 12 of Niestrawska *et al.* [228] (sample AAA-4.1). The experimental data are shown here in Fig. 3.4 in terms of the circumferential Cauchy stress (open squares) and longitudinal Cauchy stress (open circles) as functions of the equibiaxial stretch. As can be seen, the mechanical response is highly anisotropic and nonlinear. A representative set of mechanical and structural data was selected from the sets of data of Niestrawska *et al.* [228]. Figure 3.5, which is based on second-harmonic generation (SHG), shows the structure of different layers taken from two adjacently located patches. To the right there is an intensity plot indicating a highly disturbed collagen fibre structure for the luminal layer with 450μm

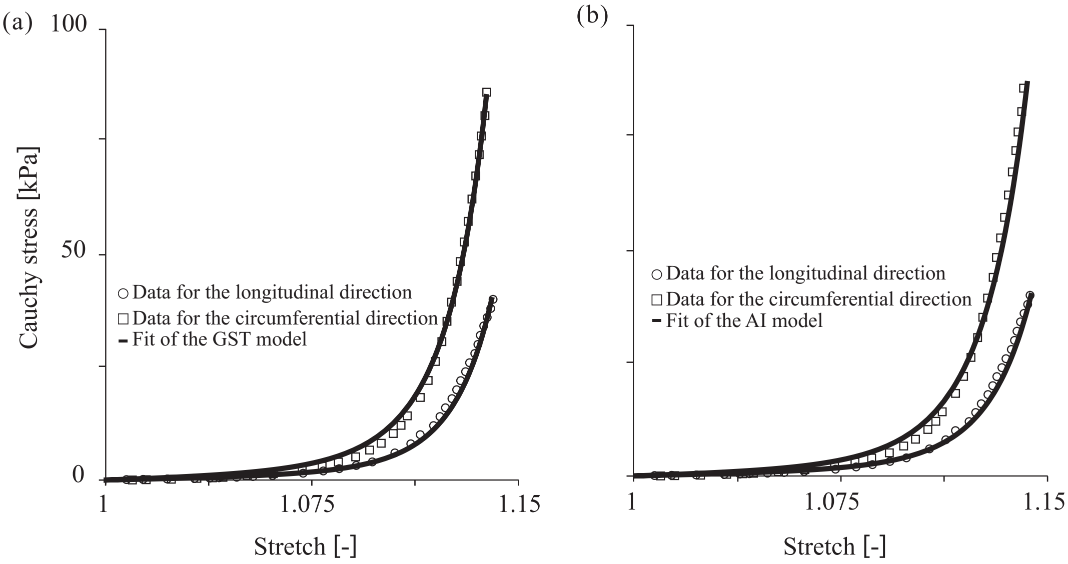

Figure 3.4 Plots of the Cauchy stress versus the stretch for representative data from an equibiaxial test of a tissue taken from an abdominal aortic aneurysm (i.e. sample AAA-4.1, as illustrated in Figure 12 of Niestrawska *et al.* [228]). Open squares and circles indicate the experimental data, while solid curves show the fitting of (a) the GST model and (b) the AI model.

thickness. The abscissa corresponds to the angle measured from the circumferential direction at the origin (0°), while ±90° refer to the axial direction. The red color identifies fibre angles at which there are fibres with that orientation, while the blue color indicates the absence of fibres. More details can be found in the caption and in the study [228].

The structural parameters for the patient AAA-4 according to [228] are $\kappa_{\text{ip}} = 0.223$, $\kappa_{\text{op}} = 0.413$ and $\alpha = 24.33°$. On that basis a GST fitting to the experimental data was performed and achieved the following set of parameters: $\mu = 1.66\,\text{kPa}$, $k_1 = 5.82\,\text{kPa}$ and $k_2 = 99.91$ with $R^2 = 0.98$, but the corresponding plot was not shown therein. The R^2 value can be improved by starting with the dispersion parameters above and the value of μ, but allowing α to be a fitting parameter so that we obtained the fit shown in Fig. 3.4(a) with the values $k_1 = 7.68\,\text{kPa}$ and $k_2 = 91.8$ and $\alpha = 25.82°$, with $R^2 = 0.997$. For the fit the equations (3.46) and (3.47) were used for the special case of equibiaxial extension. Figure 3.4(b) shows a corresponding fit of the data for the AI model by using (3.54) and (3.55) with (3.53) for the special case of equibiaxial extension, and with the von Mises distribution (3.23). The integrations were performed numerically using Mathematica [203]. The fitting process achieved the concentration parameters $a = 0.9$ and $b = 13.5$ and the mechanical parameters $\mu = 1.66\,\text{kPa}$, $c_1 = 0.46\,\text{kPa}$ and $c_2 = 37.0$. The concentration parameters a and b lead to values of $\kappa_{\text{ip}} = 0.295$ and $\kappa_{\text{op}} = 0.491$ according to $(3.23)_1$ and $(3.23)_2$, respectively, whereas the κ_{ip} and κ_{op} for

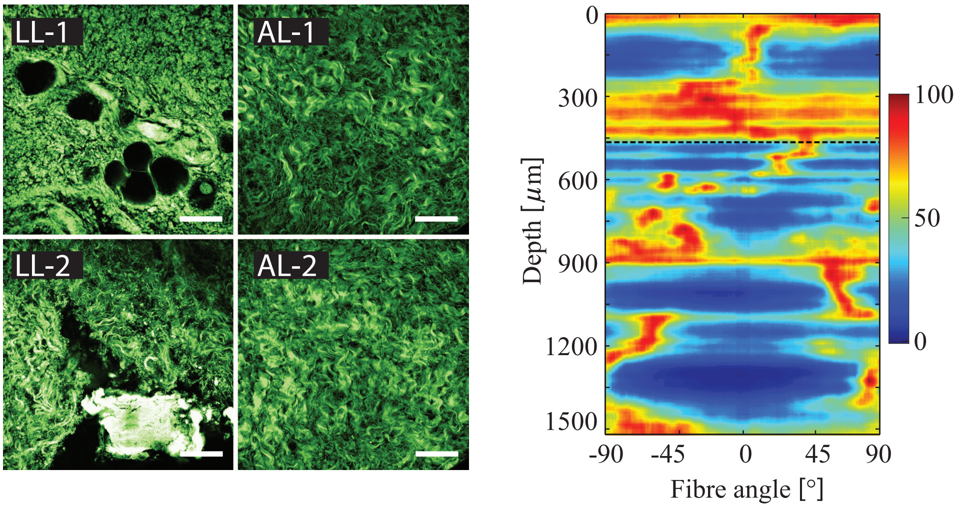

Figure 3.5 SHG images and intensity plot for a tissue taken from an abdominal aortic aneurysm (AAA-4, see Fig. 8(b) of Niestrawska *et al.* [228]): structure of luminal layer (LL-1 and LL-2), and abluminal layer (AL-1 and AL-2), of two patches taken from adjacent locations. Image LL-1 shows bright ‘stains’ representing a degenerated collagen structure, and image LL-2 indicates a different structure with calcification and wavy collagen fibres. The AL patches are similar to those of a healthy layer. The intensity plot (to the right) exhibits a highly disturbed structure for the upper 450μm and an adventitia-like structure with generally two fibre families in the remaining wall thickness. The intensity plot starts at the top with the LL. Scale bar is 100μm.

the GST model were based on imaging data, while a and b were obtained as fitting parameters. Thus, if the values a and b are associated with values of κ_{ip} and κ_{op} given by (3.23), these are reasonably consistent with the structurally obtained values. The fit is in good agreement with the experimental data and leads to an R^2 value of 0.998. It should be noted that the values of the stretches and the corresponding stresses obtained for equibiaxial tension are rather low. This is because of the experimental limitations of a biaxial extension test. Larger extensions and correspondingly larger stresses can be obtained in uniaxial extension experiments, as we now discuss.

3.4.2 Uniaxial Extension

We now fit each of the GST and the AI models to representative sets of new experimental data obtained from axial and circumferential strips from a media of a healthy human thoracic aorta (59 yrs, female). The donor sample was separated into layers, and dog-bone specimens of the media with markers for real-time tracking were prepared. The medial strips were preconditioned in five cycles and then extended until failure. The

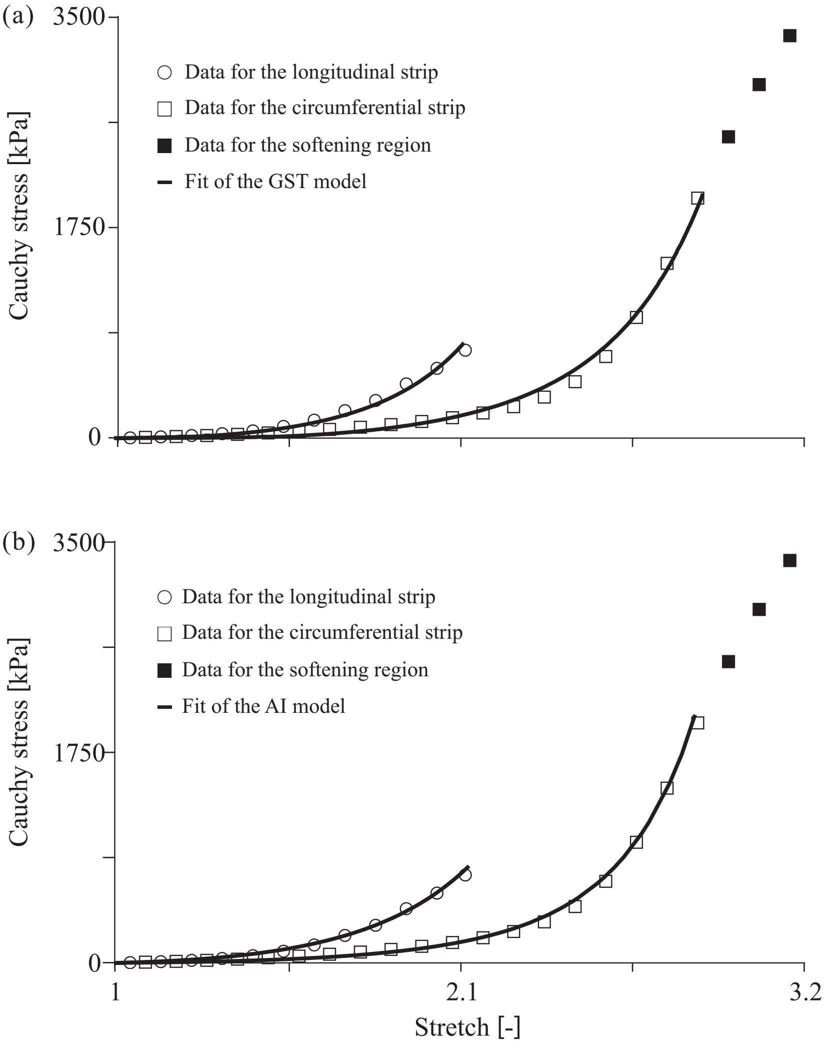

Figure 3.6 Plots of the Cauchy stress versus the stretch for a representative set of data obtained from longitudinal and circumferential strips of a media from a healthy human thoracic aorta. Open circles (longitudinal) and open squares (circumferential) indicate the experimental data for the pre-softening elastic domain; the subsequent softening data in the circumferential case are shown as solid squares. The solid curves show the fitting of (a) the GST model and (b) the AI model.

protocol took place within a container which was filled with a phosphate-buffered saline solution and kept at 37°C (as described by Sommer *et al.* [308]). For the pre-softening elastic domain the data in the form of the Cauchy stress versus stretch are presented in Fig. 3.6 as open squares (circumferential) and open circles (longitudinal), while the subsequent softening data in the circumferential case are shown as solid squares.

Structural data were obtained by using SHG according to the protocol documented by Schriefl *et al.* [287], except that the sampling was set to $0.62\times0.62\times5\,\mu$m instead of $0.62\times0.62\times1\,\mu$m. For each strip, the data were obtained separately in two orthogonal planes, namely the radial/circumferential and radial/axial (out-of-plane), and in the circumferential/axial plane (in plane). The out-of-plane data from the two orthogonal planes were fitted together using the least squares method (Sommer *et al.* [307]), which produced the concentration parameter b, from which the dispersion parameter κ_{op} was calculated via $(3.24)_2$. The in-plane data were fitted using a maximum likelihood estimation (Schriefl *et al.* [285]), which produced the mean fibre angle α and the median concentration parameter a, while the dispersion parameter κ_{ip} was obtained from $(3.24)_1$. Then, the values obtained were averaged between the two strips to give the in-plane and out-of-plane dispersion parameters, the concentration parameters, and the mean fibre angle, as represented in Table 3.1.

Table 3.1 Parameters

	Dispersion	Concentration	Mean fibre angle
In plane	$\kappa_{\text{ip}} = 0.227$	$a = 1.32$	$\alpha = 8.0°$
Out-of-plane	$\kappa_{\text{op}} = 0.484$	$b = 13.68$	–

Figure 3.7 illustrates contrast enhanced SHG images of the collagen architecture of a circumferential strip using FIJI (http://fiji.sc/Fiji, Ashburn, VA). Figure 3.7(a) shows an image obtained from the in-plane stack (axial/circumferential) which corresponds to a depth of $300\,\mu$m in the intensity plot (see Fig. 3.7(d)). Figures 3.7(b) and (c) show out-of-plane images of the radial/axial and the radial/circumferential planes, respectively. Figure 3.7(d) shows an intensity plot through the thickness of the medial strip in the circumferential direction, which is composed of multiple lamellar units. The strip in the axial direction shows a similar intensity pattern. An individual image does not show two families of fibres but the two fibre families can be identified through the stack by the zig-zag characteristic.

We now focus on fitting the data up to the point where softening is initiated. Based on the structural data for the GST fit we have assumed values of $\kappa_{\text{op}} = 0.48$ and $\kappa_{\text{ip}} = 0.25$ which are approximations of the measured data (see Table 3.1). These two values served as fixed input data for the fitting procedure of the GST model. Noting that $\bar{a}+\bar{b} = 2\kappa_{\text{op}}$, the fitting produced $\bar{a} = 0.385$, and hence $\bar{b} = 0.575$, and $\bar{c} = 0.04$, then $k_1 = 107.0\,$kPa and $k_2 = 0.155$, and $\alpha = 33.3°$. The model results are illustrated as solid curves in Fig. 3.6(a) and show good agreement with the experimental data, with $R^2 = 0.993$. While the dispersion parameters used in the fitting are very similar to those obtained from the images, the mean fibre angle α is not so close. However, this can be explained by the fact that there is quite a large range of fibre angles and the averaging within the

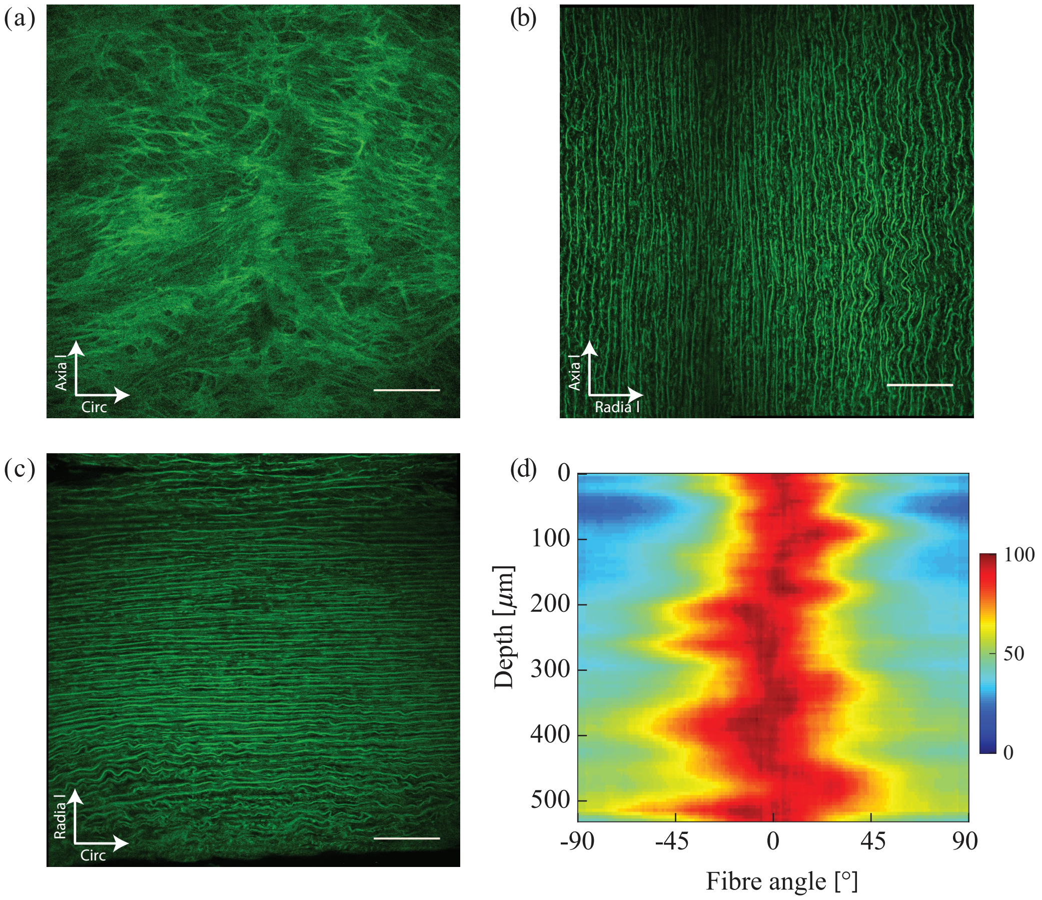

Figure 3.7 SHG images and intensity plot for a tissue taken from the media of a healthy human thoracic aorta: (a)–(c) illustrate SHG images of the collagen architecture of the circumferential strip obtained from (a) an in plane image (axial/circumferential) corresponding to 300 μm depth in the intensity plot, see (d); (b) out-of-plane image of the radial/axial plane; (c) out-of-plane image of the radial/circumferential plane; (d) intensity plot of a circumferential strip through the thickness of the media depicting highly aligned fibres along ±7.2° from the circumferential direction (with 0°). The intensity plot starts at the top with the medial side closer to the adventitia. Scale bar is 100 μm.

image stacks to obtain the structural parameters for individual strips and then between the strips has a considerable impact on the values reported in Table 3.1.

As far as the AI model is concerned the fitted parameters are $a = 1$, $b = 10$, $c_1 = 4.725$ kPa and $c_2 = 0.038$. For both models the shear modulus μ used was 1.05 kPa. Figure 3.6(b) also illustrates a good agreement with the experimental data, with $R^2 = 0.980$.

3.5 Conclusion and Perspectives

We have described both the generalized structure tensor (GST) and angular integration (AI) approaches for the modelling of fibrous tissues with dispersed fibre structures. The constitutive equations for each model have then been applied to the special cases of equibiaxial and uniaxial extension of tissue samples obtained from human aortas. For each of the GST and the AI models the agreement with experimental data has been shown to be very good.

The basic structure of the dispersion model does not take into account interactions between fibres such as cross-linking. There is some evidence that a larger number of collagen cross-links leads to a higher wall stiffness and a larger elastic modulus in older arteries (Hayashi & Hirayama [108]). In addition, the study of Xu *et al.* [373] shows that the stress–strain responses based on equibiaxial tensile tests of engineered collagen scaffolds with different degrees of cross-linking indicate the influence of the cross-links on the mechanical response; in particular, the response becomes stiffer as the proportion of cross-links increases. A similar conclusion was drawn by Wang & Chesler [356] in respect of the pressure–stretch response of isolated dynamic tests of pulmonary arteries. The more recent study of Tian *et al.* [324] uses the eight-chain Arruda–Boyce model with a parameter N which corresponds to a number of subunits per chain; the density of cross-links is larger for smaller N which is a basic way to account for cross-links. The study of Xu *et al.* [373] also attempts to model the effect of cross-links with a model based on Gasser *et al.* [88] by varying the parameters, although the cross-linking was not explicitly accounted for otherwise. There is a need for more structural data on the fibre arrangement and cross-linking and for more advanced constitutive models which are able to better capture the cross-link stabilization of the side-by-side packing of collagen molecules, and to quantify the effect on the mechanical response. New invariants might also be useful in the modelling of cross-linking and associated in-plane and out-plane dispersion. In this connection a recent relevant modelling approach aimed at capturing the mechanical response of fibrous biological tissues using a general invariant that excludes compressed fibres is documented by Li *et al.* [178].

In cardiovascular diseases such as aortic dissection there is evidence that medial weakness forms a basis for an aortic dissection, and that weakness is due to the structural abnormalities of elastic fibres; in particular a marked reduction in interlaminar elastic fibres is observed (see, e.g., Nakashima [225]; for a review of the mechanical assessment of arterial dissection see Tong *et al.* [330]). Signs of fibre degradation and/or fragmentation are similarly observed in aortic aneurysms (see, e.g., Borges *et al.* [21]), a cardiovascular disease in which the elastin content decreases significantly with increasing aneurysm diameter (Tong *et al.* [329]). Consequently, changes in the architecture of the medial elastic pattern of aortas occur, which play a significant role in the pathogenesis of aortic dissections and aneurysms. Hence, at the microscale, an extension of the dispersion models is required to capture such changes in the medial elastin structure, and hence to improve constitutive modelling, even though the mechanical response of the non-collagenous material is rather isotropic.

We also need better structural characterisations of tissue components in atherosclerotic plaques in order to inform constitutive models used to predict the mechanical environment of stenotic arteries during interaction with stents (Holzapfel *et al.* [128]). A more accurate consideration of the collagen structure, in particular of the fibrous cap (i.e. the fibrotic part at the luminal border) is important because this plaque component may become remarkably stressed, and may lead to tissue failure and to severe life-threatening clinical consequences such as stroke or myocardial infarction. The recent study of Douglas *et al.* [59] documents significant differences in the fibre architecture across the luminal region of human coronary atherosclerotic plaques. The study describes a vital pathway for improving our understanding of material stability and rupture mechanisms of plaques on the basis of considering the fibre structure.

Clearly, improved fibre dispersion models when including the nanoscale interactions between the different tissue constituents may advance the development of multiscale modelling methods, an important research area still in its infancy. Multiscale models are able to describe complex processes across multiple length, time or energy scales to inform the macroscopic response of tissues. For a brief summary of the most recent developments on multiscale modelling in biomechanics see the review article by Bhattacharya & Viceconti [16]. A collection of studies on multiscale soft tissue mechanics and mechanobiology can be found in a book edited by Holzapfel & Ogden [123].

Ethics The use of donor samples for the uniaxial extension tests was approved by the Ethics Committee at the Medical University of Graz (27-250 ex 14/15).

Funding The work of RWO was in part funded by the UK EPSRC grant no. EP/N014-642/1.

Competing interests No conflicts of interest, financial or otherwise, are declared by the authors.

Data accessibility The experimental data from the equibiaxial test of the tissue of an abdominal aortic aneurysm (Fig. 3.2) and from the uniaxial tests of the media of a healthy human thoracic aorta (Fig. 3.4) can be downloaded from `https://doi.org/10.6084/m9.figshare.7667627` [131]. In addition, on that link we have also provided 106 raw 8-bit *.tif files obtained by SHG imaging used to produce the intensity plot of a circumferential strip through the thickness of the media, as shown in Fig. 3.5(d).

The integrations required for the AI model were numerically solved using Mathematica [203]. All computational results are reproducible.

Authors' contributions G.A.H and R.W.O. conceived and designed the research, interpreted the results, and drafted the manuscript; S.S. carried out the experimental analyses on human tissues (Fig. 3.4), produced the SHG images (Fig. 3.5) and analysed the results. All authors edited and revised the manuscript, and gave final approval for publication.

4 BIOMECHANICS OF AORTIC WALL FAILURE WITH A FOCUS ON DISSECTION AND ANEURYSM: A REVIEW

Abstract Aortic dissections and aortic aneurysms are fatal events characterized by structural changes to the aortic wall. The maximum diameter criterion, typically used for aneurysm rupture risk estimations, has been challenged by more sophisticated biomechanically motivated models in the past. Although these models are very helpful for the clinicians in decision-making, they do not attempt to capture material failure. Following a short overview of the microstructure of the aorta, we analyze the failure mechanisms involved in the dissection and rupture by considering also traumatic rupture. We continue with a literature review of experimental studies relevant to quantify tissue strength. More specifically, we summarize more extensively uniaxial tensile, bulge inflation and peeling tests, and we also specify trouser, direct tension and in-plane shear tests. Finally we analyze biomechanically motivated models to predict rupture risk. Based on the findings of the reviewed studies and the rather large variations in tissue strength, we propose that an appropriate material failure criterion for aortic tissues should also reflect the microstructure in order to be effective.

Graphical Abstract

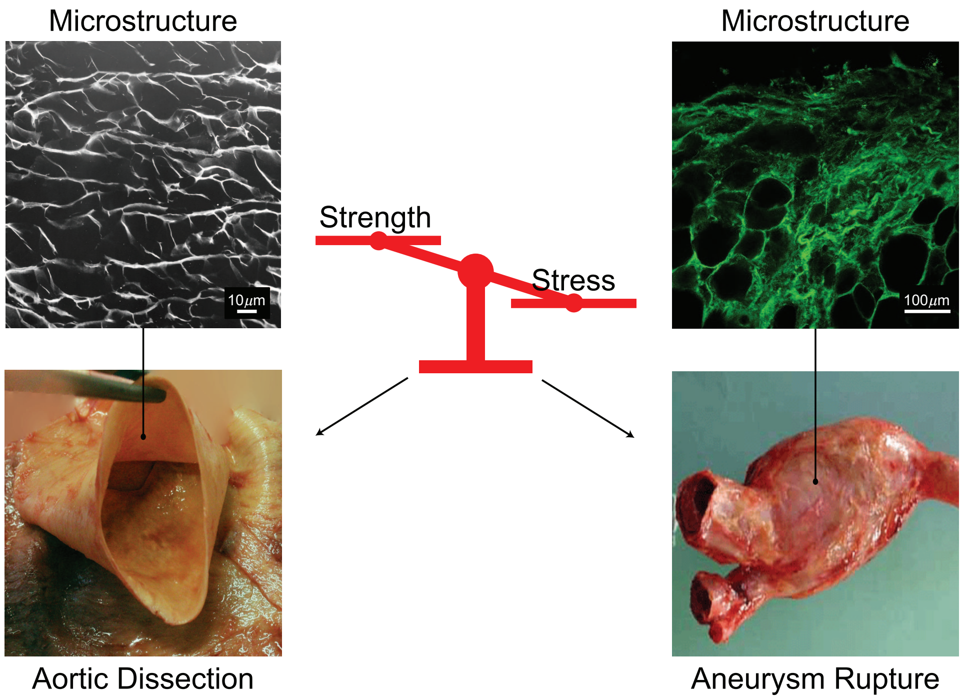

4.1 Introduction

Aortic dissection and aortic aneurysm rupture are acute life threatening events. Overall mortality rates of dissections and aneurysms of the thoracic aorta remain high despite the improvements over the years [234, 243, 318]. Ruptured aneurysms of the abdominal aorta are estimated to cause 4–5% of sudden deaths in the United States, and the event of rupture has mortality rates as high as 80% [283].

Aortic dissection is an acute condition of the aorta which typically starts with an intimal tear to the presumably already weakened wall, followed by a crack in the radial direction. The crack then proceeds within the medial layer, or between the media and the adventitia, causing the layers of the aortic wall to separate, thereby creating a false lumen where the blood can flow into [143, 216]. This leads to a dilatation and a further weakening of the intact outer wall of the false lumen. In most fatal conditions, the aorta bursts causing the patient to bleed to death quickly [48, 231]. Stanford type A dissections – affecting the ascending aorta – are shown to become chronic only rarely, whereas type B dissections – affecting the descending thoracic aorta only – are routinely chronic with a thickened, straightened intimal flap which lost its mobility due to remodeling [248]. Approximately 67% of the cases are reported to be type A dissections [243]. The risk factors include but are not limited to age, hypertension, smoking, congenital disorders such as bicuspid aortic valve (BAV), genetic disorders such as Marfan syndrome and Ehlers-Danlos syndrome [68, 141]. Intimal tears leading to ascending aortic dissection are typically located a few centimeters above the coronary arteries, whereas the ones leading to descending aortic dissection are located a few centimeters beyond the left subclavian artery [68]. For a mechanical assessment of arterial dissections see the review article by Tong et al. [330]. Figure 4.1(a) illustrates the basic anatomy of the aorta, while the sketch in Fig. 4.1(b) shows a dissected wall with arrows indicating the blood flow.

Aortic aneurysms are local dilatations of the aorta, typically more than 50% of the normal diameter [92]. The underlying mechanisms leading to aneurysm formation differ between the ascending aorta and the descending thoracic aorta [278], as well as between the thoracic and the abdominal aorta [33, 68, 275] due to different embryonic origins of the cells involved in the remodeling process. The aneurysms in the ascending aorta are usually not accompanied by atherosclerosis, whereas in the descending thoracic and the abdominal aorta it is a common finding [141]. Nevertheless, all aneurysms are characterized by alterations to the extracellular matrix. For a review on the biomechanics, mechanobiology, and modeling of aneurysms see Humphrey and Holzapfel [135].

In addition to the above mentioned pathologies, thoracic aortic trauma is accountable for a large percentage of losses involving motor vehicle accidents, and it can initiate the dissection process or cause an immediate rupture. Bertrand et al. [15] reported

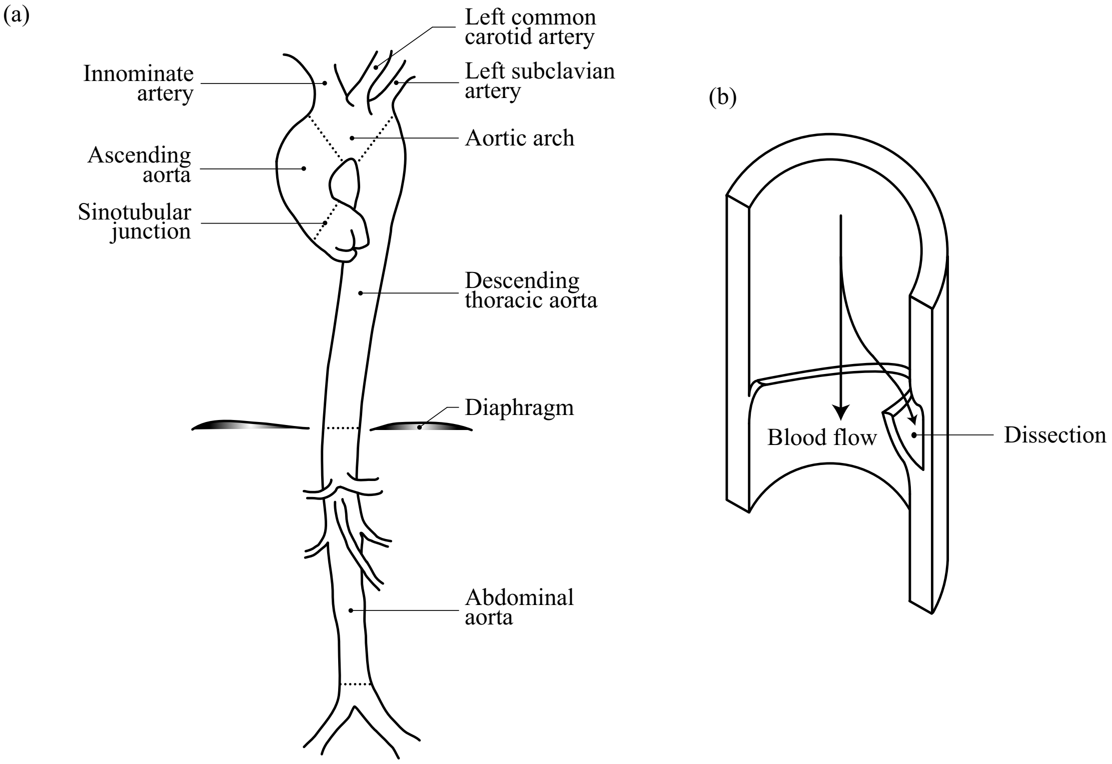

Figure 4.1 (a) Anatomy of the aorta with some of its branches; (b) sketch of a dissected wall with arrows indicating the blood flow.

1.2% of the occupants involved in vehicular accidents sustained a traumatic injury of the aorta, of which 94% were deadly, accounting for 21.4% of all fatalities. Traumatic aortic injury can also be due to heavy falls on feet, airplane crashes, suicide attempts, or surgical procedures [105, 112, 290]. The ascending aorta is reported to be the most common injury site due to trauma [198], whereas the aortic isthmus has been identified as the most vulnerable location for injury by several studies [15, 47, 296] constituting a number as high as 90% [47], followed by the aortic arch and the abdominal aorta around the bifurcations.

To prevent further complications such as rupture, dilatations of the aorta due to aneurysm or aortic dissection are surgically treated if the maximum diameter of the lesion is above 5.0 cm in women or 5.5 cm in men, or if the maximal diameter increases more than 0.5-1 cm in one year [97, 103, 175]. Clinicians consider several indicators before decision-making about a surgical intervention – such indicators include maximum diameter, expansion rate, genetic risk factors and the family history just to name a few. For example, the maximum diameter criterion is revised if the patient suffers from a connective tissue disorder such as Marfan syndrome, see [24], and Fig. 1 therein. Even though it has been shown that the risk of rupture and dissection of aneurysms increase significantly at sizes larger than 6 cm for the thoracic aorta [49], this criterion is in contradiction with the observation that aneurysms can rupture or dissect at any diameter [28, 242, 243, 278, 348], and it ignores the more complex relationships between the rupture and the material properties such as the heterogeneity of tensile strength in the wall of aortic aneurysms [338]. Clinicians need more reliable tools to assess the risk of intervention versus the risk of rupture, as the maximum diameter criterion can underestimate the rupture risk of smaller aneurysms, and overestimate it for the larger ones.

To gain a more in-depth understanding of the possible mechanisms leading to these fatal events, this review analyzes experimental studies that aim to quantify the strength of aortic walls towards a material failure perspective and reviews biomechanically motivated models to predict rupture risk. After summarizing the microstructure of the aorta in Section 4.2, we continue with a brief account of damage and failure mechanisms involved in the dissection and rupture in Section 4.3. Subsequently, in Section 4.4 we summarize some important experimental studies that quantify the strength, and in Section 4.5 we summarize the state-of-the-art on the biomechanics-based rupture risk prediction models for clinical use. Finally, within Section 4.6, we provide concluding remarks. Readers interested in damage models or computational aspects of failure are referred to, e.g., the two recent book chapters of Holzapfel and Fereidoonnezhad [116] and Gültekin and Holzapfel [99], respectively.

4.2 Microstructure

We continue with a glance at the structure of the aorta as it provides a basis for our discussion. The aorta is composed of the intima, media and adventitia, as shown in Fig. 4.2(a). The intima is mechanically negligible in a young and healthy aorta, and it is basically a single layer of endothelial cells [124]. This layer becomes mechanically significant, especially with age, due to non-atherosclerotic intimal thickening during which collagen fibers are deposited [29]. Figure. 4.2(a) shows a sketch of such an artery with intimal thickening, while Fig. 4.2(b) partly depicts the collagen architecture of a healthy (but aged) wall obtained from an abdominal aorta and produced with second-harmonic generation microscopy. The media consists of several concentric lamellar units bound together, see Fig. 4.2(a),(c). Each of these units contains smooth muscle cells with their radially tilted longer axes oriented at an angle closer to the circumferential direction, surrounded by collagen fibers embedded in the extracellular matrix [235], see Fig. 4.2(c),(d). Collagen in the media is typically present as two symmetric families of fibers with a mean orientation closer to the circumferential direction, whereas in the adventitia the mean orientation is closer to the longitudinal direction [286]. The media is the main load bearing layer for physiological loads, and the adventitia acts as a stiff 'jacket-like' tube at higher levels of pressure, which prevents the artery from overstretch and rupture [124]. The thickness of the thoracic aortic media go hand in hand with an increase in the number of lamellar units, and the thickness of a single lamellar unit

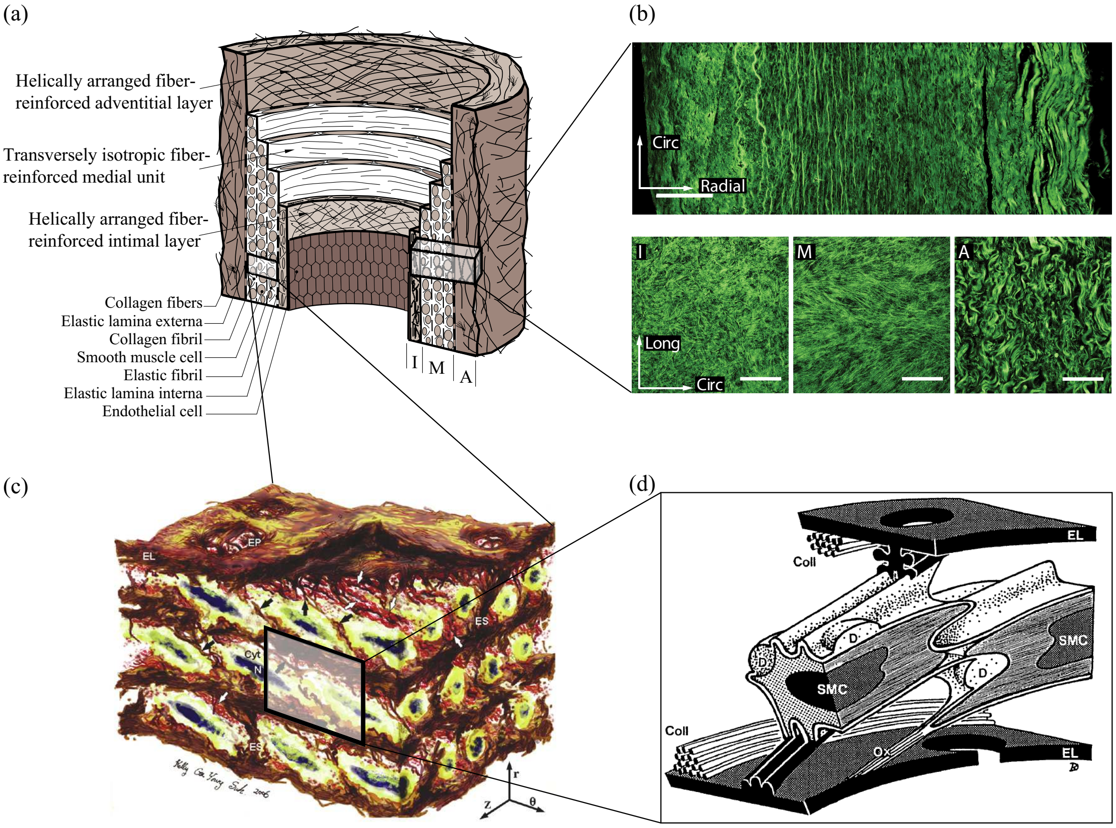

Figure 4.2 Structure of the aorta: (a) healthy but aged aortic wall with non-atherosclerotic intimal thickening composed of three layers – intima (I), media (M) and adventitia (A). Reprinted with permission from Gasser et al. [88]; (b) layered collagen architecture of a healthy and aged abdominal aorta – more specifically the top image depicts the out-of-plane structure in the circumferential-radial plane, while the three images at the bottom show in-plane sections of the intima (I), media (M) and adventitia (A) (white scale bars corresponding to 100 μm. Reprinted with permission from Niestrawska et al. [228]; (c) 3D microstructure of an aortic media consisting of several lamellar units – circumferentially-oriented radially-tilted smooth muscle cells (SMCs) with elliptical nuclei (N) sandwiched between elastic lamellas (EL) surrounded by a dense network of interlamellar elastin fibers (IEFs shown with black arrows), elastin struts (ES), and reinforced elastin pores (EP). Reprinted with permission from O'Connell et al. [235]; (d) schematic representation of two SMCs and two fenestrated EL with their interconnections – more specifically, collagen fibers (Coll) are closely associated with EL, surface ridges of the left SMC are connected to both EL via elastin protrusions, right SMC is connected to the lower El via oxytalan fiber (Ox), and larger deposits (D) containing collagen and heparan sulfate proteoglycan are found at indentations of the cell surface. Reprinted with permission from Dingemans et al. [56].

is constant amongst mammalian species (approximately 15μm) [369, 370]. However, human abdominal aortas have fewer lamellae for a given thickness compared to other species [370]. Growth of the human thoracic aorta is thought to be primarily due to the increase in the number of lamellar units, whereas in the human abdominal aorta it is mainly due to the increase in the thickness of the lamellar units [368].

A key structural change in thoracic aortic dissections is the so-called medial degeneration, as first reported by Erdheim [70]. Typically, it involves smooth muscle cell loss, elastic fiber fragmentation, and an accumulation of proteoglycans [18, 20, 371]. A weakened aortic wall due to medial degeneration is also typical for aneurysms and dissecting aneurysms of the ascending aorta [21], not only with tricuspid aortic valve (TAV) but also with BAV and bovine aortic arch phenotypes [249], see Fig. 4.3(a)–(f) for examples of proteoglycan accumulation zones. Versican and aggreacan were identified as the major components of such accumulations in thoracic aortic aneurysm and dissection patients [40]. In addition, one can see a change in the elastic fiber structure of a dissected aorta (Fig. 4.3(g)) where the elastic structure connecting the lamellar units are highly degenerated compared to a control aorta (Fig. 4.3(h)) [225]. Collagen content has been reported to increase [34, 354, 355] or decrease with an increased disruption [19, 21] for aortic dissections.

Dilatation of the aortic wall secondary to disruptions in elastin organization was reported in a mice study [146]. Although elastin content in the thoracic aortas of patients with an ascending aneurysm (TAV and BAV) decreased compared with control, it was not significantly different between BAV and TAV groups [35, 54]. In addition, changes in the elastin architecture of BAV patients compared with TAV were region-specific, and were characterized by a decrease in the number of radially oriented elastin fibers [336]. Primary elastin fiber orientation in the aneurysmatic media of TAV patients changed from longitudinal in the inner part to circumferential in the outer part distinctly in the right lateral region compared with other regions [302].

Similar collagen levels were observed between control and ascending aneurysm samples [54, 146, 168], and between BAV and TAV phenotypes [54, 250, 251] contradicting the findings of significantly higher collagen in BAV compared with TAV and control [35]. Regardless, the organization of collagen may still be significantly changed during aneurysm development in the thoracic aorta [19]. Sassani et al. [281] reported notable regional variations in the 2D collagen orientation, with the right lateral and posterior regions having diagonal fibers at smaller angles to the longitudinal axis. On the other hand, Forsell et al. [79] reported similar collagen orientations in aneurysmatic BAV and TAV groups. Phillippi et al. [250] demonstrated that both collagen and elastin fibers in the tangential plane were more aligned in BAV aneurysms and BAV control, and more disorganized in TAV aneurysms compared with TAV control. Percentage of radially oriented elastin and collagen fibers in the outer media was significantly higher in BAV patients and higher in TAV patients compared with control [335].

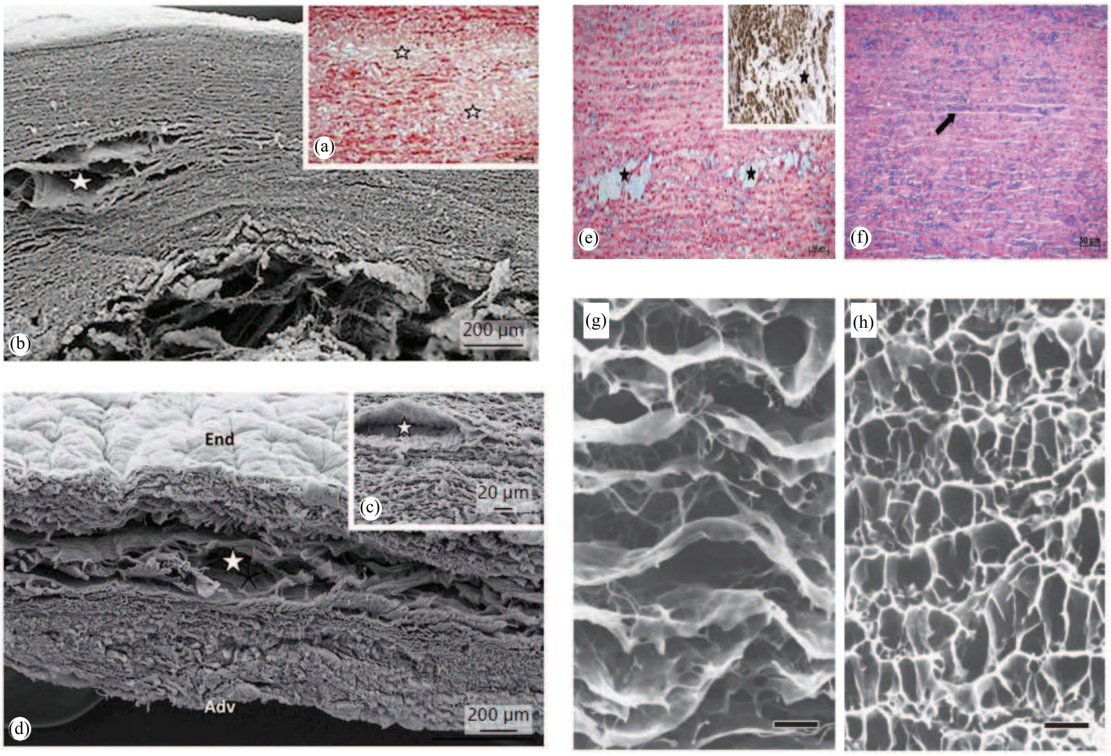

Figure 4.3 Microstructural changes due to pathological formations in human thoracic aortas with stars indicating mucoid accumulation areas (proteoglycan pools): (a),(b) disorganized collagen network visualized by (a) a histological section stained by picrosirius – collagen framework is disorganized – and (b) scanning electron microscopy (SEM); (c),(d) SEM images showing a lamellar structure disrupted probably by the proteogylcan pools (star) (Adv = Adventitia; End = endothelium coverage of the luminal face). Reprinted with permission from Borges et al. [21]; (e),(f) histological sections stained by Alcian blue showing (e) a pathological aorta with areas of mucoid accumulations (stars) – inset shows immunostaining for α-actin demonstrating the absence of SMCs inside the mucoid area; (f) control aorta where the space between elastic lamellae (arrow) is occupied by SMCs, collagen, and a normal amount of mucoid substance (light blue). Reprinted with permission from Borges et al. [20]; (g),(h) SEM images depicting the elastic fiber architecture of human aortic medias from (g) an aortic dissection patient and (h) a control subject (black scale bars indicate $20\,\mu$m. Reprinted from Nakashima [225].

Abdominal aortic aneurysms (AAAs) typically show increased collagen synthesis at earlier stages, whereas later in the process collagen degradation exceeds its synthesis, and it is accompanied by elastin degradation [295]. The out-of-plane collagen dispersion in AAAs is significantly higher when compared with abdominal aortic tissues, and the characteristic wall structure (with three distinct layers) cannot be identified anymore in AAA samples. In addition, collagen fibers in the abluminal layer of AAAs loose their waviness and appear as thick straight struts [228].

Several factors in the donor anamnesis may have an influence on the microstructure making it difficult to conclude, for example, which disease is accompanied with which structural changes and at which stages. Nevertheless, the microstructure remains a crucial contributor to mathematical models if one wishes to describe the mechanics and failure.

4.3 Failure Mechanisms Involved in Dissection and Rupture

We now study the load combinations that act on the tissues *in vivo* prior to dissection and rupture, which should be taken care of for a better understanding of tissue failure. In Section 4.3.1 we start with different theories regarding the loading conditions initiating and propagating the aortic dissections, and continue in Section 4.3.2 with theories regarding the global and local loading conditions prior to rupture in vehicular trauma. As we will see in the following sections, different loading conditions may lead to similar tissue failure.

4.3.1 Initiation and Propagation of Aortic Dissection

The study of van Baardwijk and Roach [339] applied pulse pressure to canine thoracic aortas after creating an intimal tear. The authors identified the maximum rate of pressure change $(\mathrm{d}P/\mathrm{d}t)_{\mathrm{max}}$ as the most clearly linked parameter to the propagation of dissection since the crack advanced at the upstroke of the pulse wave. Gaps between the lamellae, as identified during histological investigations, pointed to shearing mechanisms that are responsible for the crack propagation, and the crack typically propagated between adjacent elastic layers. The dissection rate was variable between the pulses, and it was inversely related to the tear depth within the medial layer in contrast to expectations, suggesting heterogeneous wall properties throughout the thickness.

On the other hand, Carson and Roach [31] reported that the medial strength of the porcine aortas does not change with depth under static pressure. The authors stated that the structures linking the lamellae are weaker than the lamellae themselves, resulting in a crack propagation between the lamellae. In addition, the fusion points of the lamallae can force the crack to change the direction. The authors reported quite high pressure values to initiate a bleb, but observed a quick drop in the pressure allowing the dissection to propagate under a physiological load level. A minimum pressure value required for

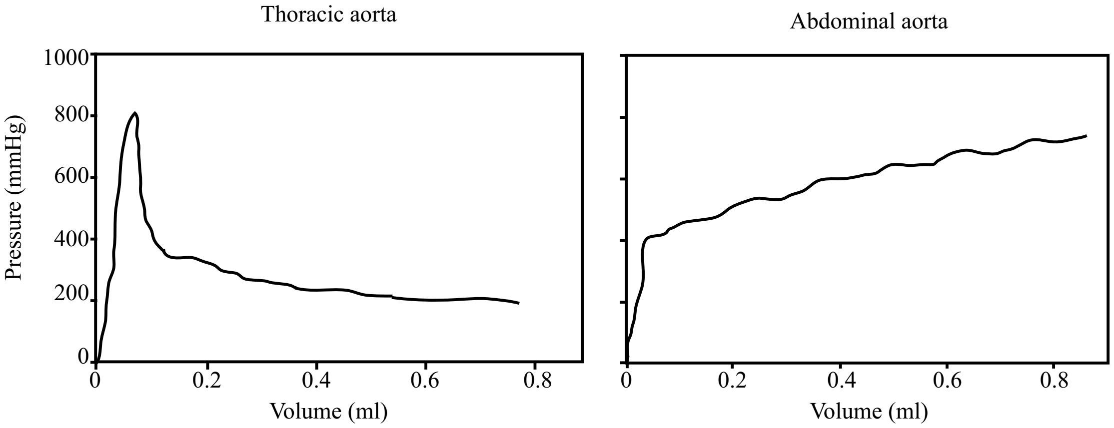

Figure 4.4 Pressure volume curves to create a bleb in the thoracic and abdominal sections of the aorta. Reprinted with permission from Roach and Song [270].

the crack to propagate was not reported therein. Using similar methods to Carson and Roach [31], Tiessen and Roach [325] reported similar results regarding the effect of the tear depth for human aortas, however, the authors noted that the dissection propagated around the plaques instead of going through them. The experiments on porcine aortas performed by Roach and Song [270] showed that although it was much easier to initiate a dissection in the abdominal aorta when compared to the thoracic aorta, the dissections propagated more easily in the thoracic aorta, see Fig. 4.4. The authors suggested that this is because of structural differences in the elastin pattern between the two sections of the aorta; parallel sheets with fenestrations in the thoracic aorta and a honeycomb-like structure in the abdominal aorta. In a later study, Tam et al. [320] reported that the dissection closer to the adventitial side required a lower pressure to propagate.

The study of Rajagopal et al. [262] suggested hemodynamics together with abnormal mechanical properties, geometry, and the anisotropic wall structure to be important factors for the initiation and the propagation of aortic dissections. The authors proposed that an increased maximum systolic pressure and the mean aortic blood pressure are responsible for the initiation, and an elevated pulse pressure and the heart rate facilitate the propagation. Mikich [216] proposed that the blood flow and the hemorrhage in the media alone cannot cause an initiation and propagation of a dissection, but the process is mainly influenced by smooth muscle cell contraction.

Haslach, Jr. et al. [206] proposed that collagen fiber pullout, during which bonds and filaments attached to the fibers rupture due to shear, is a prerequisite for rupture in circumferential aortic tensile strips and inflated ring specimens. For the longitudinal tensile strips, however, rupture is caused by a peeling mechanism during which the bonds between collagen fibers and the ground matrix rupture. In addition, hydration of the tissue is suggested to play an important role to recover from permanent deformation, loss of which eventually leads to rupture. This research group conducted more ring inflation tests, see Haslach, Jr. et al. [207, 208], concluding that, as a result of heterogeneous circumferential deformation, non-negligible circumferential shear stresses could be the reason for the crack propagation in the circumferential–longitudinal plane considering the lamellar structure of the media. Histological investigations of block shear tests showed voids between the collagen bundles, see Fig. 4.5(a)–(c), possibly resulting from the relative motion of the layers, which can be an indicator of ruptured inter-fiber cross-links [207]. Sommer et al. [308] reported similar observations within in-plane shear tests, as shown in Fig. 4.5(d), and this mechanism could explain the delaminations observed by Helfenstein-Didier et al. [111] during uniaxial tensile tests, as depicted in Fig. 4.5(e).

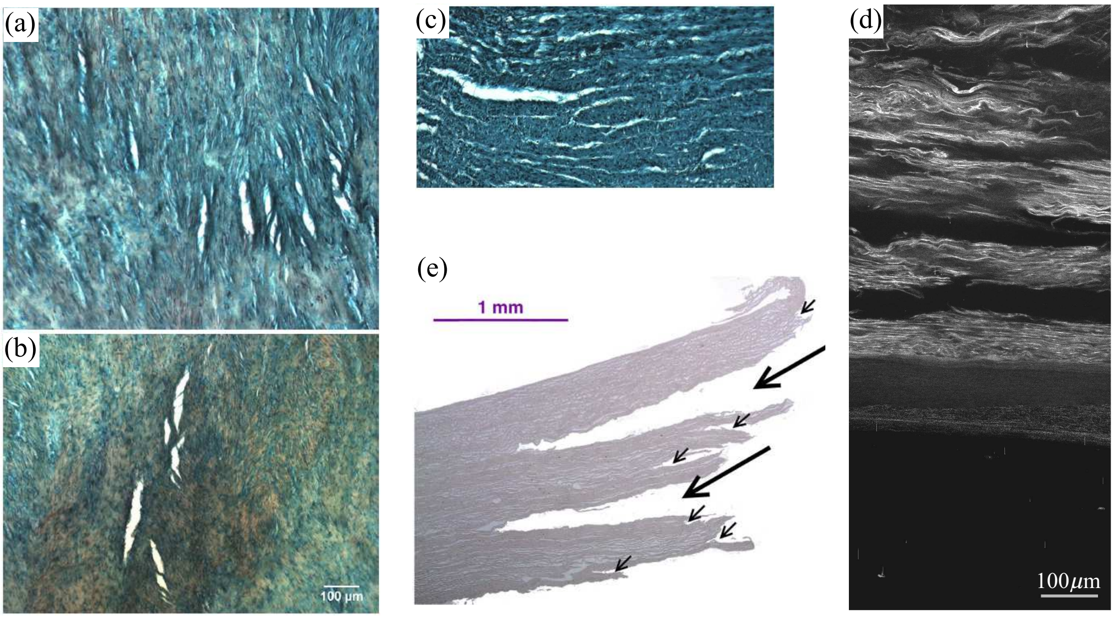

Figure 4.5 Initiation/propagation of aortic dissections due to shear stresses: (a)–(c) cracks visible after a block shear test, where the white areas are openings in the tissue. Reprinted with permission from Haslach, Jr. et al. [207]; (a),(b) are slices in the circumferential-longitudinal plane where the horizontal direction is longitudinal – (a) circumferential deformation parallel to the collagen fibers and (b) longitudinal deformation; (c) slice in the radial-circumferential plane after circumferential deformation, where the horizontal direction is circumferential; (d) cracks visible as black zones between the lamellae in the radial-circumferential plane after an in-plane shear test in the circumferential direction. Reprinted with permission from Sommer et al. [308]; (e) cracks that occurred during a uniaxial test indicated by black arrows. Reprinted with permission from Helfenstein-Didier et al. [111].

Following the protocol reported by Sugita and Matsumoto [314], recently [316] performed biaxial extension tests on thinly sliced porcine thoracic aortas with a reduced cross section in the center and reported a heterogeneous deformation field in terms of strains similar to [315]. Strain distribution and the collagen realignment were similar between the crack initiation sites and the remaining tissue sample, in contrast to the idea behind the maximum principal strain failure criterion. Since the collagen density was significantly lower at the crack initiation sites and the cracks propagated along the local collagen fiber direction, the authors suggested that the initiation and propagation of the crack is primarily effected by the collagen architecture. However, anticipated crack initiation at the lowest retardance sites – in other words the sites with the least collagen content – was not observed for all specimens. This suggests that the cross-links between the fibers might also play an important role in the dissection process.

Considering the changes to elastic fibers in aortic dissections and their role in energy dissipation, Chung et al. [37] studied elastic energy loss, defined as the hysteresis divided by the total strain energy. The authors found that an increased elastic energy loss is associated with medial degeneration and with increased collagen to elastin ratio. Furthermore, Chung et al. [38] reported a decrease in the directional differences in energy loss – hence in the degree of anisotropy – in samples with severe medial degeneration. By using newborn mice and genetic engineering to have defects in the elastic fiber structure, Kim et al. [160] suggested that not only elastin but properly assembled and cross-linked elastic fibers are responsible for a low energy loss in the aorta.

4.3.2 Traumatic Rupture

Blunt aortic trauma typically constitutes a transverse tear in the aortic wall, rarely a longitudinal one (see Fig. 4.6(a)). The mild degree trauma involves an intramural rupture (laceration), typically leading to a traumatic aortic dissection initiated by a circumferential tear to the intima, which may propagate and lead to complete rupture later in life [156, 254]. Severe trauma involves a transmural injury to the aortic wall, which can be in the form of partial, complete, or multiple transections. Figure 4.6(b)–(c) shows examples of intramural ruptures with different extents. Multiple ruptures as a combination of intramural and transmural ruptures are also reported in the literature [47, 310].

One of the first mechanisms proposed to explain traumatic rupture was the sudden increase in the intraluminal pressure. For example, the shoveling effect – the heart being trapped between the vertebral column, the sternum and the mediastinum due to the compression of the chest and the abdomen – can force the blood from the heart into the aorta suddenly increasing the intraluminal blood pressure [12]. The effect of this pressure increase can be elevated by the cardiac cycle in different ways. For example, Wilson and Roome [365] hypothesized that the aorta is more likely to rupture if an impact to the chest is received at the beginning of diastole since the aorta is completely filled with

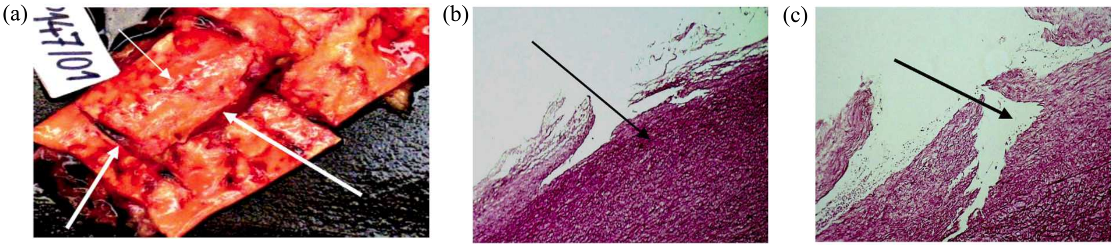

Figure 4.6 Aortic dissection and rupture due to traumatic injury. Reprinted with permission from Prijon and Ermenc [254]: (a) case presenting multiple ruptures: intramural and transmural, latter both in circumferential and longitudinal directions indicated by white arrows; (b) intramural rupture of the intima; (c) intramural rupture of the intima and the media.

blood, whereas Marsh and Moore [197] suggested that the deceleration forces acting on the heart during the systole creates a greater risk of rupture of the great vessels at the location of their attachment to the heart. In addition, a phenomenon known as water hammer effect might occur due to the sudden deceleration of the blood in the arch impacting the anterior wall of the aorta and resulting in traction forces on the isthmus region [164, 296]. The occlusion of the aortic lumen due viscoelastic effects that decrease the aortic diameter can cause formation of shock waves propagating in the counter-blood flow direction, thereby exerting high axial stresses on the aortic wall and causing a transverse rupture [164].

In addition to the hemodynamic effects, local concentrations of shear stresses may arise due to high deceleration forces [95], the rotation of the first ribs [46], or a combination of rapid deceleration and chest compression [296]. Vertical inertial forces [379], rapid deceleration occurring at different rates at different parts of the body [46, 197, 296], cranial deceleration [290], the heart being displaced in the thoracic cavity due to inertial effects [345] and the displacement of mediastinal structures [296] can all cause stretching of the aortic wall between fixation points resulting in an injury to the isthmus area due to stress concentrations. Field et al. [78] suggested that traumatic injury does not necessarily follow along the luminal/abluminal direction, considering that some patients did not present an intimal flap. The authors hypothesized that the geometry of the isthmic region in combination with the high number of small branching vessels lead to stress concentrations which are naturally occurring, and the stretching of these vessels may pronounce the effect of inertial or compressive chest loading resulting in intimal rupture, or intramural hematoma.

The above mentioned mechanisms for initiation and propagation of dissection as well as traumatic aortic injury indicate that the cardiac cycle, the blood flow and the geometry of the aorta together with the aortic attachment points are important factors to consider as they influence the boundary conditions to be imposed on the problem.

4.4 Tissue Strength Quantification

Aneurysms rupture when the wall stress exceeds the wall strength. Although it sounds simple, the requirement here is to reliably characterize both the (*in vivo*) stress state of the wall and the (*in vivo*) tissue strength, and neither is trivial. It is inarguably valuable to know how the aortic wall behaves under different loading modes – separated and mixed – to be able to predict the stress state of the wall. However, how much of the stress the tissue can bear at certain loading conditions with a given state of the microstructure remains unknown. As an essential element to a failure criterion framework, the strength quantification needs to be addressed.

In this section, we provide an overview of the documented experimental studies quantifying the strength of the aorta in health and disease. We review uniaxial tensile tests performed until failure, bulge inflation and peeling tests and (roughly) summarize related data in the Tables 4.1–4.3, respectively. Finally we describe other tests quantifying the tissue strength such as in-plane shear, direct tension and trouser tests. For an illustration of the different tests used to quantify failure properties of aortas see Fig. 4.7.

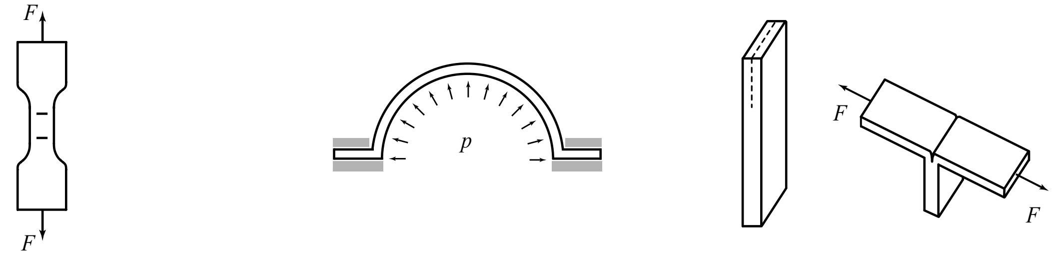
(a) Uniaxial tensile test (b) Bulge inflation test (c) Peeling test

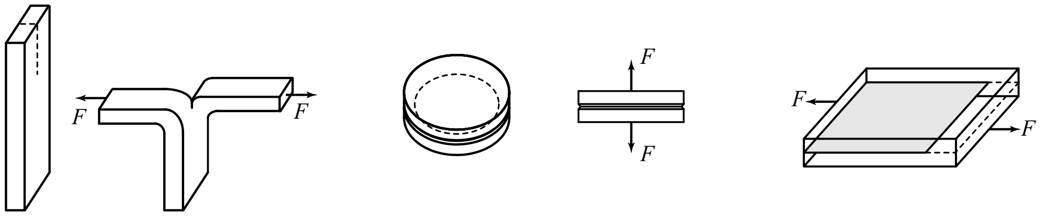
(d) Trouser test (e) Direct tension test (f) In-plane shear test

Figure 4.7 Experimental tests typically used to quantify the failure properties of aortas: (a) bone-shaped specimen for a uniaxial tensile test with load F; (b) bulge inflation test with pressure load p; (c) peeling test; (d) trouser test, as used in, e.g., [255]; (e) direct tension test to quantify radial strength, as used in, e.g., [304, 308]; (f) in-plane shear test with the sheared plane indicated in gray, as used in, e.g., [308]. Black arrows and dashed lines indicate the load direction and the incision, respectively. Tests (a),(c),(d) and (f) can be performed in any tissue direction in the tangential plane.

4.4.1 Uniaxial Tensile Tests Performed Until Rupture

Uniaxial tensile tests have been widely employed to characterize the mechanical properties of aortic tissues. Because of the anisotropic microstructure of the aortic wall, they are typically performed in circumferential and longitudinal directions to obtain direction-dependent properties. The shape of the specimen is either rectangular or (better) bone-shaped, as shown in Fig. 4.7(a). Table 4.1 summarizes some of the studies documented in the literature and provides failure stress and stretch values under uniaxial tensile loading. This table is not meant to be a complete summary of all uniaxial rupture tests published in the literature, however, it aims to provide a representative overview and points to the rather large variability in the failure stress and stretch values, also visualized in Fig. 4.8.

In terms of failure stress the thoracic aortic tissue has been reported to be stronger in the circumferential direction than in the longitudinal direction [75, 86, 138, 221, 251, 291, 308]. However, Vorp et al. [351] observed no significant differences in regard to the testing direction. The study of Mohan and Melvin [221] stated that the longitudinal aortic strength should be more than twice as high as the circumferential strength for the transverse failure to occur. Their quasi-static tests showed no such difference, however, once the strain rates were increased the strength ratios got closer to 1:2. The extension ratios were not effected by the strain rate.

In terms of the 'yield stress' the anterior region of AAAs was reported to be the weakest, especially along the longitudinal direction [322] – 'yield stress' is here related to

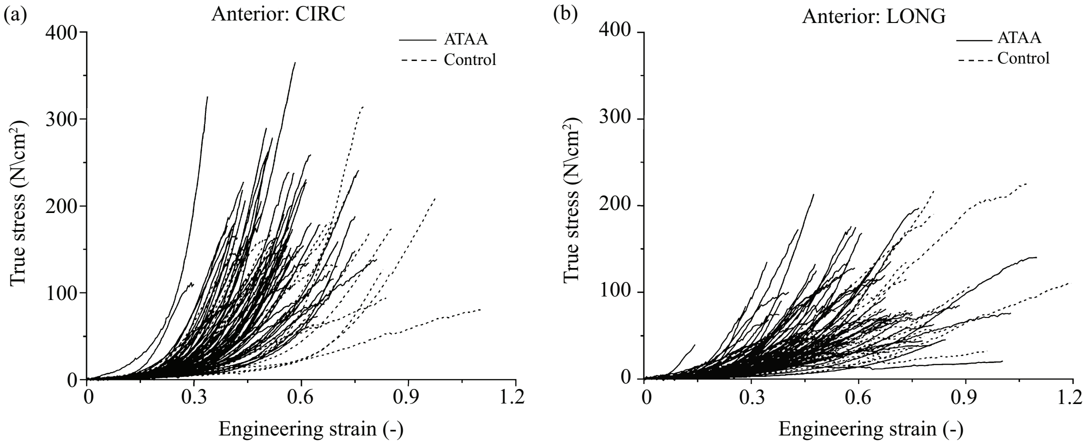

Figure 4.8 Stress-strain data of ascending thoracic aortic aneurysm (ATAA) and control specimens taken from the anterior region with (a) circumferential and (b) longitudinal orientation obtained from uniaxial tensile tests. Data show a large variability in failure properties. Reprinted with permission from Iliopoulos et al. [138].

the yield point defined as the point on the stress-strain curve where the slope starts to decrease with increasing strain. Failure stresses of anterior, right lateral, posterior and left lateral samples of the ascending aortas were not significantly different for control [138], for aneurysmatic [137, 138], and for dissected tissues [192] with respect to the circumferential direction. However, failure stresses in the longitudinal direction were significantly higher in the right lateral region compared with the anterior and posterior regions [138], but also in the left and right lateral regions compared with the anterior region for aneurysms [137]; and in the right lateral region compared with the left lateral region for dissections [192]. Ferrara et al. [75] reported stronger and stiffer posterior regions with respect to anterior in the circumferential direction for thoracic aortic aneurysms, whereas the opposite trend was observed for the longitudinal direction. Kritharis et al. [168] found similar failure properties in the noncoronary sinuses of the control and aneurysm groups for both young and old patients, whereas failure stresses in the right and left coronary sinus regions were smaller circumferentially and greater longitudinally in aneurysms compared with control.

Although all three layers of ascending thoracic aortic aneurysms exhibited higher failure stresses in the circumferential direction than in the longitudinal direction, the differences were significant only for the media from all regions and for the adventitia from the lateral region [303]. For dissected tissues, failure stresses and stretches were significantly higher in the circumferential than in the longitudinal direction in the inner media at the distal location, but the outer media did not show significant differences regarding the testing direction [192]. Failure stretches of the ascending tissue did not show notable differences between the layers [192, 303]. However, failure stresses were significantly higher for the adventitia than for the media and intima for aneurysms [303], and they were significantly higher for the outer media than for the inner media for dissections [192].

Healthy abdominal aortic tissues had significantly higher ultimate strength and yield strength compared to AAAs [258]. Failure tension (for definition see Raghavan et al. [259]) was suggested to be a better predictor of strength than failure stress [259], however, no significant differences were found between ruptured and unruptured AAAs in terms of either parameter [260]. In contrast, circumferential strips of ruptured AAA tissues were reported to have significantly lower failure stresses compared with the unruptured AAA tissue strips by Di Martino et al. [205]. Vorp et al. [349] reported isotropic failure properties for orthogonal strips taken from abdominal aortic aneurysms. Moreover, the failure stress in the longitudinal direction was significantly lower for AAA compared with control. Partially calcified AAA tissue was significantly weaker than the fibrous AAA tissue in terms of the failure stress, stretch and tension [211]. Failure stresses of the AAA wall were also reported to decrease with increasing intraluminal thrombus (ILT) thickness [202, 350].

Table 4.1 Overview of uniaxial tensile test results on aortas – tests performed until failure: ABA, abdominal aorta; AN, aneurysmatic; ASA, ascending aorta; BAV, bicuspid aortic valve; Circ, circumferential; DTA, descending thoracic aorta; H, healthy; Long, longitudinal; TAV, tricuspid aortic valve; $^{+}$ values for stress; * values for extension.

Study	Species	Location	Healthy/ Diseased	Additional information	Direction	n	Failure stress (kPa)	Failure stretch (–)
[221]	Human	DTA	H	Quasi-static	Circ	18	1720 ± 890	1.23 ± 0.28
					Long	18	1470 ± 910	1.47 ± 0.23
				Dynamic	Circ	16^{+}, 17*	5070 ± 3290	1.60 ± 0.28
					Long	18^{+}, 21*	3590 ± 2040	1.64 ± 0.28
[258]	Human	ABA	H	–	Long	7	2014 ± 394	–
			AN	–	Circ	16	1019 ± 160	–
					Long	45	864 ± 102	–
[350]	Human	ABA	AN	ILT > 4 mm	Circ	7	1380 ± 190	–
				ILT < 4 mm	Circ	7	2160 ± 340	–
[351]	Human	ASA	H	–	Circ	7	1800 ± 240	–
					Long	7	1710 ± 140	–
			AN	–	Circ	23	1180 ± 120	–
					Long	17	1210 ± 90	–
[205]	Human	ABA	AN	Ruptured	Circ	13	540 ± 60	–
				Unruptured	Circ	26	820 ± 90	–
[343]	Human	ABA	AN	For model input	Circ	60	805 ± 60	–
				For validation	Circ	21	832 ± 85	–
[86]	Human	ASA	H	< 35 yrs	Circ	–	2180 ± 240	2.35 ± 0.1
					Long	–	1140 ± 100	2.00 ± 0.1
				> 35 yrs	Circ	–	1200 ± 200	–
					Long	–	660 ± 70	–
			AN	BAV	Circ	–	1230 ± 150	1.80 ± 0.08
					Long	–	840 ± 100	1.58 ± 0.06
				TAV	Circ	–	1190 ± 130	–
					Long	–	880 ± 120	–
[251]	Human	ASA	AN	BAV	Circ	–	1656 ± 98	1.92 ± 0.04
					Long	–	698 ± 31	1.63 ± 0.02
				TAV	Circ	–	961 ± 61	1.61 ± 0.04
					Long	–	540 ± 37	1.47 ± 0.03
[291]	Porcine	ASA	–	–	Circ	11	2510 ± 439.3	1.99 ± 0.07
					Long	11	750 ± 102.6	1.92 ± 0.16
[75]	Human	ASA	AN	Anterior	Circ	37	1440 ± 700	1.35 ± 0.16
					Long	34	940 ± 490	1.34 ± 0.15
				Posterior	Circ	32	1850 ± 700	1.36 ± 0.12
					Long	19	740 ± 180	1.31 ± 0.09
[308]	Human	ASA	AN	Media	Circ	7	1282 ± 822	1.52 ± 0.20
					Long	10	565 ± 198	1.52 ± 0.18

Vorp et al. [351] reported aneurysmatic ascending aortas to have significantly lower failure stresses and stiffer behavior compared to controls. García-Herrera et al. [86] documented no significant differences between the mechanical strength of aneurysmal BAV and aneurysmal TAV aortic specimens, and the corresponding age-matched control group for the ascending aorta. Significantly higher failure stresses were reported in aneurysmatic BAV ascending aortas when compared to aneurysmatic TAV ascending aortas for the intact wall [54, 76, 79, 249, 251], and for the media [54]. The failure stretches in two valve phenotypes were similar [79, 249], but also significantly higher for BAV than for TAV [54, 76]. Histological investigations showed that proportional differences in the tensile strength between BAV and TAV groups cannot be explained by alterations in the elastin content [54] or the collagen content [54, 251]. However, the stiffness increase and extensibility reduction in ascending aneurysmatic tissues were associated with a decreased elastin content [302].

In the study of Vande Geest et al. [341] no statistically significant gender-related differences were reported in terms of strength, unlike [301] who identified that circumferential aneurysmatic specimens obtained from female patients exhibited significantly lower failure stresses compared with the ones obtained from male patients. Furthermore, failure stresses of the aorta are reported to decrease [76, 86, 168, 233], and also the failure stretches [76, 168, 233] with increasing age. In general, strength was not correlated to diameter [137, 205], but it was inversely related to wall thickness [137, 205, 322].

4.4.2 Bulge Inflation Tests

Although uniaxial tensile tests provide valuable insight into the strength characteristics of aortic tissues, they are limited when it comes to representing *in vivo* loading conditions. Methods to quantify tissue strength using planar biaxial tests are not yet developed to the authors' knowledge, therefore, biaxial tests performed via a bulge inflation method, see Fig. 4.7(b), are the focus of this section. Table 4.2 summarizes some studies documenting failure stress and (when available) extension to failure, defined in various ways (see the related table). Aortic specimens failed consistently in the direction perpendicular to the longitudinal axis in bulge inflation tests for human [222] and for porcine tissue [196], and the dynamic biaxial failure pressure was significantly higher than the quasi-static one, 2.14 times [222]. Sugita et al. [317] also documented the normal aorta to be weakest in the longitudinal direction under bulge inflation tests, but there was no dominant crack direction for the aneurysmal tissues. The authors did not observe a persistent rupture initiation at local strain concentration zones in contrast to Kim et al. [162] who reported local strain and stress concentrations at the rupture locations. The study of Kim et al. [162] deduced a stable stress parameter for rupture, quantifying the stress in the direction normal to both families of collagen fibers using the values provided in Table 4.2. Romo et al. [272] showed that localized thinning of the wall is responsible for rupture and not the location of maximum stress. The related

Table 4.2 Overview of bulge inflation test results on aortas: AN, aneurysmatic; ASA, ascending aorta; Circ, circumferential; DTA, descending thoracic aorta; Long, longitudinal; TA, thoracic aorta; ^{a} Laplace stress; ^{b} stress perpendicular to the crack direction; ^{c} mean stretch; ^{d} circumferential stretch; ^{e} average Green–Lagrange strain; ^{f} stretch perpendicular to the crack direction.

Study	Species	Location	Healthy/ Diseased	Speed (mm/min)	Additional information	Direction	n	Failure stress (kPa)	Failure extension (–)
[196]	Porcine	TA	–	60	–	Long	25	1750 ± 710	1.523 ± 0.178^c
[246]	Porcine	ASA	–	–	–	–	10	3699 ± 789	1.85 ± 0.114^d
		DTA	–			–	10	4260 ± 1626	1.70 ± 0.138^d
		Isthmus	–			–	10	3248 ± 1430	1.66 ± 0.109^d
[162]	Human	ASA	AN	15	Media	Circ	6	547.5 ± 362.6	0.192 ± 0.08^e
						Long	6	335.3 ± 103.8	0.261 ± 0.117^e
					Adventitia	Circ	3	636.6 ± 322.7	0.252 ± 0.091^e
						Long	3	976 ± 247.2	0.343 ± 0.123^e
[317]	Porcine	TA	–	15	Proximal	–	6	1810 ± 430^a	–
					Distal	–	6	2290 ± 740^a	–
	Human	TA	AN		–	–	6	980 ± 390^a	–
[272]	Human	ASA	AN	15	Media	–	9	780 ± 200^b	–
					Adventitia	–	6	1460 ± 103^b	–
[65]	Human	ASA	AN	15	Composite	–	31	1260 ± 940^b	1.37 ± 0.15^f

values in Table 4.2 are the stresses in the direction perpendicular to the crack direction at rupture. Duprey et al. [65] calculated failure stress and stretch similar to [272]. Cracks showed dissection-like properties, where the media and the intima failed first creating a sudden drop in the stress curves, but the adventitia was still able to carry (some) load. The authors found no significant differences between BAV and TAV patients, whereas age had a significant impact on the failure properties. In addition, they reported no correlation between the aneurysm diameter and the failure stress/stretch. Luo et al. [188] investigated the elastic properties, direction of maximum stiffness, stress, strain, and the energy consumption at the rupture sites of 9 aneurysmatic ascending aortic samples. The authors reported the tissues to consistently fail in the direction of maximum stiffness and highest energy, indicating that higher stiffness does not mean higher strength. Since high stiffness and energy values mean more collagen recruitment, they concluded that collagen fibers must play a significant role in the rupture process.

Pearson et al. [246] found no significant differences in rupture pressure between the ascending, descending, and isthmus regions. However, they reported significantly larger extension to failure in the ascending aortic samples compared to the isthmus samples, which is in contrast to Marra et al. [196] who found no significant influence of the aortic location on the axial failure stress or stretch. Histological investigations in [246] showed isthmus samples to have a higher collagen to elastin ratio, likely making the samples from this region less extensible. The failure stresses were significantly larger for the descending aorta than for the isthmus region, however, the overlap in the data between the isthmus and the adjacent regions let the authors conclude that the mechanical failure properties cannot account for the clinical observations pointing to the isthmus as a primary injury location.

4.4.3 Peeling Tests

As mentioned above, the propagation of the dissection is mainly attributed to the lamellar structure of the aortic wall. Peeling tests, which is not the sole appropriate method, can provide us with the delamination strength of the wall at different locations. The 'strength' of the wall is typically quantified in terms of force per width (F/w) and the dissection energy (W_{diss}). On the basis of some studies Table 4.3 provides an overview of these values for the aorta, and Fig. 4.7(c) shows a sketch of a peeling test.

Higher force per width for axial strips compared to circumferential strips of the abdominal aortic media was reported by Sommer et al. [304] – note that this difference was not significant. Furthermore, the authors observed that the damage was spread over six to seven lamellae. Figure 4.9(a),(b) depicts the histological sections of circumferential and longitudinal strips under peeling. Pasta et al. [244] investigated the dissection properties of human ascending aortas in aneurysmal BAV and TAV patients. Compared to the control group, both aneurysm groups required significantly lower force per width, where the TAV group was significantly stronger than the BAV group. The controls showed a strong anisotropy, where the axial direction was significantly stronger, which was not observed in neither aneurysm group. Scanning electron microscopy investigation showed a larger number of ruptured elastin fibers, which is in accordance with the fiber bridging failure mode, see Fig. 4.9(c).

Kozuń [166] showed that the dissection properties are direction dependent also for stage II atherosclerotic aortas (classification according to Stary [312]), in particular the force per width F/W and the dissection energy W_{diss} were higher in the longitudinal direction. In addition, a significantly higher dissection energy W_{diss} for the adventita/media + intima (A-MI) interface compared to the adventitia + media/intima (AM-I) interface was reported. Following [166], Kozuń et al. [167] found the dissection energy for A-MI and AM-I interfaces in both circumferential and longitudinal directions to decrease with later stages of atherosclerosis (classification according to [312]) until stage IV, whereas stages V and VI were characterized by an increase in the energy.

Tong et al. [328] reported a decreased dissection energy for the media/intima (MI) composite as well as a decreased anisotropy with increasing ILT age. In addition to the values provided in Table 4.3, the authors performed peeling tests on the ILT. Histological investigations showed smooth peeling surfaces in the ILT due to single fibrin fibers or smaller protein clots within the ILT. In addition, the elastin content in the wall decreased as the thrombus age increased, whereas the collagen content did not change

Table 4.3 Overview of peeling test results on aortas: A, adventitia; ABA, abdominal aorta; Age*, age of intraluminal thrombus; AM, adventitia + media; AN, aneurysmatic; AT, atherosclerosis; ASA, ascending aorta; BAV, bicuspid aortic valve; Circ, circumferential; F/w, force per width; Long, longitudinal; H, healthy; MI, media + intima; TA, thoracic aorta; TAV, tricuspid aortic valve; W_{diss}, dissection energy; $^+$ according to [312].

Study	Species	Location	Healthy/ Diseased	Additional information	Direction	n	F/w (mN/mm)	W_{diss} (mJ/cm^2)
[304]	Human	ABA	H	Media	Circ	5	22.9 ± 2.9	5.1 ± 0.6
					Long	7	34.8 ± 15.5	7.6 ± 2.7
[244]	Human	ASA	H	Control	Circ	7	126 ± 6.6	–
					Long	7	149 ± 7.6	–
			AN	TAV	Circ	8	109.1 ± 5.2	–
					Long	8	116.8 ± 6.1	–
				BAV	Circ	16	88.4 ± 4.1	–
					Long	16	100 ± 4.1	–
[328]	Human	ABA	AN	Age* II, A	Circ	11	–	10.1 ± 1.7
					Long	9	–	9.3 ± 0.9
				Age* III, A	Circ	8	–	9.2 ± 2.0
					Long	7	–	8.3 ± 1.3
				Age* IV, A	Circ	6	–	8.6 ± 1.4
					Long	7	–	7.8 ± 1.0
				Age* II, MI	Circ	12	–	6.7 ± 1.2
					Long	12	–	8.4 ± 1.9
				Age* III, MI	Circ	8	–	5.5 ± 1.1
					Long	8	–	6.8 ± 1.7
				Age* IV, MI	Circ	7	–	4.2 ± 1.1
					Long	6	–	5.1 ± 1.4
[166]	Human	TA	AT (stage II$^+$)	A–MI	Circ	26	24.5 ± 7.5	5.6 ± 0.9
					Long	7	32.4 ± 6.5	7.6 ± 1.7
				AM–I	Circ	22	26.5 ± 6.7	4.1 ± 1.0
					Long	8	34.2 ± 3.5	4.7 ± 0.9
[229]	Porcine	TA	–	Control	Circ	16	67.4 ± 11.7	15.18 ± 2.70
					Long	16	76.7 ± 25.9	18.33 ± 6.42
				Collagenase	Circ	17	49.3 ± 11.9	10.81 ± 2.80
					Long	14	53.9 ± 12.2	13.58 ± 3.12
				Elastase	Circ	16	58.8 ± 17.3	13.24 ± 4.00
					Long	14	69.1 ± 27.0	17.18 ± 7.12
				Glutaraldehyde treatment	Circ	13	91.2 ± 28.2	19.01 ± 6.05
					Long	14	83.6 ± 13.7	18.63 ± 3.35

significantly. The authors reported a rate-dependent change in the dissection properties of both the ILT and the ILT-covered wall. Noble et al. [229] analyzed the influence of collagenase, elastase, and glutaraldehyde treatment on the dissection properties of porcine thoracic aortas. Collagenase significantly decreased the resistance to dissection, whereas glutaraldehyde increased it and elastase had no significant effect. In terms of anisotropy, their results were similar to [304].

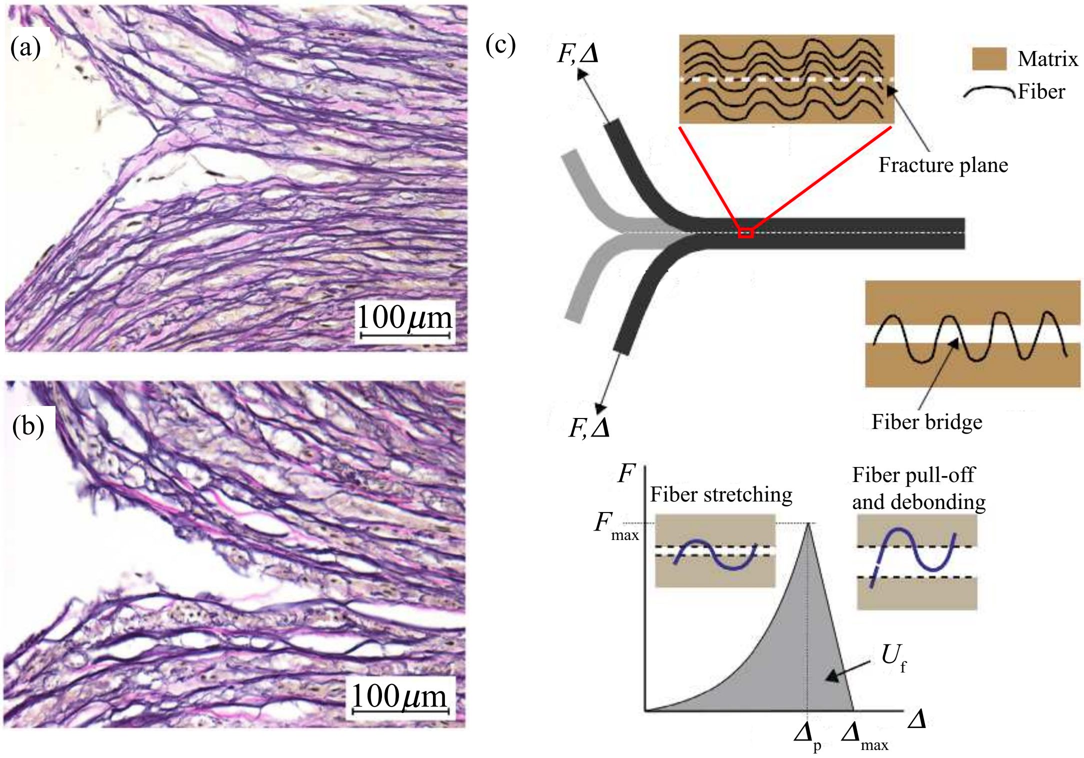

Figure 4.9 Histological images (Elastica van Gieson) of the dissection tips obtained from a peeling test of an aortic media during peeling in (a) circumferential and (b) longitudinal directions. Reprinted with permission from Sommer et al. [304]. The images highlight the irreversible mechanism of the separation at the microscopic level. (c) Schematic of fiber bridging failure; the matrix is already separated but still connected by an unruptured fiber (above); force–separation law (F vs Δ) for a collagen fiber bridge with nonlinear loading and linear post peak behavior starting at F_{max} and related Δ_{p} (below) – modes of fiber deformation and failure are depicted in the insets. Shaded region represents the energy U_{f} required for failure of the fiber bridge. Adapted from Pal et al. [238].

4.4.4 Other Tests Quantifying Tissue Strength

Trouser tests, as illustrated in Fig. 4.7(d), in addition to uniaxial tensile tests, were performed on porcine descending thoracic aortas by Purslow [255]. The author reported that the longitudinal direction is more resistant to tearing than the circumferential direction, such that some longitudinal test samples showed cracks that deviated to the circumferential direction making data from these tests unusable for further analysis. In addition, the author found that the circumferential toughness increased with increasing distance from the heart. The study of Chu et al. [36] showed that the stiffness and the fracture toughness of aortas decreased with increasing fatigue by using cyclic loading tests followed by biaxial and guillotine tests. On the basis of the guillotine method documented by Chu et al. [36], Shahmansouri et al. [292] used a custom-made toughness-tester apparatus for tests on control and aneurysmatic ascending aortic tissues taken from four quadrants, and the authors measured the circumferential toughness and the incremental elastic modulus at 10% Green-Lagrange strain. Neither parameter showed regional dependency, however, both correlated well with the total amount of structural proteins (collagen and elastin). More specifically, the toughness decreased with increasing collagen content. The average toughness was not correlated with the average circumferential or longitudinal moduli.

Curves of direct tension tests (see Fig. 4.7(e)) on abdominal aortas [304] and thoracic aortas [308] showed three characteristic regions, namely elastic, damage, and failure. The average radial failure stress for human abdominal aortas was $140.1 \pm 15.9\,\text{kPa}$ and for diseased human thoracic aortas $131 \pm 56\,\text{kPa}$. Comparing these values with the data from uniaxial tests in Table 4.1, it is clear that the aorta is weakest in terms of the failure stress under radial loading due to its lamellar structure, as also pointed out by MacLean et al. [189], see Fig. 4.2.

In-plane and out-of-plane shear tests until failure in circumferential and longitudinal directions were performed on diseased human thoracic aortas by Sommer et al. [308]. The sheared plane and the direction of shearing during an in-plane shear test is depicted in Fig. 4.7(f). Out-of-plane shear strength was almost 10-fold higher compared to the in-plane shear strength, which is a result of the lamellar structure and the collagen architecture of the aorta. The shear-lap test results of Witzenburg et al. [367] were similar to the in-plane shear tests of Sommer et al. [308], although the geometry of the samples were slightly different. The authors reported that circumferential samples exhibited significantly higher peak stresses (nominal) than longitudinal samples.

4.5 Biomechanically Motivated Models to Predict Rupture Risk

There may be different reasons for the similar locations at which traumatic injuries and the initiation of aortic dissections occur, as pointed out in the introduction. One reason may be that since the aorta is attached to the left pulmonary artery by the ligamentum arteriosum at the isthmus and to the vertebral column by the fascia, it cannot deform as extensively as other locations leading to local stress concentrations. Another reason may be that the aortic wall has an inherently different strength in these locations due to its microstructure, e.g., due to differences in collagen and elastin content, orientation, or cross-linking proteins. Since the aorta may be subjected to stress concentrations and has heterogeneous strength distributions along the tree, stress and strength are frequently used in models to predict rupture risk. Next we summarize a few existing models designed to evaluate the risk of rupture.

Doyle et al. [60, 61] performed inflation tests on silicone rubber to mimic the inflation of abdominal aortic aneurysms (AAA), and observed rupture at the regions of inflections instead of maximum diameter. They also reported rupture at peak stress locations in 80% of the cases using computational models. Nathan et al. [226] performed finite element analyses on 47 normal thoracic aortic geometries by assuming that the aortic wall is homogeneous, incompressible, isotropic and linearly elastic, a rather rough assumption. The results showed that the mean wall peak stresses occurred above the sinotubular junction ($0.43 \pm 0.07\,\mathrm{MPa}$) and distal to the left subclavian artery ($0.21 \pm 0.07\,\mathrm{MPa}$), which is in line with the common locations of dissection initiation. This led to the conclusion that the stress distribution is the main contributor to the dissection process. Biaxial extension tests on aneurysmatic ($n = 18$) and healthy ($n = 19$) ascending aortic samples showed that aneurysmatic samples are much stiffer under physiological loading conditions [9]. Hence, the authors suggested that the patient-specific wall stress could be a good predictor of rupture risk. The study did not find any correlation between the maximum diameter and the patient-specific stress levels. Addressing the large variations in strength and the uncertainties in wall stress predictions, Polzer and Gasser [252] developed a probabilistic rupture risk index (PRRI), calculated by using the wall strength and the peak stress distribution. The authors were able to distinguish between the intact and ruptured AAA cases. PRRI values were strongly correlated with the mean arterial pressure, but not with the maximum diameter.

On the basis of heterogeneous strength distribution in aneurysm walls, Vallabhaneni et al. [338] suggested that the locations with increased enzymatic activity within the wall could be responsible for a local weakening making the aneurysm more prone to rupture. Vande Geest et al. [342, 343] reported different statistical risk prediction models considering the heterogeneity of both the wall stress and the wall strength. Simulations using the model of [342] indicated that the unruptured AAAs had significantly higher failure stresses compared to the ruptured group. Even though this model could not be validated by Reeps et al. [265], it involves a non-invasive estimation of patient-specific wall strength, and it was used by Joldes et al. [145] to develop a rupture risk calculation software. The approach of Joldes et al. [145] eliminates the need to use patient-specific material parameters as the stresses are only determined by the external load and the geometry, depending only weakly on the material parameters (for a detailed discussion see [366], [220] and [144]).

Trabelsi et al. [333] compared three different rupture risk assessment methods, in particular, maximum diameter, rupture risk index, and the overpressure index (see definitions therein). The maximum diameter criterion was only weakly correlated with the other two, and, remarkably, the patient with the smallest aneurysm diameter had the highest rupture risk index. Duprey et al. [65] suggested a rupture risk criterion for aneurysms of ascending aortas based on a maximum stretch parameter γ_{stretch} the authors introduced. It indicates that the failure is reached when the stretch acting on the tissue is larger than its maximum extensibility. The data obtained via bulge inflation tests therein showed a strong correlation between γ_{stretch} and the physiological elastic modulus. Trabelsi et al. [334] were able to further correlate this rupture risk indicator with the membrane stiffness using the analysis of CT-scans, concluding that the loss of elasticity increases the rupture risk. However, the authors stated that the correlation was not strong enough for this criterion to be suggested for use in clinical practice.

Martin et al. [199] quantified the rupture diameter risk and the yield diameter risk defined as the diameter D_{sys} at systolic pressure divided by the diameter D_{f} at rupture pressure ($D_{\text{sys}}/D_{\text{f}}$) and by the diameter D_{y} at yield pressure ($D_{\text{sys}}/D_{\text{y}}$), respectively. Both risk indicators were related with increases in the clinically measured parameters such as systolic blood pressure, age, systolic wall tension and pressure-strain modulus (rupture diameter risk was additionally correlated with the aortic size index; for the related definition see Davies et al. [50]), but not with the aneurysm diameter. Building on this framework, Martin et al. [200] performed patient-specific finite element analyses using geometries reconstructed from CT scans and clinical blood pressure measurements, in addition to mechanical data from these aortas reported previously by Pham et al. [249]. The rupture diameter risk was correlated with the simulated peak wall stresses and with the tension-strain modulus, but not with the systolic hoop tension and the overall aneurysm diameter. The predicted rupture pressures decreased dramatically with increasing rupture diameter risk.

4.6 Concluding Remarks

Despite the advances in medical, biomedical and biomechanical research, the mortality rates of dissections and aortic aneurysms remain high. The present review article summarizes experimental studies that quantify the aortic wall strength and it discusses biomechanically motivated models to predict rupture risk. Following the description of the aortic microstructure and the pathological changes leading to dissection and aneurysm in Section 4.2, we summarized experimental investigations that were designed to better understand failure mechanisms involved in dissection and rupture in Section 4.3. In the case of aortic trauma, we have seen in Section 3.2 that there may be different global load cases on, e.g., the chest resulting in a similar load on the aortic wall leading to a similar material failure. As suggested by Richens et al. [267], multivariate hypotheses are more suitable to explain under what loading conditions the aorta ruptures. Such hypotheses can bring the global mechanisms together, i.e. shearing, torsion and stretching, and suggest which stresses play a more pronounced role during rupture. Various loads acting on the aortic wall prior to rupture call for the strength identification under different loading modes.

In Section 4.4 we focused on uniaxial tensile, bulge inflation and peeling tests while briefly touching upon trouser, direct tension and shear tests. We identified contradictory observations and a large variation within and between data sets, which may be due to biological variations, different sample sizes, differences in experimental protocols, etc. However, we pointed to the underlying structural similarities/differences as the main contributor to the similarities/differences of the strength values. Considering the pathological microstructural changes, aneurysmatic and dissected tissues are expected to exhibit different strength properties compared to control tissues although this is not always the case according to the mechanical test results, as pointed out in Section 4.4. However, it seems that the micro-architecture, in particular the content and organization of collagen and elastin and their cross-linking proteins play an important role during failure.

Finally, in Section 4.5 we looked at what is proposed in the literature to predict the risk of rupture as an alternative to the maximum diameter criterion. Realistic geometries and appropriate constitutive models are crucial to identify wall stresses and zones of stress concentration. Martufi and Gasser [201] elaborated on a wall-averaged stress state (membrane stress state) to be a more realistic AAA rupture risk indicator, also pointing out the importance of using appropriate constitutive models to predict wall stresses. As mentioned before and addressed by several risk prediction models, not only the stress state at a point in time but also the strength distribution is likely to be heterogeneous. Although rupture risk prediction models address an important issue in clinical practice, they do not model material failure.

Let us finally consider a few more recent findings on tissue failure. Converse et al. [44] showed that ‘arterial yielding’ was closely correlated with the onset of collagen damage, which is indicated by the binding of collagen hybridizing peptide to undulated collagen [381]. In addition, damage accumulation increased with increasing stretch beyond the ‘yield threshold’, and it occurred primarily in the fibers along the loading direction [44]. This suggests that orientation and dispersion of collagen determine the strength of, e.g., aortic tissues [293] and the pericardium [360]. Marino et al. [195] proposed a damage model considering interstrand delaminations as a source of inelastic deformation, as suggested by multiscale models of collagen fibrils [193, 194] and by atomistic computations [26, 337]. Employing the experimental protocols documented in [44], [195] showed that damage onset and excessive damage accumulation agree well with the predicted evolution of the model parameters that describe tissue softening associated with permanent molecular elongation, and tissue failure associated with loss of fibril structural integrity.

Mored advanced failure criteria for fibrous biological tissues are of pressing need to better understand aneurysm rupture and propagation of aortic dissections, and to substantially improve clinical decision making; should also go hand in hand with developments in clinical biomarkers and/or suitable imaging modalities. In the light of this review, we suggest that an ideal failure criterion should include the strength of the material under different loading cases and the effect of the tissue microstructure on the strength at different length scales. In particular, a failure criterion should be based on microstructural properties including the content and organization of remodeled collagen and remnant elastin and their cross-linking proteins, especially under the influence of proteolytic activity. Such failure criteria may also improve G&R models necessary of addressing the key issue of rupture-potential.

Acknowledgement We would like to acknowledge Yutaka Nakashima from the Division of Pathology, Japanese Red Cross Fukuoka Hospital in Japan and Justyna A. Niestrawska from the Institute of Biomechanics, Graz University of Technology in Austria for providing the two images of the microstructure of the aortic dissection and the aneurysm, as presented in the graphical abstract. In addition, we gratefully acknowledge the aneurysm image, also presented in the graphical abstract, which we received from Erasmo Simão da Silva from the Division of Vascular and Endovascular Surgery, University of São Paulo in Brazil and Madhavan L. (Suresh) Raghavan from the Department of Biomedical Engineering, University of Iowa, Iowa City, USA. This work was partly supported by the Lead Project on ‘Mechanics, Modeling and Simulation of Aortic Dissection’, granted by Graz University of Technology, Austria. Furthermore, we gratefully acknowledge the financial support of the National Institutes of Health (NIH), research Grant no. NIH R01HL117063.

5 FAILURE PROPERTIES AND MICROSTRUCTURE OF HEALTHY AND ANEURYSMATIC HUMAN THORACIC AORTAS SUBJECTED TO UNIAXIAL EXTENSION WITH A FOCUS ON THE MEDIA

Abstract Current clinical practice for aneurysmatic interventions is often based on the maximum diameter of the vessel and/or on the growth rate, although rupture can occur at any diameter and growth rate, leading to fatality. For 27 medial samples obtained from 12 non-aneurysmatic (control) and 9 aneurysmatic human descending thoracic aortas we examined: the mechanical responses up to rupture using uniaxial extension tests of circumferential and longitudinal specimens; the structure of these tissues using second-harmonic imaging and histology, in particular, the content proportions of collagen, elastic fibers and smooth muscle cells in the media. It was found that the mean failure stresses were higher in the circumferential directions (Control-C 1474 kPa; Aneurysmatic-C 1446 kPa), than in the longitudinal directions (Aneurysmatic-L 735 kPa; Control-L 579 kPa). This trend was the opposite to that observed for the mean collagen fiber directions measured from the loading axis (Control-L > Aneurysmatic-L > Aneurysmatic-C > Control-C), thus suggesting that the trend in the failure stress can in part be attributed to the collagen architecture. The difference in the mean values of the out-of-plane dispersion in the radial/longitudinal plane between the control and aneurysmatic groups was significant. The difference in the mean values of the mean fiber angle from the circumferential direction was also significant between the two groups. Most specimens showed delamination zones near the ruptured region in addition to ruptured collagen and elastic fibers. This study provides a basis for further studies on the microstructure and the uniaxial failure properties of arterial walls towards realistic modeling and prediction of tissue failure.

Statement of significance A data set relating uniaxial failure properties to the microstructure of non-aneurysmatic and aneurysmatic human thoracic aortic medias under uniaxial extension tests is presented for the first time. It was found that the mean failure stresses were higher in the circumferential directions, than in the longitudinal directions. The general trend for the failure stresses was Control-C > Aneurysmatic-C > Aneurysmatic-L > Control-L, which was the opposite of that observed for the mean collagen fiber direction relative to the loading axis (Control-L > Aneurysmatic-L > Aneurysmatic-C > Control-C) suggesting that the trend in the failure stress can in part be attributed to the collagen architecture. This study provides a first step towards more realistic modeling and prediction of tissue failure.

5.1 Introduction

Aneurysms and dissections of thoracic aortas are life threatening conditions with high mortality rates even though clinical procedures have been improved in recent years [234, 243, 318]. Current practice guidelines recommend surgical repair of large thoracic aortic aneurysms (with maximum diameter of the lesion of 5.0 cm in women or 5.5 cm in men or if the maximum diameter increases more than 0.5-1.0 cm in one year [97, 104, 175]) to prevent fatal aortic dissection or rupture, but observations have shown that adverse aortic events may already occur at smaller diameters [161]. Interestingly, more than 80% of aortic dissections develop in the absence of a pre-existing aneurysm, indicating that aneurysm formation and dissection are in general different pathophysiological conditions [242]. Since there is a variety of causes for the development of thoracic aortic diseases, a greater knowledge of patient-specific biomechanical properties reflecting the influence of the microstructure is important for predicting adverse events.

The healthy thoracic aorta has a unique structural composition that enables it to withstand the large tissue stresses created mainly by the blood pressure [35]. Of the three main layers, the innermost layer, the intima, consists of a single layer of endothelial cells in a healthy young artery, and its solid mechanical contribution is negligible [124]. However, intimas, especially from older patients, often exhibit a considerable thickening due to intimal hyperplasia, fibrosis and sclerotic changes, and therefore have a significant solid mechanical influence [127]. The medial layer is responsible for the main structural and functional properties of the thoracic aorta [153, 297]. It consists of many medial lamellar units each having a thickness of about 13-15 μm, with smooth muscle cells in the lamellar unit interconnecting the elastic laminas, and interspersed collagen fibers (mostly of type I and III) [235]. The outer layer, the adventitia, consists mainly of thick bundles of wavy collagen fibers (mostly type I) in the unloaded state, and is therefore very compliant at small strains but changes to a stiff ‘jacket-like’ tube at high strains so that the artery is prevented from over-stretching and rupture [124, 127, 347]. Schriefl et al. [286] described the media and the adventitia of aged thoracic aortas as displaying two collagen fiber families organized in separate sublayers with different orientations. The media incorporates two symmetric fiber families with mean fiber angles closer to the circumferential direction, while the adventitial layer has collagen fibers oriented closer to the longitudinal direction. In the intima, however, this organization in layers is less clear with sometimes a third or a fourth family of fibers being apparent, and in general displaying a carpet-like structure [286].

Pathological changes leading to dissection and aneurysm formation in the thoracic aorta typically alter the microstructure and weaken the media. Medial degeneration (cystic medial necrosis) is a characteristic of dissections and it involves smooth muscle cell loss, elastic fiber fragmentation and accumulation of glycosaminoglycans [18, 70, 134, 371].

A weakened aortic wall due to medial degeneration is also typical for aneurysms and aneurysms combined with dissections of the ascending thoracic aorta [21]. Although similar collagen contents were observed in control and aneurysm samples [146], the organization of collagen may nevertheless be significantly changed during aneurysm development in the thoracic aorta [19]. An increased collagen content [34, 354, 355] or a decreased collagen content with increased disruption were reported for aortic dissections [19, 21]. Thus, pathological changes are often said to weaken the aortic wall, thereby increasing the likelihood of rupture.

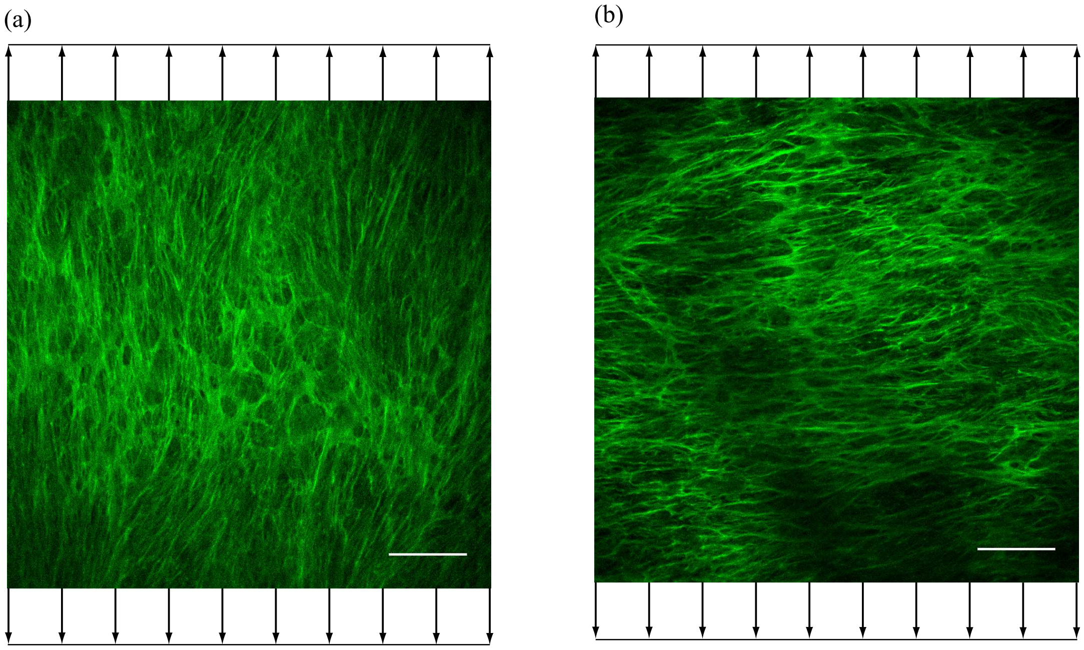

Figure 5.1 Second-harmonic generation images of two aortic medial specimens cut out from adjacent regions: (a) load applied along the main direction of fiber reinforcement for a circumferential specimen; (b) load applied orthogonal to the main direction of fiber reinforcement for a longitudinal specimen. Collagen fibers are represented in green, while the arrows indicate the direction of the load. Images were enhanced for visualization. White scale bars correspond to 100μm.

Figure 5.1 shows two aortic medial specimens with different collagen microstructures cut out from adjacent regions. As is well-known, fibrillar collagen plays an important reinforcing role in fibrous tissues and the mechanical properties of the tissues are significantly different in directions along and orthogonal to the mean collagen fiber direction. This motivated the present study of the failure properties of control and aneurysmatic human thoracic aortic medias. These were investigated using uniaxial extension tests in the circumferential and longitudinal directions. The mechanical testing was combined with second-harmonic generation imaging and histological investigations to study the influence of the collagen architecture on the mechanical failure properties.

5.2 Materials and Methods

Control samples were obtained from non-aneurysmatic human descending thoracic aortas ($n = 12$) by the Diagnostic and Research Institute of Pathology, Medical University of Graz, Austria. Aneurysmatic samples ($n = 9$) were obtained from patients undergoing ascending aortic surgical repair at the Division of Cardiac Surgery, Medical University of Graz, Austria and the Division of Cardiothoracic Surgery, University of North Carolina at Chapel Hill (UNC). The use of the donor samples was approved by the local Ethics Committee at the Medical University of Graz (27-250 ex 14/15) and the University of North Carolina at Chapel Hill Institutional Review Board (Study no. 14-2529). For the aneurysmatic samples, informed consents were obtained prior to sample collection. Upon explantation, donor samples obtained from the Medical University of Graz were placed in phosphate buffered saline (PBS) prior to freezing, whereas donor samples from UNC were placed into a tube containing Ringer's lactate with 10% dimethyl sulfoxide (DMSO) to preserve mechanical properties during transportation. This tube was placed in another container filled with isopropanol solution which was surrounded by dry ice to ensure slow freezing. Samples were placed in a freezer at -24°C upon arrival and kept therein until testing for varying time periods (minimum = 8, maximum = 154 days).

5.2.1 Mechanical Testing

Following unfreezing overnight at 4°C, each donor sample was cut open along its longitudinal axis, and separated into intimal, medial and adventitial layers using scalpel and scissors; Figs 5.2(a) and (b). Dog-bone shaped specimens were then punched out from the circumferential and longitudinal directions of each sample using a template; see Fig. 5.2(c). After the initial thickness T was measured optically using the system described in [126], for each specimen black markers were placed approximately 5 mm apart on the gage region for video tracking, and the specimen was mounted on the apparatus. The initial length L and width W values were then measured using the videoextensometer described in [309]. Each specimen was preconditioned to 50 kPa (engineering stress) in five loading-unloading cycles. Subsequently, control and aneurysmatic specimens in the circumferential and longitudinal directions were extended until failure quasi-statically with a cross-head speed of 2 mm/min. The testing protocol was similar to that used in [305, 306, 308] and took place in a PBS filled container heated up to and maintained at 37°C. Tests were regarded as unsuccessful if failure occurred outside the markers, and the results for these cases were discarded; see Figs 5.2(d) and (e) for a successful and an unsuccessful test, respectively. After a successful test, the specimen was fixed in 4% formaldehyde in preparation for microstructural investigations.

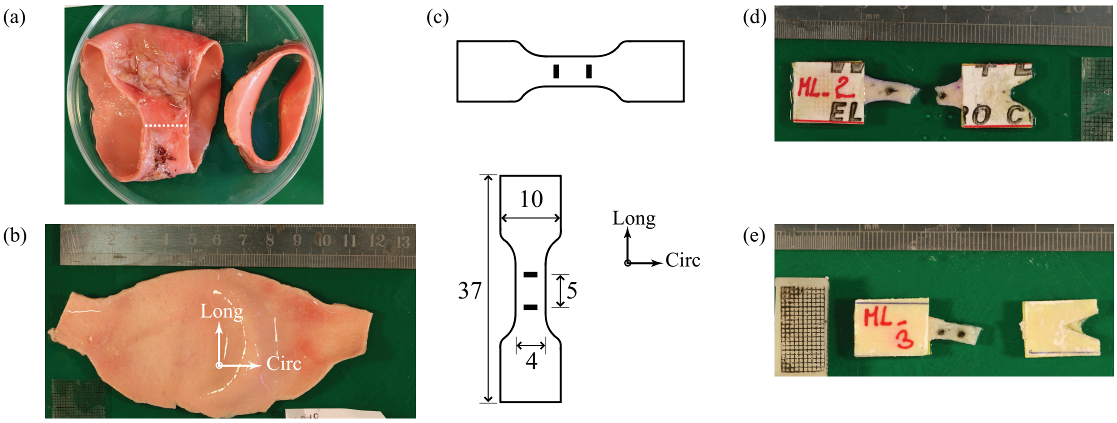

Figure 5.2 Sample preparation, template and examples of rupture in uniaxial tests: (a) donor sample ready to be cut open along its longitudinal axis indicated by the dotted white line; (b) media of the sample after cutting open and separation of the layers; (c) schematic of dog-bone shaped template in the circumferential and longitudinal directions with black markers placed approximately 5 mm apart for video tracking; (d) and (e) examples of a successful and an unsuccessful test, respectively. The included millimeter scale provides a dimensional reference.

The uniaxial Cauchy stress σ and the related stretch λ were calculated for each specimen using the force–displacement data from the formulas $\sigma = \lambda F/A$, where F is the measured force, $A = TW$ the initial cross-sectional area, while $\lambda = 1 + d/L$, where d is the measured displacement and L is the initial length. The failure stress σ_f was defined to be the value of the Cauchy stress at the maximum force. The corresponding stretch at failure is denoted by λ_f.

5.2.2 Microstructural Investigations

Half of the successful test specimens were optically cleared for subsequent second-harmonic generation (SHG) imaging in graded ethanol series and a solution of benzyl alcohol to benzyl benzoate (BABB), as described in [287]. The imaging set-up was the same as in [287] except that the in-plane image stacks in the circumferential–longitudinal plane CL (θz) were acquired using $620 \times 620 \times 5\,\mu$m sampling instead of $620 \times 620 \times 1\,\mu$m. The out-of-plane images were acquired from the radial–circumferential plane RC ($r\theta$) and radial–longitudinal plane RL (rz) orthogonal to the RC plane. Note that the word ‘fiber’ in mean fiber angle and in fiber dispersion refers to ‘collagen fiber’.

Following the SHG imaging, image stacks of the CL plane were used to obtain the mean fiber angle α, measured with respect to the circumferential direction. Note that the mean fiber angle from the specimen loading axis corresponds to α and $90° - \alpha$ for the circumferential and longitudinal test specimens, respectively. The fiber dispersion parameter κ_{ip} in the (θz) plane is given by the formula

$$\kappa_{\mathrm{ip}} = \frac{1}{2} - \frac{I_1(a)}{2I_0(a)}, \tag{5.1}$$

where I_0 and I_1 are the modified Bessel functions of the first kind of order 0 and 1, respectively, while a is a concentration parameter from the von Mises distribution [130] obtained using maximum likelihood estimation. The corresponding out-of-plane fiber dispersion parameters $\kappa_{\mathrm{op}}^{r\theta}$ and $\kappa_{\mathrm{op}}^{rz}$ were calculated according to

$$\kappa_{\mathrm{op}} = \frac{1}{2} - \frac{1}{8b} + \frac{1}{4}\sqrt{\frac{2}{\pi b}}\frac{\exp(-2b)}{\operatorname{erf}(\sqrt{2b})}, \tag{5.2}$$

which is again based on the von Mises distribution, erf being the error function defined by [130]

$$\operatorname{erf}(x) = \frac{2}{\sqrt{\pi}}\int_0^x \exp(-\xi^2)\mathrm{d}\xi. \tag{5.3}$$

Images from the RC and RL planes were used to obtain the concentration parameter b via least-square fitting. This distribution function is evaluated with a different concentration parameter b for the two planes $r\theta$ and rz. Note that $\kappa_{\mathrm{op}}^{r\theta}$ and $\kappa_{\mathrm{op}}^{rz}$ relate to the $(r\theta)$ and (rz) planes. An indication of the four structural parameters α, κ_{ip}, $\kappa_{\mathrm{op}}^{rz}$ and $\kappa_{\mathrm{op}}^{r\theta}$ relative to the coordinate system r, θ, z can be found in Fig. 5.3.

The other half of the specimens were used to obtain whole slide histological images. The

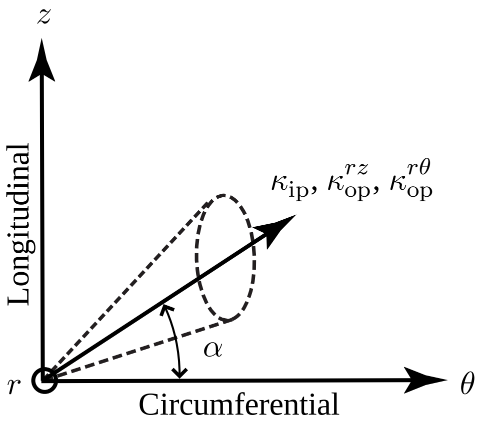

Figure 5.3 Illustration of four structural parameters α, κ_{ip}, $\kappa_{\mathrm{op}}^{rz}$ and $\kappa_{\mathrm{op}}^{r\theta}$ with respect to the coordinate axes, r (radial), θ (circumferential) and z (longitudinal). The mean fiber direction is denoted by the solid line with the arrow located in the (θz) plane, and making an angle α with the circumferential direction.

clamped ends of the specimens were marked with a dye prior to paraffin embedding to distinguish the rupture zone (area near the ruptured end) for qualitative evaluations. Following the paraffin embedding, Hematoxylin and Eosin (H&E) staining was performed together with Elastica van Gieson (EvG) on adjacent sections for the identification of collagen, elastic fibers (with all their proteins, not only elastin [6], p. 1065; for an instructive illustration see Fig. 1 in [371]) and smooth muscle cell (SMC) nuclei. Whole histological slides were scanned using a 3DHISTECH P1000 slide scanner (3DHISTECH Ltd., Budapest, Hungary), and the whole slide images were subsequently evaluated using the software CaseViewer (v2.1; 3DHISTECH Ltd., Budapest, Hungary). In particular, the specimens from the successful tests were quantified for collagen, elastic fibers and SMC content (total content 100%), without taking the ground substance into account. Content evaluations were performed independently by two experienced pathologists in a semiquantitative manner. In addition, the thickness of the media was evaluated as a percentage of the specimen thickness.

5.2.3 Statistics

The one-way analysis of variance (ANOVA) followed by Tukey's test was employed for statistical analysis. More specifically, the structural parameters α, κ_{ip}, $\kappa_{\mathrm{op}}^{r\theta}$, $\kappa_{\mathrm{op}}^{rz}$, as well as collagen, elastic fiber and SMC content percentages were compared between the control and the aneurysmatic groups of specimens. In addition, the mechanical failure parameters σ_{f}, λ_{f}, the structural parameters, and the content percentages were compared between the four groups (Control-C/Control-L and Aneurysmatic-C/Aneurysmatic-L). The groups were significantly different if $p < 0.05$. Mean (± standard deviation), median, first and third quartile values (Q1,Q3) of the aforementioned groups were computed. Linear regression was performed to see if there was any correlation between failure stress and failure stretch, and failure stress/failure stretch and aneurysm diameter. Only the specimens for which the media constituted at least 75% of the total thickness were included in the statistics, because the main focus of the present study is a comparison of medial mechanics and structure.

5.3 Results

Table 5.1 depicts the anamnesis of all donors labeled by $\mathrm{C_I}$–$\mathrm{C_{XII}}$ for control and $\mathrm{A_I}$–$\mathrm{A_{IX}}$ for aneurysmatic specimens. In total 27 uniaxial tests (Control-C, $n = 7$; Control-L, $n = 10$; Aneurysmatic-C, $n = 4$; Aneurysmatic-L, $n = 6$) from 21 thoracic aortas (Control $n = 12$, Aneurysmatic $n = 9$) were included. Table 5.2 contains a summary of the following values: the failure stress σ_{f} and the failure stretch λ_{f}; the structural parameters α, κ_{ip}, $\kappa_{\mathrm{op}}^{r\theta}$, $\kappa_{\mathrm{op}}^{rz}$; the collagen, elastic fiber and SMC content percentages; the thickness of the media after layer separation as a percentage of the whole specimen thickness; and the identification of the layers which remain attached after the separation.

Table 5.1 Anamnesis of donors for control ($\mathrm{C_I}$–$\mathrm{C_{XII}}$) and aneurysmatic ($\mathrm{A_I}$–$\mathrm{A_{IX}}$) specimens including the cause of death (COD) for the control, risk factors, age and gender. Samples were provided by the Medical University of Graz (MUG) and the University of North Carolina at Chapel Hill (UNC).

Donor	Hospital	COD	Risk Factors	Age	Gender
$\mathrm{C_I}$	MUG	Myocardial infarction	–	59	m
$\mathrm{C_{II}}$	MUG	Tumor progression	–	56	f
$\mathrm{C_{III}}$	MUG	Myocardial infarction	D, HL, HT, SM	68	m
$\mathrm{C_{IV}}$	MUG	Metastasis	–	59	f
$\mathrm{C_V}$	MUG	Multiorgan failure, sepsis	–	52	f
$\mathrm{C_{VI}}$	MUG	Tumor progression	D, HT	83	m
$\mathrm{C_{VII}}$	MUG	Tumor progression	–	69	f
$\mathrm{C_{VIII}}$	MUG	Cardiogenic shock	–	65	f
$\mathrm{C_{IX}}$	MUG	Epileptic shock	–	19	m
$\mathrm{C_X}$	MUG	Tumor progression	HT	65	f
$\mathrm{C_{XI}}$	MUG	High brain pressure	HT	68	f
$\mathrm{C_{XII}}$	MUG	Aspiration	–	52	m
$\mathrm{A_I}$	MUG	–	D, HL, HT, SM, KI	66	m
$\mathrm{A_{II}}$	UNC	–	UAV, GERD, AI, AS	51	m
$\mathrm{A_{III}}$	UNC	–	UAV, AI, AS, HL, LVH	56	m
$\mathrm{A_{IV}}$	UNC	–	HT	68	m
$\mathrm{A_V}$	UNC	–	AS, AI, BAV, GERD, O	45	m
$\mathrm{A_{VI}}$	UNC	–	HT	63	m
$\mathrm{A_{VII}}$	UNC	–	GERD, O	71	f
$\mathrm{A_{VIII}}$	UNC	–	ED, HT, SM	46	f
$\mathrm{A_{IX}}$	UNC	–	AI, AR, HFrEF	44	m

AI, aortic insufficiency; AR, aortic regurgitation; AS, aortic stenosis; BAV, biscuspid aortic valve; D, diabetes; ED, Ehlers-Danlos syndrome; GERD, gastroesophageal reflux disease; HFrEF, heart failure with reduced ejection fraction; HL, hyperlipidemia; HT, hypertension; KI, kidney insufficiency; LVH, left ventricular hypertrophy; O, obesity; SM, smoking; UAV, unicuspid aortic valve.

5.3.1 Mechanical Testing

Table 5.3 provides a summary for the mean, median and (Q1,Q3) values of the mechanical and structural data, and the collagen, elastic fibers and SMC content percentages of the four groups from Table 5.2 with exclusion of the specimens: circumferential $\mathrm{C_{III}}$, circumferential and longitudinal $\mathrm{C_X}$ and circumferential $\mathrm{A_I}$.

With reference to Table 5.3 the Control-C group showed the highest mean failure stress σ_f (1474 ± 1131 kPa), followed by Aneurysmatic-C (1446 ± 875 kPa), Aneurysmatic-L (735 ± 227 kPa) and Control-L (579 ± 172 kPa). The groups were not significantly

Table 5.2 Overview of the failure properties, the structural parameters, the content percentages for collagen, elastic fibers and SMC, the thickness of the media, and the visible layers for each specimen identified.

Donor	C/L	σ_f [kPa]	λ_f [-]	α [°]	κ_ip [-]	$\kappa_\mathrm{op}^{r\theta}$ [-]	κ_op^{rz} [-]	Collagen [%]	Elastic fibers [%]	SMC [%]	Thickness of media [%]	Visible layers
C_III	C	1200	1.39	43	0.20	0.49	0.47	30	30	40	65	IM
C_IV	C	3418	3.20	7	0.20	0.49	0.49	30	30	40	80	MA
C_V	C	1502	2.03	17	0.32	0.49	0.45	30	30	40	87	IM
C_VII	C	848	1.42	12	0.24	0.48	0.49	25	40	35	100	M
C_VIII	C	655	1.30	33	0.23	0.48	0.49	30	40	30	76	IM
C_IX	C	948	2.97	24	0.29	0.41	0.49	25	45	30	100	M
C_X	C	1541	1.59	20	0.22	0.48	0.48	30	30	40	71	IM
C_I	L	222	1.77	11	0.20	0.48	0.46	20	30	50	100	M
C_II	L	679	2.41	11	0.21	0.48	0.48	25	40	35	100	M
C_III	L	776	1.23	15	0.18	0.49	0.49	20	30	50	76	IM
C_IV	L	750	2.14	9	0.25	0.48	0.49	30	40	30	100	M
C_VI	L	413	1.26	20	0.28	0.49	0.49	30	25	45	84	IM
C_VII	L	566	1.62	6	0.21	0.49	0.50	40	50	10	100	M
C_IX	L	610	2.47	7	0.25	0.49	0.48	30	50	20	100	M
C_X	L	700	1.41	51	0.22	0.49	0.49	20	50	30	62	IM
C_XI	L	564	2.16	25	0.19	0.48	0.49	20	30	50	100	M
C_XII	L	633	2.02	8	0.23	0.47	0.48	30	40	30	84	MA
A_I	C	297	1.17	48	0.28	0.45	0.47	70	20	10	46	IM
A_II	C	2300	1.65	10	0.19	0.48	0.47	25	35	40	100	M
A_III	C	1487	1.51	31	0.29	0.47	0.46	25	35	40	100	M
A_IX	C	552	1.61	22	0.26	0.46	0.40	50	30	20	84	IM
A_II	L	636	1.81	13	0.17	0.48	0.46	20	30	50	100	M
A_IV	L	572	1.83	20	0.26	0.46	0.44	35	35	30	85	MA
A_V	L	988	1.95	34	0.35	0.47	0.44	30	30	40	80	MA
A_VI	L	501	2.19	24	0.24	0.47	0.47	30	30	40	100	M
A_VII	L	666	1.74	31	0.18	0.47	0.46	30	40	30	86	MA
A_VIII	L	1046	2.26	14	0.22	0.47	0.46	20	30	50	100	M

C/L, testing direction (circumferential or longitudinal); σ_f, failure stress; λ_f, failure stretch; α, mean fiber angle measured from the circumferential direction; κ_ip, fiber dispersion in the θz plane; $\kappa_\mathrm{op}^{r\theta}$, fiber dispersion in the $r\theta$ plane; κ_op^{rz}, fiber dispersion in the rz plane; SMC, smooth muscle cells; M, media; IM, intima–media; MA, media–adventitia.

different. From Table 5.2 it can be seen that the highest failure stress value is for the circumferential specimen C_IV (3418 kPa), whereas the lowest value was observed for the longitudinal specimen C_I (222 kPa).

Control-C showed the highest mean failure stretch λ_f (2.18 ± 0.87) followed by Control-

Table 5.3 Mean, median and (Q1,Q3) of the failure properties σ_f, λ_f, structural parameters α, κ_ip, $\kappa_\mathrm{op}^{r\theta}$, κ_op^{rz} and collagen, elastic fibers and SMC content percentages of the four groups. The following specimens were excluded from the statistical analysis: circumferential $\mathrm{C_{III}}$, circumferential and longitudinal $\mathrm{C_X}$ and circumferential $\mathrm{A_I}$.

		σ_f [kPa]	λ_f [-]	α [°]	κ_ip [-]	$\kappa_\mathrm{op}^{r\theta}$ [-]	κ_op^{rz} [-]	Collagen [%]	Elastic fibers [%]	SMC [%]
Control-C	Mean	1474	2.18	19	0.26	0.47	0.48	28	37	35
	SD	1131	0.87	10	0.05	0.04	0.02	3	7	5
	Q1	800	1.39	11	0.22	0.46	0.48	25	30	30
$n = 5$	Median	948	2.03	17	0.24	0.48	0.49	30	40	35
	Q3	1981	3.03	26	0.30	0.49	0.49	30	41	40
Control-L	Mean	579	1.9	13	0.22	0.48	0.48	27	37	36
	SD	172	0.46	6	0.04	0.01	0.01	7	9	14
	Q1	526	1.53	8	0.20	0.48	0.48	20	30	28
$n = 9$	Median	610	2.02	11	0.21	0.48	0.49	30	40	35
	Q3	697	2.22	16	0.25	0.49	0.49	30	43	50
Aneurysmatic-C	Mean	1446	1.59	21	0.25	0.47	0.44	33	33	33
	SD	875	0.07	11	0.05	0.01	0.04	14	3	12
	Q1	785	1.54	13	0.21	0.46	0.42	25	31	25
$n = 3$	Median	1487	1.61	22	0.26	0.47	0.46	25	35	40
	Q3	2097	1.64	29	0.29	0.48	0.47	44	35	40
Aneurysmatic-L	Mean	735	1.6	23	0.24	0.47	0.46	28	33	40
	SD	227	0.22	8	0.07	0.01	0.01	6	4	9
	Q1	572	1.81	14	0.18	0.47	0.44	20	30	30
$n = 6$	Median	651	1.89	22	0.23	0.47	0.46	30	30	40
	Q3	988	2.19	31	0.26	0.47	0.46	30	35	50

σ_f, failure stress; λ_f, failure stretch; α, mean fiber angle from the circumferential direction; κ_ip, fiber dispersion in the θz plane; $\kappa_\mathrm{op}^{r\theta}$, fiber dispersion in the $r\theta$ plane; κ_op^{rz}, fiber dispersion in the rz plane; SMC, smooth muscle cell; SD, standard deviation; (Q1,Q3), first and third quartiles.

L (1.9 ± 0.46), Aneurysmatic-L (1.6 ± 0.22) and Aneurysmatic-C (1.59 ± 0.07), see Table 5.3. There were no significant differences between the groups. The highest failure stretch value λ_f was observed for the circumferential specimen $\mathrm{C_{IV}}$ (3.2), whereas the lowest was observed for the circumferential specimen $\mathrm{A_I}$ (1.17), see Table 5.2.

The Cauchy stress versus stretch plots for the specimens of the four groups are depicted in Fig. 5.4, but the failure stress σ_f revealed no significant correlation with the failure stretch λ_f, as shown in Fig. 5.5. It was found that the aneurysm diameter did not correlate with either failure stress or failure stretch.

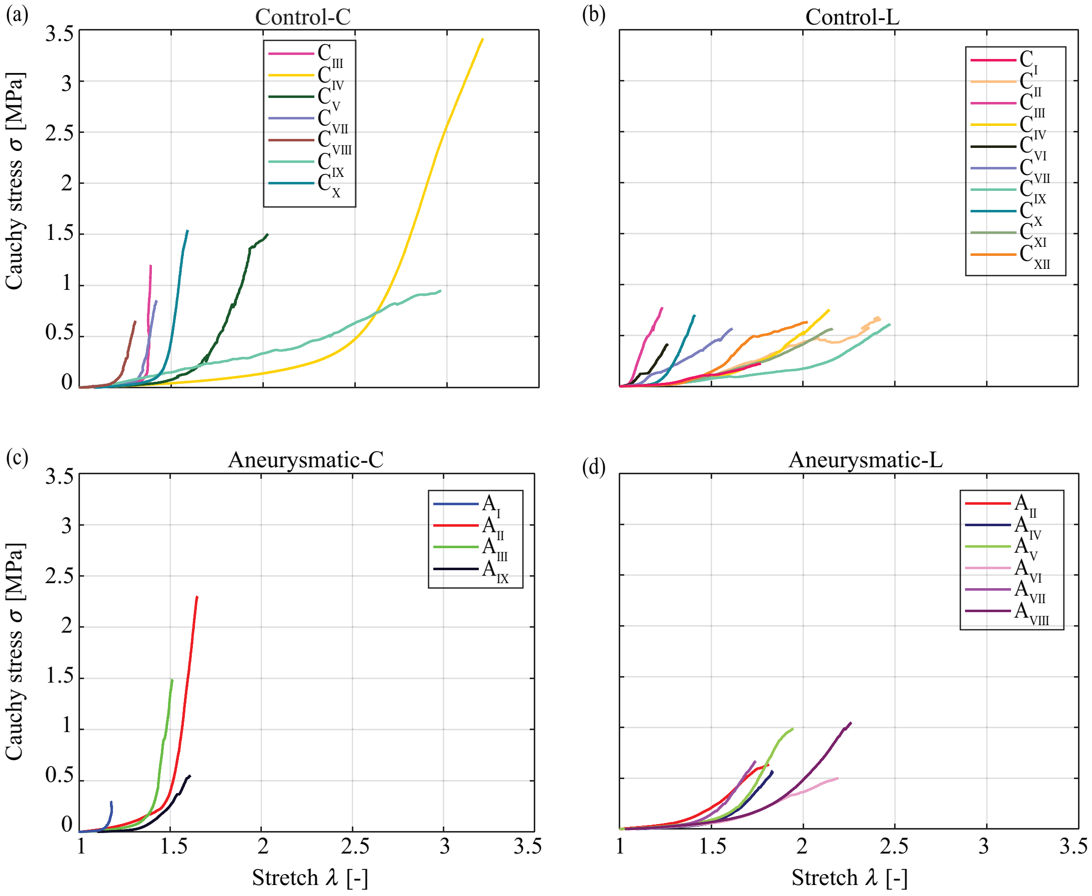

Figure 5.4 Cauchy stress σ versus stretch λ plots for all specimens in the circumferential and longitudinal directions: (a) and (b) control group; (c) and (d) aneurysmatic group.

5.3.2 Microstructural Investigations

Second-Harmonic Generation

Table 5.4 summarizes the mean, median and (Q1,Q3) values of the structural data from Table 5.2 for the control specimens and separately for the aneurysmatic specimens with more than 75% of the media present. The mean fiber direction α is closer to the circumferential direction and more aligned for the control specimens ($\alpha = 15^\circ \pm 8^\circ$, $\kappa_{\text{ip}} = 0.23 \pm 0.04$) than for the aneurysmatic specimens ($\alpha = 22^\circ \pm 9^\circ$, $\kappa_{\text{ip}} = 0.24 \pm 0.06$). The means of the two groups were significantly different for α ($p = 0.0496$) but not for κ_{ip} ($p = 0.743$). Mean values for the out-of-plane dispersions in each plane were higher for control ($\kappa_{\text{op}}^{r\theta} = 0.48 \pm 0.02$, $\kappa_{\text{op}}^{rz} = 0.48 \pm 0.01$) compared to aneurysmatic ($\kappa_{\text{op}}^{r\theta} = 0.47 \pm 0.01$, $\kappa_{\text{op}}^{rz} = 0.45 \pm 0.02$); but the difference was significant only in the rz plane ($p < 0.001$).

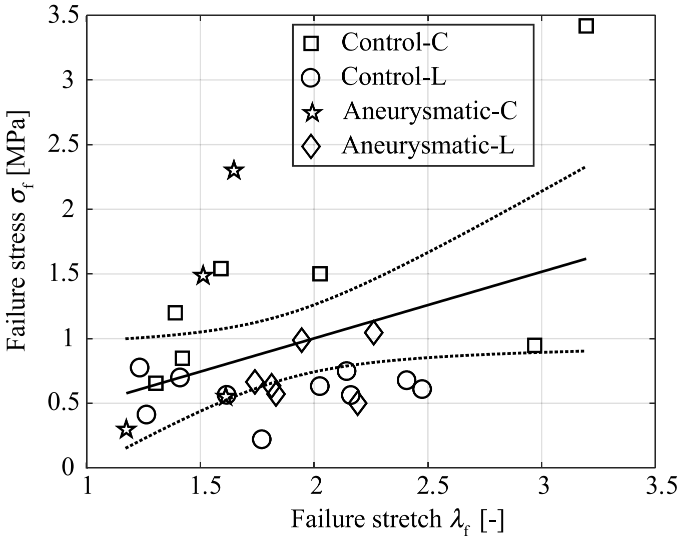

Figure 5.5 Failure stress σ_f versus failure stretch λ_f for all the specimens. The solid line corresponds to linear regression with $r^2 = 0.15$. The dotted curves correspond to the confidence bounds.

With reference to Table 5.3 there were no significant differences in α and κ_{ip} between the four groups; Control-C ($\alpha = 19° \pm 10°$; $\kappa_{ip} = 0.26 \pm 0.05$), Control-L ($\alpha = 13° \pm 6°$, $\kappa_{ip} =$

Table 5.4 Mean, median and (Q1,Q3) of the structural parameters and content percentages of collagen, elastic fibers and SMC form the Control and the Aneurysmatic groups of specimens obtained from SHG and histology. The following specimens were excluded from the statistical analysis: circumferential C_{III}, circumferential and longitudinal C_X and circumferential A_I.

		α [°]	κ_{ip} [-]	$\kappa_{op}^{r\theta}$ [-]	κ_{op}^{rz} [-]	Collagen [%]	Elastic fibers [%]	SMC [%]
Control	Mean	15	0.23	0.48	0.48	28	37	35
	SD	8	0.04	0.02	0.01	5	8	12
$n = 14$	Median	12	0.23	0.48	0.49	30	40	35
	(Q1,Q3)	(8,20)	(0.20,0.25)	(0.48,0.49)	(0.48,0.49)	(25,30)	(30,40)	(30,45)
Aneurysmatic	Mean	22	0.24	0.47	0.45	29	33	38
	SD	9	0.06	0.01	0.02	9	4	10
$n = 9$	Median	22	0.24	0.47	0.46	30	30	40
	(Q1,Q3)	(14,31)	(0.19,0.27)	(0.46,0.48)	(0.44,0.47)	(24,31)	(30,35)	(30,43)

α, mean fiber angle from the circumferential direction; κ_{ip}, fiber dispersion in the θz plane; $\kappa_{op}^{r\theta}$, fiber dispersion in the $r\theta$ plane; κ_{op}^{rz}, fiber dispersion in the rz plane; SMC, smooth muscle cells; SD, standard deviation; (Q1,Q3), first and third quartiles.

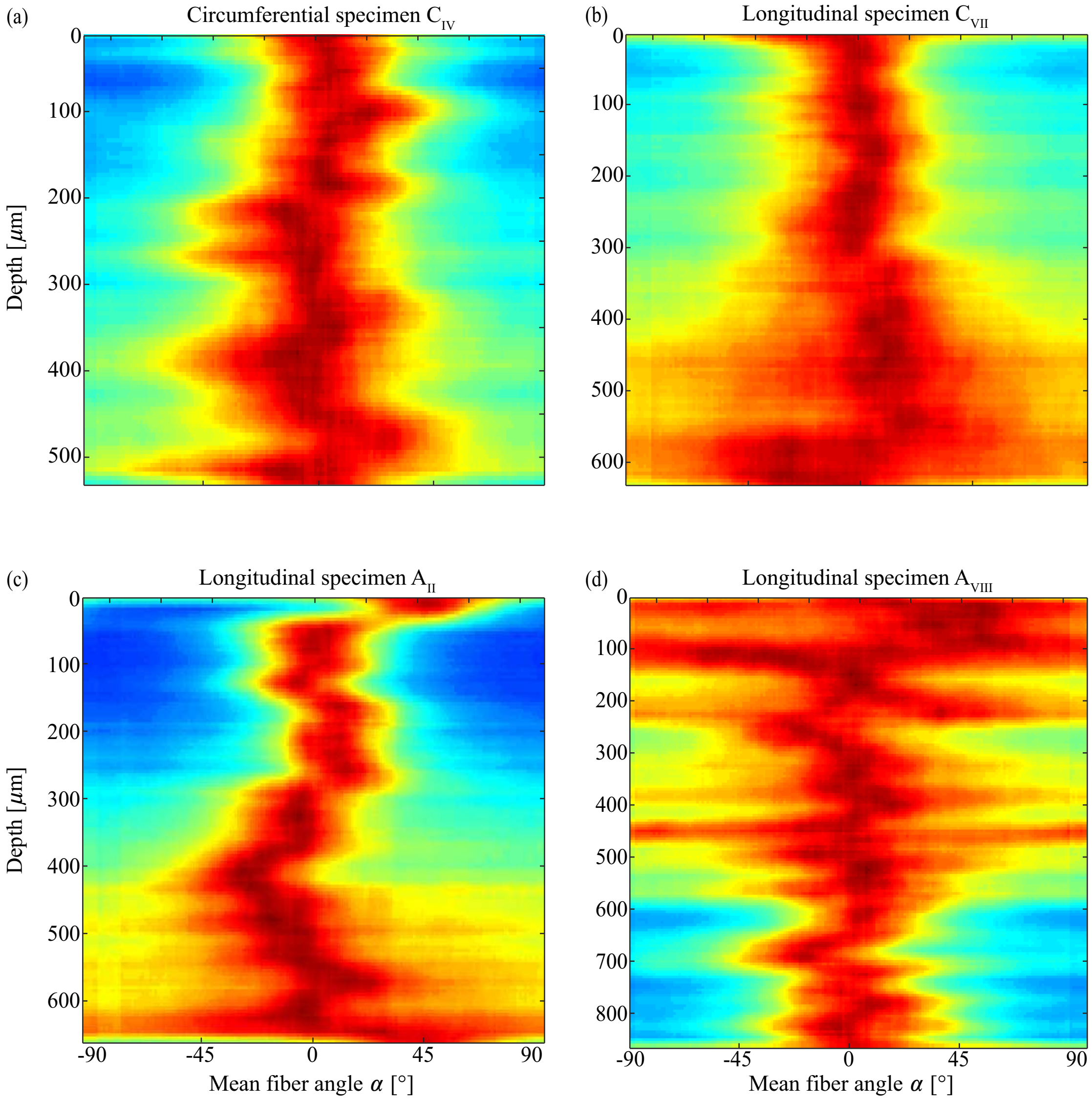

Figure 5.6 Intensity plots for four specimens: (a) circumferential C_{IV} has highly aligned fibers along ±7° relative to the circumferential direction, with a dispersion parameter of $\kappa_{ip} = 0.20$; (b) longitudinal C_{VII} has aligned fibers along ±6°, with $\kappa_{ip} = 0.21$; (c) longitudinal A_{II} has aligned fibers along ±13°, with $\kappa_{ip} = 0.17$; (d) longitudinal A_{VIII} has fibers along ±14° with less alignment ($\kappa_{ip} = 0.22$) in comparison to (c). The abscissas refer to the angle measured from the circumferential direction at the origin (0°), while (±90°) refers to the longitudinal direction. The red color identifies angles at which there are fibers with that orientation, while the blue color indicates the absence of fibers.

0.22 ± 0.04), Aneurysmatic-C ($\alpha = 21° \pm 11°$, $\kappa_{\text{ip}} = 0.25 \pm 0.05$), Aneurysmatic-L ($\alpha = 23° \pm 8°$, $\kappa_{\text{ip}} = 0.24 \pm 0.07$). The fiber dispersion $\kappa_{\text{op}}^{r\theta}$ in the $r\theta$ plane was not significantly different between Control-C (0.47 ± 0.04), Control-L (0.48 ± 0.01), Aneurysmatic-L (0.47 ± 0.01) and Aneurysmatic-C (0.47 ± 0.01). However, κ_{op}^{rz} in the rz plane was significantly lower in Aneurysmatic-C (0.44 ± 0.04) compared to Control-C (0.48 ± 0.02, $p = 0.0456$) and Control-L (0.48 ± 0.01, $p = 0.02$). The mean fiber angle from the loading direction was significantly higher ($p < 0.001$) in the Control-L ($77° \pm 6°$) and the Aneurysmatic-L groups ($67° \pm 8°$) than for Control-C ($19° \pm 10°$) and Aneurysmatic-C ($21° \pm 11°$). The general trend, namely highest in Control-L, followed by Aneurysmatic-L, Aneurysmatic-C and Control-C, was the reverse of that for σ_{f}.

With reference to Table 5.2, the circumferential specimen C_{IV} and the longitudinal specimen C_{VII} showed the lowest (7°) and highest (84°) angle relative to the loading direction, with similar κ_{ip} of 0.20 and 0.21, respectively. The intensity plots in Figs 5.6(a) and (b) depict the fiber architecture of these specimens. The abscissa corresponds to the angle measured from the circumferential direction at the origin (0°), while ±90° refer to the longitudinal direction. The red color identifies fiber angles at which there are fibers with that orientation, while the blue color indicates the absence of fibers. The slightly higher value of κ_{ip} for the specimen C_{VII} is evident from Fig. 5.6(b). Figures 5.6(c) and (d) show the in-plane fiber distributions κ_{ip} of the longitudinal specimens A_{II} (77°, $\kappa_{\text{ip}} = 0.17$), and A_{VIII} (76°, $\kappa_{\text{ip}} = 0.22$), respectively.

Histology

In regard to Table 5.4 the mean content percentages of collagen, elastic fibers and SMC were not significantly different between Control (28 ± 5%, 37 ± 8% and 35 ± 12%, respectively) and Aneurysmatic (29 ± 9%, 33 ± 4% and 38 ± 10%, respectively). The whole image slides of the specimens did not show significant cystic medial degeneration for aneurysmatic specimens, or freezing artifacts, in general. From Table 5.3 it can be seen that the mean collagen content was highest in Aneurysmatic-C (33 ± 14%), followed by Control-C (28 ± 3%), Aneurysmatic-L (28 ± 6%) and Control-L (27 ± 7%). The mean elastic fiber content was similar in Control-L (37 ± 9%) and Control-C (37 ± 7%), followed by Aneurysmatic-C (33 ± 3%) and Aneurysmatic-L (33 ± 4%). The mean SMC content was highest in Aneurysmatic-L (40 ± 9%) followed by Control-L (36 ± 14%), Control-C (35 ± 5%), and Aneurysmatic-C (33 ± 12%). The means of the groups were not significantly different for collagen, elastic fiber or SMC contents.

Figures 5.7(a) and (b) show the lamellar organization of the media with a disruption (C_{I}) and with a packed rupture zone (C_{II}), while Fig. 5.7(c) shows that layer separation was not complete for that particular circumferential specimen (C_{VIII}), see also Table 5.2 (last column). In regard to Fig. 5.7 the related colors for collagen, elastic fibers and nuclei are pale pink, black/brown and orange, respectively, while the nuclei can only be seen

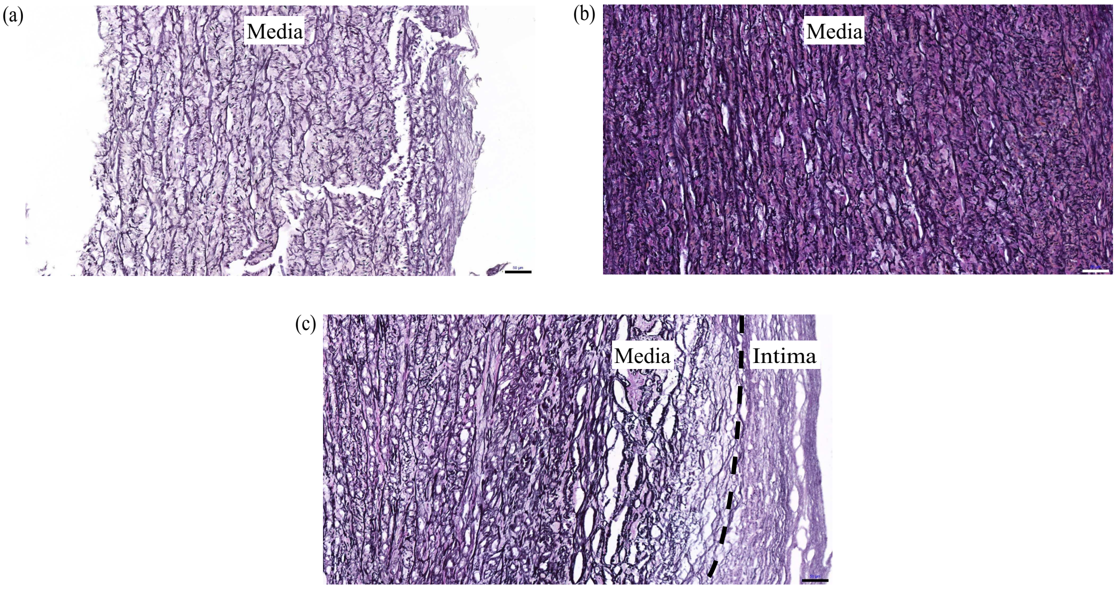

Figure 5.7 Representative histological images: (a) longitudinal specimen C_{I} consisting only of the media; (b) longitudinal specimen C_{II} consisting only of the media; (c) circumferential specimen $\mathrm{C}_{\mathrm{VIII}}$ indicating presence of the intima. Black and white scale bars correspond to $50\,\mu$m.

with a higher magnification. Most specimens showed short or long delamination zones near the ruptured region in addition to ruptured collagen and elastic fibers at the rupture ends, see Fig. 5.8.

5.3.3 Uniaxial Failure Properties and Microstructure

Figure 5.9(a) and (b) depict the failure stress σ_{f} and the failure stretch λ_{f} values in relation to the mean fiber angle relative to the loading direction. While the failure stress exhibits a strong dependence on the mean fiber angle, the failure stretch did not show any such clear dependence. The influences of the fiber dispersion parameters and the collagen, elastic fibers and SMC content percentages on σ_{f} and λ_{f} did not show any clear trends.

5.4 Discussion

We have provided a unique set of data relating the uniaxial failure properties of aortic tissues to their microstructure, which shows that the tissue is able to carry higher loads when stretched in the mean fiber direction compared with the cross fiber direction, see Figs 5.1 and 5.9, and Table 5.2. The general trend observed for the failure stresses (Control-C > Aneurysmatic-C > Aneurysmatic-L > Control-L) was the opposite of that observed for the mean fiber angle from the loading direction (Control-L > Aneurysmatic-L > Aneurysmatic-C > Control-C). Figure 5.9(a) confirms that tissue

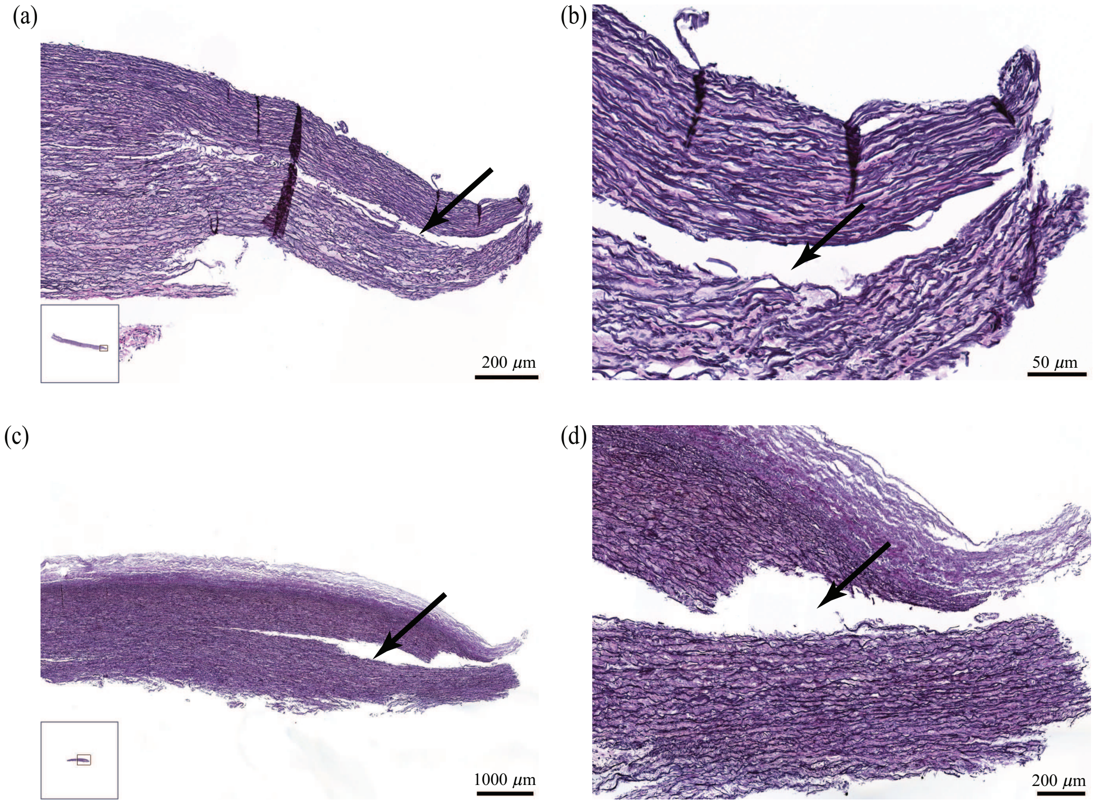

Figure 5.8 Ruptured regions with black arrows indicating delaminations: (a) circumferential specimen A_{II} with a small delamination length of approximately 1.2 mm; (b) magnification of the delamination in (a); (c) circumferential specimen C_I with a rather long delamination of approximately 5.3 mm; (d) magnification of the delamination in (c).

strips are stronger when the load is applied close to the mean fiber direction, while the failure stretch does not show any specific correlation with the mean fiber direction, see Fig. 5.9(b). Neither the failure stress nor stretch showed any clear correlation with the other structural parameters investigated herein. However, group trends indicate that in-plane fiber dispersion (Control-C > Aneurysmatic-C > Aneurysmatic-L > Control-L) and collagen content (Aneurysmatic-C > Control-C > Aneurysmatic-L > Control-L) also call for further discussion in relation to failure stresses (Control-C > Aneurysmatic-C > Aneurysmatic-L > Control-L) on the basis of specific cases.

5.4.1 Mechanics

Failure Properties

With respect to Table 5.3 the mean failure stress from uniaxial extension tests of medias from the control group are higher in the circumferential than in the longitudinal direction

(1474 versus 579 kPa). A higher mean failure stress in the circumferential than in the longitudinal direction was also found for intact healthy human thoracic aortas by Mohan & Melvin [221] (1720 versus 1470 kPa), Vorp et al. [351] (1800 versus 1710 kPa), and García-Herrera et al. [86] (2180 versus 1140 kPa), the latter being significantly different. The mean failure stress of the aneurysmatic media tested in the present study was also higher in the circumferential than in the longitudinal direction (1446 ± 875 versus 735 ± 227 kPa), but this difference was not significant. However, significantly different mean failure stresses of aneurysmatic human thoracic aortic medias in the circumferential and the longitudinal direction (1282 versus 565 kPa) were observed in a previous study by our group [308].

Several other studies also found higher failure stresses in the circumferential than in the longitudinal direction of the intact wall of human aneurysmatic thoracic aortas, i.e. 1190 versus 880 kPa in [86], 961 versus 540 kPa in [251], and 1440 versus 940 kPa in [75]. In contrast, the study [351] found almost isotropic failure properties of thoracic aortic aneurysms with similar mean failure stresses in the circumferential and longitudinal directions (1180 versus 1210 kPa). Most studies observed anisotropic failure stresses for healthy and aneurysmatic human thoracic aortic medias as well as for the intact wall, with higher stresses in the circumferential than in the longitudinal direction. The anisotropic failure stresses can be explained by the intrinsic collagen fiber assembly of the tissue, as illustrated in Fig. 5.1.

Interestingly, mean failure stretches of the thoracic aortic media were determined to be similar in the circumferential and longitudinal direction for the aneurysmatic group (1.59 versus 1.6) but different for the control group (2.18 versus 1.9). In contrast, failure stretches of the intact healthy human thoracic aortic wall were found to be smaller in the circumferential than in the longitudinal direction (1.23 versus 1.47) [221]. Failure

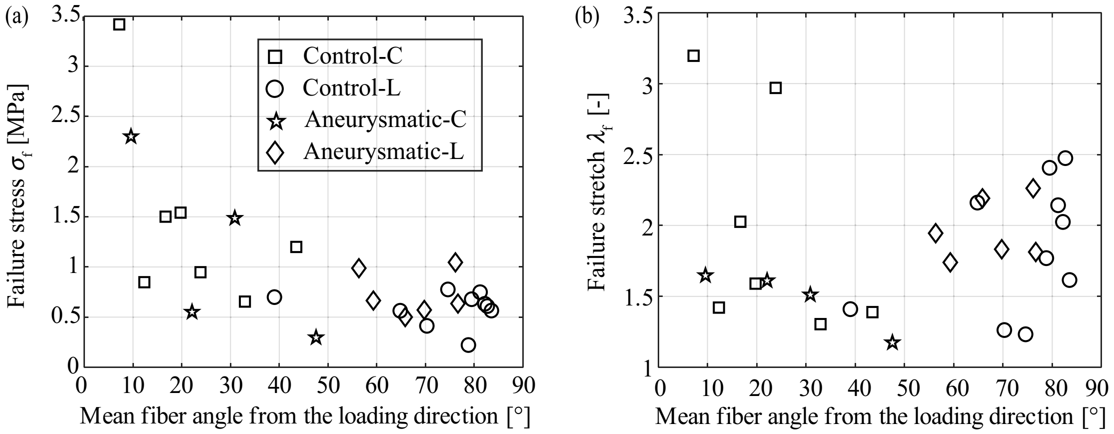

Figure 5.9 Failure properties plotted against the mean fiber angle from the loading direction: (a) failure stress σ_f; (b) failure stretch λ_f.

stretches of human aneurysmatic thoracic aortas were found to be the same in both directions (1.52 versus 1.52) for the media [308] and for the intact wall (1.34 versus 1.34) [75], but also larger in the circumferential than in the longitudinal direction (1.61 versus 1.47) [251].

Specimens investigated in this study exhibited a wide range of failure stresses and stretches, and these values were not correlated. The aneurysm diameter was not found to be correlated with failure properties. This may in part be explained by donors who may have slowly growing stable aneurysms, and the load that the specimen can withstand at different stretches can be very different, as can be seen from Fig. 5.5.

Definition of Failure

It is important to note that the definition of the failure point differs between the above mentioned studies and the present study. Hence care must be taken when interpreting a failure point. We define the failure stress as the Cauchy stress at maximum force the tissue is able to carry, and the Cauchy stress-stretch curves end at this value. After the maximum force, there was either full or partial separation, and in the latter case the specimen was still able to carry load at a decreased capacity until full separation occurred. The studies [75, 221, 251, 308, 351] defined the failure point as the point where the maximum Cauchy stress occurs prior to failure. In the present study, only two specimens showed a difference larger than 1% between these two definitions of failure, in particular 8% and 4% for circumferential C_{IX} and longitudinal $\mathrm{C}_{\mathrm{XII}}$, respectively.

On the other hand, the study [86] defined the failure point as the first point where one of the layers failed, which relates to a sudden drop in the Cauchy stress-stretch curve. In our study, we observed several of these sudden drops even at a rather low stress level but these specimens were still able to withstand much higher stresses to failure. Consequently, local failure may have already occurred at these sudden drops before the maximum force value is reached. In addition, for example, the specimens C_{IV} in Fig. 5.4(a) and A_{V} in Fig. 5.4(d) exhibit changes in the slope of the stress-stretch curve but not sharp inflections. Recent studies reported that a change in the stress-stretch slope is related to damage accumulation in collagen molecules [44, 195].

5.4.2 Microstructure

The higher values of the out-of-plane dispersion parameters $\kappa_{\mathrm{op}}^{rz}$ and $\kappa_{\mathrm{op}}^{r\theta}$ of the control group indicate that the fibers are more aligned within the lamellar units in the control group than in the aneurysmatic group, similarly to that found for abdominal aortic aneurysms [228]. The in-plane structural parameter κ_{ip} of the specimens investigated were not significantly different between the two groups, which is also in agreement with that found for human abdominal aortas [228]. Moreover, histological investigations showed that the collagen, elastic fiber and SMC content was not significantly different between the two groups (Table 5.4), and the same tendency was observed between all four groups (Table 5.3). The aforementioned similarities and differences do not necessarily indicate the absence or existence of structural changes due to aneurysm formation. They could also result from the anamnesis of the donors such as age, imperfect layer separation, imaging after testing and different sections of the aorta investigated herein. Moreover, the structure of the specimens obtained from donors who had suffered from tumors may not correspond to healthy structure, as arterial stiffening has been reported in cancer patients [7, 98, 223].

5.4.3 Uniaxial Failure Properties and Microstructure

Influence of the Fiber Angle Relative to the Loading Direction

We observed an inverse relationship between the failure stress σ_f and the mean fiber angle relative to the loading direction, as depicted in Fig. 5.9(a). Specifically, the higher the mean fiber angle from the loading direction the lower the failure stress. Further investigation is needed to clarify the possible influence of the structural parameters other than the mean fiber direction even though the failure properties did not show any clear dependencies on these parameters.

With respect to Table 5.2, the circumferential specimen C_IV showed the highest failure stress ($\sigma_\mathrm{f} = 3418\,\mathrm{kPa}$) and the lowest mean fiber angle α (7°). It is likely that this very high failure stress is not only a result of the mean fiber angle but also due to the presence of the adventitia (20% of the thickness). It is well accepted that the adventitia acts as a protective layer against tissue failure due to its high collagen content. This specimen revealed also the highest failure stretch ($\lambda_\mathrm{f} = 3.20$), which may in part be explained by the waviness of the collagen fibers in the unloaded state.

The longitudinal specimen C_I revealed the lowest failure stress ($\sigma_\mathrm{f} = 222\,\mathrm{kPa}$) and a high mean fiber angle relative to the loading direction (79°). The highest mean fiber angle relative to the loading direction (84°) was identified for the longitudinal specimen C_VII with a failure stress of $\sigma_\mathrm{f} = 566\,\mathrm{kPa}$. The higher failure stress of C_VII might be explained by the slightly more aligned out-of-plane structure indicated by the values of κ_op^{rz}, and the higher collagen and elastic fiber content since both specimens have similar κ_ip values; see Table 5.2.

Influence of Collagen and Elastic Fiber Contents

Consider now the circumferential specimens A_IX ($\sigma_\mathrm{f} = 552\,\mathrm{kPa}$, $\lambda_\mathrm{f} = 1.61$, $\alpha = 22°$, $\kappa_\mathrm{ip} = 0.26$, 50% collagen) and A_III ($\sigma_\mathrm{f} = 1487\,\mathrm{kPa}$, $\lambda_\mathrm{f} = 1.51$, $\alpha = 31°$, $\kappa_\mathrm{ip} = 0.29$, 25% collagen). These two specimens suggest that an increased collagen content correlates with lower failure stress but this is counterintuitive in the sense that it might be expected that higher collagen content would increase the strength due to the increased reinforcement. However, the presence of the intima in the circumferential specimen A_IX (16%), may have reduced the failure stress. In addition, the high percentage of the collagen and the low percentage of elastic fiber content may lead to premature failure by limiting the extensibility of the tissue [246], as in the case of the circumferential specimen $\mathrm{A_I}$ ($\sigma_\mathrm{f} = 297\,\mathrm{kPa}$, $\lambda_\mathrm{f} = 1.17$, $\alpha = 48°$, $\kappa_\mathrm{ip} = 0.28$ and 70% collagen).

Influence of Fiber Dispersion

The longitudinal specimens $\mathrm{A_{II}}$ and $\mathrm{A_{VIII}}$ show very different failure stress values σ_f, 636 and 1046 kPa, respectively, despite similar values for the mean fiber angle and $\kappa_\mathrm{op}^{r\theta}$, and the same values for κ_op^{rz} and the content percentages. Since they consist of only the media they provide a good basis for discussing the influence of the κ_ip values on the failure stress. Figures 5.6(c) and (d) depict the in-plane fiber distributions of $\mathrm{A_{II}}$ ($\alpha = 13°$, $\kappa_\mathrm{ip} = 0.17$, 100% media), and $\mathrm{A_{VIII}}$ ($\alpha = 14°$, $\kappa_\mathrm{ip} = 0.22$, 100% media), respectively. The more aligned the fibers are in a direction further away from the loading direction, in this case the longitudinal direction, the lower is the possibility of finding fibers which will be able to support the load, and hence the lower failure stress for the specimen $\mathrm{A_{II}}$.

Note that the mean fiber angle and the dispersion parameter κ_ip have a considerable influence on the failure stress, hence the dispersion parameter κ_ip should not be omitted from constitutive formulations.

Other Influences

There are some data points in Fig. 5.9(a) that have similar failure stresses but different mean fiber angles. For example, by comparing the circumferential specimen $\mathrm{C_{VIII}}$ ($\alpha = 33°$, $\kappa_\mathrm{ip} = 0.23$) to the longitudinal specimen $\mathrm{C_{XII}}$ ($\alpha = 8°$, $\kappa_\mathrm{ip} = 0.23$) and the longitudinal specimen $\mathrm{A_{VII}}$ ($\alpha = 31°$, $\kappa_\mathrm{ip} = 0.18$), one would expect that the specimen $\mathrm{C_{VIII}}$ exhibits the highest failure stress σ_f followed by $\mathrm{A_{VII}}$ and $\mathrm{C_{XII}}$, which is not the case. These specimens have similar content percentages, and hence one explanation for the lower failure stress for $\mathrm{C_{VIII}}$ being unexpected is the decreased fibrillar reinforcement due to the presence of the intimal collagen, and the presence of adventitial collagen in the other two specimens.

Although we did not investigate the influence of substructures such as collagen cross-links, their effect on the uniaxial failure properties σ_f and λ_f could be significant. The longitudinal specimen $\mathrm{C_I}$ with the lowest failure stress has very similar values of the structural parameters to those of the longitudinal specimen $\mathrm{C_{II}}$. However, the specimen $\mathrm{C_{II}}$ has a much higher failure stress ($\sigma_\mathrm{f} = 679\,\mathrm{kPa}$). As indicated in Table 5.1, donor $\mathrm{C_I}$ passed away due to myocardial infarction whereas donor $\mathrm{C_{II}}$ passed away due to tumor progression. The substructures of the aortic wall of $\mathrm{C_I}$ might be significantly different than those of $\mathrm{C_{II}}$ resulting in a decreased extensibility and a lower failure stress. Disruptions to the lamellar organization in the rupture zone of specimen $\mathrm{C_I}$ when compared to the neatly packed rupture zone of specimen C_{II}, as depicted in Fig. 5.7(a) and (b), indicate that the interlamellar connections likely play a significant role.

Although the mean fiber direction has a clear influence on the failure stress σ_f, it is not the only parameter that should be taken into account when modeling failure properties. As discussed above, the values of the dispersion parameters and the collagen and elastic fiber content seem to have a considerable influence on the failure stress. Although their combined effects are not obvious to assess and are difficult to estimate, all these parameters should be considered when attempting to model failure of soft collagenous tissues.

5.4.4 Rupture Zone

The rupture zone is characterized by ruptured collagen and elastic fibers. In some specimens delamination of the lamellas was also visible. The cracks, as illustrated in Fig. 5.8, were also observed in [110] under uniaxial tensile loading combined with X-ray microtomography, and suggest that failure initiation and propagation are complex mechanisms. Figure 5.8 shows ruptured collagen and elastic fibers at the rupture ends, as expected under loading. In addition, the delamination areas visible in Fig. 5.8(a)–(d) suggest that both interfiber collagen cross-links and interlamellar cross-links are broken.

Although the specimens are stretched along their main axes, the fibers which are not perfectly aligned with these axes may enhance the effect of shear which contributes to delamination. In the study [339] pulsatile pressure experiments were performed. The authors concluded that cracks between the lamellas indicate that shearing mechanisms are involved in the process, and the follow-up study [31] concluded that the links between the lamellas are weaker than the lamellas themselves, which leads to the cracks between them. The study [206] suggested that collagen fiber pullout from the matrix and peeling-like processes also result in broken bonds between the collagen fibers, and therefore play an important role. In addition, interfiber cross-links are possibly under higher tension than they can sustain, which also contributes to delamination [207, 208]. Based on the experimental observations in [110], the study in [25] investigated the effects of shear delamination strength on tissue failure under uniaxial loading by means of finite element analyses. The authors concluded that local wall defects may contribute directly to the initiation of dissection by reducing the shear delamination strength.

The aforementioned studies used different experimental methods, but resulted in similar histological observations to those presented here. Although we cannot identify the initial failure zone, as imaging and loading were not performed simultaneously, the delamination zones suggest that not only the collagen fiber architecture but also the different types of cross-links should be considered while attempting to model soft tissue failure under uniaxial extension loading.

5.4.5 Limitations

Due to the small sizes of the donor samples especially the aneurysmatic ones, it was not always possible to obtain circumferential and longitudinal data for each sample. Hence, we have not provided extensive details of the anisotropy. Regions with alterations such as calcification and atherosclerosis were not suitable for our investigations, thus reducing the amount of tissue available for testing. In addition, some tests failed as the rupture occurred outside the markers instead of within the gauge region. Where there was more tissue available in a sample, more specimens were prepared for testing. This also resulted in small and unmatched group sizes making it difficult to generalize the findings of the study.

The conditions from explantation to arrival were different between donor samples, and all samples were frozen until testing, as mentioned in Section 5.2. The mechanics of the biological tissues may be influenced by the duration of freezing, solution they were kept in, and the rates of freezing and thawing due to osmotic pressure imbalances and intracellular ice formation [209, 210, 376]. Solutions such as Ringer's lactate [313] and PBS [1] have been shown to help preserve the mechanical properties. Furthermore, the use of DMSO reduces the intracellular ice formation due to freezing [210], although the effect is concentration dependent [376]. It is assumed, therefore, that the influence of different solutions and duration of freezing on the mechanical properties is negligible. Regardless, cell functionality may still be damaged during thawing [210]. Aortic endothelial and smooth muscle cells, for example, are reported to significantly lose their functionality due to thawing, but no significant influences are observed for the aortic mechanics [169]. Such damage to cell functionality creates desirable effects in fact, and are discussed later.

Arteries are residually stressed in both circumferential and longitudinal directions *in vivo*, for which elastin is mainly responsible [279]. When an unloaded arterial ring is cut radially, it springs open and a longitudinal strip bends further away from the main vessel axis due to the release of stresses. As the donor samples were either received in several pieces or as a ring which was then cut open during preparation, residual stresses were partially released. Furthermore, residual stresses also depend on the contraction state of the SMCs, i.e. the basal tone [204]. However, SMC functionality is likely to be significantly impaired due to thermal injury, as discussed before, which further reduces the possible influence of residual stresses.

As the histological investigations revealed, layer separation was not complete for all specimens, and the uniaxial testing data of a particular specimen does not necessarily reflect the mechanical behavior of the media alone. Since the residual stresses are layer dependent [96], they may have an influence on the uniaxial failure properties of these specimens.

The structural similarities and differences between the control and aneurysmatic groups might arise from the different aortic segments which were available for this study, in addition to the donor anamnesis. It is assumed here that the differences in the uniaxial failure properties between the different regions and age groups are due to the microstructural differences [107]. Nevertheless, such differences may be present for various components at different length scales not investigated herein. Furthermore, the SHG images were obtained from the ruptured specimens without accounting for the fiber reorientation and recoil after failure. This might also explain some of the scatter of the data points presented in Figs 5.9(a) and (b).

The present study and the studies cited in Section 5.4.1 employed quasi-static deformation rates. However, the aorta is reported to be significantly stronger under dynamic deformation rates [221], so that the influence of the microstructure on the time-dependent failure properties needs to be further investigated. Nevertheless, the identification of failure properties under quasi-static uniaxial extension, and the influence of the microstructure on these properties constitute an important step towards the development of a more realistic failure criterion for soft biological tissues. Another limitation is the use of uniaxial extension tests instead of biaxial tests as the latter would provide a more realistic estimation of the *in vivo* stresses in the aortic wall when dilated due to aneurysm or dissection. However, to our knowledge, there are no reliable planar biaxial testing methods available for obtaining failure properties. On the other hand, bulge inflation tests were employed in several studies, and the findings also indicate the important role the microstructure plays in tissue failure [65, 188, 246].

5.5 Conclusions

The present study provides a unique set of mechanical and structural data that highlight the strong influence of the aortic media microstructure on its failure properties under uniaxial extension loading. The data presented show that not only the mean collagen fiber angle from the loading direction, but also the dispersion has a clear influence on the failure properties of the specimens subjected to uniaxial extension. Furthermore, contents of collagen and elastic fibers should also be considered – specially in the cases where they are extremely high/low. It would be of interest to investigate the influence of the microstructure on the failure properties under different loading modes, isolated and mixed. Such investigations could help predict not only when the dilated wall is likely to rupture, but also when an aorta (aneurysmatic or apparently healthy) might develop a dissection. More research is required in order to characterize the interlamellar strength under different loading modes, and the influence of the microstructure on the strength to inform the prediction of possible dissection.

In line with recent studies on aortic tissue [323] and bovine pericardium [360], the results of this work suggest that the microstructure should be taken into account when developing failure criteria. This study should be considered as a basis for further research that focuses on the predictive capabilities of the microstructural parameters for the failure properties of soft biological tissues, and it is a step towards realistic modeling of tissue failure. In addition, it might help to address clinical challenges of rupture prediction of dilated aortas with appropriate imaging techniques.

Acknowledgment The authors are indebted to Dr. Heimo Wolinski, Yeast Genetics and Molecular Biology Group, University of Graz, for his support during SHG imaging; to Augustin Donnerer, Diagnostic and Research Institute of Pathology, Medical University of Graz, for his support in collecting the control samples; to Dr. Otto Dapunt and Dr. Peter Oberwalder, Division of Cardiac Surgery, Medical University Graz, for providing the diseased sample $\mathrm{A_I}$. Furthermore, we gratefully acknowledge the financial support of the National Institutes of Health (NIH), research grant no. NIH R01HL117063. In addition, this work was partly supported by the Lead Project on 'Mechanics, Modeling and Simulation of Aortic Dissection', granted by 575 Graz University of Technology, Austria. The work of R.W.O. was, in part, funded by the UK EPSRC grant no. EP/N014642/1.

Disclosures Authors declare no conflict of interest.

REFERENCES

[1] M. Adham, J. P. Gournier, J. P. Favre, E. De La Roche, C. Ducerf, J. Baulieux, X. Barral, and M. Pouyet. Mechanical characteristics of fresh and frozen human descending thoracic aorta. *J. Surg. Res.*, 64:32–34, 1996.

[2] S. G. Advani and C. L. Tucker III. The use of tensors to describe and predict fiber orientation in short fiber composites. *J. Rheol.*, 31:751–784, 1987.

[3] A. Agianniotis, R. Rezakhaniha, and N. Stergiopulos. A structural constitutive model considering angular dispersion and waviness of collagen fibres of rabbit facial veins. *Biomed. Eng. Online*, 10:18, 2011.

[4] R. J. Akhurst. The paradoxical TGF-β vasculopathies. *Nature Genet.*, 44:838–839, 2012.

[5] V. Alastrué, M. A. Martínez, A. Menzel, and M. Doblaré. On the use of non-linear transformations for the evaluation of anisotropic rotationally symmetric directional integrals. Application to the stress analysis in fibred soft tissues. *Int. J. Numer. Meth. Engng*, 79:474–504, 2009.

[6] B. Alberts, A. Johnson, J. Lewis, D. Morgan, M. Raff, K. Roberts, and P. Walter. *Molecular Biology of the Cell*. Garland Science, New York, 6th edition, 2015.

[7] M. Alivon, J. Giroux, M. Briet, F. Goldwasser, S. Laurent, and P. Boutouyrie. Large artery stiffness and hypertension after antiangiogenic drugs: influence on cancer progression. *J. Hypertension*, 33:1310–1317, 2015.

[8] G. A. Ateshian, V. Rajan, N. O. Chahine, C. E. Canal, and C. T. Hung. Modeling the matrix of articular cartilage using a continuous fiber angular distribution predicts many observed phenomena. *J. Biomech. Eng.*, 131:61003, 2009.

[9] A. N. Azadani, S. Chitsaz, A. Mannion, A. Mookhoek, A. Wisneski, J. M. Guccione, J. M. Hope, M. D. Ge, and E. E. Tseng. Biomechanical properties of human ascending thoracic aortic aneurysms. *Ann. Thorac. Surg.*, 96:50–58, 2013.

[10] A. R. Babu, A. G. Byju, and N. Gundiah. Biomechanical properties of human ascending thoracic aortic dissections. *J. Biomech. Eng.*, 137:081013–081013–9, 2015.

[11] A. K. Baldwin, A. Simpson, R. Steer, S. A. Cain, and C. M. Kielty. Elastic fibres in health and disease. *Expert Reviews in Molecular Medicine*, 15:e8, 2013.

[12] Y. Ben-Menachem and S. Handel. *Angiography in Trauma: A Work Atlas*. WB Saunders, 1981.

[13] E. J. Benjamin, P. Muntner, A. Alonso, M. S. Bittencourt, C. W. Callaway, A. P. Carson, A. M. Chamberlain, A. R. Chang, S. Cheng, S. R. Das, F. N. Delling, L. Djousse, M. S. V. Elkind, J. F. Fergusaon, M. Fornage, L. C. Jordan, S. S. Khan, B. M. Kissela, K. L. Knutson, T. W. Kwan, T. T. Lackland, D. T. Lewis, J. H. Lichtman, C. T. Longenecker, M. S. Loop, P. L. Lutsey, S. S. Martin, K. Matsushita, A. E. Moran, M. E. Mussolino, M. O'Flaherty, A. Pandey, A. M. Perak, W. D. Rosamond, G. A. Roth, S. U. K. A., G. M. Satou, E. B. Schroeder, S. H. Shah, S. N. L., A. Stokes, D. L. Tirschwell, C. W. Tsao, M. P. Turakhia, L. B. VanWagner, J. T. Wilkins, and S. S. Wong, S. S. Virani. Heart disease and stroke statistics–2019 Update: A report from the American Heart Association. *Circulation*, 139:e56–e528, 2019.

[14] A. M. Bertoli-Avella, E. Gillis, H. Morisaki, J. M. A. Verhagen, B. M. de Graaf, G. van de Beek, E. Gallo, B. P. T. Kruithof, H. Venselaar, L. A. Myers, S. Laga, A. J. Doyle, G. Oswald, G. W. A. van Cappellen, I. Yamanaka, R. M. van der Helm, B. Beverloo, A. de Klein, L. Pardo, M. Lammens, C. Evers, K. Devriendt, M. Dumoulein, J. Timmermans, H. T. Bruggenwirth, F. Verheijen, I. Rodrigus, G. Baynam, M. Kempers, J. Saenen, E. M. Van Craenenbroeck, K. Minatoya, R. Matsukawa, T. Tsukube, N. Kubo, M. J. Hofstra, R.and Goumans, J. A. Bekkers, J. W. Roos-Hesselink, I. M. B. H. van de Laar, H. C. Dietz, L. Van Laer, T. Morisaki, M. W. Wessels, and B. L. Loeys. Mutations in a TGF-β ligand, TGFB3, cause syndromic aortic aneurysms and dissections. *J. Am. Coll. Cardiol.*, 65:1324–1336, 2015.

[15] S. Bertrand, S. Cuny, P. Petit, X. Trosseille, Y. Page, H. Guillemot, and P. Drazetic. Traumatic rupture of thoracic aorta in real-world motor vehicle crashes. *Traffic Inj. Prev.*, 9:153–161, 2008.

[16] P. Bhattacharya and M. Viceconti. Multiscale modeling methods in biomechanics. *Wiley Interdiscip. Rev. Syst. Biol. Med.*, 9:e1375, 2019.

[17] K. L. Billiar and M. S. Sacks. Biaxial mechanical properties of fresh and glutaraldehyde treated porcine aortic valve cusps – Part II: A structurally guided constitutive model. *J. Biomech.*, 122:327–335, 2000.

[18] S. Bode-Jänisch, A. Schmidt, D. Günther, M. Stuhrmann, and A. Fieguth. Aortic dissecting aneurysms – histopathological findings. *Forensic. Sci. Int.*, 214:13–17, 2012.

[19] L. F. Borges, R. G. Jaldin, R. R. Dias, N. A. Stolf, J. B. Michel, and P. S. Gutierrez. Collagen is reduced and disrupted in human aneurysms and dissections of ascending aorta. *Hum. Pathol.*, 39:437–443, 2008.

[20] L. F. Borges, Z. Touat, A. Leclercq, A. A. Zen, G. Jondeau', B. Franc, M. Philippe, O. Melihac, P. S. Gutierrez, and J. B. Michel. Tissue diffusion and retention of metalloproteinases in ascending aortic aneurysms and dissections. *Hum. Pathol.*, 40:306–313, 2009.

[21] L. F. Borges, J. P. F. Blini, R. R. Dias, and P. S. Gutierrez. Why do aortas cleave or dilate? Clues from an electronic scanning microscopy study in human ascending aortas. *J. Vasc. Res.*, 51:50–57, 2014.

[22] P. Boutouyrie, D. P. Germain, J. Fiessinger, B. Laloux, J. Perdu, and S. Laurent. Increased carotid wall stress in vascular Ehlers-Danlos syndrome. *Circulation*, 109:1530–1535, 2004.

[23] A. J. Brownstein, V. Kostiuk, B. A. Ziganshin, M. A. Zafar, H. Kuivaniemi, S. C. Body, A. E. Bale, and J. A. Elefteriades. Genes associated with thoracic aortic aneurysm and dissection: 2018 Update and clinical implications. *Aorta*, 6:13–20, 2018. doi: 10.1007/s12055-018-0659-6.

[24] A. J. Brownstein, B. A. Ziganshin, and J. A. Elefteriades. Human aortic aneurysm genomic dictionary: is it possible? *Indian J. Thorac. Cardiovasc. Surg.*, 2018. doi: 10.1055/s-0038-1639612.

[25] J. Brunet, B. Pierrat, E. Maire, J. Adrien, and P. Badel. A combined experimental-numerical lamellar-scale approach of tensile rupture in arterial medial tissue using x-ray tomography. *J. Mech. Behav. Biomed. Mater.*, 95:116–123, 2019.

[26] M. J. Buehler. Nanomechanics of collagen fibrils under varying cross-link densities: Atomistic and continuum studies. *J. Mech. Behav. Biomed. Mater.*, 1:59–67, 2008.

[27] P. H. Byers, K. A. Holbrook, B. McGillivray, P. M. MacLeod, and R. B. Lowry. Clinical and ultrastructural heterogeneity of type IV Ehlers-Danlos syndrome. *Hum. Genet.*, 47:141–150, 1979.

[28] J. S. Campa, R. M. Greenhalgh, and J. T. Powell. Elastin degradation in abdominal aortic aneurysms. *Atherosclerosis*, 65:13–21, 1987.

[29] P. B. Canham, H. M. Finlay, J. G. Dixon, D. R. Boughner, and A. Chen. Measurements from light and polarised light microscopy of human coronary arteries fixed at distending pressure. *Cardiovasc. Res.*, 23:973–982, 1989.

[30] T. E. Carew, R. N. Vaishnav, and D. J. Patel. Compressibility of the arterial wall. *Circ. Res.*, 23:61–68, 1968.

[31] M. W. Carson and M. R. Roach. The strength of the aortic media and its role in the propagation of aortic dissection. *J. Biomech.*, 23:579–588, 1990.

[32] J. A. Carvajal, A. M. Germain, J. P. Huidobro-Toro, and C. P. Weiner. Molecular mechanism of cGMP-mediated smooth muscle relaxation. *J. Cell Physiology*, 184:409–420, 2000.

[33] H. Cherifi, B. Gogly, L.-S. Loison-Robert, L. Couty, F. C. Ferré, A. Nassif, A. Lafont, and B. P. J. Fournier. Comparative study of abdominal and thoracic aortic aneurysms: Their pathogenesis and a gingival fibroblasts-based ex vivo treatment. *SpringerPlus*, 4:231, 2015.

[34] B. L. Y. Cheuk and S. W. K. Cheng. Differential expression of elastin assembly genes in patients with Stanford Type A aortic dissection using microarray analysis. *J. Vasc. Surg.*, 53:1071–1078, 2011.

[35] N. Choudhury, O. Bouchot, L. Rouleau, D. Tremblay, R. Cartier, J. Butany, R. Mongrain, and R. L. Leask. Local mechanical and structural properties of healthy and diseased human ascending aorta tissue. *Cardiovasc. Pathol.*, 18:83–91, 2009.

[36] B. Chu, E. Gaillard, R. Mongrain, S. Reiter, and J. C. Tardif. Characterization of fracture toughness exhaustion in pig aorta. *J. Mech. Behav. Biomed. Mater.*, 17: 126–136, 2013.

[37] J. Chung, K. Lachapelle, E. Wener, R. Cartier, B. De Varennes, R. Fraser, and R. L. Leask. Energy loss, a novel biomechanical parameter, correlates with aortic aneurysm size and histopathologic findings. *J. Thorac. Cardiovasc. Surg.*, 148: 1082–1089, 2014.

[38] J. Chung, K. Lachapelle, R. Cartier, R. Mongrain, and R. L. Leask. Loss of mechanical directional dependency of the ascending aorta with severe medial degeneration. *Cardiovasc. Pathol.*, 26:45–50, 2017.

[39] C. J. Chuong and Y. C. Fung. On residual stress in arteries. *J. Biomech. Eng.*, 108:189–192, 1986.

[40] F. S. Cikach, C. D. Koch, T. J. Mead, J. Galatioto, B. B. Willard, K. B. Emerton, M. J. Eagleton, E. H. Blackstone, F. Ramirez, E. E. Roselli, and S. S. Apte. Massive aggrecan and versican accumulation in thoracic aortic aneurysm and dissection. *JCI Insight*, 3:e97167, 2018.

[41] J. F. Clark and G. Pyne-Geithman. Vascular smooth muscle function: The physiology and pathology of vasoconstriction. *Pathophysiology*, 12:35–45, 2005.

[42] M. A. Coady, J. A. Rizzo, G. L. Hammond, D. Mandapati, U. Darr, G. S. Kopf, and J. A. Elefteriades. What is the appropriate size criterion for resection of thoracic aortic aneurysms? *J. Thorac. Cardiovasc. Surg.*, 113:476–491, 1997.

[43] M. J. Collins, V. Dev, B. H. Strauss, P. W. M. Fedak, and J. Butany. Variation in the histopathological features of patients with ascending aortic aneurysms: a study of 111 surgically excised cases. *J. Clin. Pathol.*, 61:519–523, 2008.

[44] M. I. Converse, R. G. Walther, J. T. Ingram, Y. Li, S. M. Yu, and K. L. Monson. Detection and characterization of molecular-level collagen damage in overstretched cerebral arteries. *Acta Biomater.*, 67:307–318, 2018.

[45] D. H. Cortes, S. P. Lake, J. A. Kadlowec, L. J. Soslowsky, and D. M. Elliot. Characterizing the mechanical contribution of fiber angular distribution in connective tissue: comparison of two modeling approaches. *Biomech. Model. Mechanobiol.*, 9:651–658, 2010.

[46] J. R. Crass, A. M. Cohen, A. O. Motta, J. F. Tomashefski Jr, and E. J. Wiesen. A proposed new mechanism of traumatic aortic rupture: the osseous pinch. *Radiology*, 176:645–649, 1990.

[47] J. D. Creasy, C. Chiles, W. D. Routh, and R. B. Dyer. Overview of traumatic injury of the thoracic aorta. *Radiographics*, 17:27–45, 1997.

[48] F. J. Criado. Aortic dissection: a 250-year perspective. *Tex. Heart Inst. J.*, 38: 694–700, 2011.

[49] R. R. Davies, L. J. Goldstein, M. A. Coady, S. L. Tittle, J. A. Rizzo, G. S. Kopf, and J. A. Elefteriades. Yearly rupture or dissection rates for thoracic aortic aneurysms: simple prediction based on size. *Ann. Thorac. Surg.*, 73:17–27, 2002.

[50] R. R. Davies, A. Gallo, M. A. Coady, G. Tellides, D. M. Botta, B. Burke, M. P. Coe, G. S. Kopf, and J. A. Elefteriades. Novel measurement of relative aortic size predicts rupture of thoracic aortic aneurysms. *Ann. Thorac. Surg.*, 81:169–177, 2006.

[51] J. De Backer. Marfan and Sartans: time to wake up! *Eur. Heart J.*, 36:2131–2133, 2015.

[52] M. de Sa, Y. Moshkovitz, J. Butany, and T. E. David. Histologic abnormalities of the ascending aorta and pulmonary trunk in patients with bicuspid aortic valve disease: Clinical relevance to the ross procedure. *J. Thorac. Cardiovasc. Surg.*, 118:588–596, 1999.

[53] S. X. Deng, J. Tomioka, J. C. Debes, and Y. C. Fung. New experiments on shear modulus of elasticity of arteries. *Am. J. Physiol. Heart Circ. Physiol.*, 266:H1–H10, 1994.

[54] R. P. Deveja, D. C. Iliopoulos, E. P. Kritharis, D. C. Angouras, D. Sfyris, S. A. Papadodima, and D. P. Sokolis. Effect of aneurysm and bicuspid aortic valve on layer-specific ascending aorta mechanics. *Ann. Thorac. Surg.*, 106:1692–1701, 2018.

[55] H. C. Dietz, G. R. Cutting, R. E. Pyeritz, C. L. Maslen, L. Y. Sakai, G. M. Corson, E. G. Puffenberger, A. Hamosh, E. J. Nanthakumar, S. M. Curristin, and et al. Marfan syndrome caused by a recurrent de novo missense mutation in the fibrillin gene. *Nature*, 352:337–339, 1991.

[56] K. P. Dingemans, P. Teeling, J. H. Lagendijk, and A. E. Becker. Extracellular matrix of the human aortic media: An ultrastructural histochemical and immunohistochemical study of the adult aortic media. *Anat. Rec.*, 258:1–14, 2000.

[57] P. B. Dobrin and A. A. Rovick. Influence of vascular smooth muscle on contractile mechanics and elasticity of arteries. *Am. J. Physiol.*, 217:1644–1651, 1969.

[58] S. Dokos, B. H. Smaill, A. A. Young, and I. J. LeGrice. Shear properties of passive ventricular myocardium. *Am. J. Physiol.*, 283:H2650–H2659, 2002.

[59] G. R. Douglas, A. J. Brown, J. H. Gillard, M. R. Bennett, M. P. F. Sutcliffe, and Z. Teng. Impact of fiber structure on the material stability and rupture mechanisms of coronary atherosclerotic plaques. *Ann. Biomed. Eng.*, 45:1462–1474, 2017.

[60] B. J. Doyle, T. J. Corbett, A. Callanan, M. T. Walsh, D. A. Vorp, and T. M. McGloughlin. An experimental and numerical comparison of the rupture locations of an abdominal aortic aneurysm. *J. Endovasc. Ther.*, 16:322–335, 2009.

[61] B. J. Doyle, A. J. Cloonan, M. T. Walsh, D. A. Vorp, and T. M. McGloughlin. Identification of rupture locations in patient-specific abdominal aortic aneurysms using experimental and computational techniques. *J. Biomech.*, 43:1408–1416, 2010.

[62] N. J. B. Driessen, C. V. C. Bouten, and F. P. T. Baaijens. A structural constitutive model for collagenous cardiovascular tissue incorporating the angular fiber distribution. *J. Biomech. Eng.*, 127:494–503, 2005.

[63] C. C. DuFort, M. J. Paszek, and V. M. Weaver. Balancing forces: architectural control of mechanotransduction. *Nat. Rev. Mol. Cell Bio.*, 12:308–319, 2011.

[64] A. Duprey, K. Khanafer, M. Schlicht, S. Avril, D. Williams, and R. Berguer. In vitro characterisation of physiological and maximum elastic modulus of ascending thoracic aortic aneurysms using uniaxial tensile testing. *Eur. J. Vasc. Endovasc. Surg.*, 39:700–707, 2010.

[65] A. Duprey, O. Trabelsi, M. Vola, J. P. Favre, and S. Avril. Biaxial rupture properties of ascending thoracic aortic aneurysms. *Acta Biomater.*, 42:273–285, 2016.

[66] R. Ebner, R. H. Chen, L. Shum, S. Lawler, T. F. Zioncheck, A. Lee, A. R. Lopez, and R. Derynck. Cloning of a type I TGF-β receptor and its effect on TGF-β binding to the type II receptor. *Science*, 260:1344–1348, 1993.

[67] I. El-Hamamsy and M. H. Yacoub. Cellular and molecular mechanisms of thoracic aortic aneurysms. *Nat. Rev. Cardiol.*, 6:771–786, 2009.

[68] J. A. Elefteriades. Thoracic aortic aneurysm: Reading enemy's playbook. *Yale J. Biol. Med.*, 81:175–186, 2008.

[69] J. A. Elefteriades and E. A. Farkas. Thoracic Aortic Aneurysm: Clinically Pertinent Controversies and Uncertainties. *J. Am. Coll. Cardiol.*, 55:841–857, 2010.

[70] J. Erdheim. Medionecrosis aortae idiopathica. *Virch. Arch. Pathol. Anat.*, 273: 454–479, 1929.

[71] T. S. E. Eriksson, A. J. Prassl, G. Plank, and G. A. Holzapfel. Modeling the dispersion in electro-mechanically coupled myocardium. *Int. J. Numer. Method Biomed. Eng.*, 29:1267–1284, 2013.

[72] P. W. M. Fedak, M. P. L. de Sa, S. Verma, N. Nili, P. Kazemian, J. Butany, B. H. Strauss, R. D. Weisel, and T. E. David. Vascular matrix remodeling in patients with bicuspid aortic valve malformations: implications for aortic dilatation. *J. Thorac. Cardiovasc. Surg.*, 126:797–805, 2003.

[73] S. Federico and T. C. Gasser. Nonlinear elasticity of biological tissues with statistical fibre orientation. *J. R. Soc. Interface*, 7:955–966, 2010.

[74] S. Federico and W. Herzog. Towards an analytical model of soft biological tissues. *J. Biomech.*, 41:3309–3313, 2008.

[75] A. Ferrara, S. Morganti, P. Totaro, A. Mazzola, and F. Auricchio. Human dilated ascending aorta: Mechanical characterization via uniaxial tensile tests. *J. Mech. Behav. Biomed. Mater.*, 53:257–271, 2016.

[76] A. Ferrara, P. Totaro, S. Morganti, and F. Auricchio. Effects of clinico-pathological risk factors on in-vitro mechanical properties of human dilated ascending aorta. *J. Mech. Behav. Biomed. Mater.*, 77:1–11, 2018.

[77] J. P. S. Ferreira, M. P. L. Parente, M. Jabareen, and R. M. N. Jorge. A general framework for the numerical implementation of anisotropic hyperelastic material models including non-local damage. *Biomech. Model. Mechanobiol.*, 16:1119–1140, 2017.

[78] M. L. Field, P. Sastry, A. R. Zhao, and D. Richens. Small vessel avulsion and acute aortic syndrome: A putative aetiology for initiation and propagation of blunt traumatic aortic injury at the isthmus. *Med. Hypotheses*, 68:1392–1398, 2007.

[79] C. Forsell, H. M. Björck, P. Eriksson, A. Franco-Cereceda, and T. C. Gasser. Biomechanical properties of the thoracic aneurysmal wall: Differences between bicuspid aortic valve and tricuspid aortic valve patients. *Ann. Thorac. Surg.*, 98: 65–71, 2014.

[80] T. M. Foundation. MASS Phenotype. `https://www.marfan.org/mass-phenotype`. [Online; accessed 28-January-2019].

[81] P. Fratzl, editor. *Collagen. Structure and Mechanics*. Springer, New York, 2008.

[82] P. Fratzl and R. Weinkamer. Nature's hierarchical materials. *Prog. Mater. Sci.*, 52:1263 – 1334, 2007.

[83] A. D. Freed, D. R. Einstein, and I. Vesely. Invariant formulation for dispersed transverse isotropy in aortic heart valves: An efficient means for modeling fiber splay. *Biomech. Model. Mechanobiol.*, 4:100–117, 2005.

[84] Y. C. Fung. *Biomechanics. Mechanical Properties of Living Tissues*. Springer-Verlag, New York, 2nd edition, 1993.

[85] H. F. Galley and N. R. Webster. Physiology of the endothelium. *Br. J. Anaesth.*, 93:105–113, 2004.

[86] C. M. García-Herrera, J. M. Atienza, F. J. Rojo, E. Claes, G. V. Guinea, D. J. Celentano, C. García-Montero, and R. L. Burgos. Mechanical behaviour and rupture of normal and pathological human ascending aortic wall. *Med. Biol. Eng. Comput.*, 50:559–566, 2012.

[87] V. Garg, A. N. Muth, J. F. Ransom, M. K. Schluterman, R. Barnes, I. N. King, P. D. Grossfeld, and D. Srivastava. Mutations in NOTCH1 cause aortic valve disease. *Nature*, 437:270–274, 2005.

[88] T. C. Gasser, R. W. Ogden, and G. A. Holzapfel. Hyperelastic modelling of arterial layers with distributed collagen fibre orientations. *J. R. Soc. Interface*, 3: 15–35, 2006.

[89] T. C. Gasser, S. Gallinetti, X. Xing, C. Forsell, J. Swedenborg, and J. Roy. Spatial orientation of collagen fibers in the abdominal aortic aneurysm's wall and its relation to wall mechanics. *Acta Biomater.*, 8:3091–3103, 2012.

[90] A. Gizzi, A. Pandolfi, and M. Vasta. Statistical characterization of the anisotropic strain energy in soft materials with distributed fibers. *Mech. Mat.*, 92:119–138, 2016.

[91] A. Gizzi, A. Pandolfi, and M. Vasta. A generalized statistical approach for modeling fiber-reinforced materials. *J. Engr. Math.*, 109:211–226, 2018.

[92] J. Z. Goldfinger, J. L. Halperin, M. L. Marin, A. S. Stewart, K. A. Eagle, and V. Fuster. Thoracic aortic aneurysm and dissection. *J. Am. Coll. Cardiol.*, 64: 1725–1739, 2014.

[93] J. Golledge and K. A. Eagle. Acute aortic dissection. *Lancet*, 372:55–66, 2008.

[94] D. R. Goudie, M. D'Alessandro, B. Merriman, H. Lee, I. Szeveréyi, S. Avery, B. D. O'Connor, S. F. Nelson, S. E. Coats, A. Stewart, L. Christie, G. Pichert, J. Friedel, I. Hayes, N. Burrows, S. Whittaker, S. Gerdes, A.-M.and Broesby-Olsen, M. A. Ferguson-Smith, C. Verma, D. P. Lunny, B. Reversade, and E. B. Lane. Multiple self-healing squamous epithelioma is caused by a disease-specific spectrum of mutations in TGFBR1. *Nature Genet.*, 43:365–369, 2011.

[95] R. M. Greendyke. Traumatic rupture of aorta. *J. Am. Med. Assoc.*, 195:527–530, 1966.

[96] S. E. Greenwald, J. E. Moore, Jr., A. Rachev, T. P. C. Kane, and J.-J. Meister. Experimental investigation of the distribution of residual strains in the artery wall. *J. Biomech. Eng.*, 119:438–444, 1997.

[97] N. Grootenboer, J. L. Bosch, J. M. Hendriks, and M. R. van Sambeek. Epidemiology, aetiology, risk of rupture and treatment of abdominal aortic aneurysms: does sex matter? *Eur. J. Vasc. Endovasc. Surg.*, 38:278–284, 2009.

[98] S. Grover, P. W. Lou, C. Bradbrook, K. Cheong, D. Kotasek, D. P. Leong, B. Koczwara, and J. B. Selvanayagam. Early and late changes in markers of aortic stiffness with breast cancer therapy. *Intern. Med. J.*, 45:140–147, 2015.

[99] O. Gültekin and G. A. Holzapfel. A brief review on computational modeling of rupture in soft biological tissues. Computational methods in applied sciences. In O. Oñate, D. Peric, E. de Souza Neto, and M. Chiumenti, editors, *Advances in Computational Plasticity. A Book in Honour of D. Roger J. Owen*, volume 46, pages 113–144. Springer Nature, 2018.

[100] D.-C. Guo, H. Pannu, V. Tran-Fadulu, C. L. Papke, R. K. Yu, N. Avidan, S. Bourgeois, A. L. Estrera, H. J. Safi, E. Sparks, D. Amor, L. Ades, V. McConnell, C. E. Willoughby, D. Abuelo, M. Willing, R. A. Lewis, D. H. Kim, S. Scherer, P. P.

Tung, C. Ahn, L. M. Buja, C. S. Raman, S. S. Shete, and D. M. Milewicz. Mutations in smooth muscle α-actin (ACTA2) lead to thoracic aortic aneurysms and dissection. *Nature Genet.*, 39:1488–1493, 2007.

[101] G. S. Gupta. Lectican protein family. In *Animal Lectins: Form, Function and Clinical Applications*, pages 801–823. Springer Vienna, 2012.

[102] P. G. Hagan, C. A. Nienaber, E. M. Isselbacher, D. Bruckman, D. J. Karavite, P. L. Russman, A. Evangelista, R. Fattori, T. Suzuki, J. K. Oh, A. G. Moore, J. F. Malouf, L. A. Pape, C. Gaca, U. Sechtem, S. Lenferink, H. J. Deutsch, H. Diedrichs, J. Marcos y Robles, A. Llovet, D. Gilon, S. K. Das, W. F. Armstrong, G. M. Deeb, and K. A. Eagle. The International Registry of Acute Aortic Dissection (IRAD): New Insights Into an Old Disease. *JAMA*, 283:897–903, 2000.

[103] S. S. Hans, O. Jareunpoon, M. Balasubramaniam, and G. B. Zelenock. Size and location of thrombus in intact and ruptured abdominal aortic aneurysms. *J. Vasc. Surg.*, 41:584–588, 2005.

[104] S. O. Hansson. Implant ethics. *J. Med. Ethics*, 000:1–7, 2005.

[105] J. G. Harvey and M. H. Gough. A comparison of the traumatic effects of vascular clamps. *Br. J. Surg.*, 68:267–272, 1981.

[106] K. Hashlamoun, A. Grillo, and S. Federico. Efficient evaluation of the material response of tissues reinforced by statistically oriented fibres. *Z. Angew. Math. Phys.*, 67:113, 2016.

[107] D. Haskett, G. Johnson, A. Zhou, U. Utzinger, and J. Vande Geest. Microstructural and biomechanical alterations of the human aorta as a function of age and location. *Biomech. Model. Mechanobiol.*, 9:725–736, 2010.

[108] K. Hayashi and E. Hirayama. Age-related changes of wall composition and collagen cross-linking in the rat carotid artery – in relation with arterial mechanics. *J. Mech. Behav. Biomed. Mater.*, 65:881–889, 2017.

[109] K. Hayashi and X.-Y. Li. Histo-dimensional analysis of strain distribution in the arterial wall. *Proc. of the Third Conference of Biomechanics, JSME, Tokyo*, pages 61–62, 1993.

[110] C. Helfenstein-Didier, D. Taïnoff, J. Viville, J. Adrien, É. Maire, and P. Badel. Tensile rupture of medial arterial tissue studied by X-ray micro-tomography on stained samples. *J. Mech. Behav. Biomed. Mater.*, 78:362–368, 2018.

[111] C. Helfenstein-Didier, D. Taïnoff, J. Viville, J. Adrien, É. Maire, and P. Badel. Tensile rupture of medial arterial tissue studied by X-ray micro-tomography on stained samples. *J. Mech. Behav. Biomed. Mater.*, 78:362–368, 2018.

[112] G. F. Henson and C. G. Rob. A comparative study of the effects of different arterial clamps on the vessel wall. *Br. J. Surg.*, 43:561–564, 1956.

[113] D. F. Holmes, Y. Lu, T. Starborg, and K. E. Kadler. Collagen fibril assembly and function. *Curr. Top. Dev. Biol.*, 130:107–142, 2018.

[114] G. A. Holzapfel. *Nonlinear Solid Mechanics. A Continuum Approach for Engineering*. John Wiley & Sons, Chichester, 2000.

[115] G. A. Holzapfel. *Mechanical Modeling of Biosolids*. Lecture Notes in Mechanics of Biological Tissues. Graz, 2018.

[116] G. A. Holzapfel and B. Fereidoonnezhad. Modeling of damage in soft biological tissues. In Y. Payan and J. Ohayon, editors, *Biomechanics of Living Organs. Hyperelastic Constitutive Laws for Finite Element Modeling*, pages 101–123. Academic Press, 2017.

[117] G. A. Holzapfel and R. W. Ogden. On planar biaxial tests for anisotropic nonlinearly elastic solids. a continuum mechanical framework. *Math. Mech. Solids*, 14: 474–489, 2009.

[118] G. A. Holzapfel and R. W. Ogden. Constitutive modelling of arteries. *Proc. R. Soc. Lond. A*, 466:1551–1597, 2010.

[119] G. A. Holzapfel and R. W. Ogden. On the tension–compression switch in soft fibrous solids. *Eur. J. Mech. A/Solids*, 49:561–569, 2015.

[120] G. A. Holzapfel and R. W. Ogden. On fiber dispersion models: exclusion of compressed fibers and spurious model comparisons. *J. Elasticity*, 129:49–68, 2017.

[121] G. A. Holzapfel and R. W. Ogden. Comparison of two model frameworks for fiber dispersion in the elasticity of soft biological tissues. *Eur. J. Mech. A/Solids*, 66:193–200, 2017.

[122] G. A. Holzapfel and R. W. Ogden. Biomechanical relevance of the microstructure in artery walls with a focus on passive and active components. *Am. J. Physiol. Heart Circ. Physiol.*, 315:H540–H549, 2018.

[123] G. A. Holzapfel and R. W. Ogden, editors. *Multiscale Soft Tissue Mechanics and Mechanobiology: State-of-the-Art Modeling*. Springer Nature, 2018.

[124] G. A. Holzapfel, T. C. Gasser, and R. W. Ogden. A new constitutive framework for arterial wall mechanics and a comparative study of material models. *J. Elasticity*, 61:1–48, 2000.

[125] G. A. Holzapfel, T. C. Gasser, and R. W. Ogden. Comparison of a multi-layer structural model for arterial walls with a Fung-type model, and issues of material stability. *J. Biomech. Eng.*, 126:264–275, 2004.

[126] G. A. Holzapfel, G. Sommer, and P. Regitnig. Anisotropic mechanical properties of tissue components in human atherosclerotic plaques. *J. Biomech. Eng.*, 126: 657–665, 2004.

[127] G. A. Holzapfel, G. Sommer, C. T. Gasser, and P. Regitnig. Determination of layer-specific mechanical properties of human coronary arteries with non-atherosclerotic intimal thickening, and related constitutive modeling. *Am. J. Physiol. Heart Circ. Physiol.*, 289:H2048–2058, 2005.

[128] G. A. Holzapfel, M. Stadler, and T. C. Gasser. Changes in the mechanical environment of stenotic arteries during interaction with stents: Computational assessment of parametric stent design. *J. Biomech. Eng.*, 127:166–180, 2005.

[129] G. A. Holzapfel, G. Sommer, M. Auer, P. Regitnig, and R. W. Ogden. Layer-specific 3D residual deformations of human aortas with non-atherosclerotic intimal thickening. *Ann. Biomed. Eng.*, 35:530–545, 2007.

[130] G. A. Holzapfel, J. A. Niestrawska, R. W. Ogden, A. J. Reinisch, and A. J. Schriefl. Modelling non-symmetric collagen fibre dispersion in arterial walls. *J. R. Soc. Interface*, 12:20150188, 2015.

[131] G. A. Holzapfel, R. W. Ogden, and S. Sherifova. 2019. Data from: On fibre dispersion modelling of soft biological tissues: a review. (doi:10.6084/m9.figshare.7667627).

[132] L. Horný, J. Kronek, H. Chlup, R. Žitný, J. Veselý, and M. Hulan. Orientations of collagen fibers in aortic histological section. *Bulletin of Applied Mechanics*, 6:25–29, 2010.

[133] J. D. Humphrey. Mechanisms of arterial remodeling in hypertension. *Hypertension*, 52:195–200, 2008.

[134] J. D. Humphrey. Possible mechanical roles of glycosaminoglycans in thoracic aortic dissection and associations with dysregulated transforming growth factor-β. *J. Vasc. Res.*, 50:1–10, 2013.

[135] J. D. Humphrey and G. A. Holzapfel. Mechanics, mechanobiology, and modeling of human abdominal aorta and aneurysms. *J. Biomech.*, 45:805–814, 2012.

[136] J. D. Humphrey, M. A. Schwartz, G. Tellides, and D. M. Milewicz. Role of mechanotransduction in vascular biology. *Circ. Res.*, 116:1448–1461, 2015.

[137] D. C. Iliopoulos, R. P. Deveja, E. P. Kritharis, D. Perrea, G. D. Sionis, K. Toutouzas, C. Stefanadis, and D. P. Sokolis. Regional and directional variations in the mechanical properties of ascending thoracic aortic aneurysms. *Med. Eng. Phys.*, 31:1–9, 2009.

[138] D. C. Iliopoulos, E. P. Kritharis, A. T. Giagini, S. A. Papadodima, and D. P. Sokolis. Ascending thoracic aortic aneurysms are associated with compositional remodeling and vessel stiffening but not weakening in age-matched subjects. *J. Thorac. Cardiovasc. Surg.*, 137:101–109, 2009.

[139] F. F. Immer, A. G. Bansi, A. S. Immer-Bansi, J. McDougall, K. J. Zehr, H. V. Schaff, and T. P. Carrel. Aortic dissection in pregnancy: analysis of risk factors and outcome. *Ann. Thorac. Surg.*, 76:309–314, 2003.

[140] R. V. Iozzo and L. Schaefer. Proteoglycan form and function: A comprehensive nomenclature of proteoglycans. *Matrix Biol.*, 42:11–55, 2015.

[141] E. M. Isselbacher. Thoracic and abdominal aortic aneurysms. *Circulation*, 111: 816–828, 2005.

[142] E. M. Isselbacher, C. L. L. Cardenas, and M. E. Lindsay. Hereditary influence in thoracic aortic aneurysm and dissection. *Circulation*, 133:2516–2528, 2016.

[143] J. L. Jameson, A. S. Fauci, D. L. Kasper, S. L. Hauser, D. L. Longo, and J. Loscalzo. *Harrison's Principle of Internal Medicine*. McGraw-Hill Education, 20th edition, 2018.

[144] G. R. Joldes, K. Miller, A. Wittek, and B. Doyle. A simple, effective and clinically applicable method to compute abdominal aortic aneurysm wall stress. *J. Mech. Behav. Biomed. Mater.*, 58:139–148, 2016.

[145] G. R. Joldes, K. Miller, A. Wittek, R. Forsythe, D. E. Newby, and B. J. Doyle. BioPARR: A software system for estimating the rupture potential index for abdominal aortic aneurysms. *Sci. Rep.*, 7:4641, 2017.

[146] J. A. Jones, C. Beck, J. R. Barbour, J. A. Zavadzkas, R. Mukherjee, F. G. Spinale, and J. S. Ikonomidis. Alterations in aortic cellular constituents during thoracic aortic aneurysm development: myofibroblast-mediated vascular remodeling. *Am. J. Pathol.*, 175:1746–1756, 2009.

[147] D. P. Judge and H. C. Dietz. Marfan's syndrome. *Lancet*, 366:1965–1976, 2005.

[148] K. E. Kadler, D. F. Holmes, J. A. Trotter, and J. A. Chapman. Collagen fibril formation. *Biochem. J.*, 316:1–11, 1996.

[149] K. E. Kadler, C. Baldock, J. Bella, and R. P. Boot-Handford. Collagens at a glance. *J. Cell Sci.*, 120:1955–1958, 2007.

[150] K. E. Kadler, A. Hill, and E. G. Canty-Laird. Collagen fibrillogenesis: fibronectin, integrins, and minor collagens as organizers and nucleators. *Curr. Opin. Cell Biol.*, 20:495–501, 2008.

[151] S. Kalamajski and A. Oldberg. The role of small leucine-rich proteoglycans in collagen fibrillogenesis. *Matrix Biol.*, 29:248–253, 2010.

[152] N. K. Karamanos, A. D. Theocharis, T. Neill, and R. V. Iozzo. Matrix modeling and remodeling: A biological interplay regulating tissue homeostasis and diseases. *Matrix Biol.*, 75-76:1–11, 2019.

[153] A. Karimi and D. M. Milewicz. Structure of the elastin-contractile units in the thoracic aorta and how genes that cause thoracic aortic aneurysms and dissections disrupt this structure. *Canad. J. Cardiol.*, 32:26–34, 2016.

[154] D. L. Kasper, A. S. Fauci, D. L. Longo, S. L. Hauser, J. L. Jameson, and J. Loscalzo. *Harrison's Principle of Internal Medicine*. Mcgraw-Hill Professional, 19th edition edition, 2015.

[155] V. A. Kas'yanov, B. A. Purinya, and É. É. Tseders. Determination of the shear modulus of human blood-vessel walls. *Polymer Mechanics*, 14:753–755, 1978.

[156] G. Keen. Closed injuries of the thoracic aorta. *Ann. Roy. Coll. Surg. Engl.*, 51: 137–156, 1972.

[157] K. Khanafer, A. Duprey, M. Zainal, M. Schlicht, D. Williams, and R. Berguer. Determination of the elastic modulus of ascending thoracic aortic aneurysm at different ranges of pressure using uniaxial tensile testing. *J. Thorac. Cardiovasc. Surg.*, 142:682–686, 2011.

[158] C. M. Kielty, M. J. Sherratt, and C. A. Shuttleworth. Elastic fibres. *J. Cell Sci.*, 115:2817–2828, 2002.

[159] C. M. Kielty, T. J. Wess, L. Haston, J. L. Ashworth, M. J. Sherratt, and C. A. Shuttleworth. Fibrillin–rich microfibrils: elastic biopolymers of the extracellular matrix. *J. Muscle Res. Cell Motil.*, 23:581–596, 2002.

[160] J. Kim, M. C. Staiculescu, A. J. Cocciolone, H. Yanagisawa, R. P. Mecham, and J. E. Wagenseil. Crosslinked elastic fibers are necessary for low energy loss in the ascending aorta. *J. Biomech.*, 61:199–207, 2017.

[161] J. B. Kim, K. Kim, M. E. Lindsay, T. MacGillivray, E. M. Isselbacher, R. P. Cambria, and T. M. 3rd Sundt. Risk of rupture or dissection in descending thoracic aortic aneurysm. *Circulation*, 132:1620–29, 2015.

[162] J. H. Kim, S. Avril, A. Duprey, and J. P. Favre. Experimental characterization of rupture in human aortic aneurysms using a full-field measurement technique. *Biomech. Model. Mechanobiol.*, 11:841–853, 2012.

[163] M. G. Kinsella and T. N. Wight. Modulation of sulfated proteoglycan synthesis by bovine aortic endothelial cells during migration. *J. Cell Biol.*, 102:679–687, 1986.

[164] Y. Kivity and R. Collins. Nonlinear wave propagation in viscoelastic tubes: Application to aortic rupture. *J. Biomech.*, 7:67–76, 1974.

[165] G. Koullias, R. Modak, M. Tranquilli, D. P. Korkolis, P. Barash, and J. A. Elefteriades. Mechanical deterioration underlies malignant behavior of aneurysmal human ascending aorta. *J. Thorac. Cardiovasc. Surg.*, 130:677.e1–677.e9, 2005.

[166] M. Kozuń. Delamination properties of the human thoracic arterial wall with early stage of atherosclerosis lesions. *J. Theor. Appl. Mech.*, 54:229–238, 2016.

[167] M. Kozuń, M. Kobielarz, A. Chwiłkowska, and C. Pezowicz. The impact of development of atherosclerosis on delamination resistance of the thoracic aortic wall. *J. Mech. Behav. Biomed. Mater.*, 79:292–300, 2018.

[168] E. P. Kritharis, D. C. Iliopoulos, S. A. Papadodima, and D. P. Sokolis. Effects of aneurysm on the mechanical properties and histologic structure of aortic sinuses. *Ann. Thorac. Surg.*, 98:72–79, 2014.

[169] S. E. Langerak, M. Groenink, E. E. van der Wall, C. Wassenaar, E. Vanbavel, M. C. van Baal, and J. A. E. Spaan. Impact of current cryopreservation procedures on mechanical and functional properties of human aortic homografts. *Transpl. Int.*, 14:248–255, 2001.

[170] Y. Lanir. Constitutive equations for fibrous connective tissues. *J. Biomech.*, 16: 1–12, 1983.

[171] Y. Lanir and R. Namani. Reliability of structure tensors in representing soft tissues structure. *J. Mech. Behav. Biomed. Mater.*, 46:222–228, 2015.

[172] J. Larsson, M.-J. Goumans, L. J. Sjöstrand, M. A. van Rooijen, D. Ward, P. Levéen, X. Xu, P. ten Dijke, C. L. Mummery, and S. Karlsson. Abnormal angiogenesis but intact hematopoietic potential in TGF-β type I receptor-deficient mice. *EMBO J.*, 20:1663–1673, 2001.

[173] M. Latorre and F. J. Montáns. On the tension-compression switch of the Gasser–Ogden–Holzapfel model: Analysis and a new pre-integrated proposal. *J. Mech. Behav. Biomed. Mater.*, 57:175–189, 2016.

[174] R. W. Lawton. The thermoelastic behavior of isolated aortic strips of the dog. *Circ. Res.*, 2:344–353, 1954.

[175] F. A. Lederle, S. E. Wilson, G. R. Johnson, D. B. Reinke, F. N. Littooy, C. W. Acher, D. J. Ballard, L. M. Messina, I. L. Gordon, E. P. Chute, W. C. Krupski, S. J. Busuttil, G. W. Barone, S. Sparks, L. M. Graham, J. H. Rapp, M. S. Makaroun, G. L. Moneta, R. A. Cambria, R. G. Makhoul, D. Eton, H. J. Ansel, J. A. Freischlag, D. Bandyk, and Aneurysm Detection and Management Veterans Affairs Cooperative Study Group. Immediate repair compared with surveillance of small abdominal aortic aneurysms. *N. Engl. J. Med.*, 346:1437–1444, 2002.

[176] K. Li, R. W. Ogden, and G. A. Holzapfel. Computational method for excluding fibers under compression in modeling soft fibrous solids. *Eur. J. Mech. A/Solids*, 57:178–193, 2016.

[177] K. Li, R. W. Ogden, and G. A. Holzapfel. An exponential constitutive model excluding fibers under compression: application to extension-inflation of a residually stressed carotid artery. *Math. Mech. Solids*, 23:1206–1224, 2018.

[178] K. Li, R. W. Ogden, and G. A. Holzapfel. Modeling of fibrous biological tissues with a general invariant that excludes compressed fibers. *J. Mech. Phys. Solids*, 110:38–53, 2018.

[179] K. Li, R. W. Ogden, and G. A. Holzapfel. A discrete fibre dispersion method for excluding fibres under compression in the modelling of fibrous tissues. *J. R. Soc. Interface*, 15:20170766, 2018. doi: 10.1098/rsif.2017.0766.

[180] G. Limbert. Mathematical and computational modelling of skin biophysics: a review. *Proc. R. Soc. Lond. A*, 473:20170257, 2017.

[181] C.-J. Lin, C.-Y. Lin, and N. O. Stitziel. Genetics of the extracellular matrix in aortic aneurysmal diseases. *Matrix Biol.*, 71–72:128–143, 2018.

[182] M. E. Lindsay and H. C. Dietz. Lessons on the pathogenesis of aneurysm from heritable conditions. *Nature*, 473:308–316, 2011.

[183] M. E. Lindsay, D. Schepers, N. A. Bolar, J. J. Doyle, E. Gallo, J. Fert-Bober, M. J. E. Kempers, E. K. Fishman, Y. Chen, L. Myers, D. Bjeda, G. Oswald, A. F. Elias, H. P. Levy, B.-M. Anderlid, M. H. Yang, E. M. H. F. Bongers, J. Timmermans, A. C. Braverman, N. Canham, G. R. Mortier, H. G. Brunner, P. H. Byers,

J. Van Eyk, L. Van Laer, H. C. Dietz, and B. L. Loeys. Loss-of-function mutations in TGFB2 cause a syndromic presentation of thoracic aortic aneurysm. *Nature Genet.*, 44:922–927, 2012.

[184] X. Liu, H. Wu, M. Byrne, S. Krane, and R. Jaenisch. Type III collagen is crucial for collagen I fibrillogenesis and for normal cardiovascular development. *Proc. Natl. Acad. Sci. USA*, 94:1852–1856, 1997.

[185] Z. Liu and R. A. Khalil. Evolving mechanisms of vascular smooth muscle contraction highlight key targets in vascular disease. *Biochem. Pharmacol.*, 153: 91–122, 2018.

[186] B. L. Loeys, J. Chen, E. R. Neptune, D. P. Judge, M. Podowski, T. Holm, J. Meyers, C. C. Leitch, N. Katsanis, N. Sharifi, F. L. Xu, L. A. Myers, P. J. Spevak, D. E. Cameron, J. De Backer, J. Hellemans, Y. Chen, E. C. Davis, C. L. Webb, W. Kress, P. Coucke, D. B. Rifkin, A. M. De Paepe, and H. C. Dietz. A syndrome of altered cardiovascular, craniofacial, neurocognitive and skeletal development caused by mutations in TGFBR1 or TGFBR2. *Nature Genet.*, 37:275–281, 2005.

[187] X. Lu, J. Yang, J. B. Zhao, H. Gregersen, and G. S. Kassab. Shear modulus of porcine coronary artery: contributions of media and adventitia. *Am. J. Physiol. Heart Circ. Physiol.*, 285:1966–1975, 2003.

[188] Y. Luo, A. Duprey, A. Avril, and J. Lu. Characteristics of thoracic aortic aneurysm rupture in vitro. *Acta Biomater.*, 42:286–295, 2016.

[189] N. F. MacLean, N. L. Dudek, and M. R. Roach. The role of radial elastic properties in the development of aortic dissections. *J. Vasc. Surg.*, 29:703–710, 1999.

[190] R. A. Majack and A. W. Clowes. Inhibition of vascular smooth muscle cell migration by heparin-like glycosaminoglycans. *J. Cell Physiology*, 118:253–256, 1984.

[191] A. Malashicheva, D. Kostina, A. Kostina, O. Irtyuga, I. Voronkina, L. Smagina, E. Ignatieva, N. Gavriliuk, V. Uspensky, O. Moiseeva, J. Vaage, and A. Kostareva. Phenotypic and functional changes of endothelial and smooth muscle cells in thoracic aortic aneurysms. *Int. J. Vasc. Med*, 2016. doi: 10.1155/2016/3107879.

[192] C. Manopoulos, I. Karathanasis, I. Kouerinis, D. C. Angouras, A. Lazaris, S. Tsangaris, and D. P. Sokolis. Identification of regional/layer differences in failure properties and thickness as important biomechanical factors responsible for the initiation of aortic dissections. *J. Biomech.*, 80:102–110, 2018.

[193] M. Marino. Molecular and intermolecular effects in collagen fibril mechanics: a multiscale analytical model compared with atomistic and experimental studies. *Biomech. Model. Mechanobiol.*, 15:133–154, 2016.

[194] M. Marino and G. Vairo. Influence of inter-molecular interactions on the elasto-damage mechanics of collagen fibrils: A bottom-up approach towards macroscopic tissue modeling. *J. Mech. Phys. Solids*, 73:38–54, 2014.

[195] M. Marino, M. I. Converse, K. L. Monson, and P. Wriggers. Molecular-level collagen damage explains softening and failure of arterial tissues: A quantitative interpretation of chp data with a novel elasto-damage model. *J. Mech. Behav. Biomed. Mater.*, 97:254–271, 2019.

[196] S. P. Marra, F. E. Kennedy, J. N. Kinkaid, and M. F. Fillinger. Elastic and rupture properties of porcine aortic tissue measured using inflation testing. *Cardiovasc. Eng.*, 6:123–131, 2006.

[197] C. L. Marsh and R. C. Moore. Deceleration trauma. *Am. J. Surg.*, 93:623–631, 1957.

[198] T. K. Marshall. Traumatic dissecting aneurysms. *J. Clin. Pathol.*, 11:36–39, 1958.

[199] C. Martin, W. Sun, T. Pham, and J. Elefteriades. Predictive biomechanical analysis of ascending aortic aneurysm rupture potential. *Acta Biomater.*, 9:9392–9400, 2013.

[200] C. Martin, W. Sun, and J. Elefteriades. Patient-specific finite element analysis of ascending aorta aneurysms. *Am. J. Physiol. Heart Circ. Physiol.*, 308:H1306–H1316, 2015.

[201] G. Martufi and T. C. Gasser. Review: the role of biomechanical modeling in the rupture risk assessment for abdominal aortic aneurysms. *J. Biomech. Eng.*, 135: 021010, 2013.

[202] G. Martufi, A. Satriano, R. D. Moore, D. A. Vorp, and E. S. Di Martino. Local quantification of wall thickness and intraluminal thrombus offer insight into the mechanical properties of the aneurysmal aorta. *Ann. Biomed. Eng.*, 43:1759–1771, 2015.

[203] Mathematica 11.3. Wolfram Research Inc., Champaign, IL, USA, 2018.

[204] T. Matsumoto, M. Tsuchida, and M. Sato. Change in intramural strain distribution in rat aorta due to smooth muscle contraction and relaxation. *Am. J. Physiol. Heart Circ. Physiol.*, 271:H1711–H1716, 1996.

[205] E. S. Di Martino, A. Bohra, J. P. Vande Geest, N. Y. Gupta, M. S. Makaroun, and D. A. Vorp. Biomechanical properties of ruptured versus electively repaired abdominal aortic aneurysm wall tissue. *J. Vasc. Surg.*, 43:570–576, 2006.

[206] H. W. Haslach, Jr., P. Riley, and A. Molotsky. The influence of medial substructures on rupture in bovine aortas. *Cardiovasc. Eng. Technol.*, 2:372–387, 2011.

[207] H. W. Haslach, Jr., L. N. Leahy, P. Fathi, J. M. Barrett, A. E. Heyes, T. A. Dumsha, and E. L. McMahon. Crack propagation and its shear mechanisms in the bovine descending aorta. *Cardiovasc. Eng. Technol.*, 6:501–518, 2015.

[208] H. W. Haslach, Jr., A. Siddiqui, A. Weerasooriya, R. Nguyen, J. Roshgadol, N. Monforte, and E. McMahon. Fracture mechanics of shear crack propagation and dissection in the healthy bovine descending aortic media. *Acta Biomater.*, 68:53–66, 2018.

[209] L. E. McGann, H. Yang, and M. Walterson. Manifestations of cell damage after freezing and thawing. *Cryobiology*, 25:178–185, 1988.

[210] E. Müller-Schweinitzer. Cryopreservation of vascular tissues. *Organogenesis*, 5: 97–104, 2009.

[211] S. A. O'Leary, J. J. Mulvihill, H. E. Barrett, E. G. Kavanagh, M. T. Walsh, T. McGloughlin, and B. J. Doyle. Determining the influence of calcification on the failure properties of abdominal aortic aneurysm (aaa) tissue. *J. Mech. Behav. Biomed. Mater.*, 42:154 – 167, 2015.

[212] A. Superti Furga and B. Steinmann. Impaired secretion of type III procollagen in Ehlers-Danlos syndrome type IV fibroblasts: Correction of the defect by incubation at reduced temperature and demonstration of subtle alterations in the triple-helical region of the molecule. *Biochem. Biophys. Res. Commun.*, 150: 140–147, 1988.

[213] A. Superti Furga, B. Steinmann, F. Ramirez, and P. H. Byers. Molecular defects of type III procollagen in Ehlers-Danlos syndrome type IV. *Biochem. Biophys. Res. Commun.*, 150:140–147, 1988.

[214] A. V. Melnik, H. Borja Da Rocha, and A. Goriely. On the modeling of fiber dispersion in fiber-reinforced elastic materials. *Int. J. Non-Linear Mech.*, 75: 92–106, 2015.

[215] A. V. Melnik, X. Luo, and R. W. Ogden. A generalised structure tensor model for the mixed invariant i_8. *Int. J. Non-Linear Mech.*, 107:137–148, 2018.

[216] M. Mikich. Dissection of the aorta: a new approach. *Heart*, 89:6–8, 2003.

[217] D. M. Milewicz and R. Francesco. Therapies for thoracic aortic aneurysms and acute aortic dissections. *Arterioscler. Thromb. Vasc. Biol.*, 39:126–136, 2019.

[218] D. M. Milewicz, E. S. Regalado, J. Shendure, D. A. Nickerson, and D.-C. Guo. Successes and challenges of using whole exome sequencing to identify novel genes underlying an inherited predisposition for thoracic aortic aneurysms and acute aortic dissections. *Trends Cardiovasc. Med.*, 24:53–60, 2014.

[219] D. M. Milewicz, K. M. Trybus, D.-C. Guo, H. L. Sweeney, E. Regalado, K. Kamm, and J. T. Stull. Altered smooth muscle cell force generation as a driver of thoracic aortic aneurysms and dissections. *Arterioscler. Thromb. Vasc. Biol.*, 37:26–34, 2016.

[220] K. Miller and J. Lu. On the prospect of patient-specific biomechanics without patient-specific properties of tissues. *J. Mech. Behav. Biomed. Mater.*, 27:154–166, 2013.

[221] D. Mohan and J. W. Melvin. Failure properties of passive human aortic tissue. I – uniaxial tension tests. *J. Biomech.*, 15:887–902, 1982.

[222] D. Mohan and J. W. Melvin. Failure properties of passive human aortic tissue. II – biaxial tension tests. *J. Biomech.*, 16:31–44, 1983.

[223] I. Mozos, G. Borzak, A. Caraba, and R. Mihaescu. Arterial stiffness in hematologic malignancies. *OncoTargets Ther.*, 10:1381–1388, 2017.

[224] L. D. Muiznieks and F. W. Keeley. Molecular assembly and mechanical properties of the extracellular matrix: A fibrous protein perspective. *Biochim. Biophys. Acta, Mol. Basis Dis.*, 1832:866–875, 2013.

[225] Y. Nakashima. Pathogenesis of aortic dissection: Elastic fiber abnormalities and aortic medial weakness. *Ann. Vasc. Dis.*, 3:28–36, 2010.

[226] D. P. Nathan, C. Xu, J. H. Gorman III, R. M. Fairman, J. E. Bavaria, R. C. Gorman, K. B. Chandran, and B. M. Jackson. Pathogenesis of acute aortic dissection: A finite element stress analysis. *Ann. Thorac. Surg.*, 91:458–463, 2011.

[227] C. A. Nienaber, R. E. Clough, N. Sakalihasan, T. Suzuki, R. Gibbs, F. Mussa, M. P. Jenkins, M. M. Thompson, A. Evangelista, J. S. M. Yeh, N. Cheshire, U. Rosendahl, and J. Pepper. Aortic dissection. *Nat. Rev. Dis. Primers*, 2:16071, 2016.

[228] J. A. Niestrawska, C. Viertler, P. Regitnig, T. U. Cohnert, G. Sommer, and G. A. Holzapfel. Microstructure and mechanics of healthy and aneurysmatic abdominal aortas: experimental analysis and modeling. *J. R. Soc. Interface*, 13:20160620, 2016.

[229] C. Noble, N. Smulders, R. Lewis, M. J. Carré, S. E. Franklin, S. MacNeil, and T. A. Taylor. Controlled peel testing of a model tissue for diseased aorta. *J. Biomech.*, 49:3667–3675, 2016.

[230] D. R. Nolan and J. P. McGarry. On the compressibility of arterial tissue. *Ann. Biomed. Eng.*, 44:993–1007, 2016.

[231] P. J. Oberwalder. Aneurysmen und Dissektionen der thorakalen Aorten: Definition und Pathologie. *J. Kardiol.*, 8:2–4, 2001.

[232] P. O'Boynick, K. D. Green, S. Batnitzky, J. J. Kepes, and R. Pietak. Aneurysm of the left middle cerebral artery caused by myxoid degeneration of the vessel wall. *Stroke*, 25:2283–2286, 1994.

[233] R. J. Okamoto, J. E. Wagenseil, W. R. DeLong, S. J. Peterson, N. T. Kouchoukos, and T. M. Sundt. Mechanical properties of dilated human ascending aorta. *Ann. Biomed. Eng.*, 30:624–635, 2002.

[234] C. Olsson, S. Thelin, E. Ståhle, A. Ekbom, and F. Granath. Thoracic aortic aneurysm and dissection: increasing prevalence and improved outcomes reported in a nationwide population-based study of more than 14,000 cases from 1987 to 2002. *Circulation*, 114:2611–2618, 2006.

[235] M. K. O'Connell, S. Murthy, S. Phan, C. Xu, J. Buchanan, R. Spilker, R. L. Dalman, C. K. Zarins, W. Denk, and C. A. Taylor. The three–dimensional micro– and nanostructure of the aortic medial lamellar unit measured using 3D confocal and electron microscopy imaging. *Matrix Biol.*, 27:171–181, 2008.

[236] Online Mendelian Inheritance in Man, OMIM ®. Johns Hopkins University, Baltimore, MD. `https://omim.org/`.

[237] V. Ottani, M. Raspanti, and A. Ruggeri. Collagen structure and functional implications. *Micron*, 32:251–260, 2001.

[238] S. Pal, A. Tsamis, S. Pasta, A. D'Amore, T. G. Gleason, D. A. Vorp, and S. Maiti. A mechanistic model on the role of radially-running collagen fibers on dissection properties of human ascending thoracic aorta. *J. Biomech.*, 47:981–988, 2014.

[239] A. Pandolfi and G. A. Holzapfel. Three-dimensional modeling and computational analysis of the human cornea considering distributed collagen fibril orientations. *J. Biomech. Eng.*, 130:061006 (12 pages), 2008.

[240] A. Pandolfi and M. Vasta. Fiber distributed hyperelastic modeling of biological tissues. *Mech. Mat.*, 44:151–162, 2012.

[241] H. Pannu, V. Tran-Fadulu, C. L. Papke, S. Scherer, Y. Liu, C. Presley, D. Guo, A. L. Estrera, H. J. Safi, A. R. Brasier, G. W. Vick, A. J. Marian, C. S. Raman, L. M. Buja, and D. M. Milewicz. MYH11 mutations result in a distinct vascular pathology driven by insulin-like growth factor 1 and angiotensin II. *Hum. Mole. Gen.*, 16:2453–2462, 2007.

[242] L. A. Pape, T. T. Tsai, E. M. Isselbacher, J. K. Oh, P. T. O'Gara, A. Evangelista, R. Fattori, G. Meinhardt, S. Trimarchi, E. Bossone, T. Suzuki, J. V. Cooper, J. B. Froehlich, C. A. Nienaber, K. A. Eagle, and International Registry of Acute Aortic Dissection (IRAD) Investigators. Aortic diameter > or = 5.5 cm is not a good predictor of type A aortic dissection: Observations from the International Registry of Acute Aortic Dissection (IRAD). *Circulation*, 116:1120–1127, 2007.

[243] L. A. Pape, M. Awais, E. M. Woznicki, T. Suzuki, S. Trimarchi, A. Evangelista, T. Myrmel, M. Larsen, K. M. Harris, K. Greason, M. Di Eusanio, E. Bossone, D. G. Montgomery, K. A. Eagle, C. A. Nienaber, E. M. Isselbacher, and P. O'Gara. Presentation, diagnosis, and outcomes of acute aortic dissection: 17-year trends from the international registry of acute aortic dissection. *J. Am. Coll. Cardiol.*, 66:350–358, 2015.

[244] S. Pasta, J. A. Phillippi, T. G. Gleason, and D. A. Vorp. Effect of aneurysm on the mechanical dissection properties of the human ascending thoracic aorta. *J. Thorac. Cardiovasc. Surg.*, 143:460–467, 2012.

[245] K. Patel, M. A. Zafar, B. A. Ziganshin, and J. A. Elefteriades. Diabetes Mellitus: Is it protective against aneurysm? A narrative review. *Cardiol.*, 141:107–122, 2018.

[246] R. Pearson, N. Philips, R. Hancock, S. Hashim, M. Field, D. Richens, and D. McNally. Regional wall mechanics and blunt traumatic aortic rupture at the isthmus. *Eur. J. Cardiothorac. Surg.*, 34:616–622, 2008.

[247] L. Pereira, K. Andrikopoulos, J. Tian, S. Y. Lee, D. R. Keene, R. Ono, D. P. Reinhardt, L. Y. Sakai, N. J. Biery, T. Bunton, H. C. Dietz, and F. Ramirez. Targetting of the gene encoding fibrillin-1 recapitulates the vascular aspect of Marfan syndrome. *Nature Genet.*, 17:218–222, 1997.

[248] S. Peterss, A. M. Mansour, J. A. Ross, I. Vaitkeviciute, P. Charilaou, J. Dumfarth, H. Fang, B. A. Ziganshin, J. A. Rizzo, A. J. Adeniran, and J. A. Elefteriades. Changing pathology of the thoracic aorta from acute to chronic dissection: Literature review and insights. *J. Am. Coll. Cardiol.*, 68:1054–1065, 2016.

[249] T. Pham, C. Martin, J. Elefteriades, and W. Sun. Biomechanical characterization of ascending aortic aneurysm with concomitant bicuspid aortic valve and bovine aortic arch. *Acta Biomater.*, 9:7927–7936, 2013.

[250] J. A. Phillippi, B. R. Green, M. A. Eskay, M. P. Kotlarczyk, M. R. Hill, A. M. Robertson, S. C. Watkins, D. A. Vorp, and T. G. Gleason. Mechanism of aortic medial matrix remodeling is distinct in patients with bicuspid aortic valve. *J. Thorac. Cardiovasc. Surg.*, 147:1056–1064, 2014.

[251] J. E. Pichamuthu, J. A. Phillippi, D. A. Cleary, D. W. Chew, J. Hempel, D. A. Vorp, and T. G. Gleason. Differential tensile strength and collagen composition in ascending aortic aneurysms by aortic valve phenotype. *Ann. Thorac. Surg.*, 96: 2147–2154, 2013.

[252] S. Polzer and C. T. Gasser. Biomechanical rupture risk assessment of abdominal aortic aneurysms based on a novel probabilistic rupture risk index. *J. R. Soc. Interface*, 12:20150852, 2015.

[253] P. Pomianowski and J. A. Elefteriades. The genetics and genomics of thoracic aortic disease. *Ann. Cardiothorac. Surg.*, 2:271–279, 2013.

[254] T. Prijon and B. Ermenc. Classification of blunt aortic injuries a new systematic overview of aortic trauma. *Forensic. Sci. Int.*, 195:6–9, 2010.

[255] P. P. Purslow. Positional variations in fracture toughness, stiffness and strength of descending thoracic pig aorta. *J. Biomech.*, 16:947–953, 1983.

[256] R. A. Quintana and R. W. Taylor. Cellular mechanisms of aortic aneurysm formation. *Circ. Res.*, 124:607–618, 2019.

[257] A. Rachev and K. Hayashi. Theoretical study of the effects of vascular smooth muscle contraction on strain and stress distributions in arteries. *Ann. Biomed. Eng.*, 27:459–468, 1999.

[258] M. L. Raghavan, M. W. Webster, and D. A. Vorp. Ex vivo biomechanical behavior of abdominal aortic aneurysm: assesment using a new mathematical model. *Ann. Biomed. Eng.*, 24:573–582, 1996.

[259] M. L. Raghavan, J. Kratzberg, E. M. Castro de Tolosa, M. M. Hanaoka, P. Walker, and E. S. da Silva. Regional distribution of wall thickness and failure properties of human abdominal aortic aneurysm. *J. Biomech.*, 39:3010–3016, 2006.

[260] M. L. Raghavan, M. M. Hanaoka, J. A. Kratzberg, M. de Lourdes Higuchi, and E. S. da Silva. Biomechanical failure properties and microstructural content of ruptured and unruptured abdominal aortic aneurysms. *J. Biomech.*, 44:2501–2507, 2011.

[261] R. Raghupathy and V. H. Barocas. A closed-form structural model of planar fibrous tissue mechanics. *J. Biomech.*, 42:1424–1428, 2009.

[262] K. Rajagopal, C. Bridges, and K. R. Rajagopal. Towards an understanding of the mechanics underlying aortic dissection. *Biomech. Model. Mechanobiol.*, 6: 345–359, 2007.

[263] F. Ramirez and H. C. Dietz. Fibrillin-rich microfibrils: Structural determinants of morphogenetic and homeostatic events. *J. Cell Physiology*, 213:326–330, 2007.

[264] F. Ramirez, C. Caescu, E. Wondimu, and J. Galatioto. Marfan syndrome; A connective tissue disease at the crossroads of mechanotransduction, TGF-β signaling and cell stemness. *Matrix Biol.*, 71–72:82–89, 2018.

[265] C. Reeps, A. Maier, J. Pelisek, F. Härtl, V. Grabher-Meier, W. A. Wall, M. Essler, H. H. Eckstein, and M. W. Gee. Measuring and modeling patient-specific distributions of material properties in abdominal aortic aneurysm wall. *Biomech. Model. Mechanobiol.*, 12:717–733, 2013.

[266] J. A. G. Rhodin. Architecture of the vessel wall. In D. F. Bohr, A. D. Somlyo, and H. V. Sparks, editors, *Handbook of Physiology, The Cardiovascular System*, volume 2, pages 1–31. American Physiologial Society, Bethesda, Maryland, 1980.

[267] D. Richens, M. Field, M. Neale, and C. Oakley. Review: The mechnanism of injury in blunt traumatic rupture of the aorta. *Eur. J. Cardio-thorac.*, 21:288–293, 2002.

[268] M. R. Roach. The pattern of elastin in the aorta and large arteries of mammals. *Ciba Foundation Symp.*, 100:37–55, 1983.

[269] M. R. Roach and A. C. Burton. The reason for the shape of the distensibility curves of arteries. *Canad. J. Biochem. Physiol.*, 35:681–690, 1957.

[270] M. R. Roach and S. H. Song. Variations in strength of the porcine aorta as a function of location. *Clin. Invest. Med.*, 17:308–318, 1994.

[271] S. Roccabianca, G. A. Ateshian, and J. D. Humphrey. Biomechanical roles of medial pooling of glycosaminoglycans in thoracic aortic dissection. *Biomech. Model. Mechanobiol.*, 13:13–25, 2014.

[272] A. Romo, P. Badel, A. Duprey, J. P. Favre, and S. Avril. In vitro analysis of localized aneurysm rupture. *J. Biomech.*, 47:607–616, 2014.

[273] F. Roohbakhshan and R. A. Sauer. Efficient isogeometric thin shell formulations for soft biological materials. *Biomech. Model. Mechanobiol.*, 16:1569–1597, 2017.

[274] F. Roohbakhshan, T. X. Duong, and R. A. Sauer. A projection method to extract biological membrane models from 3D material models. *J. Mech. Behav. Biomed. Mater.*, 58:90–104, 2016.

[275] J. M. Ruddy, J. A. Jones, and J. S. Ikonomidis. Pathophysiology of thoracic aortic aneurysm (TAA): is it not one uniform aorta? Role of embryologic origin. *Prog. Cardiovasc. Dis.*, 56:68–73, 2013.

[276] L. Sabatier, J. Djokic, D. Hubmacher, D. Dzafik, V. Nelea, and D. P. Reinhardt. Heparin/heparan sulfate controls fibrillin-1, -2 and -3 self-interactions in microfibril assembly. *Feb.*, 588:2890–2897, 2014.

[277] M. S. Sacks. Incorporation of experimentally-derived fiber orientation into a structural constitutive model for planar collagenous tissues. *J. Biomech. Eng.*, 125:280–287, 2003.

[278] A. A. Saeyeldin, C. A. Velasquez, S. U. B. Mahmood, A. J. Brownstein, M. A. Zafar, B. A. Ziganshin, and J. A. Elefteriades. Thoracic aortic aneurysm: unlocking the “silent killer” secrets. *Gen. Thorac. Cardiovasc. Surg.*, 2017.

[279] A. Saini, C. Berry, and S. Greenwald. Effect of age and sex on residual stress in the aorta. *J. Vasc. Res.*, 32:398–405, 1995.

[280] L. Sanford, I. Ormsby, A. Gittenberger-de Groot, H. Sariola, R. Friedman, G. Boivin, E. Cardell, and T. Doetschman. TGFβ2 knockout mice have multiple developmental defects that are non-overlapping with other TGFβ knockout phenotypes. *Development*, 124:2659–2670, 1997.

[281] S. G. Sassani, S. Tsangaris, and D. P. Sokolis. Layer- and region-specific material characterization of ascending thoracic aortic aneurysms by microstructure-based models. *J. Biomech.*, 48:3757–3765, 2015.

[282] P. Sawadkar, S. Alexander, M. Tolk, J. Wong, D. McGrouther, L. Bozec, and V. Mudera. Development of a surgically optimized graft insertion suture technique to accommodate a tissue-engineered tendon in vivo. *BioResearch Open Access*, 2:327–335, 2013.

[283] M. Schermerhorn. A 66-year-old man with an abdominal aortic aneurysm: review of screening and treatment. *J. Am. Med. Assoc.*, 302:2015–2022, 2009.

[284] F. Schmid, G. Sommer, M. Rappolt, C. A. J. Schulze-Bauer, P. Regitnig, G. A. Holzapfel, P. Laggner, and H. Amenitsch. In situ tensile testing of human aortas by time-resolved small angle X-ray scattering. *Synchro. Rad.*, 12:727–733, 2005.

[285] A. J. Schriefl, A. J. Reinisch, S. Sankaran, D. M. Pierce, and G. A. Holzapfel. Quantitative assessment of collagen fiber orientations from 2D images of soft biological tissues. *J. R. Soc. Interface*, 9:3081–3093, 2012.

[286] A. J. Schriefl, G. Zeindlinger, D. M. Pierce, P. Regitnig, and G. A. Holzapfel. Determination of the layer-specific distributed collagen fiber orientations in human thoracic and abdominal aortas and common iliac arteries. *J. R. Soc. Interface*, 9: 1275–1286, 2012.

[287] A. J. Schriefl, H. Wolinski, P. Regitnig, S. D. Kohlwein, and G. A. Holzapfel. An automated approach for three-dimensional quantification of fibrillar structures in optically cleared soft biological tissues. *J. R. Soc. Interface*, 10:20120760, 2013.

[288] U. Schwarze, M. Atkinson, G. G. Hoffman, D. S. Greenspan, and P. H. Byers. Null alleles of the COL5A1 gene of type V collagen are a cause of the classical forms of Ehlers-Danlos syndrome (types I and II). *Am. J. Hum. Genet.*, 66:1757–1765, 2000.

[289] U. Schwarze, W. I. Schievink, E. Petty, M. R. Jaff, D. Babovic-Vuksanovic, K. J. Cherry, M. Pepin, and P. H. Byers. Haploinsufficiency for one COL3A1 allele of type III procollagen results in a phenotype similar to the vascular form of Ehlers-Danlos syndrome, Ehlers-Danlos syndrome type IV. *Am. J. Hum. Genet.*, 69: 989–1001, 2001.

[290] S. Sevitt. The mechanisms of traumatic rupture of the thoracic aorta. *Br. J. Surg.*, 64:166–173, 1977.

[291] S. B. Shah, C. Witzenburg, M. F. Hadi, H. P. Wagner, J. M. Goodrich, P. W. Alford, and V. H. Barocas. Prefailure and failure mechanics of the porcine ascending thoracic aorta: experiments and a multiscale model. *J. Biomech. Eng.*, 136:021028–1, 2014.

[292] N. Shahmansouri, M. Alreshidan, A. Emmott, K. Lachapelle, R. Cartier, R. L. Leask, and R. Mongrain. Evaluating ascending aortic aneurysm tissue toughness: Dependence on collagen and elastin contents. *J. Mech. Behav. Biomed. Mater.*, 64:262 – 271, 2016.

[293] S. Sherifova, G. Sommer, C. Viertler, P. Regitnig, T. Caranasos, M. A. Smith, B. E. Griffith, R. W. Ogden, and G. A. Holzapfel. Failure properties and microstructure of healthy and aneurysmatic human thoracic aortas subjected to uniaxial extension with a focus on the media. *Acta Biomater.*, 2019. in press.

[294] V. R. Sherman, W. Yang, and M. A. Meyers. The material science of collagen. *J. Mech. Behav. Biomed. Mater.*, 52:22–50, 2015.

[295] K. Shimizu, R. N. Mitchell, and P. Libby. Inflammation and cellular immune responses in abdominal aortic aneurysms. *Arterioscler. Thromb. Vasc. Biol.*, 26: 987–994, 2006.

[296] M. J. Shkrum, K. J. McClafferty, R. N. Green, E. S. Nowak, and J. G. Young. Mechanisms of aortic injury in fatalities occurring in motor vehicle collisions. *J. Forensic Sci.*, 44:44–56, 1999.

[297] F. H. Silver, D. L. Christiansen, and C. M. Buntin. Mechanical properties of the aorta: A review. *Crit. Rev. Biomed. Eng.*, 17:323–358, 1989.

[298] P. Skacel and J. Bursa. Poisson's ratio of arterial wall - inconsistency of constitutive models with experimental data. *J. Mech. Behav. Biomed. Mater.*, 54: 316–327, 2016.

[299] R. Skalak, G. Dasgupta, M. Moss, E. Otten, P. Dullemeijer, and H. Vilmann. Analytical description of growth. *J. Theor. Biol.*, 94:555–577, 1982.

[300] R. Skalak, S. Zargaryan, R. K. Jain, P. A. Netti, and A. Hoger. Compatibility and the genesis of residual stress by volumetric growth. *J. Math. Biol.*, 34:889–914, 1996.

[301] D. P. Sokolis and D. C. Iliopoulos. Impaired mechanics and matrix metalloproteinases/inhibitors expression in female ascending thoracic aortic aneurysms. *J. Mech. Behav. Biomed. Mater.*, 34:154–164, 2014.

[302] D. P. Sokolis, E. P. Kritharis, A. T. Giagini, K. M. Lampropoulos, S. A. Papadodima, and D. C. Iliopoulos. Biomechanical response of ascending thoracic aortic aneurysms: association with structural remodelling. *Comput. Methods Biomech. Biomed. Engin.*, 15:231–248, 2012.

[303] D. P. Sokolis, E. P. Kritharis, and D. C. Iliopoulos. Effect of layer heterogeneity on the biomechanical properties of ascending thoracic aortic aneurysms. *Med. Biol. Eng. Comput.*, 50:1227–1237, 2012.

[304] G. Sommer, T. C. Gasser, P. Regitnig, M. Auer, and G. A. Holzapfel. Dissection properties of the human aortic media: an experimental study. *J. Biomech. Eng.*, 130:021007–1–12, 2008.

[305] G. Sommer, M. Eder, L. Kovacs, H. Pathak, L. Bonitz, C. Mueller, P. Regitnig, and G. A. Holzapfel. Multiaxial mechanical properties and constitutive modeling of human adipose tissue: a basis for preoperative simulations in plastic and reconstructive surgery. *Acta Biomater.*, 9:9036–9048, 2013.

[306] G. Sommer, A. Schriefl, G. Zeindlinger, A. Katzensteiner, H. Ainödhofer, A. Saxena, and G. A. Holzapfel. Multiaxial mechanical response and constitutive modeling of esophageal tissues: impact on esophageal tissue engineering. *Acta Biomater.*, 9:9379–9091, 2013.

[307] G. Sommer, A. J. Schriefl, M. Andrä, M. Sacherer, C. Viertler, H. Wolinski, and G. A. Holzapfel. Biomechanical properties and microstructure of human ventricular myocardium. *Acta Biomater.*, 24:172–192, 2015.

[308] G. Sommer, S. Sherifova, P. J. Oberwalder, O. E. Dapunt, P. A. Ursomanno, A. DeAnda, B. E. Griffith, and G. A. Holzapfel. Mechanical strength of aneurysmatic and dissected human thoracic aortas at different shear loading modes. *J. Biomech.*, 49:2374–2382, 2016.

[309] G. Sommer, C. Benedikt, J. A. Niestrawska, G. Hohenberger, C. Viertler, P. Regitnig, T. U. Cohnert, and G. A. Holzapfel. Mechanical response of human subclavian and iliac arteries to extension, inflation and torsion. *Acta Biomater.*, 75: 235–252, 2018.

[310] R. Soyer, J. P. Bessou, F. Bouchart, A. Tabley, D. Mouton-Schleifer, J. Arrignon, and M. Redonnet. Acute traumatic isthmic aortic rupture: Long-term results in 49 patients. *Eur. J. Cardiothorac. Surg.*, 6:431–437, 1992.

[311] S. Sprangers and V. Everts. Molecular pathways of cell-mediated degradation of fibrillar collagen. *Matrix Biol.*, 75-76:190–200, 2019.

[312] H. C. Stary. *Atlas of Atherosclerosis: Progression and Regression*. The Parthenon Publishing Group, Boca Raton, London, New York, Washington, D.C., 2nd edition, 2003.

[313] B. D. Stemper, N. Yoganandan, M. R. Stineman, T. A. Gennarelli, J. L. Baisden, and F. A. Pintar. Mechanics of fresh, refrigerated, and frozen arterial tissue. *J. Surg. Res.*, 139(2):236–242, 2007.

[314] S. Sugita and T. Matsumoto. Novel biaxial tensile test for studying aortic failure phenomena at a microscopic level. *Biomed. Eng. Online*, 12:3, 2013.

[315] S. Sugita and T. Matsumoto. Heterogeneity of deformation of aortic wall at the microscopic level:contribution of heterogeneous distribution of collagen fibers in the wall. *Biomed. Mater. Eng.*, 23:447–461, 2013.

[316] S. Sugita and T. Matsumoto. Local distribution of collagen fibers determines crack initiation site and its propagation direction during aortic rupture. *Biomech. Model. Mechanobiol.*, 17:577–587, 2018.

[317] S. Sugita, T. Matsumoto, T. Ohashi, K. Kumagai, H. Akimoto, K. Tabayashi, and M. Sato. Evaluation of rupture properties of thoracic aortic aneurysms in a pressure-imposed test for rupture risk estimation. *Cardiovascular Engineering and Technology*, 3:41–51, 2012.

[318] L. G. Svensson, N. T. Kouchoukos, D. C. Miller, J. E. Bavaria, J. S. Coselli, M. A. Curi, H. Eggebrecht, J. A. Elefteriades, R. Erbel, T. G. Gleason, B. W. Lytle, R. S. Mitchell, C. A. Nienaber, E. E. Roselli, H. J. Safi, R. J. Shemin, G. A. Sicard, T. M. Sundt 3rd, W. Y. Szeto, G. H. Wheatley 3rd, and Society of Thoracic Surgeons Endovascular Surgery Task Force. Expert consensus document on the treatment of descending thoracic aortic disease using endovascular stent-grafts. *Ann. Thorac. Surg.*, 85:S1–S41, 2008.

[319] K. Takamizawa and K. Hayashi. Strain energy density function and uniform strain hypothesis for arterial mechanics. *J. Biomech.*, 20:7–17, 1987.

[320] A. S. M. Tam, M. C. Sapp, and M. R. Roach. The effect of tear depth on the propagation of aortic dissections in isolated porcine thoracic aorta. *J. Biomech.*, 31:673–676, 1998.

[321] R. L. Taylor. *FEAP – A Finite Element Analysis Program, Version 8.4 User Manual*. University of California at Berkeley, Berkeley, California, 2013.

[322] M. J. Thubrikar, M. Labrosse, F. Robicsek, J. Al-Soudi, and B. Fowler. Mechanical properties of abdominal aortic aneurysm wall. *J. Med. Eng. Technol.*, 25: 133–142, 2001.

[323] J. R. Thunes, J. A. Phillippi, T. G. Gleason, D. A. Vorp, and S. Maiti. Structural modeling reveals microstructure-strength relationship for human ascending thoracic aorta. *J. Bioeng.*, 71:84 – 93, 2018.

[324] L. Tian, Z. Wang, Y. Liu, J. C. Eickhoff, K. W. Eliceiri, and N. C. Chesler. Validation of an arterial constitutive model accounting for collagen content and crosslinking. *Acta Biomater.*, 131:276–287, 2016.

[325] I. M. Tiessen and M. R. Roach. Factors in the initiation and propagation of aortic dissections in human autopsy aortas. *J. Biomech. Eng.*, 115:123–125, 1993.

[326] J. Tong, T. Cohnert, P. Regitnig, and G. A. Holzapfel. Effects of age on the elastic properties of the intraluminal thrombus and the thrombus-covered wall in abdominal aortic aneurysms: biaxial extension behavior and material modeling. *Eur. J. Vasc. Endovasc. Surg.*, 42:207–219, 2011.

[327] J. Tong, A. J. Schriefl, T. Cohnert, and G. A. Holzapfel. Gender differences in biomechanical properties, thrombus age, mass fraction and clinical factors of abdominal aortic aneurysms. *Eur. J. Vasc. Endovasc. Surg.*, 45:364–372, 2013.

[328] J. Tong, T. Cohnert, P. Regitnig, J. Kohlbacher, R. Birner-Gruenberger, A. J. Schriefl, G. Sommer, and G. A. Holzapfel. Variations of dissection properties and mass fractions with thrombus age in human abdominal aortic aneurysms. *J. Biomech.*, 47:14–23, 2014.

[329] J. Tong, T. Cohnert, and G. A. Holzapfel. Diameter-related variations of geometrical, mechanical and mass fraction data in the anterior portion of abdominal aortic aneurysms. *Eur. J. Vasc. Endovasc. Surg.*, 49:262–270, 2015.

[330] J. Tong, Y. Cheng, and G. A. Holzapfel. Mechanical assessment of arterial dissection in health and disease: advancements and challenges. *J. Biomech.*, 49: 2366–2373, 2016.

[331] G. J. Tortora and B. Derrickson. *Principles of Anatomy and Physiology*. John Wiley & Sons, 13th edition, 2011.

[332] R. M. Touyz, R. Alves-Lopes, F. J. Rios, L. L. Camargo, A. Anagnostopoulou, and A. C. Montezano. Vascular smooth muscle contraction in hypertension. *Cardiovasc. Res.*, 114:529–539, 2018.

[333] O. Trabelsi, F. M. Davis, J. F. Rodriguez-Matas, A. Duprey, and S. Avril. Patient specific stress and rupture analysis of ascending thoracic aneurysms. *J. Biomech.*, 48:1836–1843, 2015.

[334] O. Trabelsi, M. Gutierrez, S. Farzaneh, A. Duprey, and S. Avril. A non-invasive methodology for ATAA rupture risk estimation. *J. Biomech.*, 66:119–126, 2018.

[335] A. Tsamis, J. A. Phillippi, R. G. Koch, S. Pasta, A. D'Amore, S. C. Watkins, W. R. Wagner, T. G. Gleason, and D. A. Vorp. Fiber micro-architecture in the longitudinal-radial and circumferential-radial planes of ascending thoracic aortic aneurysm media. *J. Biomech.*, 46:2787–2794, 2013.

[336] A. Tsamis, J. A. Phillippi, R. G. Koch, P. G. Chan, J. T. Krawiec, A. D'Amore, S. C. Watkins, W. R. Wagner, D. A. Vorp, and T. G. Gleason. Extracellular matrix fiber microarchitecture is region-specific in bicuspid aortic valve-associated ascending aortopathy. *J. Thorac. Cardiovasc. Surg.*, 151:1718–1728.e5, 2016.

[337] S. G. M. Uzel and M. J. Buehler. Molecular structure, mechanical behavior and failure mechanism of the C-terminal cross-link domain in type I collagen. *J. Mech. Behav. Biomed. Mater.*, 4:153–161, 2011.

[338] S. R. Vallabhaneni, G. L. Gilling-Smith, T. V. How, S. D. Carter, J. A. Brennan, and P. L. Harris. Heterogeneity of tensile strength and matrix metalloproteinase activity in the wall of abdominal aortic aneurysms. *J. Endovasc. Ther.*, 11:494–502, 2004.

[339] C. van Baardwijk and M. R. Roach. Factors in the propagation of aortic dissection in canine thoracic aortas. *J. Biomech.*, 20:67–73, 1987.

[340] V. W. M. van Hinsberg. Physiology of blood vessels. In *The ESC Textbook of Vascular Biology*, pages 17–30. Oxford University Press, 2017.

[341] J. P. Vande Geest, E. D. Dillavou, E. S. Di Martino, M. Oberdier, A. Bohra, M. S. Makaroun, and D. A. Vorp. Gender-related differences in the tensile strength of abdominal aortic aneurysm. *Ann. N.Y. Acad. Sci.*, 1085:400–402, 2006.

[342] J. P. Vande Geest, E. S. Di Martino, A. Bohra, M. S. Makaroun, and D. A. Vorp. A biomechanics-based rupture potential index for abdominal aortic aneurysm risk assessment: demonstrative application. *Ann. N. Y. Acad. Sci.*, 1085:11–21, 2006.

[343] J. P. Vande Geest, D. H. J. Wang, S. R. Wisniewski, M. S. Makaroun, and D. A. Vorp. Towards a noninvasive method for determination of patient-specific wall strength distribution in abdominal aortic aneurysms. *Ann. Biomed. Eng.*, 34: 1098–1106, 2006.

[344] M. Vasta, A. Gizzi, and A. Pandolfi. On three- and two-dimensional fiber distributed models of biological tissues. *Probabilist. Eng. Mech.*, 37:170–179, 2014.

[345] D. Viano. Biomechanics of nonpenetrating aortic trauma: a review. *SAE Technical Paper 831608*, pages 109–114, 1983.

[346] K. Y. Volokh. On arterial fiber dispersion and auxetic effect. *J. Biomech.*, 61: 123–130, 2017.

[347] K. von der Mark. Localization of collagen types in tissues. *Int. Rev. Conn. Tiss. Res.*, 9:265–324, 1981.

[348] D. A. Vorp. Biomechanics of abdominal aortic aneurysm. *J. Biomech.*, 40:1887–1902, 2007.

[349] D. A. Vorp, M. L. Raghavan, S. C. Muluk, M. S. Makaroun, D. L. Steed, R. Shapiro, and M. W. Webster. Wall strength and stiffness of aneurysmal and nonaneurysmal abdominal aorta. *Ann. N.Y. Acad. Sci.*, 800:274–276, 1996.

[350] D. A. Vorp, P. C. Lee, D. H. Wang, M. S. Makaroun, E. M. Nemoto, S. Ogawa, and M. W. Webster. Association of intraluminal thrombus in abdominal aortic aneurysm with local hypoxia and wall weakening. *J. Vasc. Surg.*, 34:291–299, 2001.

[351] D. A. Vorp, B. J. Schiro, M. P. Ehrlich, T. S. Juvonen, M. A. Ergin, and B. P. Griffith. Effect of aneurysm on the tensile strength and biomechanical behavior of the ascending thoracic aorta. *Ann. Thorac. Surg.*, 800:1210–1214, 2003.

[352] J. E. Wagenseil and R. P. Mecham. Vascular extracellular matrix and arterial mechanics. *Physiol. Rev.*, 89:957–989, 2009.

[353] L. Wang, D.-C. Guo, J. Cao, L. Gong, K. E. Kamm, E. Regalado, L. Li, S. Shete, W.-Q. He, M.-S. Zhu, S. Offermanns, D. Gilchrist, J. Elefteriades, J. T. Stull, and D. M. Milewicz. Mutations in myosin light chain kinase cause familial aortic dissections. *Am. J. Hum. Genet.*, 87:701–707, 2010.

[354] L. Wang, J. Zhang, W. Fu, D. Guo, J. Jiang, and Y. Wang. Association of smooth muscle cell phenotypes with extracellular matrix disorders in thoracic aortic dissection. *J. Vasc. Surg.*, 56:1698–1709, 2012.

[355] X. Wang, S. A. LeMaire, L. Chen, Y. H. Shen, Y. Gan, H. Bartsch, S. A. Carter, B. Utama, H. Ou, J. S. Coselli, and X. L. Wang. Increased collagen deposition and elevated expression of connective tissue growth factor in human thoracic aortic dissection. *Circulation*, 114:I–200–I–205, 2006.

[356] Z. Wang and N. C. Chesler. Role of collagen content and cross-linking in large pulmonary arterial stiffening after chronic hypoxia. *Biomech. Model. Mechanobiol.*, 11:279–289, 2012.

[357] H. Weisbecker, C. Viertler, D. M. Pierce, and G. A. Holzapfel. The role of elastin and collagen in the softening behavior of the human thoracic aortic media. *J. Biomech.*, 46:1859–1865, 2013.

[358] J. A. Weiss, B. N. Maker, and S. Govindjee. Finite element implementation of incompressible, transversely isotropic hyperelasticity. *Comput. Meth. Appl. Mech. Eng.*, 135:107–128, 1996.

[359] T. J. Wess. Collagen fibril form and function. *Adv. Protein Chem.*, 70:341–374, 2005.

[360] A. Whelan, J. Duffy, R. Gaul, D. O'Reilly, D. R. Nolan, P. Gunning, C. Lally, and B. Murphy. Collagen fibre orientation and dispersion govern ultimate tensile strength, stiffness and the fatigue performance of bovine pericardium. *J. Mech. Behav. Biomed. Mater.*, 90:54–60, 2019.

[361] T. N. Wight. Cell biology of arterial proteoglycans. *Arterioscler. Thromb. Vasc. Biol.*, 9:1–20, 1989.

[362] T. N. Wight and M. J. Merrilees. Proteoglycans in atherosclerosis and restenosis. *Circ. Res.*, 94:1158–1167, 2004.

[363] T. N. Wight, M. G. Kinsella, and E. E. Qwarnström. The role of proteoglycans in cell adhesion, migration and proliferation. *Curr. Opin. Cell Biol.*, 4:793–801, 1992.

[364] T. N. Wight, B. P. Toole, and V. C. Hascall. Hyaluronan and the aggregating proteoglycans. In M. R. P., editor, *The Extracellular Matrix: an Overview*, pages 147–195. Springer Berlin Heidelberg, 2011.

[365] H. Wilson and N. W. Roome. Traumatic shock syndrome following rupture of the aorta and multiple fractures. *Am. J. Surg.*, 23:333, 1933.

[366] A. Wittek, T. Hawkins, and K. Miller. On the unimportance of constitutive models in computing brain deformation for image-guided surgery. *Biomech. Model. Mechanobiol.*, 8:77–84, 2009.

[367] C. M. Witzenburg, R. Y. Dhume, S. B. Shah, C. E. Korenczuk, H. P. Wagner, P. W. Alford, and V. H. Barocas. Failure of the porcine ascending aorta: multidirectional experiments and a unifying microstructural model. *J. Biomech. Eng.*, 139:031005–031005–14, 2017.

[368] H. Wolinsky. Comparison of medial growth of human thoracic and abdominal aortas. *Circ. Res.*, 27:531–538, 1970.

[369] H. Wolinsky and S. Glagov. A lamellar unit of aortic medial structure and function in mammals. *Circ. Res.*, 20:90–111, 1967.

[370] H. Wolinsky and S. Glagov. Comparison of abdominal and thoracic aortic medial structure in mammals. deviation of man from the usual pattern. *Circ. Res.*, 25: 677–686, 1969.

[371] D. Wu, Y. H. Shen, L. Russell, J. S. Coselli, and S. A. LeMaire. Molecular mechanisms of thoracic aortic dissection. *J. Surg. Res.*, 184:907–924, 2013.

[372] J. Xiong, Z. Wu, C. Chen, Y. Wei, and W. Guo. Association between diabetes and prevalence and growth rate of abdominal aortic aneurysms: A meta-analysis. *Int. J. Cardiol.*, 221:484–495, 2016.

[373] B. Xu, M. J. Chow, and Y. Zhang. Experimental and modeling study of collagen scaffolds with the effects of crosslinking and fiber alignment. *Int. J. Biomater.*, 2011:172389, 2011.

[374] C. Xu, S. Lee, T. M. Singh, E. Sho, X. Li, M. Sho, H. Masuda, and C. K. Zarins. Molecular mechanisms of aortic wall remodeling in response to hypertension. *J. Vasc. Surg.*, 33:570–578, 2001.

[375] J. Xu and G.-P. Shi. Vascular wall extracellular matrix proteins and vascular diseases. *Biochim. Biophys. Acta, Mol. Basis Dis.*, 1842:2106–2119, 2014.

[376] Y. Xu, m. Hua, m. Sun, m. Zhou, and F. Xu. Effects of freezing rates and dimethyl sulfoxide concentrations on thermal expansion of rabbit aorta during freezing phase change as measured by thermo mechanical analysis. *J. Biomech.*, 40:3201–3206, 2007.

[377] C. Yu and R. W. Jeremy. Angiotensin, transforming growth factor β and aortic dilatation in Marfan syndrome: Of mice and humans. *IJC Heart & Vasc.*, 18: 71–80, 2018.

[378] P. D. Yurchenco and B. L. Patton. Developmental and pathogenic mechanisms of basement membrane assembly, 2009.

[379] M. A. Zehnder. Delayed post-traumatic rupture of the aorta in a young healthy individual after closed injury; mechanical-etiological considerations. *Angiology*, 7:252–267, 1956.

[380] L. Zhu, R. Vranckx, P. K. Van Kien, A. Lalande, N. Boisset, F. Mathieu, M. Wegman, L. Glancy, J.-M. Gasc, F. Brunotte, P. Bruneval, J.-E. Wolf, J.-B. Michel, and X. Jeunemaitre. Mutations in myosin heavy chain 11 cause a syndrome associating thoracic aortic aneurysm/aortic dissection and patent ductus arteriosus. *Nature Genet.*, 38:343–349, 2006.

[381] J. L. Zitnay, Y. Li, Z. Qin, B. H. San, B. Depalle, S. P. Reese, M. J. Buehler, S. M. Yu, and J. A. Weiss. Molecular level detection and localization of mechanical damage in collagen enabled by collagen hybridizing peptides. *Nat. Commun.*, 8: 14913, 2017.